Numerical simulations of inductively coupled plasmas for applications in the microelectronics industry

Proefschrift voorgelegd tot het behalen van
de graad van Doctor in de Wetenschappen aan
de Universiteit Antwerpen te verdedigen door

Stefan Tinck

Promotor
Prof. Dr. Annemie Bogaerts

Faculteit Wetenschappen
Departement Chemie
Antwerpen 2011

Universiteit Antwerpen

Universiteit Antwerpen

Faculteit Wetenschappen
Departement Chemie

Numerical simulations of inductively coupled plasmas for applications in the microelectronics industry

Proefschrift voorgelegd tot het behalen
van de graad van Doctor in de Wetenschappen
aan de Universiteit Antwerpen
te verdedigen door

Stefan Tinck

Promotor: Prof. Dr. Annemie Bogaerts

Antwerpen, 2011

Contents

Part III Results and discussion

Acknowledgements

First and foremost, I would like to express my utmost gratitude and respect to my promoter, Prof. Dr. Annemie Bogaerts; the “mother” of our research group. I would like to thank her for giving me the opportunity to start a PhD in the research group PLASMANT and for introducing me to plasma etching as applied in the microelectronics industry; a topic that I loved to investigate. I would also like to mention my appreciation for her remarkable and inexhaustible assistance in solving the various problems encountered during my PhD. I am also very grateful for the many opportunities I got from Annemie to attend a great number of conferences in different countries during my PhD.

The Interuniversitary Microelectronics Center (IMEC) and the Institute for the Promotion of Innovation through Science and Technology Flanders (IWT Flanders) are acknowledged for financial support. Also the CalcUA computing facilities of the University of Antwerp are acknowledged.

My utmost thanks also go to Prof. Mark Kushner for providing the computational model applied in this work (HPEM), and for interesting discussions and advice. Not only Mark, but also co-workers, especially Yang Yang and Mingmei Wang are acknowledged for helping me to get a better understanding of the model.

As a member of PLASMANT, which is a modeling group, I am grateful for the fact that I also got the chance to acquire experimental experience at

IMEC in Leuven. This would not have been possible without the help of a large number of people from IMEC. Particularly I would like to thank Werner Boullart, Denis Shamiryan and Stefan De Gendt for valuable (experimental) advice and discussions. Also Alexey Milenin, Marc Schaekers, Dries Dictus, Johan Wouters and Elisabeth Camerotto are acknowledged for answering my many various questions and for making it fun to be at IMEC.

However, during my PhD, most of my time was spent in the research group PLASMANT. I would therefore like to thank all my colleagues from the group for uncountable interesting discussions and for creating a nice atmosphere at work. So, Ming, Shuxia, Fujun, Violeta, Evi, Maxie, Axel, Steluta, Maksudbek, Wouter (Woody), David, Helmut, Maryam, Christophe, Wouter (Ewout), Tom, Péter, Erik, Robby, Umedjon, Chen, Luc, Prof. Gijbels, Neyda, Antonio and all the others I forgot to mention… I had lots of fun at work thanks to you!

Some members of the group deserve my special thanks:

In particular, I would like to thank Ming once more for helping me really a lot with my PhD in various ways. Ming, you are one of the most helpful persons I know. I wish you good luck in your future career!

Special thanks also go to Neyda with whom I always had very nice and helpful non-work related conversations at the office. Thank you Neyda for making it fun to come to the office!

I would also like to thank Luc for his willingness to solve all kinds of practical problems and for having really everything you can imagine in his drawer.

Moreover, Wouter Wendelen is also acknowledged for his unbelievable talent to draw cartoons.

I am also thankful to know Antonio Martin, who taught me a lot about playing guitar. The time you were in our group was way too short!

Besides people from work, some people from my personal life have encouraged or helped me in one way or another and also deserve my utmost gratitude:

I would like to thank my best friends for bringing so much joy to my life. Tim, Sara, Jo, Bart, Anke, Koen, Zonhild and Aline, thank you for being there! I love you all!

Also many thanks go to the people from the Zondal skiing club and the Zondal Racing Team for sharing the same hobby and making it a joy every time we have training.

Finally, I would like to express my deepest respect and utmost gratitude to my parents, who have always been there for me and who have supported me my entire life. A son could not wish for better parents. I love you!

Stefan Tinck, July 2011

Part I

Background

Chapter 1

Microchip manufacturing

1.1 The integrated circuit

From the most advanced supercomputer to a kitchen bread toaster, integrated circuits are used in virtually all electronic equipment today and have caused a revolution in electronics over the last few decades. The integrated circuit, also called chip or microchip, is an electronic circuit consisting of a number of integrated electronic components (i.e. transistors). Indeed, the chip is manufactured as a unit rather than by constructing one transistor at a time, which reduces production cost significantly.

Basically, the active components of the integrated circuit are built on a circular slice of monocrystalline silicon (i.e. a wafer; 0.75 *mm* thick) by consecutive processes such as imaging (i.e. mapping), etching and deposition. So, all active components are fabricated as a unit by constructing layer after layer of different overlapping materials. **Figure 1** shows a scheme of an integrated circuit [1]. On top of the Si substrate, different layers are fabricated to manufacture a great number of active components (i.e. transistors) which are connected through various interconnects (Cu) depending on the functionality of the integrated circuit. After wafer processing, the wafer is cut in so-called “chips”.

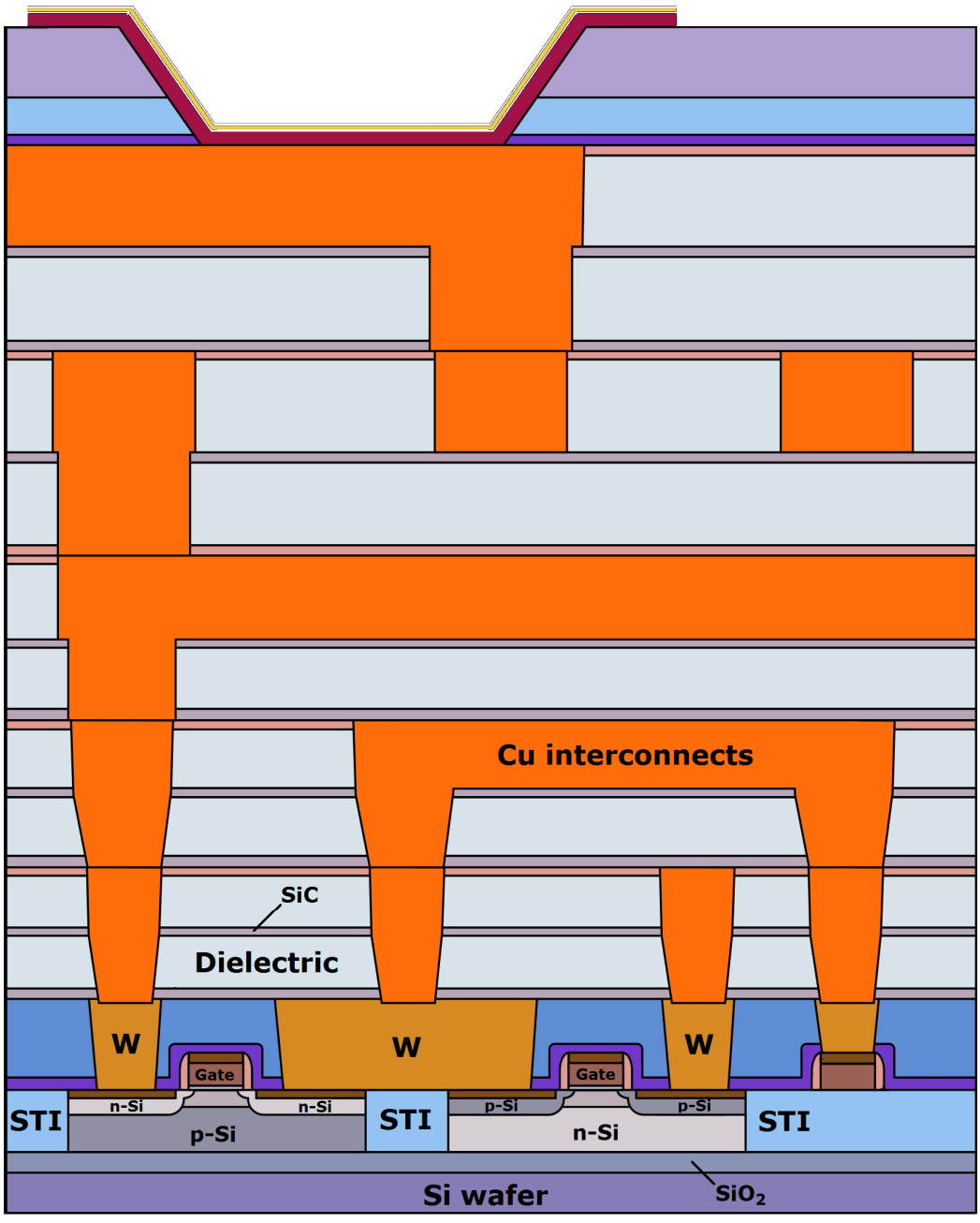

Figure 1. Basic scheme of a cross section of an integrated circuit. The lowest layer is the Si wafer. STI regions consist of SiO_2 that isolate the *n*- or *p*-doped layers from each other.

In practice, to make the surface conducting, the Si wafer is *p*- or *n*-doped, creating a *p*- or *n*-body. Subsequently, the Si is further *p*- or *n*-doped locally to create *pn* junctions on which the transistors will be fabricated.
It is common to first create a small buried SiO_2 layer to prevent electron flow from the transistors into the bulk Si wafer. This layer can be created by bonding two wafers together (by annealing) where one wafer has a SiO_2 surface. The wafer on top is thinned to obtain a top Si layer of a few *nm* onto which the transistors can be fabricated.
In certain locations, trenches are etched in the Si and filled with isolating material (SiO_2), a process called shallow trench isolation (STI) which will be discussed in more detail in section 1.8. STI is performed to isolate certain conducting surface areas from each other.
Next, different layers are deposited and subsequently etched in specific locations to create the transistors. The areas right underneath the gate electrodes in **Figure 1** are the conduction channels that are created if the transistor is in the *on*-state (see next section 1.2). After the transistors are fabricated, they are connected together by Cu layers (i.e. interconnects) in a desired way depending on the layout (and purpose) of the integrated circuit. These Cu interconnects are created by etching trenches in a dielectric material with high crack resistance and subsequently filling them with a Cu layer.
As can be clearly seen in **Figure 1**, the interconnects are fabricated layer after layer, embedded in dielectric. Indeed, a dielectric layer is deposited and holes (i.e. “vias”) are etched and filled with Cu to form the network of interconnects embedded in dielectric. In between these layers, a thin SiC etch stop layer is present which serves to properly connect the different dielectric layers and to indicate the end of the dielectric trench etching.
Whereas the wafer is about 0.75 *mm* thick for structural stability, the complete stack fabricated on top of the wafer is usually between 0 – 5 μm thick, depending on the application and complexity of the microchip [2].

1.2 The MOSFET

The most essential part of the IC is the so-called MOSFET or Metal-Oxide-Semiconductor Field Effect Transistor. The MOSFET is a device that can amplify or switch electronic signals between source and drain electrodes by applying a certain voltage on the gate electrode. It is currently by far the most common transistor in both analogous and digital circuits [3, 4]. A basic design of the MOSFET is presented in **Figure 2**. In this figure an example of an nMOSFET is illustrated showing an *n*-type conduction channel, but both *n*MOSFETs and *p*MOSFETs occur in integrated circuits.

In the *n*MOSFET, the source and drain electrodes are connected to *n*-doped regions while the Si body is *p*-doped. In the *off*-state (**Figure 2(a)**), current can not flow from source to drain electrode. However, if a voltage is applied on the gate electrode (**Figure 2(b)**), the positive holes in the *p*-doped body can be driven away creating an *n*-channel on the interface between the gate oxide and the *p*-doped Si. The voltage on the gate electrode can therefore induce an induction channel allowing current to flow from the source to the drain electrode (i.e. the field effect). Moreover, depending on the strength of the gate voltage, the signal can be amplified.

In the last few decades, the MOSFET has continuously scaled down in size. Indeed, smaller MOSFETS have several advantages. The main advantage is the packing of more devices on a given chip area, increasing functionality of the chip. Moreover, smaller chips allow for the production of more chips per wafer, decreasing the cost per chip. Another advantage is that smaller transistors can switch signals faster due to decreased gate capacitance. However, in current technology, the operating speed is not limited by the switch time of the transistors but rather by the interconnect delay [5].

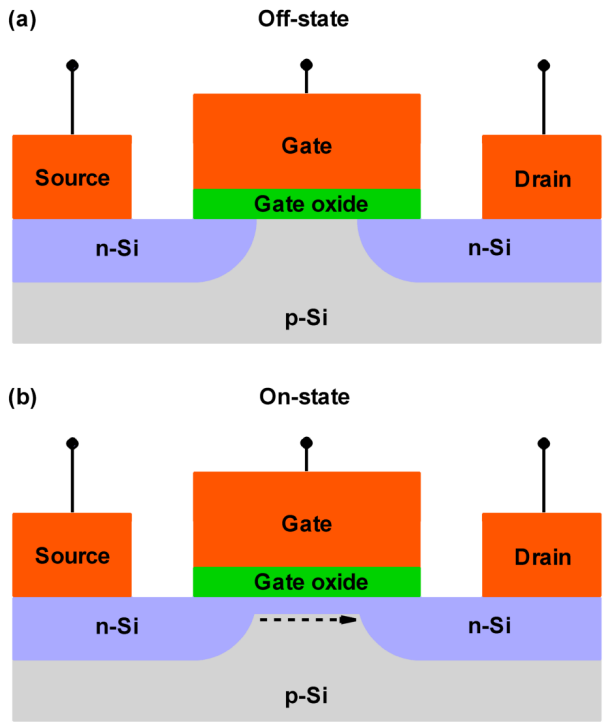

Figure 2. Basic scheme of an nMOSFET in *off*-state **(a)**, and *on*-state **(b)** where an *n*-type conduction channel is formed to allow current to flow from source to drain electrode.

Decreasing the transistor dimensions also creates some manufacturing challenges. Indeed, the dielectric between the gate electrode and the channel should be as thin as possible for a high performance of the transistor. However, if this layer is only a few atoms thick, electron tunnelling effects (i.e. current leakage) become an important effect. This, in turn can be reduced by choosing gate dielectric materials with higher dielectric constant to reduce this leakage current (i.e. high-k materials). Another challenge is increased heat production. Indeed, the increased number density of MOSFETs on a chip creates a higher local heat generation. Heated devices have a shorter lifetime and reliability and heat sinks are therefore required.

1.3 Moore's law

Integrated circuits have consistently been manufactured with smaller feature sizes over the years, allowing more components to be packed on each chip. The increased functionality per given area reduces cost per chip.

In a paper published in 1965 [6], Gordon Moore came to the conclusion that the number of components in integrated circuits doubled every two years from the invention of the integrated circuit in 1958 until 1965. Furthermore, he predicted that this trend would continue for at least ten years. In fact, this trend has continued until now and is expected to continue until 2020 or later.

His prediction that the number of transistors that can be placed on an integrated circuit doubles approximately every two years is also called "Moore's law". A simple sketch of Moore's law is illustrated in **Figure 3**.

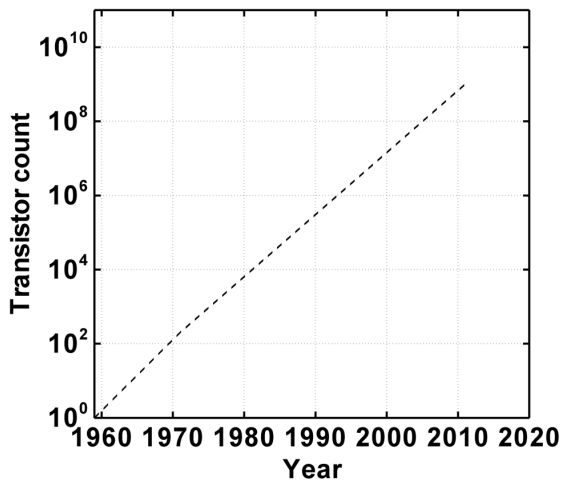

Figure 3. Sketch of Moore's law stating that the number of transistors on an integrated circuit doubles approximately every two years (adopted from [2]).

In fact, this law is a powerful incentive for microdevice manufacturing in the microelectronics industry. Indeed, research and development targets are commonly set based on Moore's law predictions.
However, fulfilling Moore's law in the 21st century is not obvious. Indeed, putting more transistors on an integrated circuit inevitably means creating smaller component structures. Since the dimensions of parts of the components are currently reaching the atomic-scale-range, the downscaling of reliable electronic devices becomes increasingly more difficult and eventually limited. For example, as mentioned before, if the transistor gate material is only a few atomic layers thin, leakage current becomes more and more pronounced, reducing the reliability of the system. Also, as will be discussed in more detail in section 1.8, trenches are etched in the Si to isolate active areas on the wafer. As dimensions (and hence trench widths) decrease, anisotropic etching (section 1.7.2) becomes increasingly challenging and important to prevent short circuiting.

1.4 Promising new developments

A large amount of effort is put into continuously decreasing feature dimensions. Indeed, as is clear from **Figure 4**, in the last forty years, the so-called "technology node" decreased from 10 μm in 1971 to 32 nm in 2010 [2].
The "technology node" can be considered as the smallest half-pitch of contacted metal lines [2]. The so-called "pitch" is the size of a repeating unit on the wafer. Technically, pitches for different repeating units can be defined. This repeating unit includes for example the size of the transistor and the width of the STI trench that isolates neighboring components. However, the definition of the technology node being the half-pitch should not be taken too literally because this is usually not

exact and differs for each technology node. A schematic picture of the pitch and technology node is illustrated in **Figure 5**.

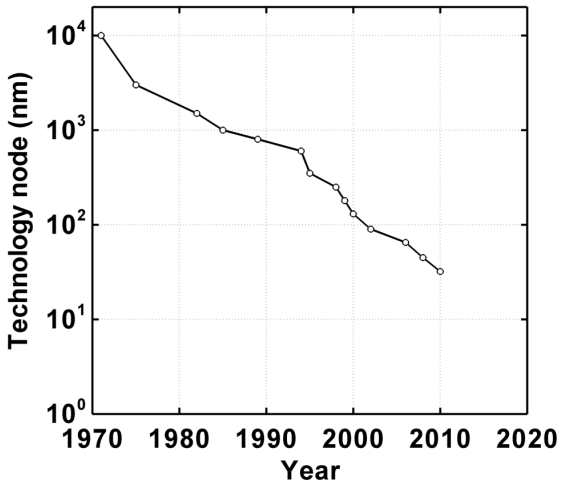

Figure 4. Technology node decrease during the last decades [2].

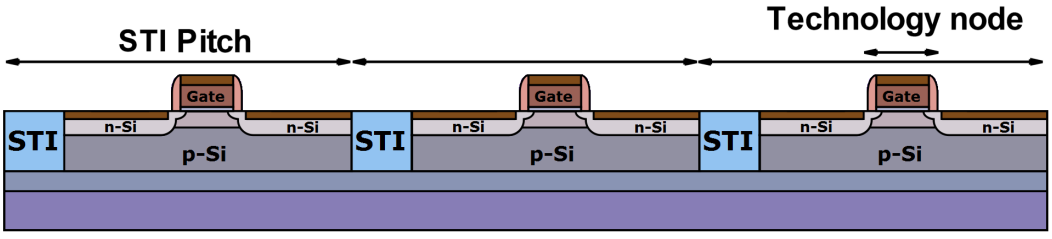

Figure 5. Schematic picture of pitch and technology node, which is usually close to the half pitch.

Besides constantly decreasing component dimensions, in order to further increase the overall performance of computerchips, new developments are made such as the search for “new materials” and “new device layouts”, as will be discussed below.

1.4.1 New materials

In the latest years, the diversity of materials in an integrated circuit (IC) has grown significantly. State of the art ICs contain a huge amount of different (exotic) elements to fabricate materials with the desired electrical properties.
For example, high-*k* dielectric materials (e.g. Hf- and Zr-silicates) are frequently examined to serve for transistor gate materials instead of conventional low-*k* SiO_2 [2]. High-*k* materials have a high dielectric constant, reducing leakage current through the (thin) gate material which is important if device dimensions keep decreasing. High-*k* materials have been introduced in electronic devices since 2007 (45 *nm* technology node) [2].
Another example are the "carbon nanotube based components". Carbon nanotube field effect transistors (CNTFET) make use of one or more carbon nanotubes as channel material instead of Si and have the advantage of better conduction of charge and heat. This makes them a promising "new material" for semiconductor devices. However, disadvantages are currently still the lower reliability due to faster degradation and difficulties with mass production. Different CNT based transistors exist, but are not applied commercially so far [2].

1.4.2 New architectures

Besides the search for new materials with better properties, also new basic IC architectures are under development.
An example of a promising new device layout is "3D integration" [2]. A three-dimensional IC (3D-IC) is a chip where two or more layers of active components are integrated into a single circuit, both vertically and

horizontally. One technology to create a 3D-IC is the so-called “wafer-on-wafer” method where two or more wafers are aligned and connected together. Advantages are an increased functionality in a smaller space, making the device powerful and very small at the same time, and an increase in performance due to an increased speed since the average conduction channel lengths become shorter.
Disadvantages (or challenges) are an increased chance for defects since the structure is much more complex to manufacture, as well as heat dissipation. Heat building up inside the stack could damage the device which must be avoided.
Other examples are the so-called “3D transistors” or MuGFETs (i.e. Multi-Gate Field Effect Transistors) which refer to MOSFETs that incorporate more than one gate electrode in a single component. The advantage is that multiple gates can better retain leakage current in the *off*-state of the transistor. 3D integration is a strongly pursued technology, but is not yet widely used today [7, 8].

1.5 Plasmas used for wafer processing

Plasma etching (see section 1.7) and deposition are currently the only commonly used technologies that meet the high resolution requirements for wafer processing. Indeed, the creation of nanoscale active components happens through various processing steps, and a significant number of these steps involve plasmas for surface treatment, whether it is etching, deposition or cleaning steps. In general, it is stated that for at least 20 % of all wafer processing steps including testing and packaging, low pressure plasmas are used [9].

1.5.1 Plasma

A plasma, also called the “fourth state of matter”, is a (partially) ionised gas. Besides the neutral atoms or molecules that are already present in the gas, the plasma also contains charged particles (i.e. cations, anions and free electrons), excited species and radicals. Typical examples of plasmas are the sun, lightning and fire. These are all plasmas that occur in nature, but also many different man-made plasmas exist. Well known artificial plasmas are light bulbs and plasma displays.

Distinction can be made between high and low temperature plasmas. High temperature plasma occurs for example in fusion reactors where it can obtain a few million *K*. Typical low temperature plasmas (or “gas discharges”) are lamps and plasma displays, as well as plasmas used in the microelectronics industry (see further), for materials technology, environmental and medical applications [10].

Moreover, distinction can also be made between LTE and non-LTE plasmas, where LTE stands for “Local Thermodynamic Equilibrium”, meaning that all plasma species have similar temperatures. Typical examples of LTE plasmas can be found in nature, but also man-made plasma arcs and atmospheric pressure inductively coupled plasmas are LTE plasmas.

In non-LTE plasmas, there is a significant difference in the temperature of the electrons (hot) and the heavy plasma species (cold; room temperature). The applications mentioned above on low-temperature plasmas, i.e. in the microelectronics industry, for materials technology, environmental and medical applications, as well as plasma displays and several lamp types, are typically based on non-LTE plasmas. In this work, only non-LTE plasmas are studied.

1.5.2 Capacitively and inductively coupled plasmas

In its most simple form, an artificial non-LTE plasma or gas discharge can be created by applying a potential difference between two electrodes, located in a reactor chamber filled with a certain gas. The electric field generated by the electrodes causes so-called "gas breakdown", i.e. the creation of positive ions and electrons in the neutral gas. The electric field will then further accelerate the charged particles which gives rise to a variety of collisions such as various ionization, excitation and dissociation reactions, which create more ions and electrons (in order to sustain the plasma), as well as excited species and radicals.
Often a pre-defined radiofrequent (rf) frequency is applied on one or more electrodes (e.g. 13.56 *MHz*). A plasma generated by an rf electric field between two electrodes is also called a capacitively coupled plasma (CCP); see **Figure 6**.

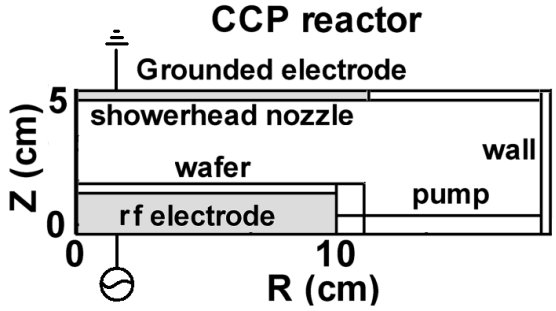

Figure 6. Schematic illustration of a typical CCP reactor geometry.

CCPs are commonly used in plasma processing, but a disadvantage is that current and voltage can not be controlled separately. In other words, this means that the flux and the energy of ions arriving at the substrate cannot be controlled separately. This is a disadvantage because, for a

high etch rate, a high ion flux is needed but this typically corresponds in CCPs to a high ion energy as well, which forms a large risk for damaging the substrate.
This problem does not apply for inductively coupled plasmas (ICPs). Indeed, in an ICP reactor, the plasma is generated by a coil that can have different geometries (e.g. planar or cylindrical). Rf currents flowing through the coil will generate an induced electric field to sustain the plasma. In addition, an electrode underneath the substrate can create a separate electric field to attract the ions from the plasma towards the substrate. In this setup, the number of ions in the plasma as well as their energy when they arrive at the wafer can be controlled separately. Therefore, ICP reactors are commonly applied in the microelectronics industry for various applications such as etching and deposition [11].

1.6 ICP reactor geometry

Most common ICP reactor geometries for wafer processing are those with a planar coil on top of the chamber and those with a cylindrical coil wound around the plasma chamber. Also combinations of different coil configurations exist [11]. **Figure 7** shows a basic scheme of a typical ICP reactor used for etching applications, with a planar coil on top of the chamber. This geometry resembles an existing reactor used for wafer processing, called the Lam Research 2300 Versys Kiyo 300 *mm* wafer ICP reactor [12].

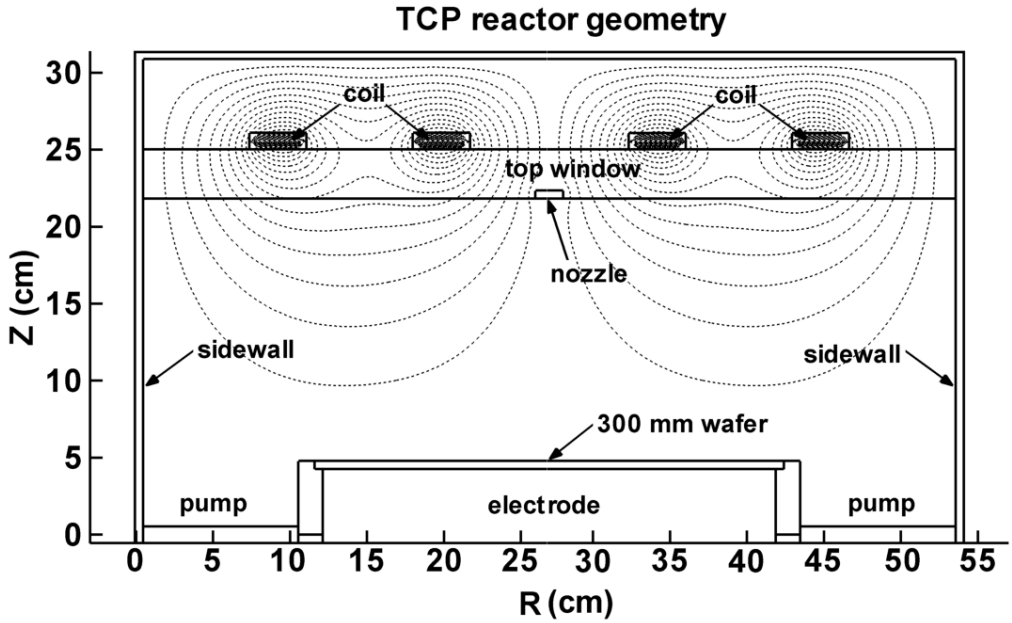

Figure 7. Cross section of an ICP reactor with a planar coil on top of the reactor chamber. This geometry is also referred to as a Transformer Coupled Plasma (TCP) reactor.

Reactors for wafer processing are typically cylindrically symmetric for higher uniformity because the wafer is a circular substrate. An rf current (i.e. typically 13.56 *MHz*) is applied to the coil that generates an rf magnetic field based on the "right-hand rule for conventional current". The typical form of the magnetic field penetrating into the plasma chamber is illustrated as dashed lines in **Figure 7**.

The charged particles in the plasma are accelerated based on the principle of induction; hence the name "inductively coupled plasma". Indeed, if a magnetic field changes in time, an electric field is generated with a strength related to the time-variation of the magnetic field. Moreover, this induced electric field is generated in such a direction that the current it drives opposes the magnetic field that created this induced electric field. This results in an acceleration of the charged particles in the plasma in the same way as the coil, but in opposite directions. The

plasma can therefore be considered as the complementary coil (as opposed to the real coil) as in a transformer. This reactor geometry, with a planar coil on top of the chamber, is therefore also called a "transformer coupled plasma" reactor or TCP reactor.
By controlling the current in the coil, the creation of charged plasma species can be varied. Furthermore, by defining a certain bias voltage on the electrode underneath the substrate (i.e. 300 *mm* wafer), the energy of the ions bombarding the surface can also be controlled.
The top dielectric window forms the separation between the plasma and the power source for preventing heavy sputtering (and damaging) of the coil.
In this particular reactor geometry, the gas is fed into the chamber by a central nozzle in the top window, but other setups exist as well, such as side nozzles and showerhead nozzles [11].
Finally, the gas is pumped out of the reactor underneath the substrate electrode.
Plasmas created in this particular ICP reactor geometry, where the gas is fed through a central nozzle in the top window, will be thoroughly investigated in this work.

1.7 Plasma etching

Plasma etching is one of many processing steps for the creation of an IC. As mentioned before, it is a technology that meets the high resolution requirements for nanoscale features. Basically it involves creating a plasma of an appropriate gas mixture to selectively remove certain parts of the surface layer. The gas mixture must be chosen according to the surface that needs to be etched. Indeed, the gas (or plasma) species should react with the surface to form volatile products.
Usually a high substrate surface temperature is needed to create volatile

products, but by applying a plasma the etch rate can be significantly higher even on a low-temperature substrate. Indeed, in the plasma, more reactive species (i.e. radicals) are created that react faster with the surface and, moreover, ions are generated that can sputter the surface. Both effects, where the surface is chemically "softened" and subsequently sputtered by ions, cause a relatively high (and desired) etch rate.
In addition to a high etch rate, three other parameters of plasma etching are important for wafer processing. These are briefly discussed in the following sections.

1.7.1 Uniformity

Etching uniformity is a measure for how the etch rate varies over the complete surface of the wafer. A highly uniform etch process is always desired, meaning that the etch rate should be the same on every location of the wafer. Usually this is not a major problem, but achieving high uniformity becomes increasingly challenging when performing ultra-large-scale integration (i.e. large wafer area). Nowadays, usually 300 *mm* wafers are processed, but 450 *mm* wafers will probably make an entry in the near future [2].
Indeed, a larger wafer surface allows for more devices in a same number of processing steps, reducing the cost per chip. The larger the substrate area, the more difficult it is to achieve high uniformity. Optimising the uniformity is often a difficult task. A great amount of effort is put into designing plasma reactors that meet high uniformity requirements [11]. Moreover, to increase the uniformity, a good knowledge of the bulk plasma behavior can be useful, which can be provided by numerical simulations (see further in this PhD dissertation).

1.7.2 Anisotropy

For etching trenches as applied in STI (see section 1.8), it is important that the material is only etched in the vertical direction. Anisotropic etching means etching in one particular direction, as illustrated in **Figure 8(a)**. As opposed to anisotropic etching, during isotropic etching, the material is removed at the same rate in every direction (**Figure 8(b)**). Chemical etching is often isotropic while sputtering is a more anisotropic process. Indeed, chemical etching occurs mostly by reactive neutrals that arrive at the surface from any given angle and therefore etch in all directions, while ions are accelerated through the sheath (see section 2.1.3), bombarding the surface at a fixed angle (typically perpendicular to the surface).

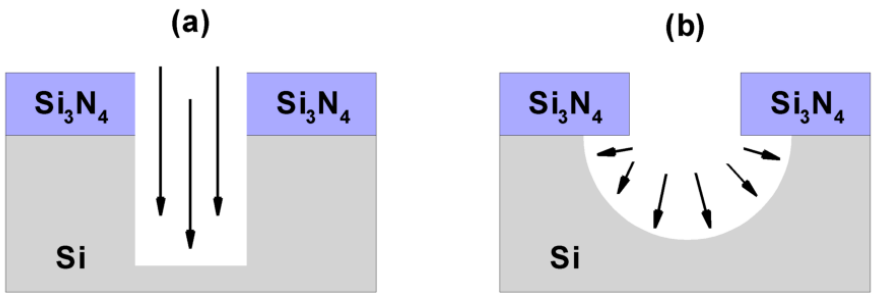

Figure 8. Schematic picture of anisotropic etching **(a)** and isotropic etching **(b)**.

As is clear from **Figure 8(b)**, in the case of isotropic etching, Si is removed underneath the mask, an effect which is also called "undercutting". Undercutting becomes more important if narrower trenches are etched and must be avoided. In the case where Si is etched by Cl_2, often a small amount of O_2 is added to protect the sidewalls from lateral etching and hence undercutting, as will be discussed in Part III

later. Indeed, a SiO_x protective passivation layer is formed on the sidewalls that can not be etched chemically by chlorine, while the bottom is still sputtered, increasing the anisotropy.

1.7.3 Selectivity

In addition to highly uniform and highly anisotropic, the etch process should also be selective, meaning that one material must be etched much faster than another. In the case of Si etching as applied in STI (see section 1.8), this means a high etch rate for Si and an as-low-as-possible etch rate for the mask (Si_3N_4). This is illustrated in **Figure 9**, showing a highly selective Si etching process **(a)** and a non-selective process **(b)** where all materials are etched at the same rate.

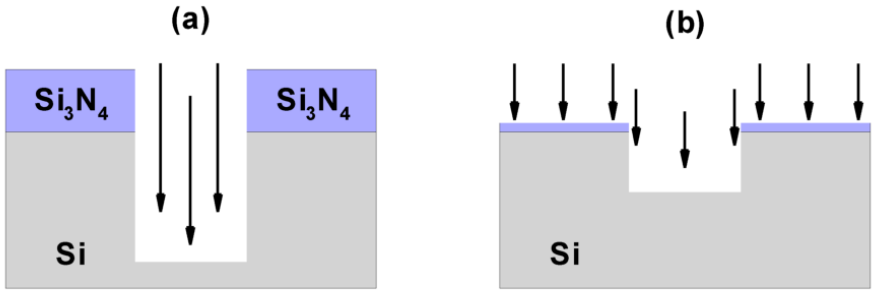

Figure 9. Schematic picture of selective etching **(a)** and non-selective etching **(b)**.

In general, chemical etching is highly selective while sputtering is not. Indeed, chlorine will etch the Si surface by forming volatile $SiCl_4$ molecules, while it does not react with the mask. On the other hand, sputtering is a physical process, depending merely on the energy of the bombarding ions, and therefore it is less selective towards different surfaces.
Often, a high selectivity goes at the expense of anisotropy and vice versa.

Chemical etching is highly selective but also isotropic, while sputtering is highly anisotropic but non-selective. Therefore, a proper balance must be found between chemical etching and physical sputtering. This can be achieved by tuning the operating conditions such as power, pressure, substrate bias and gas mixture. For example, it is common to include Ar in the Cl_2/O_2 based plasma as a diluting agent to tune the chemical etching "component" against the physical sputtering "component".
In reality, often a combination of chemical etching and physical sputtering yields the best results in terms of etch rate. Indeed, usually the surface is "softened" chemically so it can be easily sputtered (i.e. at lower threshold energy) by energetic ions. This is discussed in more detail in the tables of Part II (section 4.4).

1.8 Shallow trench isolation

Shallow trench isolation (STI) can be considered as the first step in chip manufacturing, even before transistors are fabricated. As mentioned before, the electronic device is constructed by building all components step by step on a Si base material, the wafer. First, the Si wafer is doped so that the surface of the wafer becomes conductive.
However, the active components (transistors) that are built upon this wafer must be isolated from each other to prevent current leakage between adjacent components. To isolate active areas on the wafer surface, shallow trenches are etched in the Si and subsequently filled with isolating material such as SiO_2.
Indeed, the trenches only need to be relatively shallow since only the surface is conductive. **Figure 10** illustrates the different main processing steps undertaken during the STI process. These main steps will be briefly discussed in the following sections.

1.8.1 Deposition of Si_3N_4

Starting from a *p*- or *n*-doped blanket Si wafer, first a Si_3N_4 layer is deposited on the wafer surface by means of plasma deposition. A SiH_4/NH_3 plasma can be used for this purpose [13]. This nitride layer is typically about 100 *nm* in thickness [2]. (**Figure 10(a)**)

1.8.2 Lithography

Next, a UV-light sensitive photoresist layer of about 250 *nm* thick is deposited. The photoresist layer is typically an organic polymer layer that changes its structure if exposed to UV light. The photoresist is typically deposited by spin-coating, where an organic solution is dripped onto the rotating wafer. Subsequently, UV light following a geometric pattern (i.e. mapping) is shined on the substrate to selectively remove parts of the photoresist. Indeed, the parts of the photoresist that have been exposed to UV light can be selectively removed. However, there exist also photoresists where the exposed parts are the only parts remaining after treatment. If the exposed parts are removed, the photoresist is also called positive tone photoresist. In the opposite situation it is called negative tone photoresist. (**Figure 10(b, c)**)

1.8.3 Etching of the Si_3N_4 layer

The mapped photoresist layer serves as a mask material to etch the nitride layer (**Figure 10(d)**). Typical plasmas used for this purpose are based on $He/CF_4/CH_2F_2/O_2$ gas mixtures. After etching the nitride layer, the photoresist mask is removed with an O_2 containing plasma.
This process is also called “resist-strip”, leaving a surface of Si with a

mapped Si_3N_4 mask. (**Figure 10(e)**)

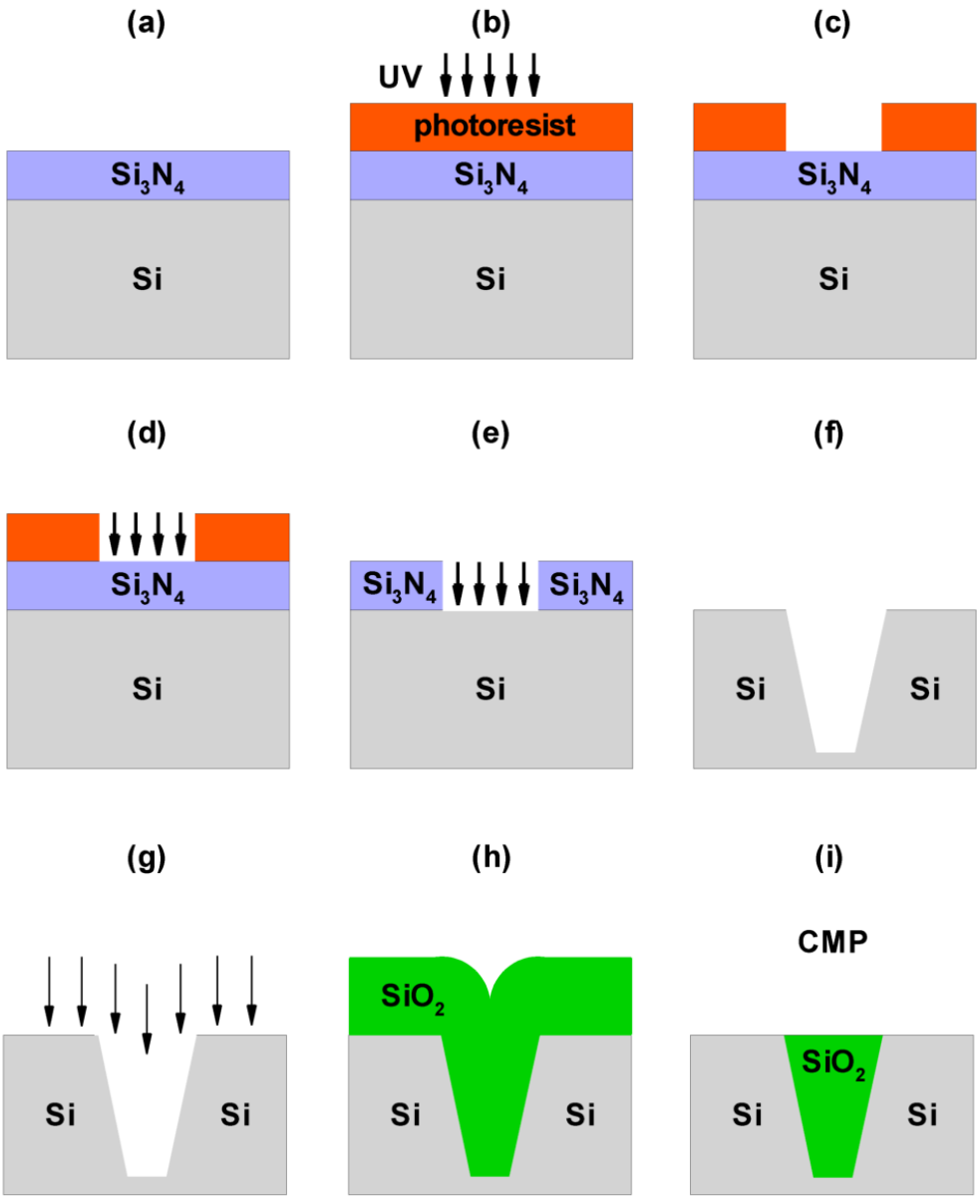

Figure 10. Scheme of the different processing steps in shallow trench isolation (STI).

1.8.4 Etching of Si

In this step, trenches are etched in the Si wafer, selective to the nitride mask. This step is typically performed with an $Ar/Cl_2/O_2$ or $N_2/Cl_2/O_2$ plasma since chlorine shows good etch selectivity between Si and Si_3N_4 while O_2 protects the sidewalls of the trenches from lateral etching (i.e. undercutting; see Section 1.7.2 above). It is this step of STI which is thoroughly investigated in this PhD work. (**Figure 10(e, f)**)

1.8.5 Deposition of SiO_2

After the complete removal of the nitride mask, the trenches are filled with isolating material (SiO_2). The oxide layer is typically deposited by means of an $Ar/SiH_4/O_2$ plasma. This plasma deposition step is also investigated in detail in this work (see Chapter 9). (**Figure 10(g, h)**)

1.8.6 Chemical mechanical polishing

Chemical mechanical polishing (CMP; also called chemical mechanical planarization) is a technique to smooth surfaces by using chemical as well as mechanical forces. Indeed, since SiO_2 was deposited onto the complete wafer surface, it must be removed so that the underlying Si can be exposed again, while the trenches are still filled with SiO_2 (**Figure 10(i)**). For chemical removal of the SiO_2 layer, often a highly basic solution is used (i.e. *pH* 10 - 11) based on NH_4OH or KOH [14]. Mechanical removal of the layer usually involves grinding with SiO_2 nanoparticles (i.e. 50 - 100 *nm*).

1.8.7 Trench width evolution

As component dimensions decrease, also the trench width must go down to be able to fabricate more transistors on the same area. Indeed, for example, the STI trench width in the so-called 90 *nm* technology node (i.e. around 2002 - 2003) was about 120 *nm*, while in the 65 *nm* technology node (2006 - 2007) it is about 60 *nm*. State of the art is the current 32 *nm* node (2010 - 2011) and beyond, where trenches reach widths of 20 - 22 *nm* [2].

1.9 Aim of the work

As mentioned above, the shrinking of active components in order to be able to fabricate more transistors on the same surface area according to Moore's law, becomes more and more challenging. Not only the transistors need to shrink, but also the isolating trench width that separates them from each other (i.e. the STI process; cf. above). In order to be able to improve and optimize the STI process, a good insight in the underlying mechanisms is needed. A large amount of experimental work is carried out for optimizing the STI process. In practice, this usually means etching the wafer under certain operating conditions and examining the etch profile afterwards, for example by SEM. Indeed, it is not obvious to obtain a great deal of information on the plasma properties during the etching or deposition process.

For this reason, numerical investigations can be an interesting alternative or addition. Indeed, a great number of plasma properties that are hard or impossible to measure experimentally can be calculated and investigated in this way.

The goal of this work is, therefore, to obtain a better understanding of the

etching and deposition processes as applied in STI by performing numerical simulations, as well as experiments for validation of the simulations.

As mentioned earlier, the two processing steps of STI under study in this work are the trench etching of Si with an $Ar/Cl_2/O_2$ ICP and the deposition (i.e. trench filling) of SiO_2 with an $Ar/SiH_4/O_2$ ICP.

Therefore, in this work, first the effects of typical operating conditions, such as pressure, power and substrate bias, on the general Ar/Cl_2 plasma properties and resulting etch process will be investigated numerically and experimentally (Chapter 5). This investigation was carried out in an early stage of the work for an Ar/Cl_2 plasma where the O_2 reaction set was not yet included in the simulations.

Subsequently, by adding O_2 to the Ar/Cl_2 gas mixture, the etch process will be investigated under various operating conditions, including gas mixtures with different ratios of Cl_2/O_2, and it will be studied which plasma properties have the most significant influence on the resulting etch rate (Chapter 6).

Moreover, the simultaneous etching and deposition processes on the wafer as a function of Cl_2/O_2 gas ratio will be investigated in more detail experimentally and numerically in Chapter 7, including, at this stage, also $SiCl_{0-4}$ and SiO_{1-2} etch products in the calculations.

Also the effects of a chamber wall coating will be investigated numerically. Cleaning the chamber and introducing a new coating between etch experiments increases the wafer-after-wafer etching reproducibility and can have beneficial effects for the etching process in terms of etch rate and uniformity which will be discussed in detail in Chapter 8.

Finally, the SiO_2 deposition process will also be numerically investigated (in Chapter 9) by varying the gas fractions of Ar, SiH_4 and O_2 in the gas mixture. Under these different conditions the properties of the plasma will be investigated as well as the resulting trench filling process.

Chapter 2

Physical plasma processes

Before describing in detail the modelling work carried out in this PhD thesis, first we will discuss in this chapter how power is deposited from the power source (i.e. the coil(s) in an ICP reactor) to sustain the plasma, or in other words, how the various plasma species such as ions, excited species and radicals are created through a great number of different plasma reactions. Moreover, plasma temperature, sheath properties and typical plasma reactions will also be discussed, as well as transport properties of the plasma species.

2.1 General plasma properties

2.1.1 Plasma frequency

As mentioned before, different operating frequencies can be applied in wafer processing, but an operating frequency typically used is 13.56 *MHz*. It has been generally agreed to use this frequency, for example to prevent interference with other electronic devices. This frequency is also applied in the cases under study in this work.
With this frequency the current in the coil changes direction and hence with this frequency also the electromagnetic field in the plasma changes

its direction.

The plasma frequency of a certain plasma species can be considered as the maximum frequency this species can follow or "feel". It is defined as follows [11]:

$$\omega = \sqrt{\frac{ne^2}{m\varepsilon_0}}$$

ω is the plasma frequency (*radians* s^{-1}), n is the species density (m^{-3}), e is the elementary charge (1.60×10^{-19} C), ε_0 the vacuum permittivity (8.85×10^{-12} $F\ m^{-1}$) and m the mass of the species (*kg*). It should be noted that, based on this formula, one should divide by 2π to display the frequency in Hz.

The ion and electron densities for the ICPs under study are typically in the order of 10^{16} m^{-3}. Based on this value, the plasma frequency is found to be roughly 9×10^{8} *Hz* for electrons and 3.6 *MHz* for Cl^+ ions, for example. From these values, it can be concluded that, at an operating frequency of 13.56 *MHz*, only the electrons are able to follow the field oscillations. This is due to their low mass compared to the ions. The ions therefore only feel the time-averaged field generated by the coil, which is theoretically zero, so it can be concluded that only the electrons are accelerated by the power source. However, the ions can be accelerated towards the wafer when an rf bias voltage is applied at the electrode underneath the wafer. Indeed, this rf bias voltage results in a time-averaged dc bias which the ions can "feel". This will be discussed in more detail in Chapter 5.

As the electrons move rapidly, they will collide with the heavy plasma species causing all kinds of reactions, such as ionization, dissociation and excitation (see section 2.2). Through the ionization processes new free electrons and ions are created that sustain the plasma.

2.1.2 Plasma temperature

As mentioned before, only the electrons are accelerated by the power source (i.e. the coil), and energy transfer to the other plasma species through collisions is limited because of the large mass difference between electrons and the other (heavy) plasma species. The heavy species therefore only gain a small amount of energy from collisions with electrons. As a result, two distinct temperatures are present in the bulk plasma, i.e. the electron temperature T_e, and the heavy particle temperature T_h. For the low pressure plasmas under study (< 100 *mTorr*), T_e is typically 3-8 *eV* depending on source power and pressure [15, 16] (where 1 *eV* corresponds to ~11600 *K*). This is much higher than the heavy species temperature, also called the "gas temperature", which is typically 300 - 1000 *K* (i.e. much closer to room temperature). Because of the different temperatures of electrons and heavy species the plasma is said to be not in thermal equilibrium, which is typical for low pressure plasmas.

2.1.3 Debye length

The much higher temperature (and hence speed) of electrons compared to the ions makes that the electrons should be lost faster at the reactor walls, which would eventually result in a non-neutral bulk plasma. To maintain neutrality in the bulk, the plasma creates a potential drop region to prevent the electrons from being lost at the walls so rapidly. Indeed, the faster moving electrons will charge the wall, creating a negative potential that accelerates the ions and slows down the electrons until both ion and electron fluxes to the wall are equal. The plasma potential is therefore typically positive and drops near the reactor wall.

This region where the potential drops significantly in the neighbourhood of an object or wall is called the plasma "sheath".

The thickness of the sheath can be described by the Debye length. The Debye length is the distance over which charge carriers can damp out an electric field or, in other words, the distance over which charge separation can occur in the plasma. For a plasma, the Debye length λ_D can be calculated as follows [11]:

$$\lambda_D = \sqrt{\frac{\varepsilon_0 k_B T_e}{n_e e^2}}$$

where ε_0 is the vacuum permittivity (8.85×10^{-12} $F\ m^{-1}$), k_B is the Boltzmann constant (1.38×10^{-23} $J\ K^{-1}$), T_e is the average electron temperature (K), n_e is the electron density (m^{-3}) and e is the elementary charge. For typical conditions (i.e. T_e = 3 eV = 34800 K and n_e = 10^{16} m^{-3}) the sheath thickness is calculated as 128 μm. For higher density plasmas the sheath is even thinner. Indeed, if the electron density is 10^{17} m^{-3}, the sheath thickness calculated with this formula is only 41 μm.

As mentioned above, the potential in the plasma is positive to keep quasi-neutrality in the bulk plasma. This results in a typical energy of 10 - 20 eV of the positive ions being accelerated through the sheath towards the wall.

However, for wafer processing steps including sputtering, higher ion energies are required and usually the substrate electrode will create a negative dc bias, typically up to 500 V, that pulls the positive ions towards the substrate with a much higher energy. The potential drop and sheath thickness λ_s (m) are therefore much higher at the substrate than at the other walls. The sheath thickness in front of the substrate can be calculated from a derived formula of the Child-Langmuir law describing the sheath thickness as a function of applied voltage V_a (V) [11]:

$$\lambda_s = \frac{\sqrt{2}}{3}\lambda_D\left(\frac{2V_a e}{k_b T_e}\right)^{3/4}$$

The sheath thickness as a function of applied substrate voltage under typical operating conditions (i.e. T_e = 3 eV = 34800 K and n_e = 10^{16} m^{-3}) is illustrated in **Figure 11**. It should be noted that the substrate bias is usually negative, but for predicting the sheath thickness the absolute value counts. As is clear from the figure, when applying a voltage on the substrate electrode, the sheath thickness significantly increases and can reach values close to 2 *mm* for typical operating conditions.

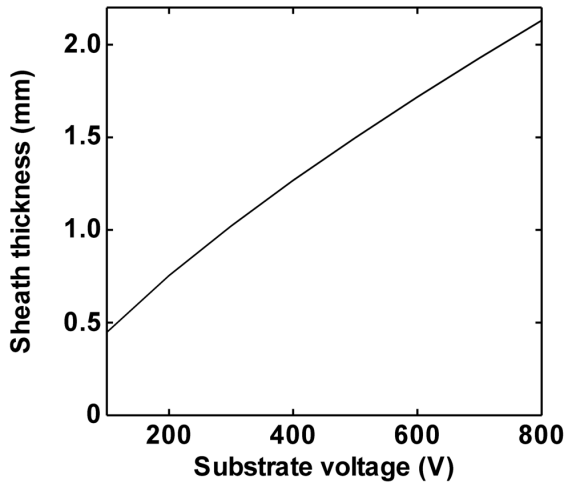

Figure 11. Sheath thickness as a function of the applied substrate voltage, in the range 100-800 *V*, as calculated with the Child-Langmuir law, for typical operating conditions of T_e = 3 eV and n_e = 10^{16} m^{-3}.

2.2 Plasma reactions

The electrons that are accelerated by the rf electromagnetic field will collide with other (heavy) plasma species which results in a great variety of possible reactions, creating more ions and free electrons to sustain the plasma, as well as excited and reactive species (radicals). The different types of common reactions will be briefly discussed in the following sections.

2.2.1 Elastic and inelastic collisions

An elastic collision is a collision where only kinetic energy is exchanged between colliding species. After an elastic collision, the colliding species are unchanged and only their direction of movement and speeds are altered. The amount of kinetic energy that can be exchanged depends on the mass difference of colliding species. Indeed, the maximum fraction of energy that can be exchanged f_{max} is given by [17]:

$$f_{\max} = \frac{4m_1 m_2}{\left(m_1 + m_2\right)^2}$$

where m_1 and m_2 are the masses of the colliding species. The exchange of kinetic energy during an elastic collision is most efficient when the colliding species have the same mass. Indeed, for two colliding Ar atoms, f_{max} is 1, while for a colliding electron and an Ar atom it is about 5×10^{-5}. This is also the reason why the heavy plasma species stay near room temperature while the electrons are heated to a few *eV*, and hence why the plasma is not in thermal equilibrium.

As opposed to elastic collisions, during inelastic collisions also potential energy is exchanged. This can happen through numerous different reactions which are briefly discussed in the following sections.

2.2.2 Dissociation

In a dissociation reaction, a bond of a molecule is broken, yielding two or more separate reaction products. Breaking of a bond typically takes a few *eV* so it is expected that this process will only happen by electron impact. Indeed, as mentioned before, the heavy species are near room temperature and therefore do not have sufficient kinetic energy to break a chemical bond during collision. As an example, the dissociation of Cl_2 by electron impact is shown:

$$e + Cl_2 \rightarrow e + Cl + Cl \text{ (Threshold = 3.12 } eV\text{)}$$

The Cl-Cl bond energy is about 2.5 *eV*. Therefore, theoretically the electron should have at least a kinetic energy of 2.5 *eV* to be able to break the bond. In practice, the threshold is usually slightly higher than the bond energy. Indeed, during collision, the ground state molecule is excited to a repulsive state with a higher threshold than the bond energy, which leads to dissociation of the molecule. The remaining energy is shared among the dissociation products and hence usually hot neutrals are created in this dissociation process. Similarly, the threshold energy for dissociation of the O_2 double bond is about 6 *eV*, whereas the bond energy is 5.2 *eV*.

Another common dissociation process is dissociative attachment where the electron attaches to one of the dissociation products to form a negative ion, e.g.:

$$e + Cl_2 \rightarrow Cl + Cl^-$$

This process is common for atoms with high electronegativity because it is characterized by a zero energy barrier. Indeed, in the case of Cl_2, the electron affinity for Cl (to form Cl^-) is 3.6 *eV*, which is higher than the Cl-Cl bond energy (2.5 *eV*), making the Cl + Cl^- system lower in total energy than the Cl_2 molecule.

2.2.3 Excitation

In an excitation reaction, an atom or molecule is brought into an excited state, again usually by electron impact. There exist different types of excitations. Indeed, a molecule can be rotationally, vibrationally and electronically excited. Of course, an atom can only be electronically excited. In all cases, the electron loses the amount of kinetic energy equal to the rise in potential energy of the heavy species. Moreover, different electronic, rotational and vibrational states occur for a single species, yielding numerous reactions with different energy thresholds. In practice, only the most common states are included in the simulations as will be explained in more detail in section 4.3.1. In general, rotational and vibrational excitations are characterized by a low energy barrier. Indeed, for example, an electron impact rotational excitation of O_2:

$$e + O_2 \rightarrow e + O_2^{*(rot)}$$

has a low threshold energy of 0.02 *eV*. Vibrational excitations have a slightly higher energy barrier, depending on the vibrational state. Common vibrational excitations of O_2 typically have thresholds of 0.19 – 0.8 *eV*:

$$e + O_2 \rightarrow e + O_2^{*(vib)}$$

Due to the low energy barriers of rotational and vibrational excitations, these reactions can occur very often, and hence the electrons transfer a considerable amount of energy to the heavy species during these excitation reactions. The average electron energy is therefore usually smaller in a molecular plasma compared to an atomic plasma under the same operating conditions.

Finally, atoms or molecules can also be electronically excited. Again, many different excited states exist for a single species but only the most common excited states are taken into account in our simulations (see section 4.3.1). Electronic excitations typically have higher threshold energies, corresponding to the energy needed to bring the species into a particular excited state. Indeed, for example, the electron impact electronic excitation of Ar to Ar*:

$$e + Ar \rightarrow e + Ar^{*(elec)}$$

has a threshold energy of 11.60 *eV*, corresponding to the energy of the Ar(4*s*) excited state.

The excited species can return to the ground state (or a lower excited level) by collisions or by emitting radiation of a wavelength corresponding to the energy difference of the electronic states. Typical lifetimes for excited states of Ar are found to be 7 – 10 *ns* which are shorter than the time between collisions (see section 2.3.3). Therefore, radiative decay, i.e. decay by emission of radiation, is typically the most important loss process for excited species [18]. However, metastable states (i.e. states with forbidden state transitions) can have significantly longer lifetimes (i.e. in the order of *ms*) and usually return to ground state by collisions.

2.2.4 Ionization

During an ionization reaction, an electron and an ion are created. In fact, these reactions ensure that the plasma is sustained. Ionization reactions typically have higher thresholds than other reactions such as dissociation and excitation.
Most common ionization reactions are electron impact ionizations, where an energetic electron will collide with a neutral species and "liberate" a second electron, resulting in a positive ion and two free electrons. An example is the electron impact ionization of Ar to Ar^+:

$$e + Ar \rightarrow Ar^+ + 2\ e \quad (\text{Threshold} = 15.76\ eV)$$

For this particular ionization reaction to occur, the electron must have at least a kinetic energy of 15.76 *eV* to overcome the energy barrier for ionization. The heavy plasma species typically are near room temperature and do not reach such high energies, so ionizations mainly occur by electron impact.
However, an exception is Penning ionization where the ionization potential of one species is lower than the internal energy of the other. For example, the ionization of Cl_2 to Cl_2^+ during collision with an excited Ar atom (Ar*):

$$Ar^* + Cl_2 \rightarrow Ar + Cl_2^+ + e$$

Ar* is an excited state of Ar (11.60 *eV*; see section 4.3.1) whereas the threshold for ionization of Cl_2 to Cl_2^+ is 11.47 *eV*. During collision, the internal energy of Ar* (11.60 *eV*) can therefore be used to ionize Cl_2, yielding ground state Ar, a Cl_2^+ ion and a free electron.

Finally, species can also become ionized through charge transfer. In a charge transfer reaction, positive and negative charge is not really created but exchanged between colliding species. For example, the charge transfer between Cl^+ and Cl_2:

$$Cl^+ + Cl_2 \rightarrow Cl + Cl_2^+$$

In this particular reaction, Cl^+ donates its positive charge to Cl_2 (or more specifically, Cl_2 donates its electron to Cl^+). Of course, this reaction can happen in both directions, but it is usually faster in one particular direction. Indeed, the formation of Cl_2^+ is preferred to the formation of Cl^+ because Cl_2^+ is a more stable ion. Indeed, it only takes 11.47 *eV* to create Cl_2^+ from Cl_2 while it takes 12.99 *eV* to form Cl^+ from Cl.

2.2.5 Neutralization

As opposed to ionization reactions where positive and negative charge is created, neutralization reactions will remove charges. Most of these reactions happen at the wall or by collision of a positively and negatively charged heavy species. For example, the neutralization of Cl^- and Ar^+ is illustrated:

$$Cl^- + Ar^+ \rightarrow Cl + Ar$$

Electron impact neutralizations (or recombinations) occur less frequently because they are highly exothermic processes. These processes therefore require a specific channel to release the energy during recombination. The three main mechanisms for energy release are dissociative electron-ion recombination, three-body collisions and radiative recombination. In dissociative electron-ion recombination, the energy is channelled into

breaking a bond of a molecule. In three body collisions, the energy released by the recombination process is absorbed by a third body. However, probabilities for three body collisions are very low, especially at the low pressure under study here, making this process not likely to happen. Finally, the released energy can be converted into radiation. However, this process is also not likely to happen, and the collision probability is comparable to the three body collision probability. Hence, it can be concluded that only dissociative electron-ion recombination is important, and that electron-ion neutralizations for atomic ions are not likely to happen in the plasma.

2.2.6 Chemical reactions

Finally, also chemical reactions can occur, where new reaction products are formed after collision of two or more heavy particles. For example, in a Cl_2/O_2 mixture, reaction products such as ClO, Cl_2O, ClO_2 and Cl_2O_2 can be formed. The formation of ClO from Cl_2 and excited oxygen (O*) is illustrated as an example:

$$Cl_2 + O^* \rightarrow ClO + Cl$$

The rate coefficient of this reaction, as well as of all other reactions included in our simulations, will be discussed in Part II.

2.3 Transport of plasma species

2.3.1 Thermal velocity

As mentioned before, electrons have a significantly higher mean energy than the heavy plasma species. In addition, the electron mass is much lower, so it is expected that the free electrons will move with a much higher average speed than the heavy species. The mean thermal velocity υ_{th} is given by:

$$v_{th} = \sqrt{\frac{8k_B T_e}{\pi m}}$$

where k_B is the Boltzmann constant (1.380×10^{-23} $J\,K^{-1}$), T_e is the average electron temperature (K) and m is the mass of the species (kg). For typical conditions under study in this work (i.e. T_e = 3 eV = 34800 K and $T_{neutrals}$ = 500 K) it is found that the thermal electron velocity is about 1.1×10^6 $m\,s^{-1}$ while the mean thermal velocity of Ar, for example, is roughly 514 $m\,s^{-1}$. **Figure 12** illustrates the thermal velocity as a function of temperature for electrons and Ar atoms. Ar can have velocities up to 700 $m\,s^{-1}$ at 1000 K, while electrons easily exceed velocities of 10^6 $m\,s^{-1}$. Indeed, for typical conditions investigated in this work, temperatures for neutrals range between 300 and 1000 K while electrons usually have an average energy close to 3-5 eV which may increase up to 10 eV at very low pressure (~1 mTorr).

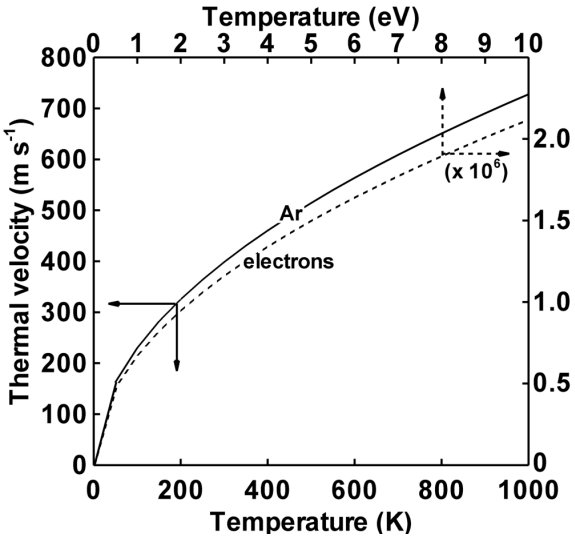

Figure 12. Thermal velocities of Ar neutrals (solid line, left and bottom axis) and electrons (dashed line, right and top axis) as a function of temperature.

2.3.2 Mean free path

The mean free path is the average distance that a plasma species travels in between two collisions. Naturally, it is dependent on the chamber pressure and kinetic energy (i.e. speed) of the species. The mean free path l (m) as a function of temperature T (K) and pressure P (Pa; $N\ m^{-2}$) can be calculated as follows:

$$l = \frac{k_B T_e}{\sqrt{2}\pi d^2 P}$$

where d (m) is the diameter of the species and k_B the Boltzmann constant ($1.380 \times 10^{-23}\ J\ K^{-1}$). The mean free path is shown in **Figure 13** for a pure Ar plasma, where d is about 212 pm, at typical operating pressures of 1 - 100 $mTorr$.

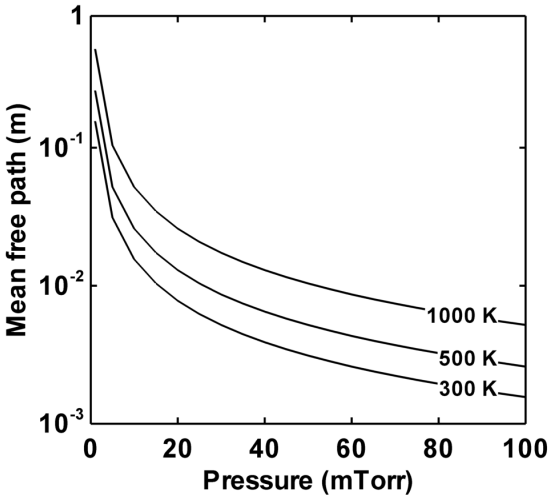

Figure 13. Mean free path of Ar gas as a function of pressure, for different gas temperatures.

From **Figure 13** it can clearly be seen that the mean free paths, at the typical pressures under study, are in the range of 1 *mm* to 1 *cm*. Especially in the lower pressure region (below 20 *mTorr*), the mean free path can obtain a length comparable to the reactor dimensions, making wall processes very important compared to the gas phase plasma reactions.

Naturally, at higher temperature the mean free path increases due to a lower species density which is a direct result from the ideal gas law.

2.3.3 Collision frequency

The collision frequency is strongly correlated to the mean free path. It is the number of collisions happening for a certain species in a unit of time, and it is dependent on the pressure and temperature of the gas. The collision frequency υ_{col} (s^{-1}) of species *A* with species *B* can be calculated

as follows:

$$v_{col} = n\sigma_{AB}\sqrt{\frac{8k_BT}{\pi\mu_{AB}}} \text{ where } \quad \mu_{AB} = \frac{m_A m_B}{m_A + m_B}$$

n is the density (m^{-3}) of species B, σ_{AB} is the reaction cross section (m^2), k_b the Boltzmann constant (1.38×10^{-23} $J\ K^{-1}$), T the temperature (K) and $m_{A/B}$ the mass (kg) of species A/B. The collision frequency between Ar atoms, as well as between electrons and Ar atoms, is illustrated in **Figure 14** as a function of pressure. For colliding Ar atoms, σ_{AB} can be considered as πd^2 (i.e. 1.4×10^{-15} cm^2) and μ_{Ar} as 3.32×10^{-26} kg. For an electron colliding with an Ar atom, σ_{AB} can be considered to be 1×10^{-15} cm^2, and $\mu_{e\text{-}Ar}$ as 1.33×10^{-25} kg. Furthermore, the gas temperature was chosen as 500 K and the electron temperature as 3 eV.

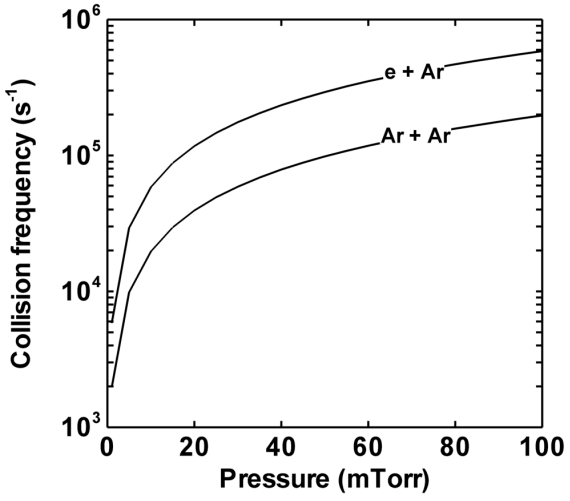

Figure 14. Collision frequency between Ar atoms and between electrons and Ar atoms as a function of pressure for 500 K gas temperature and 3 eV electron temperature.

2.3.4 Diffusion

The mean free path of the plasma species is typically smaller than the reactor dimensions, except at very low pressure (cf. **Figure 13**), which results in random trajectories for the species. However, a flux of species in a general direction (i.e. diffusion due to a concentration gradient) can occur. Indeed, species will tend to flow from a high density region to a low density region, which is described by Fick's law of diffusion:

$$\Gamma_i = -D\nabla n_i$$

where Γ_i is the flux of species i ($m^{-2}\ s^{-1}$), D the diffusion coefficient ($m^2\ s^{-1}$) and n_i the density of species i (m^{-3}). The diffusion coefficient consists of two parts describing "free-diffusion" (D_{free}), and "interaction diffusion" (D_{ij}) [19]:

$$\frac{1}{D} = \frac{1}{D_{free}} + \frac{1}{D_{ij}}$$

where D_{free} is dependent on the thermal velocity of the species v_{th} ($m\ s^{-1}$) (see section 2.3.1) and the "effective reactor dimension" Λ (m):

$$D = \frac{v_{th}\Lambda}{3}$$

Λ is dependent on the size and geometry of the reactor. For a cylindrical reactor, Λ can be calculated as follows [20]:

$$\left(\frac{1}{\Lambda}\right)^2 = \left(\frac{\pi}{height}\right)^2 + \left(\frac{2.405}{radius}\right)^2$$

For the cylindrical reactor that will be mainly under study in this work, Λ is about 4.8 *cm*. For Ar atoms at 500 *K*, the thermal velocity is about 500 $m\ s^{-1}$ and D_{free} therefore about 8.1 $m^2\ s^{-1}$.

The interaction diffusion coefficient D_{ij} (also called the "binary diffusion coefficient)" describes the diffusion of a certain species *i* in a "background" of species *j* and is calculated based on the following equation [21, 22]:

$$D_{ij} = \frac{3}{16} \frac{\sqrt{2\pi k_B^3 T^3 \mu_{ij}}}{P\pi\sigma_{ij}^2 \Omega_{ij}^{(1,1)*} \psi_{ij}}$$

where k_B is the Boltzmann constant ($1.38 \times 10^{-23}\ J\ K^{-1}$), *T* the temperature (*K*), *P* the pressure ($N\ m^{-2}$), σ_{AB} the momentum transfer cross section and μ_{ij} the reduced mass, as already shown in section 2.3.3.

In this equation, the species are considered as rigid spheres that collide based on their Lennard-Jones interaction potentials. Indeed, $\Omega_{ij}\psi_{ij}$ denotes a collision integral which is a function of temperature and the Lennard-Jones potential [22].

For the conditions under study in this work, D_{ij} is typically in the order of $10^{-1} - 1\ m^2\ s^{-1}$.

The (effective) diffusion coefficient therefore is typically about 0.1 - 1 $m^2\ s^{-1}$. Based on the effective dimension of the reactor (4.8 *cm*; cf above) and the diffusion coefficient, a characteristic time for diffusion τ_{diff} (s) can be defined as follows:

$$\tau_{diff} = \frac{\Lambda^2}{D}$$

For typical conditions under study in this work, τ_{diff} is in the order of 2 - 20 *ms*. The characteristic diffusion time can be considered as the time it takes for a species to travel the effective reactor dimension.

Charged species do not only move in the plasma based on diffusion due to a concentration gradient but they also move by migration in the electric field. Indeed, for example in the sheath, the ions are accelerated due to the electric field and therefore they move faster than the neutrals, while the electrons move slower in the sheath than expected, because transport by migration occurs in the opposite direction as transport by diffusion (for electrons). This effect where both the electrons and the ions move at the same rate to maintain charge neutrality is also called ambipolar diffusion.

2.4 Summary of the basic plasma characteristics

To summarize, an overview is presented here of the typical operating conditions applied for STI etching with an ICP, because these conditions will be assumed in our simulations presented in Part III. Moreover, also the typical values of the plasma characteristics under these conditions will be given. The data are summarized in **Table 1**.

As is clear from the table, at low pressure, the mean free path can reach values comparable to the reactor dimensions. Furthermore, the characteristic diffusion time is in the order of *ms* where the gas residence time is close to 1 *s*. The plasma species therefore can travel the distance of the reactor dimensions and can hit the walls many times before being

pumped out. This means that wall processes are very important for determining the bulk plasma properties as well as the substrate process, as will be further discussed in more detail in Part III.

Table 1. Summary of typical operating conditions and corresponding basic plasma characteristics.

Process parameter	Typical value
Operating frequency	13.56 *MHz*
Power	0 - 1200 *W*
Pressure	1 - 100 *mTorr*
Substrate bias	0 to -500 *V*
Gas flow	1 - 500 *sccm*
Reactor volume	~ 40 dm^3
Wall/wafer temperature	60 *°C*
Etch time (STI)	~ 60 *s*

Plasma characteristic	Typical value
Electron energy	2 – 8 *eV*
Gas temperature	300 – 1000 *K*
Sheath at walls	40 – 130 *μm*
Sheath at substrate	40 *μm* – 2 *mm*
Electron thermal velocity	(1 – 2) × 10^6 $m\ s^{-1}$
Heavy species thermal velocity	300 - 700 $m\ s^{-1}$
Mean free path	1 *mm* - 1 *dm*
Collision frequency	~10^4 - 10^6 s^{-1}
Characteristic diffusion time	2 - 20 *ms*
Gas residence time	0.01 - 10 *s* (**Figure 15**)

The gas residence time is calculated as follows:

$$\text{Residence time} = \frac{\text{Total number of gas species in the reactor}}{\text{Gas flow } (s^{-1})}$$

The gas residence time as a function of gas flow (in *sccm*; "*standard cubic cm per minute*") is plotted for different pressures in **Figure 15**.

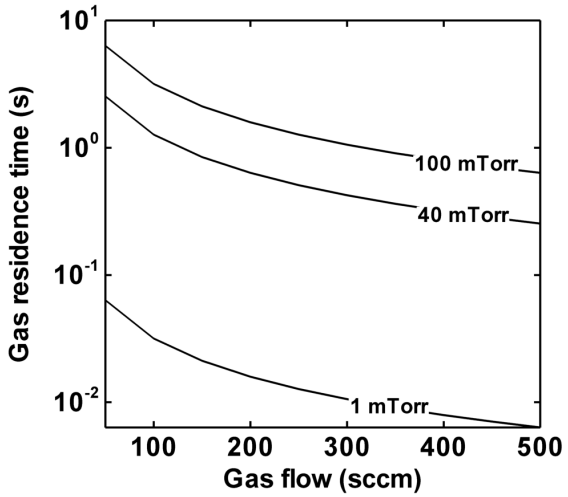

Figure 15. Residence time of the gas as a function of gas flow, at 1, 40 and 100 *mTorr* in a typical TCP reactor applied for etching.

It should be noted that the gas flow (in *sccm*) has units of $cm^3\ s^{-1}$. Indeed, this is the volume that enters the reactor chamber per second. However, this is converted to "number of species that enter the reactor per second", which can be calculated from the ideal gas law. For 1 *sccm*, 4.10×10^{17} species flow in and out the reactor per second, where standard conditions are 1 *atm* and 293 *K*. The total number of species in the reactor volume is again calculated from the ideal gas law and is dependent on pressure. Therefore the residence time increases with chamber pressure as is also clear from **Figure 15**.

Part II

Description of the simulations

Chapter 3

Description of the model

Different mathematical models exist in literature to describe the various processes occurring in a discharge and to predict the plasma behavior under specific operating conditions. Each of these mathematical models is characterized by its specific advantages and disadvantages. First, a brief discussion of the most common models applied for addressing the plasma behavior will be given, followed by a more detailed discussion on the models applied in this work.

3.1 General overview

3.1.1 Analytical models

The most simple way of describing the plasma behavior is by means of an analytical model [23-25]. Analytical models are based on solving analytical formulas which predict plasma properties as a function of one or more macroscopic quantities; for instance, the minimum distance needed between two electrodes to sustain the discharge for a certain gas:

$$\alpha L = \ln\left(1+\frac{1}{\gamma}\right)$$

where α (m^{-1}) and γ are the first and second Townsend coefficients, respectively, and L (m) is the distance between both electrodes [26]. The first Townsend coefficient (α) expresses the number of charged pairs created per unit length. The second coefficient (γ) denotes the ion-induced secondary electron emission coefficient.
Analytical models have the advantage of a very short calculation time to predict simple plasma properties. This, however, goes at the expense of accuracy due to approximations in the analytical equations. These models are mostly zero-dimensional, meaning that plasma characteristics are calculated at a specific point or averaged over the entire plasma reactor. Therefore, these models are most suited for quickly calculating simple general properties, as illustrated above.

3.1.2 Zero-dimensional models or global models

Zero-dimensional models calculate plasma properties such as species densities by solving balance equations for each species based on production and loss by chemical reactions, but without transport (i.e. without spatial variations, assuming a uniform plasma) [27, 28]. Indeed, properties are calculated independent of position and hence the plasma is considered uniform. These models are especially appropriate for describing complex chemistries without too much computational effort. A drawback is that the available information is limited (i.e. no information on transport or position dependent plasma properties).
One example of a global model is Global_kin, developed by Dorai and Kushner [29] which can be used to quickly predict initial plasma conditions for the simulations performed with the two-dimensional model applied in this work (HPEM; see section 3.4).

3.1.3 Boltzmann models

As its name implies, a Boltzmann model is based on solving the Boltzmann equation [30, 31]. This equation describes the evolution of a velocity distribution function $f_i(r,v,t)$, denoting which fraction of a certain species i has a certain speed v ($m\ s^{-1}$) at a certain location r, and has the following form:

$$\frac{\delta f_i\left(\vec{r},\vec{v},t\right)}{\delta t}+\vec{v}\cdot\overrightarrow{\nabla}_r f_i\left(\vec{r},\vec{v},t\right)+\vec{a}\cdot\overrightarrow{\nabla}_v f_i\left(\vec{r},\vec{v},t\right)=Col\left[\ f_i\left(\vec{r},\vec{v},t\right)\right]$$

where a is the acceleration ($m\ s^{-2}$) and Col a term describing changes due to collisions. This distribution function can in principle be calculated for all different plasma species present in the plasma.

Solving this equation yields very accurate results but it is a hard mathematical task, especially for more complex systems, like the systems under study in this work. Therefore, often approximations need to be made to be able to solve the problem under study. For example, as an alternative solution, we can assume that the main plasma characteristics are well described in terms of some mean properties like density, mean velocity, mean energy, etc. In this way, the Boltzmann equation can be replaced by some characteristic continuity equations which correspond to the equations typically solved in a fluid model (see next section 3.1.4) [32].

3.1.4 Fluid models

A fluid model is based on solving the continuity equations for mass, momentum and energy for all plasma species, i.e. different types of ions, radicals, molecules and the electrons. These equations are also called the first three moments of the Boltzmann transport equation (see previous section 3.1.3) [33-36]. In practice, the momentum equation is often replaced by a drift-diffusion approximation, although in the model used in this PhD work, the full momentum equation is used (see below), and the energy conservation equation is solved for both the electrons and the heavy species. It is a powerful and fast technique to calculate plasma properties. However, in fluid models the plasma is considered as a continuum (or fluid) which is less suitable for low-pressure plasmas since the electrons gain much more energy from the electromagnetic field than is lost due to collisions with heavy species. The plasma is therefore not in thermal equilibrium and can not simply be considered as a continuum at low pressure. Fluid models are very suitable for calculating complex chemistry systems in a reasonable calculation time, but start to fail at lower pressures. The fluid technique is used in this work as part of the hybrid model, and will therefore be discussed in more detail in section 3.3.

3.1.5 Monte Carlo models

The Monte Carlo (MC) method is a very appropriate calculation method at low pressure since individual particles are followed and the plasma is not considered as a continuum [37-38]. Moreover, it is a quite straightforward approach, based on simple equations. The trajectory and collisions of these MC particles are calculated at successive time steps,

usually in an electromagnetic field which is predefined. The Monte Carlo models are therefore usually not self-consistent, which means that external input is needed. The trajectory of the particles is calculated by Newton's laws. Collisions between the MC particles are treated probabilistically (i.e. based on random numbers), so the MC method is a statistical method. A drawback of the MC method is that, since individual particles are followed, the calculation is more time consuming compared to other techniques, because a proper number of particles should be followed in order to obtain good statistics. Although the MC method is very accurate, it is less suitable for addressing large numbers of different plasma species in a reasonable calculation time. The MC method is also used in this work and is therefore discussed in more detail in section 3.2.

3.1.6 Particle-in-cell - Monte Carlo models

As mentioned above, the MC method is not self-consistent. Indeed, the force acting on the (charged) MC particles originates from the electric field which is not calculated in the MC method. The electric field must therefore be predefined. The MC method can, however, be made self-consistent, in so-called particle-in-cell – Monte Carlo simulations. In this method, the charge density is calculated from the particle positions on certain predefined locations for each timestep, hence the name "particle-in-cell - MC". Subsequently, by solving Poisson's equation, the electric field can now be calculated based on the charge distribution. This method is very accurate and also self-consistent but suffers from an even longer calculation time [39-41].

3.1.7 Hybrid models

Hybrid models combine two or more of the above mentioned calculation methods [42-45]. In this manner, the advantages of the different models can be combined, and the disadvantages of individual models can be avoided. For example, a Monte Carlo – fluid model will allow for a relatively fast calculation of a complex chemistry system (in the fluid part), while it is still able to properly calculate low-pressure systems (by considering the electrons with the MC method). Therefore, hybrid models do not have real disadvantages compared to the other models (except that they can also be rather time-consuming). Depending on the desired information, often a set of other models (or modules) are coupled for a self-consistent calculation of the plasma, such as additional circuit, sheath or surface modules (see also below).

3.1.8 Molecular dynamics simulations

Molecular dynamics (MD) simulations do not describe the plasma behavior, but it is a commonly used method for predicting plasma-surface interactions on the atomic scale [46-50]. It is a deterministic simulation technique that follows the time evolution of a set of interacting particles by solving the laws of classical mechanics. Forces acting on the particles are calculated based on interatomic interaction potentials. In this setup, the reaction mechanisms are not predefined, but are a result of the calculation, making it very suitable for investigating the mechanism of plasma-surface interactions. A disadvantage of MD simulations is that only a limited number of atoms can be considered in a reasonable calculation time. Therefore, the MD method is limited to atomic scale processes.

3.1.9 The computational models applied in this work

A hybrid MC – fluid model, which allows to calculate properties of low-pressure plasmas accurately and relatively fast, is considered to be most appropriate for the plasmas under study in this work. Therefore, the simulation results presented throughout this work are obtained from a hybrid MC – fluid model, called the "Hybrid Plasma Equipment Model" (HPEM). This model was developed by M Kushner and co-workers [51]. In addition to this model to calculate bulk plasma properties, a set of other modules is coupled to address plasma-surface interactions and profile evolutions on a microscale. These are a MC model for heavy plasma species, an analytical model for surface chemistry and a MC model for microstructure profile evolution during plasma treatment.
In the following sections, the MC and fluid computational techniques, as well as the HPEM code with the above mentioned coupled modules, are discussed in more detail.

3.2 Monte Carlo

As mentioned above, in a Monte Carlo (MC) simulation, the behavior (i.e. positions and velocities) of a set of interacting particles is described by solving the laws of classical mechanics for a number of successive, discrete time steps. Positions and velocities are initially chosen, for example a uniform distribution for positions and a Maxwell distribution for velocities.
After defining the initial conditions, the trajectory of each MC particle is calculated by solving Newton's laws:

$$\vec{x} = \vec{x_0} + \vec{v}dt + \frac{1}{2}\vec{a}dt^2$$
$$\vec{v} = \vec{v_0} + \vec{a}dt$$

where x is the new position of the particle after time step t (s). x_0 is the initial position or more in general, the position at the previous time step, v is the speed ($m\ s^{-1}$), a is the acceleration ($m\ s^{-2}$) and v_0 is the initial speed ($m\ s^{-1}$) or speed at previous time step. The acceleration a can be calculated from the forces acting on the MC particle (Newton's second law):

$$\vec{F} = m\vec{a}$$

F is the force (N) acting on the particle with mass m (kg). For a charged particle in an electromagnetic field, the force acting on it, also called the Lorentz force F_L, can be written as:

$$\vec{F_L} = q\left(\vec{E} + \vec{v_0} \times \vec{B}\right)$$

where E is the electric field ($V\ m^{-1}$), B the magnetic field ($V\ s\ m^{-2}$; *tesla*) and q the charge (C) of the particle. For an electron, this (elementary) charge is -1.6×10^{-19} C. The electromagnetic field is often a predefined input in the MC calculation, so E and B are initially known. It should be noted that the acceleration a is considered to be constant during the given time step t. This is only true if this time step is small enough so that the E and B fields do not change significantly during this time step. Therefore, typical time steps in MC simulations are in the order of a few picoseconds or more (10^{-12} - 10^{-10} s). Moreover, often dynamic time steps are defined, usually based on the operating frequency of the power

source creating the electromagnetic fields. Indeed, it is common to define for example 100 time steps in one rf cycle [52].

Trajectories of MC particles are not only dependent on the force acting upon them, but also on collisions between particles. The collision probability P in a given time step can be defined as:

$$P = 1 - \exp\left[-\Delta s \sum_i n_i \sigma_i (\varepsilon) \right]$$

where Δs is the distance (m) the particle travels during that time step. n_i is the density (m^{-3}) of the target species of collision type i and σ_i the cross section (m^2) of this collision type. This cross section is typically energy (ε) dependent.

In this way, making the sum of all possible reactions that can occur with all different species, the above equation yields a probability between 0 and 1. Based on a random number generator, a random number is introduced between 0 and 1. If this number is smaller than P, a collision will occur. If this number is larger than P, no collision occurs and the particle is followed during the next time-step. If a collision occurs, another random number will decide which reaction will happen. If a reaction occurs, the new energy and direction of the particle (i.e. the velocities) are updated based on the kind of reaction, typically by means of another random number and formulas for energy loss or scattering formulas. So, the MC method is a statistical method and therefore enough MC particles should be considered to reduce the statistical error. Typically, at least several 1000 particles need to be followed to obtain reasonable statistics.

3.3 Fluid

A fluid simulation is based on solving the continuity equations for mass, momentum and energy, i.e. quantities which are always conserved [51]. Unlike the MC method, where individual particles are considered, the fluid model treats each kind of species as a group (or continuum). The continuity equations are derived from the Boltzmann equation (see section 3.1.3).

The change in density n of a species i in a certain time interval t is described by the continuity equation of mass (i.e. the first moment of the Boltzmann transport equation):

$$\frac{\partial n_i}{\partial t} = S_i - \vec{\nabla}_r \cdot \vec{\Gamma}_i$$

where S_i is the net production or loss rate ($m^{-3}\ s^{-1}$) for that kind of species (i.e. due to chemical reactions in the plasma). S_i is determined based on the reaction rate coefficients in which this species is lost and formed and on the densities of the species involved in these reactions. The second term in the right-hand side of this equation describes the loss or gain of a certain species due to its mass flow in and out a certain volume.

Γ_i is defined based on the continuity equation for momentum (i.e. the second moment of the Boltzmann transport equation). Often, the electron fluxes are determined using the so-called “drift-diffusion approximation”:

$$\Gamma_i = \mu_i q_i n_i \vec{E} - D_i \vec{\nabla} n_i$$

where q_i is the charge of the species (C), μ_i is the mobility ($m^2\ V^{-1}\ s^{-1}$) and D_i is the diffusion coefficient ($m^2\ s^{-1}$). This equation describes the flux as a

function of drift in the electric field E ($V\ m^{-1}$) (first term on right-hand side), and diffusion due to concentration gradients (second term on right-hand side). The drift term is of course only present for charged species. So, in the drift-diffusion approximation the transport of charged particles is seen as the combined effect of a drift flux caused by an electric field, and a diffusion flux caused by a density gradient. This approximation is justified in the "collisional regime" where the variations of the electric field are small within a collision time, which is true for the electrons.
The equation in the form presented here is valid if there is no static magnetic field present, which is true for the cases considered in this work. The diffusion coefficient D_i is related to the mobility μ_i as follows:

$$\mu_i = \frac{q_i}{k_B T} D_i$$

where k_B is the Boltzmann constant ($1.380 \times 10^{-23}\ J\ K^{-1}$). The mobility μ_i in a gas (or plasma) can be calculated from the following equation:

$$\mu_i = \frac{q_i}{m_i \upsilon_{col}}$$

where q_i is the charge ($C = kg\ m^2\ V^{-1}\ s^{-2}$) and m_i is the mass (kg) of species i. υ_{col} is the collision frequency (s^{-1}) which can be calculated as follows, as is explained in more detail in section 2.3.3 earlier.
At low pressure, however, this drift-diffusion approximation is less suitable for heavy plasma species and usually the full momentum equation is considered for these species:

$$\frac{\partial \Gamma_i}{\partial t} = -\frac{1}{m_i}\nabla\left(n_i k_B T_i\right) - \nabla\cdot\left(n_i \vec{v}_i \vec{v}_i\right) + \frac{q_i}{m_i} n_i \vec{E} - \sum_j \frac{m_j}{m_i + m_j} n_i n_j \left(\vec{v}_i - \vec{v}_j\right)\upsilon_{ij}$$

where υ_i is the species velocity ($m\ s^{-1}$) and υ_{ij} is the collision frequency (s^{-1}) between species i and j, and the other symbols have been explained above.

The temperatures are obtained from the energy continuity equation (i.e. the third moment of the Boltzmann transport equation):

$$\frac{\partial n_i c_i T_i}{\partial t} = \nabla \cdot \kappa_i \nabla T_i - P_i \nabla \cdot \vec{v}_i - \nabla \cdot \left(\vec{\Gamma}_i \varepsilon_i \right) + \frac{n_i q_i^2}{m_i \upsilon_i} E_s^2 + \frac{n_i q_i^2 \upsilon_i}{m_i \left(\upsilon_i^2 + \omega^2 \right)} E^2$$

$$+ \sum_j 3 \frac{\mu_{ij}}{m_i + m_j} n_i n_j \upsilon_{ij} k_B \left(T_j - T_i \right)$$

where c_i is the specific heat capacity ($J\ K^{-1}$), κ_i the thermal conductivity of species i ($W\ m^{-1}\ K^{-1}$), P_i the partial pressure of species i ($N\ m^{-2}$), ε_i the internal energy of species i (J), E_s the electrostatic field ($V\ m^{-1}$), E the rf electric field ($V\ m^{-1}$) and ω the operating frequency (s^{-1}).

Finally, these continuity equations are solved together with the Poisson equation, which calculates the electric field E from the charge distribution:

$$\nabla^2 V = \frac{e}{\varepsilon_0} \left[\sum_{i+} n_{i+} - \sum_{i-} n_{i-} \right] \quad ; \quad \vec{E} = -\vec{\nabla} V$$

where V is the potential (V), e the elementary charge ($1.6 \times 10^{-19}\ C$) and ε_0 the vacuum permittivity ($8.85 \times 10^{-12}\ F\ m^{-1}$). n_{i+} and n_{i-} are the densities of positive and negative ions i, respectively.

3.4 The hybrid plasma equipment model

3.4.1 Overview

The Hybrid Plasma Equipment Model (HPEM) is a two-dimensional hybrid Monte Carlo – fluid model developed by M Kushner and co-workers [51-60]. The HPEM is especially designed to investigate low-pressure plasma processing reactors. It is a powerful code in the sense that a wide variety of reactors and operating conditions can be modelled. It allows the calculation of macroscopic bulk plasma properties as well as microscale surface processes such as etching or deposition.

The plasma physics and chemistry are calculated in the HPEM through a series of modules. An overview of the different modules of the HPEM used in this work is illustrated in **Figure 16**.

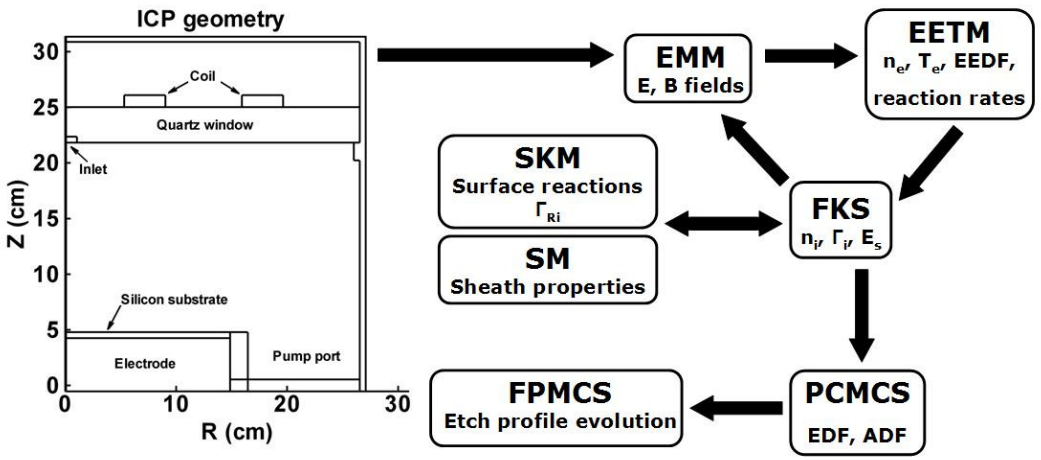

Figure 16. Schematic overview of the different modules of the HPEM used in this work. EEDF is electron energy distribution. EDF and ADF are the energy and angle distributions. E_s is the electrostatic field and Γ_{Ri} is the "returning" flux which is the flux of species being launched from the walls into the plasma.

The main body of HPEM consists of three modules: an electromagnetics module (EMM), an electron energy transport module (EETM) and a fluid kinetics simulation (FKS). In addition, a number of other modules can be activated as well, depending on the situation and desired output. The additional modules used in this work are a sheath module (SM), a plasma chemistry Monte Carlo simulation (PCMCS), a surface kinetics module (SKM) and a feature profile Monte Carlo simulation (FPMCS). A more detailed discussion of each module is given in the following sections. To calculate the bulk plasma properties, the HPEM cycles through the three main modules (EMM, EETM and FKS) until convergence is reached. One cycle through all modules is considered to be an iteration. Convergence is said to be reached if the result from the latest iteration does not differ more than a predefined margin (i.e. the convergence criterion, which is typically around 0.01 %) from the result of the previous iteration.

3.4.2 The electromagnetics module (EMM)

The EMM calculates the time-varying electromagnetic fields in the plasma, generated by the power source or by permanent magnets. Metals with a certain voltage will generate an electromagnetic field that penetrates into the plasma. Basically, the fields can be calculated by solving the Maxwell equations.
These include Gauss's laws for the electric and magnetic field, Faraday's law and the Ampère-Maxwell law. Gauss's law for the electric field gives the relation between charge distribution (in the plasma) and the electric field:

$$\nabla \cdot \vec{E} = \frac{q}{\varepsilon_0}$$

where E is the electric field ($V\ m^{-1}$), q is the charge (C) and ε_0 the vacuum permittivity ($8.85 \times 10^{-12}\ F\ m^{-1}$).
Gauss's law for the magnetic field (B) states that the magnetic field lines alway form loops and that the total magnetic flux through a volume is always zero:

$$\nabla \cdot \vec{B} = 0$$

Faraday's law describes how a changing magnetic field induces an electric field that will try to counteract the magnetic field; hence the negative sign:

$$curl\vec{E} = -\frac{\partial \vec{B}}{\partial t}$$

Finally, the Ampère-Maxwell law states that a magnetic field can be created by electrical current and/or by a changing electric field:

$$curl\vec{B} = \mu_0 \vec{j} + \mu_0 \varepsilon_0 \frac{\partial \vec{E}}{\partial t}$$

where j is the electrical current and μ_0 the vacuum permeability ($4\pi \times 10^{-7}\ V\ s\ A^{-1}\ m^{-1}$).
Based on these equations the time-varying electromagnetic field can be calculated within the reactor volume. However, in practice the actual equation that is solved in the EMM is derived from the above Maxwell equations and has the following form [51-60]:

$$\nabla\left(\frac{1}{\mu_0}\nabla\cdot\vec{E}\right)-\nabla\cdot\left(\frac{1}{\mu_0}\nabla\vec{E}\right)-\omega^2\varepsilon_0\vec{E}=-i\omega\left(\vec{J}+\sigma\cdot\vec{E}\right)$$

where ω is the operating frequency (s^{-1}), J the coil current density ($C\ m^2\ s^{-1}$) and σ the conductivity which can be calculated as follows, if there are no static magnetic fields present:

$$\sigma=\frac{q_e^2 n_e}{m_e\left(\upsilon_{col}+i\omega\right)}$$

where q_e is the elementary charge ($1.6 \times 10^{-19}\ C$), n_e the electron density (m^{-3}), m_e the electron mass ($9.11 \times 10^{-31}\ kg$) and υ_{col} the collision frequency (s^{-1}) (see section 2.3.3).
Due to the cylindrical symmetry, the magnetic field B is calculated through a vector A as follows [54]:

$$\nabla\times\vec{A}=\vec{B}\quad\text{where}\quad\nabla\times\frac{1}{\mu}\nabla\times\vec{A}=J$$

where J is the current density of the coil(s).

3.4.3 The electron energy transport module (EETM)

Based on these electromagnetic fields, the EETM will calculate the electron density, temperature, energy distribution function and electron impact reaction rates [51-60]. The acceleration of electrons by the electromagnetic fields in the plasma gives rise to high enough energies, so that electron collisions with heavy species result in dissociation, excitation and ionization reactions. This electron behavior can be

calculated by two different methods in the EETM.
One method for determining the electron behavior is by a MC procedure. The electrons are accelerated in the electromagnetic field and followed for many rf cycles (> 100) where the time step is usually not larger than 1 % of the rf cycle. The electron density is calculated by "counting" the MC particles, while the energy distribution can be calculated by "binning" the energies and "counting" how many electrons have a certain energy. The electron temperature T_e (eV) is calculated as [54]:

$$T_e = \frac{2}{3}\int f(\varepsilon)\cdot\varepsilon\cdot\partial\varepsilon$$

where $f(\varepsilon)$ is the electron energy distribution function and ε the electron energy.
A second method for calculating the electron behavior is by solving the electron energy equation in the following form [54]:

$$\nabla\kappa\nabla T_e + \nabla\cdot\left(\Gamma_e T_e\right) = P_{heat} - P_{loss}$$

where κ is the thermal conductivity ($W\ m^{-1}\ K^{-1}$), T_e the electron temperature (K), Γ_e the electron flux ($m^{-2}\ s^{-1}$) and P ($W\ m^{-3}$) the change in energy due to power deposition (heating) and inelastic collisions (loss). P_{heat} is calculated from the time averaged value of:

$$P_{heat} = \vec{J}\cdot\vec{E}$$

where J ($C\ m^{-2}\ s^{-1}$) is the current density obtained from the FKS and E ($V\ m^{-1}$) the electric field obtained from the EMM.
In order to solve this equation, transport coefficients as a function of

average electron energy are needed. These can be obtained by solving the zero-dimensional Boltzmann equation for a range of different E/n ratios (see section 3.1.3). Subsequently, electron properties such as electron temperature, electron mobility and electron impact reaction rates are obtained from the calculated electron energy distribution function [54].
The electron energy equation method has the advantage of a shorter calculation time because no individual particles need to be followed as in the MC method. However, solving the energy equation is less reliable at very low pressure, where the MC method can still provide proper results. For the simulations performed in this work, both methods have been considered, but mostly the electron energy equation method was used.

3.4.4 The fluid kinetics simulation (FKS)

As explain in section 3.3 above, the FKS solves the continuity equations for mass, momentum and energy to determine the spatially dependent densities of all plasma species, as well as the electric field based on the charge distribution, by solving the Poisson equation [51-60]. Also fluxes and species temperatures are calculated in this fluid module. More details were given in section 3.3 on fluid models.

3.4.5 The sheath module (SM)

In high density plasmas as investigated in this work, the sheath thickness is often in the order of 100 μm or less. Even at very high substrate bias the sheath thickness reaches at maximum values close to 2 *mm* (see section 2.1.3), which is still much smaller than the typical reactor dimensions for wafer processing (~20 *cm*). Resolving the potential drop in the sheath in this kind of reactors can therefore be problematic when using practical grid resolutions [61]. If the sheath is not well

resolved, the potential drop might not be well represented. To solve this, a one-dimensional analytical model is addressed during the plasma calculation to obtain the time-dependent sheath voltage drop during the rf cycle, based on the charge in the sheath and the plasma conditions at the sheath edge. More details on the sheath module can be found in references [60, 61]. The SM calculates the potential drop (i.e. sheath thickness) in every mesh cell at the boundary of the plasma.

3.4.6 The surface kinetics module (SKM)

Especially for low pressure plasmas where the mean free path is relatively long, wall processes are very important. Usually in plasma simulations, the wall processes are defined in a relatively simple way. For example, when a neutral species arrives at the boundary (i.e. wall) it is often assumed to be reflected or to stick with a certain probability. It is also common to define that all excited and charged species are returned into the plasma as their ground state neutral equivalents when hitting the wall. However, many more complex surface reactions can happen, such as physical and chemical sputtering, chemical reactions such as chlorination and oxidation, and redeposition of non-volatile plasma species, as will be described in more detail in the next chapter.

To address these surface processes, the SKM calculates surface properties, such as chemical compositions, etch and deposition rates, based on a predefined surface reaction set. Also “returning” fluxes are calculated in this module. These are fluxes of species that are launched from the wall back into the plasma, as would happen for example during sputtering where etch products are removed from the surface and brought into the bulk plasma.

The SKM is performed in each computational cell at the plasma-wall boundary of the two-dimensional reactor geometry [54], and is solved

together with the FKS in an iterative way, similar to cycling through the three mean modules of HPEM. Indeed, first the plasma properties are calculated in the FKS, including fluxes towards the surfaces. Based on these fluxes, a change in surface composition is calculated in the SKM, as well as the returning fluxes of species towards the plasma. Subsequently, based on the newly obtained surface composition and returning fluxes, the plasma properties are updated in the FKS.

3.4.7 The plasma chemistry MC simulation (PCMCS)

As mentioned before, the heavy plasma species properties, such as density, flux and temperature, are calculated in the fluid module (FKS). Therefore, no information is available on the energy distribution of the species when they arrive at the substrate. This is especially important for the ions that are accelerated towards the substrate and can sputter the surface (with an energy dependent sputter yield; see next chapter). Also angular distributions of the species (i.e. both ions and neutrals) arriving at the wafer are not available from the FKS. However, the latter is important for predicting the shape of the trenches during etching (see below).

Therefore, an extra MC simulation is performed after convergence is reached in the general HPEM calculation.

Based on the densities calculated in each computational cell by the FKS, a number of MC particles (i.e., both ions and neutrals) is launched in the reactor volume. The MC particles can collide with each other in the plasma and the trajectories of these species are calculated in a comparable way as already discussed in section 3.2 on the Monte Carlo method. In this way, energy and angular distributions of the different heavy plasma species (i.e., both ions and neutrals) arriving at the wafer and reactor walls can be obtained, by counting. More details on how the

energy and angular distributions of the species are calculated in the PCMCS can be found in references [54, 57-59].
It should be noted that this MC calculation is performed at the end of the plasma simulation, and not during every iteration, which can save a significant amount of calculation time [62].

3.4.8 The feature profile MC simulation (FPMCS)

Finally, to predict the profile evolution of a microstructure, such as the etching or filling of Si trenches, as a function of time, an offline microscale MC simulation is performed in the FPMCS [54, 57-59]. Indeed, the FPMCS is an offlline module meaning that it is addressed after the plasma simulation is completely finished. The output of the FPMCS is therefore not used in the plasma simulation (HPEM). The influence of surface processes on the bulk plasma is indeed already addressed in the SKM during the plasma calculation.
The two-dimensional FPMCS uses the calculated fluxes (obtained in the FKS), and energy and angle distributions (from the PCMCS) as input to launch MC particles towards a microscale surface (feature), in order to calculate how the surface will change in time, i.e. during plasma treatment. Besides the fluxes, energy and angle distributions calculated in the plasma modules, also the created mesh indicating the initial feature shape and the material properties are input in this FPMCS, as well as a reaction set describing the surface processes. Naturally, the same surface reaction set is used in both the SKM and the FPMCS. Feature profiles are altered in time due to the reactions of the plasma species with the surface cells. If a plasma species arrives at a certain "material cell", the cell can be removed or altered based on the reaction set. If deposition occurs, a new material cell will be created on top of the "reacting" cell. **Figure 17** shows an example of a created grid before the

launch of MC particles (left) as well as the calculated profile after launch, in case of etching (right). More details on calculated profiles will be given in Part III.

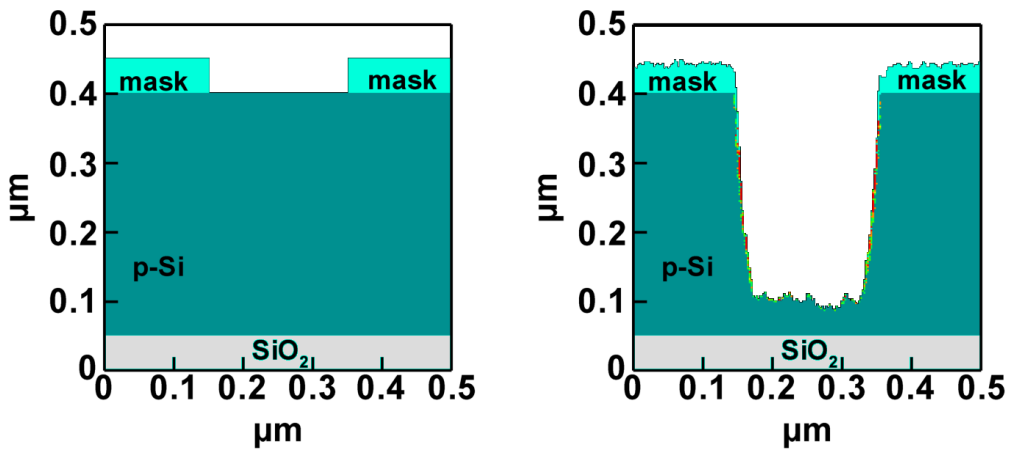

Figure 17. **Left**: two-dimensional mesh predefined in the FPMCS. **Right**: calculated profile after launch of MC particles, in case of etching.

3.5 The computational mesh

As mentioned before, the HPEM is a two-dimensional model, so only a half cross section of the complete reactor is calculated. This is possible due to the fact that plasma processing reactors for electronic device fabrication often are cylindrically symmetric. The substrate commonly is a circular Si plate (wafer) and a cylindrical reactor therefore increases process uniformity.

The reactor geometry defined in the model for this work is based on an existing Lam Research 2300 Versys Kiyo 300 *mm* wafer ICP reactor with a planar coil on top of the chamber (TCP geometry; see section 1.6 above). This reactor is applied in industry for etching of Si with $Ar/Cl_2/O_2$ plasmas as applied in STI. The reactor geometry considered in the last

chapter of this PhD thesis, which deals with the trench filling study by an $Ar/SiH_4/O_2$ plasma, is only slightly different, as will be illustrated in Chapter 9. The geometry and computational grid are presented in **Figure 18**.

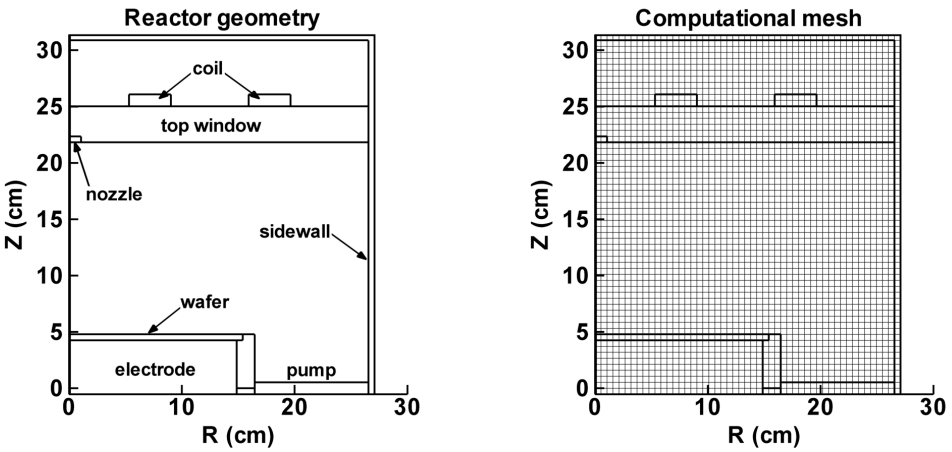

Figure 18. **Left**: Two-dimensional reactor geometry defined in the model based on the Lam Research 2300 Versys Kiyo TCP reactor. **Right**: The computational grid showing all computational cells.

Each computational cell on the grid is defined as a specific "material" (e.g. quartz, metal, silicon or plasma). Plasma properties are calculated on the vertices of the grid cells. Creating more grid cells will increase the resolution for more smooth profiles, but it has the disadvantage of a longer calculation time. Therefore, a number of mesh cells are chosen so that proper results can be obtained in a reasonable calculation time. Typically, around 2500 mesh cells are used in the simulations carried out in this work.

To obtain the complete reactor geometry (in three dimensions), the plane shown in **Figure 18** should be rotated around the left Z-axis. The power source (the planar coil) is located on top of the chamber above the top dielectric window (quartz). The area surrounding the coil is air at atmospheric pressure, while the area underneath the dielectric window is

plasma region (at low pressure). The gas can be fed into the reactor through the nozzle(s) in different ways. Common setups are a nozzle in the centre of the top window (as presented here), or in combination with a nozzle located at the sidewall (as will be the case in Chapter 9). Showerhead nozzles are also common, where the gas is fed through various holes from the ceiling to increase plasma uniformity. The gas is pumped out at the bottom of the reactor. The substrate is a Si wafer with a cross section of 300 *mm* and 0.75 *mm* in thickness. The substrate electrode is located underneath the wafer to attract the positive ions from the plasma. The sidewall is a grounded metal, with the surface (in contact with the plasma) consisting of Al_2O_3.

Since each computational cell in the grid is defined as a specific "material", certain properties must be defined for these materials to allow for an accurate calculation, including proper electrical conduction and electromagnetic field propagation. In fact, the only properties that need to be defined are the relative permittivity ε_r, the electrical conductivity σ, and the temperature of the materials. It is possible to include thermal conduction for materials, but usually a fixed temperature is defined for simplicity.

ε_r and σ of the relevant "materials" considered in our simulations are listed in **Table 2**.

Table 2. Relative permittivities (ε_r) and electrical conductivities (σ) of some relevant "materials" used in our simulations.

"material"	ε_r	σ ($S\ m^{-1}$)
air (1 *atm*)	1.000.589	4×10^{-15}
quartz window	3.9	1.3×10^{-18}
Si wafer	11.68	1.56×10^{-3}
plasma	1 (considered ε_0)	(calculated; see text)

Relative permittivity and conductivity of air are listed in the table because it is the "material" above the dielectric window surrounding the coil, which is also taken into account in our simulations to allow for a proper calculation of the electromagnetic field distribution in the reactor. Other dielectrics present in the reactor are the quartz window and the Si wafer.
The permittivity of the plasma (i.e. low pressure; near vacuum) can be considered equal to that of vacuum. The plasma conductivity is not predefined but calculated, since it depends on the electron properties as follows:

$$\sigma = \frac{n_e e^2}{m_e \upsilon_{col}}$$

where n_e and m_e are the electron density (m^{-3}) and mass (kg) respectively. e is the elementary charge (1.6×10^{-19} C) and υ_{col} the collision frequency (s^{-1}) (see section 2.3.3 on collision frequency and also section 3.4.2 on cycle dependent conductivity). The typical conductivity of the plasmas under study is calculated to be in the order of $10^4 - 10^5$ $S\ m^{-1}$. Indeed, generally, plasmas are good conductors.
Finally, it should be noted that operating conditions such as gas mixture, gas flow, chamber pressure, source power and operating frequency are defined for each case specifically and are not directly connected to the creation of the computational mesh.

Chapter 4

Reaction sets

4.1 General overview

In the following sections it will be discussed how the specific plasma and surface chemistry is implemented in the code for addressing, on the one hand, $Ar/Cl_2/O_2$ plasmas used for etching of Si, and on the other hand, $Ar/SiH_4/O_2$ plasmas used for deposition of SiO_2 (i.e. trench filling).
In the first sections of this chapter, general information is presented on the various gases mentioned above, as well as a brief description of the materials the plasma is in contact with in the reactor, more specifically, the silicon substrate (i.e. the wafer), the top dielectric window (i.e. quartz) and the reactor wall, which consists of anodized aluminium (Al_2O_3).
A great number of different reactions take place in the plasma, such as ionization, dissociation, excitation, neutralization etc., creating various reaction products such as ions, radicals, excited species and free electrons. Moreover, during the etching process, etch products coming from the substrate are loaded into the plasma as well. To be able to address all these processes, a reaction set is created describing the typical plasma chemistry under study. Therefore, in the following sections it is discussed how this complex plasma and surface chemistry is translated into a reaction set which can be implemented in the model

to predict the plasma properties under various operating conditions. Reaction sets are presented for bulk plasma chemistry of $Ar/Cl_2/O_2$ and $Ar/SiH_4/O_2$ mixtures, as well as detailed reaction sets describing the possible surface processes such as chemical etching, surface oxidation, sputtering and deposition reactions.

4.2 Basic information on components

Two processing steps of STI that have been investigated in this work are the etching of Si with an $Ar/Cl_2/O_2$ plasma, and the deposition of SiO_2 with an $Ar/SiH_4/O_2$ plasma. All the gases in these mixtures are fed into the reactor chamber and will come into contact with the reactor wall (Al_2O_3), the top dielectric window (quartz; SiO_2) and the substrate (a Si wafer). General properties for these gases and materials are illustrated in **Table 3**. It should be noted that atomic radius, bond length and energy, as well as material density are actually no input parameters for the plasma modelling performed in this work, but they can help in understanding the overall plasma-surface processes. A brief description of the mentioned gases and materials, including their general properties and common applications, is also presented in the following sections.

Tabel 3. General properties of the gases and materials considered in this work.

Gas	Mass ($g\ mol^{-1}$)
Ar	39.948
Cl_2	70.906
O_2	31.998
SiH_4	32.008

Material	Density ($g\ cm^{-3}$)
Si	2.33
SiO_2 (α-quartz)	2.66
Al_2O_3	3.70

Bond type	Bond lenght (*Å*)
Cl-Cl	1.99
O=O	1.21
Cl-O	1.49
O-H	0.95
H-H	0.74
Si-H	1.48
Si-Cl	2.02
Si-Si (solid)	~2.33
Si-O (α-quartz)	~1.63
Al-O (solid)	~1.75
Gas residence time	0.01 - 10 *s* (**Figure 15**)

4.2.1 Argon gas

Ar is a safe, colourless, odourless and noble gas. Its name is derived from its inertness, or in other words its inactivity towards chemical reactions, due to its octet structure in its outer atomic shell. Common uses for Ar are as a shielding gas in high-temperature industrial applications (e.g. welding), as filling in light bulbs and as isolating material in double glazing. Ar lights are known to emit blue light. In plasma processing, it is commonly used in a mixture as chemically-inactive (diluting) agent.

4.2.2 Chlorine gas

Cl_2 is a yellow-green gas which has a strong bleach odour. Its chemical bond is relatively weak (2.5 *eV*) which makes it highly reactive. The most

famous use for pure Cl_2 gas was as a weapon during World War II. Due to its high oxidising power, Cl_2 can react with water and cells making it a toxic gas even at relatively low concentration. In plasma processing applications, Cl_2 gas is commonly applied in dry etching since it spontaneously reacts with Si to form volatile $SiCl_4$. A pure Cl_2 plasma has a reddish violet color.

4.2.3 Oxygen gas

O_2 is a pale blue odourless gas and is a main component in air (21 %). Common uses for pure O_2 gas include production of steel and plastics, oxygen therapy and life support equipment such as oxygen diving cylinders. In plasma processing it is mainly applied as oxidising agent in plasma cleaning (i.e. removing impurities from surfaces) and plasma ashing (i.e. removing photoresist). It reacts with Si to form a passivation layer of SiO_2. Pure O_2 plasmas emit a light blue colour.

4.2.4 Silane gas

SiH_4 is a colourless and fairly toxic gas with a repulsive smell. It is highly flammable since it undergoes spontaneous combustion when in contact with air. SiH_4 is mainly applied for the deposition of amorphous or polycrystalline Si in semiconductor or solar cell manufacturing through chemical vapour deposition. Deposition of amorphous or polycrystalline Si can be controlled by varying the power or the substrate temperature. Indeed, more power will create more dissociation products (and hence more H), which can perturbate the Si-Si bonds, so that polycrystalline Si is formed instead of amorphous Si. Similarly, by increasing the temperature, rather *poly*-Si will be deposited compared to amorphous Si. Other applications include coupling bio-inert layers to titanium implants

for medical applications. Similar to Cl_2, SiH_4 plasma is known to emit a reddish violet color.

4.2.5 Silicon

Si is the eighth most common element in the universe by mass but is very rarely found in nature as a pure material (e.g. in volcanic exhalation). In its crystalline form Si is a semiconductor with a gray colour and a metallic shine. Like glass, it is rather strong but very brittle. Main applications of metallurgic Si are in constructing alloys (e.g. for the automotive industry) and in the semiconductor industry for the fabrication of ultra-pure Si wafers applied for electronic devices or for photovoltaic applications. Si, as a semiconductor, is most useful for constructing electronic devices since the conductivity can easily be modified and controlled by introducing dopants in the crystal lattice. This control is necessary for fabricating e.g. transistors or solar cells in high-tech applications.

More specifically, in electronic device fabrication, one should distinguish between poly- and monocrystalline Si. A polycrystalline Si (polysilicon; *poly*-Si) layer consists of a number of small crystals (crystallites) and can therefore be recognised by a visible metal grain-like look. It is a key component for ICs as a conducting gate material for MOSFET technologies [63]. In these technologies, *poly*-Si is deposited by means of PECVD and usually heavily doped for desired conductivity. An advantage is that it shows a much higher mobility for charge carriers compared to amorphous Si.

Monocrystalline Si (*mono*-Si) has a homogenous crystal lattice showing a uniform colouring. In essence it is the base material of the electronics industry. A *mono*-Si layer is used as a base material (e.g. a 300 *mm* wafer) where nanostructures are built upon. Indeed, grain boundaries (in *poly*-

Si) can entail discontinuities and imperfections in electronic properties of the material. On the scale the devices are created on, these imperfections have significant impact on the reliability of the devices. Therefore, *mono*-Si is more suitable for ultra large scale integration (ULSI) since it has uniform electronic properties. *Mono*-Si can be grown by the Czochralski process [64], creating a monocrystal in the shape of a cylinder which can be up to 2 *m* long and 30 *cm* wide. 300 *mm* wafers are obtained by cutting the *mono*-Si cylinder in slices. In the Czochralski process, *poly*-Si is melted and a small rod with a seed crystal is introduced. In this process the crystal is grown and a large monocrystalline Si rod is pulled from the "silicon bath".

4.2.6 Quartz

Quartz is a mineral with a chemical formula of SiO_2. It is common in nature and can occur in many different varieties. In the microelectronics industry, quartz is a useful material as dielectric window in ICP reactors because it is relatively cheap compared to other ceramic materials, and it is not contaminating for wafer processing steps under study in this work.

4.2.7 Anodised aluminium

Aluminium alloys are often anodised to increase the thickness of the surface oxide layer (Al_2O_3) for improving corrosion resistivity and surface hardness. The anodic (surface) layer is non-conductive. For processing reactors Al_2O_3 has proven to be a suitable wall material, because it shows proper resistivity against a large variety of plasma chemistries occurring in electronic device fabrication. It is also much stronger than quartz (for example) and sputtering of Al_2O_3 is negligible.

4.3 Literature overview relevant for the chemistries under study

The development of continuously shrinking electronic devices is a popular field of research in a sense that a very large number of experimental and modeling papers on this topic exist in literature. Indeed, the fabrication of a chip includes hundreds of different steps where a large variety of different chemistries is applied.

As mentioned earlier, the processing steps investigated in this work are the etching of Si with an $Ar/Cl_2/O_2$ ICP and the deposition of SiO_2 with an $Ar/SiH_4/O_2$ ICP, as applied in STI (section 1.8). Therefore, the most relevant papers for this work describe experimental as well as modeling results for $Ar/Cl_2/O_2$ and $Ar/SiH_4/O_2$ ICPs. Indeed, these data are indispensable for validating our simulation results.

Several experimental studies [65-73] and numerical simulation results [61, 62, 74-85] have been reported on inductively coupled Ar/Cl_2 plasmas and their surface reactions used for etching applications. Also, a lot of work has been performed on the modeling of O_2 plasmas [12-18], but not so many groups have reported on the modeling of Cl_2/O_2 based plasmas [86-88]. The main difficulty with modeling Cl_2/O_2 plasmas is that a large number of different Cl_xO_y reaction products can be formed. Nevertheless, also information on the reaction kinetics for a wide variety of Cl_xO_y products is available from literature [89-100].

During the etching process, Si etch products are launched in the plasma and reactions for these species must therefore be included as well in detailed modeling of plasmas used for Si etching. A number of papers are published on the modeling of Cl_2 based plasmas including etch products [101-104]. Most of these papers, however, focus on etch product behavior

without oxygen as a part of the reaction mixture. To our knowledge, only Agarwal and Kushner [105] simulated plasma etching reactors for the etching of Si in an Ar/Cl_2 plasma, while oxygen can be sputtered from the dielectric quartz window.

Besides bulk plasma simulations, also extensive experimental and modeling research has been carried out with respect to the surface reactions of chlorine and oxygen species on Si [106-127]. However, of the numerous papers on etching of Si with a Cl_2/O_2 based plasma that are available from literature, only a few present results on the actual formation and growth of an etch-blocking oxy-chloride layer [105, 128-131] as is thoroughly investigated in this thesis (Chapter 6 and 7).

Another topic that is numerically investigated in this work is the effect of chamber wall coating on the plasma etching process (Chapter 8). To validate these simulation results, a number of papers have been addressed that presented experimental results on the effects of chamber wall conditions and the behavior of etch products in a Cl_2 based plasma applied for etching of Si [132-139].

Finally, in Chapter 9, the deposition process of SiO_2 with an $Ar/SiH_4/O_2$ plasma will be numerically investigated. Modeling work on Ar/SiH_4 plasmas used for deposition has been reported in literature [140, 141], where a few papers also included O_2 to the gas mixture [142, 143]. In these cases, a detailed reaction set for the gas-phase oxidation of silane was given, but deposition and surface oxidation were not considered in these publications. On the other hand, there exist some papers in literature on modeling the oxide deposition process on a surface [144, 145], but in these papers, no bulk plasma calculations are taken into account.

In the following sections, both detailed plasma chemistry and surface chemistry sets for both $Ar/Cl_2/O_2$ and $Ar/SiH_4/O_2$ gas mixtures will be presented, based on the above mentioned papers.

4.4 $Ar/Cl_2/O_2$ plasma chemistry

4.4.1 Species considered in the model

a. Overview

When the $Ar/Cl_2/O_2$ gas mixture is introduced in the reactor chamber and the plasma is ignited, "new" species are created, such as radicals, ions and excited species, through various reactions such as dissociation, ionization, excitation, etc. To properly address the plasma chemistry, all these species must be included in the simulation. It is virtually impossible to include "all" possible reaction products due to the complex chemistry and lack of data. It is therefore common to include only the most relevant/important species for simplicity. For the $Ar/Cl_2/O_2$ plasma chemistry, 32 different species are taken into account in the model, including etch products coming from the wafer or the reactor walls. The complete list of species is presented in **Table 4**. For information, the ionization potential, i.e. the (threshold) energy needed for ionization, of each neutral species is illustrated in **Table 5**.

Table 4. Overview of the species included in the model.

Ground state neutrals:	Ar, Cl_2, Cl, O_2, O, ClO
Positive ions:	Ar^+, Cl_2^+, Cl^+, O_2^+, O^+, ClO^+
Excited species:	Ar*, Cl*, O*
Negatively charged species:	Cl^-, O^-, electrons
Etch products:	Si, SiCl, $SiCl_2$, $SiCl_3$, $SiCl_4$, SiO, SiO_2
Etch product ions:	Si^+, $SiCl^+$, $SiCl_2^+$, $SiCl_3^+$, $SiCl_4^+$, SiO^+, SiO_2^+

Table 5. Overview of the ionization energies defined in the model.

Ionization	Ionization (threshold) energy (*eV*)
$Ar \rightarrow Ar^+$	15.76
$Cl_2 \rightarrow Cl_2^+$	11.47
$Cl \rightarrow Cl^+$	12.99
$O_2 \rightarrow O_2^+$	12.06
$O \rightarrow O^+$	13.62
$ClO \rightarrow ClO^+$	10.95
$Si \rightarrow Si^+$	8.15
$SiCl \rightarrow SiCl^+$	12.45
$SiCl_2 \rightarrow SiCl_2^+$	10.93
$SiCl_3 \rightarrow SiCl_3^+$	14.25
$SiCl_4 \rightarrow SiCl_4^+$	11.97
$SiO \rightarrow SiO^+$	11.55
$SiO_2 \rightarrow SiO_2^+$	12.15

b. Excited species

As for the excited species, we have included only one effective excited level for Ar, denoted as Ar*. It consists of a collection of *4s* and *4p* excited levels. Indeed, these levels typically have the highest population density of the various excited levels of Ar. In reality there are, of course, many more possible excited states for Ar*. However, the goal of the simulations performed in this work is not to obtain detailed information on excited level population so it is sufficient to include only the most common states. The main reason why excited states are included is because a significant amount of electron energy is transferred to the atoms or molecules through excitations, lowering the average electron energy. In addition to only considering the most common states, they are grouped together into two collective states for simplicity.

For example, for Ar* the real electronic *4s* and *4p* states are grouped into

two fabricated states called *4S* and *4P* with a defined threshold energy of 11.60 *eV* and 13.10 *eV* respectively. In addition, these two states are joined into only one kind of species (Ar*) for simplicity. Hence, two excitations are considered in the model for creating Ar*, but only one species is included. This is summarized as follows:

Electronic states (Ar)	Energy	Fabricated states		Actual species
$4s[3/2]_2$	11.548 *eV*			
$4s[3/2]_1$	11.624 *eV*			
$4s'[1/2]_0$	11.723 *eV*	$\longrightarrow \mathrm{Ar}^*(4S)$	11.60 *eV*	
$4s'[1/2]_1$	11.822 *eV*			
				$\longrightarrow \mathrm{Ar}^*$
$4p[1/2]_1$	12.907 *eV*			
$4p[3/2]_{1,2}+[5/2]_{2,3}$	13.116 *eV*			
$4p'[3/2]_{1,2}$	13.295 *eV*			
$4p'[1/2]_1$	13.328 *eV*	$\longrightarrow \mathrm{Ar}^*(4P)$	13.10 *eV*	
$4p[1/2]_0$	13.273 *eV*			
$4p'[1/2]_1$	11.480 *eV*			

The same principle is applied for the other excited species. Cl* is a combined state of the *4s* (8.90 *eV*), *3d* (10.40 *eV*), *4p* (11.80 *eV*), *5s* (12.00 *eV*), *4d* (12.0 *eV*) and *5p* (12.40 *eV*) excited levels while O* consists of the *3s* (9.15 *eV*) and *3p* (10.73 *eV*) excited states.

Electron impact vibrational and rotational excitations are included for Cl_2 and O_2, but not for the other molecular reaction products because their densities are significantly lower (except for $SiCl_{2\text{-}4}$). The excited levels of Cl_2 and O_2 are, however, not explicitly taken into account as separate species. Indeed, the species Cl_2 as considered in the model consists of

the ground state and two electronic excited levels with energies of 2.49 *eV* and 9.25 *eV*; for these three states, one vibrational and one rotational excitation is included with a threshold of 0.07 *eV* and 0.02 *eV*, respectively. For Cl_2, this yields therefore six electron impact excitation reactions with the stated thresholds. Similarly, O_2 includes the ground state molecule and two electronic excited levels with thresholds of 8.40 *eV* and 10.00 *eV*; for these three states, one rotational excitation and two vibrational excitations are included with thresholds of 0.02 *eV*, 0.19 *eV*, and 0.38 *eV*, which yields a total of nine electron impact excitation reactions for O_2.

c. Species not considered in the model

Naturally, the model considers only the most important plasma species. There is some evidence in literature of other species that might be present in the plasma, but their densities are typically very low and hence they can be neglected in the calculations. This is the case for some negative ions. For instance, Moylan *et al* [146] presented evidence of $SiCl_x^-$ (x = 0 - 5) anions in a pure $SiCl_4$ plasma but concluded that the densities of these negative ions are very low and the dominating negative ion is always Cl^-. For this reason, we did not include negative ions of etch species in our model. The same applies to O_2^-, which is stated [87, 147, 148] to be lost more rapidly by charge transfer to O^- than formed, because the threshold for the formation of O_2^- is relatively high. Hence, the density of O_2^- in the plasma will be much lower than the O^- density.
With respect to the neutral species, O_3 is not included in our model because, at the very low pressures under study, O_3 is not likely to be abundant in the plasma [88]. Similarly, although in a Cl_2/O_2 plasma different Cl_xO_y products might exist, such as ClO, Cl_2O, ClO_2 and Cl_2O_2, only ClO is included in our model. Indeed, Thorsteinsson and

Gudmundsson [88] have investigated the role of ClO in the plasma and found that other Cl_xO_y products have low densities. Finally, there has been some evidence of $SiCl_xO_y$ species in the plasma during etching, measured by mass spectrometry [132]. However, not much information can be found in literature about the chemical properties and reaction rates of these species. In [149] it is stated that $SiCl_x$ molecules will only be oxidised in the gas phase at a gas temperature of at least 1500 *K*, which is much higher than the typical gas temperature under study in this paper (~ 500 *K*). Therefore, $SiCl_xO_y$ plasma species are not included in our model either.

4.4.2 Plasma chemistry reactions

To describe the plasma chemistry of the $Cl_2/O_2/Ar$ plasma, a detailed reaction set was constructed. The complete reaction set is presented in **Tables 6** - **10**, subdivided according to the reactants, for the sake of clarity. Elastic collisions are included in the model but are not listed in the tables. The reaction rates of the electron-induced collisions are defined by energy dependent cross sections $\sigma(E)$ that are plotted in the corresponding figures. The rates of the ion-ion, ion-neutral and neutral-neutral reactions are determined by reaction rate coefficients that are directly presented in the tables, as well as the references where these data are adopted from. One paper [150] states that the thermal dissociation of $SiCl_4$ is only important at much higher temperatures (> 1500 *K*). For this reason, it can be expected that the etch products will be mostly dissociated or ionized in the plasma by electron impact reactions and not thermally.

It should be mentioned that the complete reaction set for an $Ar/Cl_2/O_2$ plasma in this work was created step by step. This means that first a reaction set for pure Ar was created and tested by performing

simulations of pure Ar plasmas. Subsequently, the same was done for pure Cl_2 and pure O_2 plasmas. Next, reactions between Ar and Cl_2 species were added and again tested by performing numerous simulations of Ar/Cl_2 plasmas under varying operating conditions (such as different gas ratios). After the addition of O_2 to the Ar/Cl_2 mixture, finally reactions concerning etch products were included as well, yielding the complete reaction set as presented in the following tables.

a. Pure Ar plasma

Ar is an atomic gas and can therefore not be rotationally and vibrationally excited. The main reactions that happen in the plasma are ionization and electronic excitation, by electron impact. Besides electron impact ionization from the ground state, also ionization from the excited atoms (Ar*) is included, as it requires less energy. Moreover, de-excitation of the Ar* excited levels to the ground state, upon collision with electrons (also called "electron quenching"), is also included. Finally, the formation of Ar^+ can also occur by the collision of two excited Ar atoms (Ar*), where the energy of the excited atoms is used for the ionization of one of the Ar atoms. **Table 6** lists all the different plasma reactions for Ar where the labels refer to the cross sections in **Figure 19**.

Table 6. Chemical reactions for pure Ar defined in the model. The labels in the second column refer to **Figure 19**. The cross sections and rate coefficient for these reactions were all adopted from [131].

Reaction	Cross section or rate constant
$e + Ar \rightarrow Ar^* + e$	$\sigma(E)$ (label 1,2)
$e + Ar \rightarrow Ar^+ + 2\ e$	$\sigma(E)$ (label 3)
$e + Ar^* \rightarrow Ar^+ + 2\ e$	$\sigma(E)$ (label 4,5)
$e + Ar^* \rightarrow Ar + e$	$\sigma(E)$ (label 6,7)
$Ar^* + Ar^* \rightarrow Ar^+ + Ar + e$	$5.00 \times 10^{-10}\ cm^3\ s^{-1}$

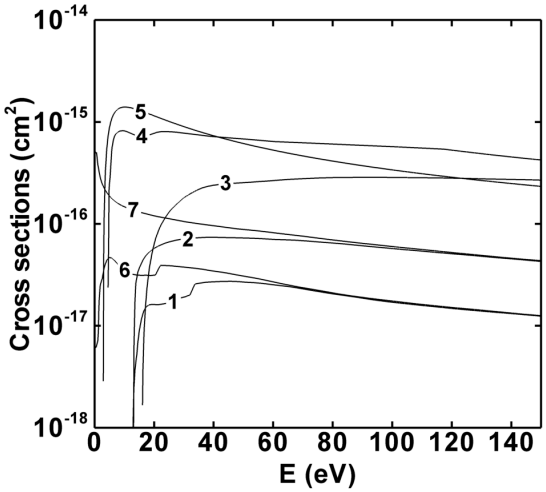

Figure 19. Cross sections as a function of electron energy for the reactions defined in the model in the pure Ar case. The labels correspond to the reactions in **Table 6**.

b. Pure Cl_2 plasma

As Cl_2 is a molecular gas, besides electronic excitation and ionization also dissociation and rotational or vibrational excitations can occur. The Cl-Cl bond energy is relatively low (2.5 *eV*) so a large fraction of Cl_2 will be dissociated into Cl atoms. Indeed, as will be shown in Part III, the Cl atom density often exceeds the Cl_2 density in the plasma. Moreover, Cl is a highly electronegative element and it will eagerly accept an electron to form Cl^-. A very important reaction is therefore electron impact dissociative attachment. In this process, the Cl_2 molecule is dissociated into Cl and Cl^-, which happens at a zero energy barrier. Therefore, the Cl^- density is usually higher than the electron density (see further in Part III), making a Cl_2 plasma highly electronegative. In our model, electron impact dissociative attachment, electron impact dissociation and ionization are included for Cl_2 molecules. Electron impact vibrational and rotational excitations of Cl_2 are included as well. Electron impact dissociative ionization is not taken into account because it is much less

significant compared to the dissociation and dissociative attachment processes of Cl_2 which have much lower threshold energies. As the Cl atoms are present at high densities in a Cl_2 plasma, electron impact excitation and ionization of Cl are also included in the model, as well as ionization from the Cl excited atom. Electron – Cl_2^+ dissociative recombination is also incorporated, as this type of recombination process is much more probable than recombination with atomic ions (see section 2.2.5). Finally, the reaction between an electron and a Cl^- ion is also included, leading to the detachment of a second electron. This reaction is, in fact, very similar to a direct electron impact ionization reaction and it is found to have a significant cross section at higher energies (> 10 *eV*).
Since both positive and negative ions occur in the plasma, heavy particle neutralizations (i.e. recombination between Cl^- ions and either Cl^+ or Cl_2^+ ions) are also included, as well as charge transfer reactions between Cl_2 and Cl^+. Strictly speaking, charge transfer can occur in both directions (i.e. not only between Cl^+ and Cl_2, but also between Cl_2^+ and Cl), but Cl_2^+ can better "tolerate" the positive charge, so the charge transfer reaction of Cl^+ with Cl_2, to form Cl_2^+, is favored. Finally, recombination of Cl atoms to form Cl_2 can also occur, but at lower probability since this can only happen by a three-body reaction to channel the released energy. **Table 7** lists all the different plasma reactions for Cl_2 where the labels refer to the cross sections in **Figure 20**.

Table 7. Chemical reactions for pure Cl_2 defined in the model. The labels in the second column refer to **Figure 20**. The cross sections and rate coefficients for these reactions were all adopted from [131].

Reaction	Cross section or rate constant
$e + Cl_2 \rightarrow Cl + Cl^-$	$\sigma(E)$ (label 1)
$e + Cl_2 \rightarrow Cl + Cl + e$	$\sigma(E)$ (label 2)
$e + Cl_2 \rightarrow Cl_2^+ + e + e$	$\sigma(E)$ (label 3)
$e + Cl \rightarrow Cl^* + e$	$\sigma(E)$ (label 4-9)

$e + Cl \rightarrow Cl^+ + e + e$	$\sigma(E)$ (label 10)
$e + Cl^* \rightarrow Cl^+ + e + e$	$\sigma(E)$ (label 11)
$e + Cl_2^+ \rightarrow Cl + Cl$	$\sigma(E)$ (label 12)
$e + Cl^- \rightarrow Cl + e + e$	$\sigma(E)$ (label 13)
$Cl^- + Cl^+ \rightarrow Cl + Cl$	$1.00 \times 10^{-7} [T / 298\ K]^{0.5}\ cm^3\ s^{-1}$
$Cl^- + Cl_2^+ \rightarrow Cl + Cl + Cl$	$1.00 \times 10^{-7} [T / 298\ K]^{0.5}\ cm^3\ s^{-1}$
$Cl + Cl + Cl \rightarrow Cl_2 + Cl$	$1.28 \times 10^{-32}\ cm^6\ s^{-1}$
$Cl + Cl + Cl_2 \rightarrow Cl_2 + Cl_2$	$5.40 \times 10^{-32}\ cm^6\ s^{-1}$
$Cl^+ + Cl_2 \rightarrow Cl + Cl_2^+$	$5.40 \times 10^{-10} [T / 298\ K]^{0.5}\ cm^3\ s^{-1}$

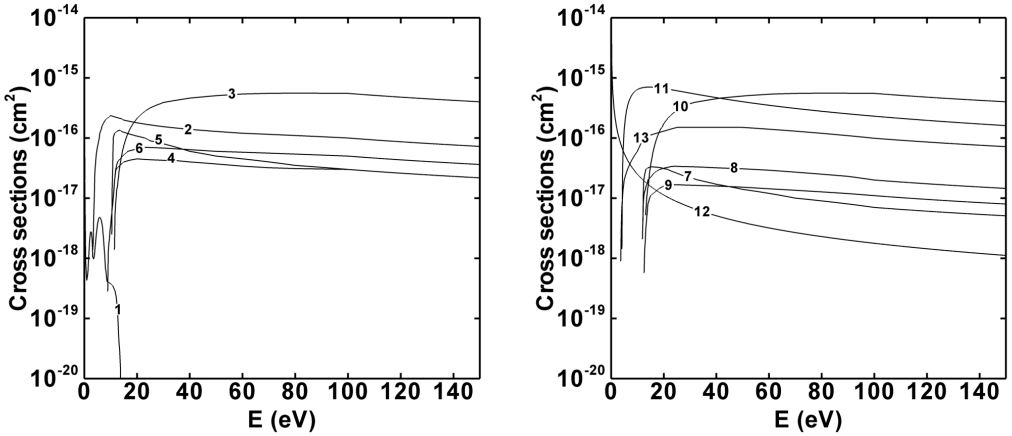

Figure 20. Cross sections as a function of electron energy for the reactions defined in the model for the pure Cl_2 plasma. The labels correspond to the reactions in **Table 7**.

c. Pure O_2 plasma

An O_2 plasma is in many ways similar to a Cl_2 plasma. It is also a molecular gas, and the O atom is even more electronegative. Therfore, in general, similar reactions occur for O_2 as for Cl_2, where again dissociative attachment of O_2 to form O and O^- is a very important process. Like Cl_2, an O_2 plasma is usually an electronegative plasma, although at high power and very low pressure it can be electropositive [15, 16, 86, 90, 104, 151, 152]. The O=O double bond is stronger compared to the Cl-Cl bond

(i.e. 5.2 *eV* compared to 2.5 *eV*) so it is expected that O_2 will not dissociate as much as Cl_2. Indeed, the O_2 density is usually significantly higher than the O atom density, as will be shown later in Part III. **Table 8** lists all the different plasma reactions for O_2 where the labels refer to the cross sections in **Figure 21**.

For the O_2 molecules, besides electron impact dissociative attachment, dissociation and ionization (which are the important reactions for Cl_2 molecules), now also electron impact dissociative ionization and dissociative excitation are included. Indeed, dissociation and dissociative attachment of O_2 occur less easily compared to Cl_2 due to the stronger double O=O bond that needs to be broken, and therefore dissociative ionization and excitation processes become relatively more important compared to Cl_2. For the O atoms, electron impact ionization and excitation, as well as ionization and de-excitation from the excited levels, is considered, like in the case of the Cl atoms. Furthermore, again electron – O_2^+ dissociative recombination and electron collisions with O^-, yielding detachment of a second electron, are included, like in the Cl_2 plasma.

Also for the heavy particles, neutralization, i.e. recombination between O^- ions and either O_2^+ or O^+ ions is considered, as well as charge transfer between O^+ and O_2. Again, the opposite reaction can occur as well, but similar to Cl_2^+, O_2^+ can better "tolerate" the positive charge. Finally, quenching of O* excited atoms upon collision with O atoms or O_2 molecules is included.

Most important reactions are the dissociation and dissociative attachment of O_2, as well as the dissociative neutralization of O_2^+ and ion-ion neutralization between heavy particles.

Table 8. Chemical reactions for pure O_2 defined in the model, as well as the references where the cross sections or rate coefficients were adopted from. The labels in the second column refer to **Figure 21.**

Reaction	Cross section / rate constant	Reference
$e + O_2 \rightarrow O^- + O$	$\sigma(E)$ (label 1)	[131]
$e + O_2 \rightarrow O + O + e$	$\sigma(E)$ (label 2)	[131]
$e + O_2 \rightarrow O + O^+ + 2\ e$	$\sigma(E)$ (label 3)	[131]
$e + O_2 \rightarrow O_2^+ + 2\ e$	$\sigma(E)$ (label 4)	[131]
$e + O \rightarrow O^* + e$	$\sigma(E)$ (label 5,6)	[131]
$e + O \rightarrow O^+ + 2\ e$	$\sigma(E)$ (label 7)	[131]
$e + O^* \rightarrow O + e$	$\sigma(E)$ (label 8)	[131]
$e + O^* \rightarrow O^+ + 2\ e$	$\sigma(E)$ (label 9)	[131]
$e + O_2^+ \rightarrow O + O$	$\sigma(E)$ (label 10)	[131]
$e + O^- \rightarrow O + 2\ e$	$1.95 \times 10^{-12}\ T_e^{-0.7}\ exp[-3.4\ eV / T_e]\ cm^3\ s^{-1}$	[153]
$O^- + O_2^+ \rightarrow O + O_2$	$2.00 \times 10^{-7}\ [T / 298\ K]^{-0.5}\ cm^3\ s^{-1}$	[154]
$O^- + O_2^+ \rightarrow O + O + O$	$1.00 \times 10^{-7}\ cm^3\ s^{-1}$	[131]
$O^- + O^+ \rightarrow O + O$	$2.70 \times 10^{-7}\ [T / 298\ K]^{-0.5}\ cm^3\ s^{-1}$	[155]
$O^* + O \rightarrow O + O$	$8.00 \times 10^{-12}\ cm^3\ s^{-1}$	[131]
$O^* + O_2 \rightarrow O + O_2$	$2.65 \times 10^{-11}\ exp[67\ K / T]\ cm^3\ s^{-1}$	[154]
$O^+ + O_2 \rightarrow O + O_2^+$	$2.00 \times 10^{-11}\ cm^3\ s^{-1}$	[156]

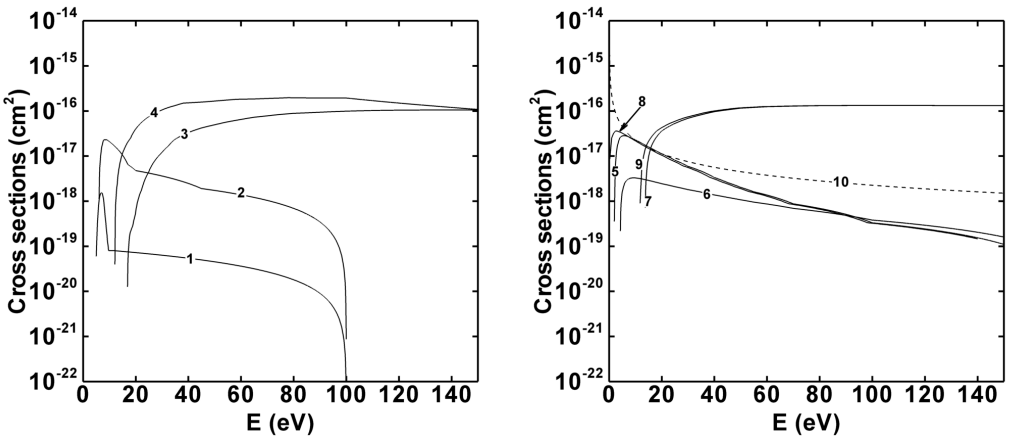

Figure 21. Cross sections as a function of electron energy for the reactions defined in the model for the pure O_2 plasma. The labels correspond to the reactions in **Table 8**.

d. Reactions between Ar, Cl_2 and O_2

As mentioned before, for the etching of Si, a gas mixture of $Ar/Cl_2/O_2$ is typically applied. To be able to properly simulate this gas mixture, heavy particle reactions between all the possible plasma species must be considered. All reactions can be subdivided into three main groups, namely (i) charge transfer reactions where the most "stable" ion is formed (i.e. usually the molecules, although dissociation of the molecule can also occur, yielding an atom and atomic ion), (ii) neutralization reactions between all positive and negative ions and (iii) chemical reactions where new species are created. As mentioned earlier, Ar is a noble gas and does not react chemically with other species. Chlorine and oxygen, on the other hand, can react to form a large variety of Cl_xO_y products. However, only ClO has a significant density compared to the other species [88] (see also section 4.4.1.c). Therefore, also electron impact ionization and dissociation are included for ClO. **Table 9** lists all the different plasma chemistry reactions between Ar, Cl_2, and O_2 species, included in our model.

Table 9. Chemical reactions between Ar, Cl_2 and O_2 species defined in the model, as well as the references where the rate coefficients were adopted from. * means that the rate coefficient was based on a comparable reaction from the given reference.

Reaction	Cross section or rate constant	Reference
$Cl^- + Ar^+ \rightarrow Cl + Ar$	$1.00 \times 10^{-7}\ [T / 298\ K]^{0.5}\ cm^3\ s^{-1}$	[131]
$Ar^* + Cl_2 \rightarrow Ar + Cl_2^+ + e$	$7.10 \times 10^{-10}\ [T / 298\ K]^{0.5}\ cm^3\ s^{-1}$	[131]
$Ar^* + Cl \rightarrow Ar + Cl^*$	$0.70 \times 10^{-11}\ [T / 298\ K]^{0.5}\ cm^3\ s^{-1}$	[131]
$Ar^+ + Cl_2 \rightarrow Ar + Cl_2^+$	$0.84 \times 10^{-10}\ [T / 298\ K]^{0.5}\ cm^3\ s^{-1}$	[131]
$Ar^+ + Cl_2 \rightarrow Ar + Cl^+ + Cl$	$0.64 \times 10^{-10}\ [T / 298\ K]^{0.5}\ cm^3\ s^{-1}$	[131]
$Ar^+ + Cl \rightarrow Ar + Cl^+$	$2.00 \times 10^{-10}\ [T / 298\ K]^{0.5}\ cm^3\ s^{-1}$	[131]
$Cl + Cl + Ar \rightarrow Cl_2 + Ar$	$1.28 \times 10^{-32}\ cm^6\ s^{-1}$	[131]

$Ar^+ + O_2 \rightarrow Ar + O_2^+$	5.10 x 10^{-11} $cm^3\ s^{-1}$	[131]
$Ar^+ + O \rightarrow Ar + O^+$	1.20 x 10^{-11} $cm^3\ s^{-1}$	[157]
$Cl^+ + O_2 \rightarrow Cl + O_2^+$	5.10 x 10^{-11} $cm^3\ s^{-1}$	[131]*
$O^- + Cl^+ \rightarrow O + Cl$	5.00 × 10^{-8} $[T / 298\ K]^{0.5}$ $cm^3\ s^{-1}$	[88]*
$O^- + Cl_2^+ \rightarrow O + Cl_2$	5.00 × 10^{-8} $[T / 298\ K]^{0.5}$ $cm^3\ s^{-1}$	[88]*
$Cl^- + O_2^+ \rightarrow Cl + O_2$	5.00 × 10^{-8} $[T / 298\ K]^{0.5}$ $cm^3\ s^{-1}$	[88]
$Cl^- + O^+ \rightarrow Cl + O$	5.00 × 10^{-8} $[T / 298\ K]^{0.5}$ $cm^3\ s^{-1}$	[88]
$Cl_2 + O^* \rightarrow ClO + Cl$	2.11 x 10^{-10} $cm^3\ s^{-1}$	[88]
$ClO + O \rightarrow O_2 + Cl$	4.11 × 10^{-11} $exp[42\ K / T]$ $cm^3\ s^{-1}$	[88]
$e + ClO \rightarrow Cl + O + e$	1.27 × 10^{-7} $T_e^{-1.36}$ $exp[-6.84\ eV/T_e]$ $cm^3\ s^{-1}$	[88]
$e + ClO \rightarrow ClO^+ + 2\ e$	9.48 × 10^{-9} $T_e^{0.85}$ $exp[-12.24\ eV / T_e]$ $cm^3\ s^{-1}$	[88]
$O^+ + ClO \rightarrow O + ClO^+$	4.90 x 10^{-10} $cm^3\ s^{-1}$	[88]
$O_2^+ + ClO \rightarrow O_2 + ClO^+$	4.90 x 10^{-10} $cm^3\ s^{-1}$	[88]
$Cl^+ + ClO \rightarrow Cl + ClO^+$	4.90 x 10^{-10} $cm^3\ s^{-1}$	[88]
$Cl_2^+ + ClO \rightarrow Cl_2 + ClO^+$	4.90 x 10^{-10} $cm^3\ s^{-1}$	[88]
$Cl^- + ClO^+ \rightarrow Cl + ClO$	5.00 × 10^{-8} $[T / 298\ K]^{-0.5}$ $cm^3\ s^{-1}$	[88]
$O^- + ClO^+ \rightarrow O + ClO$	2.60 × 10^{-8} $[T / 298\ K]^{-0.44}$ $cm^3\ s^{-1}$	[88]

e. Etch product reactions

The $Ar/Cl_2/O_2$ plasma is used to etch Si from the wafer, meaning that the removed material (i.e. the etch products) are loaded into the plasma during etching. As will be shown in Part III, the etch products can have a density similar to that of the neutral gas species in the plasma, so reactions for the etch products must be considered as well. Etch products considered are Si, $SiCl_{1-4}$ and SiO_{1-2} (see section 4.4.1.c). The most important reactions that can happen in the plasma with these species, and that are included in our model, are various types of electron impact (dissociative) ionization, ion-ion neutralizations, and some chemical reactions, i.e. the oxidation and chlorination of Si. It should be noted that oxidation and chlorination of the etch products is addressed

in more detail in the surface reactions. **Table 10** lists all the different plasma reactions included for the various etch products, where the labels of the cross sections correspond to those shown in **Figure 22**.

Table 10. Chemical reactions for Si-containing species included in the model, as well as the references where the cross sections or rate coefficients were adopted from. The labels in the second column refer to **Figure 22**. * means that the rate coefficient was based on a comparable reaction from the given reference.

Reaction	Cross section or rate constant	Reference
$e + Si \rightarrow Si^+ + 2\ e$	*σ(E)* (label 1)	[56]
$e + SiCl_4 \rightarrow SiCl_4^+ + 2\ e$	*σ(E)* (label 2)	[158, 159]
$e + SiCl_4 \rightarrow SiCl_3^+ + Cl + 2\ e$	*σ(E)* (label 3)	[158, 159]
$e + SiCl_4 \rightarrow SiCl_2^+ + Cl_2 + 2\ e$	*σ(E)* (label 4)	[158, 159]
$e + SiCl_4 \rightarrow SiCl^+ + Cl_2 + Cl + 2\ e$	*σ(E)* (label 5)	[158, 159]
$e + SiCl_4 \rightarrow Si^+ + Cl_2 + Cl_2 + 2\ e$	*σ(E)* (label 6)	[158, 159]
$e + SiCl_4 \rightarrow SiCl_3 + Cl^+ + 2\ e$	*σ(E)* (label 7)	[158, 159]
$e + SiCl_3 \rightarrow SiCl_3^+ + 2\ e$	*σ(E)* (label 8)	[158, 160]
$e + SiCl_3 \rightarrow SiCl_2^+ + Cl + 2\ e$	*σ(E)* (label 9)	[158, 160]
$e + SiCl_3 \rightarrow SiCl^+ + Cl_2 + 2\ e$	*σ(E)* (label 10)	[158, 160]
$e + SiCl_3 \rightarrow Si^+ + Cl_2 + Cl + 2\ e$	*σ(E)* (label 11)	[158, 160]
$e + SiCl_3 \rightarrow SiCl_2 + Cl^+ + 2\ e$	*σ(E)* (label 12)	[158, 160]
$e + SiCl_2 \rightarrow SiCl_2^+ + 2\ e$	*σ(E)* (label 13)	[158, 161]
$e + SiCl_2 \rightarrow SiCl^+ + Cl + 2\ e$	*σ(E)* (label 14)	[158, 161]
$e + SiCl_2 \rightarrow Si^+ + Cl_2 + 2\ e$	*σ(E)* (label 15)	[158, 161]
$e + SiCl_2 \rightarrow SiCl + Cl^+ + 2\ e$	*σ(E)* (label 16)	[158, 161]
$e + SiCl \rightarrow SiCl^+ + 2\ e$	*σ(E)* (label 17)	[158, 161]
$e + SiCl \rightarrow Si^+ + Cl + 2\ e$	*σ(E)* (label 18)	[158, 161]
$e + SiCl \rightarrow Si + Cl^+ + 2\ e$	*σ(E)* (label 19)	[158, 161]
$Si^+ + Cl^- \rightarrow Si + Cl$	$10^{-7}\ [T / 298\ K]^{0.5}\ cm^3\ s^{-1}$	[131]*
$Si^+ + O^- \rightarrow Si + O$	$10^{-7}\ [T / 298\ K]^{0.5}\ cm^3\ s^{-1}$	[131]*
$SiCl^+ + Cl^- \rightarrow SiCl + Cl$	$10^{-7}\ [T / 298\ K]^{0.5}\ cm^3\ s^{-1}$	[131]*
$SiCl^+ + O^- \rightarrow SiCl + O$	$10^{-7}\ [T / 298\ K]^{0.5}\ cm^3\ s^{-1}$	[131]*

$SiCl_2^+ + Cl^- \rightarrow SiCl_2 + Cl$	$10^{-7}\ [T / 298\ K]^{0.5}\ cm^3\ s^{-1}$	[131]*
$SiCl_2^+ + O^- \rightarrow SiCl_2 + O$	$10^{-7}\ [T / 298\ K]^{0.5}\ cm^3\ s^{-1}$	[131]*
$SiCl_3^+ + Cl^- \rightarrow SiCl_3 + Cl$	$10^{-7}\ [T / 298\ K]^{0.5}\ cm^3\ s^{-1}$	[131]*
$SiCl_3^+ + O^- \rightarrow SiCl_3 + O$	$10^{-7}\ [T / 298\ K]^{0.5}\ cm^3\ s^{-1}$	[131]*
$SiCl_4^+ + Cl^- \rightarrow SiCl_4 + Cl$	$10^{-7}\ [T / 298\ K]^{0.5}\ cm^3\ s^{-1}$	[131]*
$SiCl_4^+ + O^- \rightarrow SiCl_4 + O$	$10^{-7}\ [T / 298\ K]^{0.5}\ cm^3\ s^{-1}$	[131]*
$Si + Cl_2 \rightarrow SiCl + Cl$	$3.30 \times 10^{-10}\ cm^3\ s^{-1}$	[162]
$Si + O_2 \rightarrow SiO + O^*$	$1.73 \times 10^{-10}\ [T/298\ K]^{-0.53}\ exp[-17\ K / T]\ cm^3\ s^{-1}$	[163]
$SiCl + Cl_2 \rightarrow SiCl_2 + Cl$	$5.30 \times 10^{-11}\ cm^3\ s^{-1}$	[135]
$e + SiO \rightarrow SiO^+ + 2\ e$	$\sigma(E)$ (label 20)	[142]
$e + SiO_2 \rightarrow SiO_2^+ + 2\ e$	$\sigma(E)$ (label 21)	[142]
$SiO + O_2 \rightarrow SiO_2 + O$	$2.36 \times 10^{-10}\ exp[-3266.3\ K / T]\ cm^3\ s^{-1}$	[163]
$SiO^+ + Cl^- \rightarrow SiO + Cl$	$10^{-7}\ [T / 298\ K]^{0.5}\ cm^3\ s^{-1}$	[131]*
$SiO^+ + O^- \rightarrow SiO + O$	$10^{-7}\ [T / 298\ K]^{0.5}\ cm^3\ s^{-1}$	[131]*
$SiO_2^+ + Cl^- \rightarrow SiO_2 + Cl$	$10^{-7}\ [T / 298\ K]^{0.5}\ cm^3\ s^{-1}$	[131]*
$SiO_2^+ + O^- \rightarrow SiO_2 + O$	$10^{-7}\ [T / 298\ K]^{0.5}\ cm^3\ s^{-1}$	[131]*

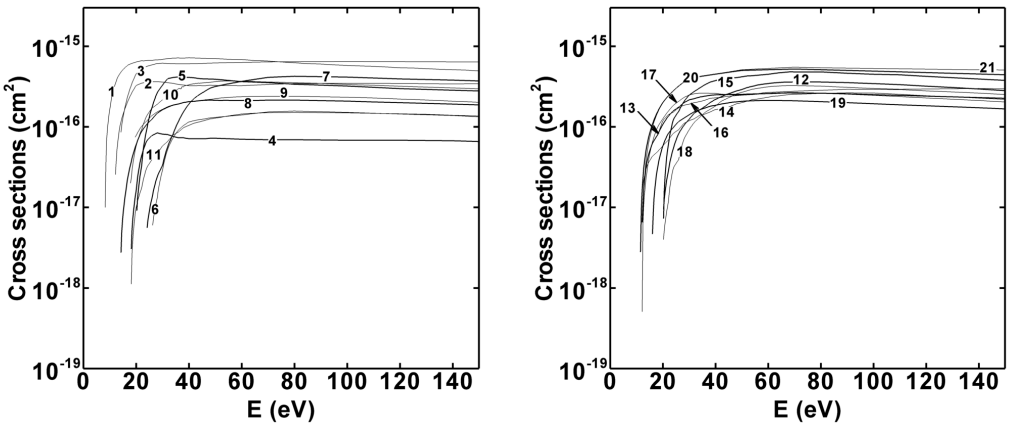

Figure 22. Cross sections as a function of electron energy for the reactions defined in the model for the Si-containing species. The labels correspond to the reactions in **Table 10**.

4.5 Surface chemistry of $Ar/Cl_2/O_2$ on Si

4.5.1 Overview

In the following sections, tables are presented with reaction probabilities for the interactions of the different $Ar/Cl_2/O_2$ plasma species with the various surface layers, of importance during the etching of Si. **Table 11** lists the different surface layers included in the simulations.

Table 11. Surface layers included in the model. Chlorinated $wall_{(s)}$ means the wall (i.e. Al_2O_3) covered by a passivation layer of adsorbed chlorine.

clean $wall_{(s)}$, chlorinated $wall_{(s)}$
$Si_{(s)}$, $SiCl_{(s)}$, $SiCl_{2(s)}$, $SiCl_{3(s)}$
$SiClO_{(s)}$, $SiCl_2O_{(s)}$, $SiCl_3O_{(s)}$, $SiO_{(s)}$, $SiO_{2(s)}$

In the surface reaction sets, the following general processes are taken into account:

1) Chlorination of Si and $SiCl_x$ layers to volatile $SiCl_4$
2) Oxidation of Si and $SiCl_xO_y$ layers
3) Redeposition of non-/low-volatile etch products
4) Sputter processes such as physical sputtering, chemical sputtering and sputter deposition

A summary of the reactions for these surface processes, and their reaction probabilities, are presented in **Table 12**. It should be noted that in this case, the reactions are indeed not specified by reaction rate coefficients like in the plasma chemistry, but with probabilities, as this is needed in the SKM used for this purpose (see section 3.4.7 for more

details). Moreover, etching by chlorine and oxidation can also occur with Cl_2 and O_2, but at a much lower rate as will be discussed later. Therefore, only the atomic reactants are presented in this brief summary. More detailed reaction sets are presented in the following sections, including a more substantial discussion on the different surface processes listed in **Table 12**.

Table 12. Summary of surface processes taken into account in the model. SY(*E*) stands for an energy-dependent sputter yield, which will be presented later in this Chapter. $Surf_{(s)}$ and M represent all included surfaces and species, respectively.

Surface reaction	Probability
1. Chlorination of silicon (chemical etching)	
$Cl + SiCl_{x(s)} \rightarrow SiCl_{x+1(s)}$ (x = 0 - 2)	0.99, 0.20, 0.15
$Cl + SiCl_{3(s)} \rightarrow SiCl_4$	0.001
2. Oxidation of silicon and $SiCl_xO_y$ layers	
$O + Si_{(s)} \rightarrow SiO_{(s)}$	0.99
$O + SiO_{x(s)} \rightarrow SiO_{x+1(s)}$ (x = 0, 1)	0.99
$O + SiCl_{x(s)} \rightarrow SiCl_xO_{(s)}$ (x = 1 - 3)	0.99
$O + SiCl_xO_{(s)} \rightarrow SiCl_{x-1}O_{2(s)} + Cl$ (x = 1 - 3)	0.99
3. Redeposition of etch products	
$(Si, SiCl, SiO, SiO_2) + Surf_{(s)} \rightarrow (Si, SiCl, SiO, SiO_2)_{(s)} + Surf_{(s)}$	0.99
$(SiCl_2, SiCl_3) + Surf_{(s)} \rightarrow (SiCl_2, SiCl_3)_{(s)} + Surf_{(s)}$	0.05
4. Sputtering	
$M^+ + SiCl_{x(s)} \rightarrow SiCl_x + M$ (x = 0 - 3)	SY(*E*)
$M^+ + SiCl_xO_{y(s)} \rightarrow SiCl_xO_{y-1} + M + O$ (x = 0 - 3, y = 1, 2)	SY(*E*)

It should be noted that for most surface reactions, the exact reaction probabilities are not available in literature. In these cases, reaction sets were created based on experimental data and consistent with experimental observations, as explained below in the various sections. The surface reactions (and their probabilities) presented here are applied in the SKM and FPMCS modules (see details in section 3.4.6 and 3.4.8).

4.5.2 Chemical etching of Si by chlorine

Table 13 shows the surface reactions included in the model for describing the chemical etching of silicon with chlorine. It is well known from numerous experimental and simulation studies that, when a chlorine plasma is in contact with a clean silicon surface, the silicon surface layer will become rapidly chlorinated and silicon atoms can be chemically etched from the surface [137].

Cl atoms or Cl_2 molecules will bind with Si surface atoms to form a $SiCl_x$ (x = 1 - 4) layer. The more Cl atoms are bonded to a Si surface atom, the more the $SiCl_x$ molecule will become volatile until the Si atom finally can be extracted from the surface in the form of $SiCl_4$, which is a volatile molecule. However, the spontaneous chemical etching of Si in the form of $SiCl_4$, without ion bombarding effects, is very slow and almost negligible. This is due to the fact that, when $SiCl_4$ is formed, it will remain stuck to the surface before it can thermodynamically desorb. The actual desorption of $SiCl_4$ can be assisted by ion bombardment or by heating of the surface [150].

It is well known that Cl atoms are very reactive towards a clean silicon surface. The sticking coefficient of Cl on Si is close to 1, which results in a fast chlorine saturation on the surface. However, as soon as the surface becomes chlorinated, the sticking of Cl atoms onto the surface drops. It is, however, not well known to what extent the reaction probabilities decrease in the stepwise chlorination of Si. Compared to Cl atoms, Cl_2 molecules are less reactive towards a silicon surface because Cl_2 is more stable and less eager to chemically react with silicon.

Hoekstra *et al* [102] have presented a reaction probability set for the chlorine etching of silicon, based on results from molecular dynamics simulations. The reaction set here is adopted from [102]; it gives rise to a

very low calculated etch rate as has been confirmed by our experiments. Again, it should be noted that this set only describes chemical etching, without ion bombardment.

Table 13. Surface reaction set for chlorine etching of *poly*-Si.

Surface reaction	Probability
$Cl + Si_{(s)} \rightarrow SiCl_{(s)}$	0.99
$Cl + SiCl_{(s)} \rightarrow SiCl_{2(s)}$	0.20
$Cl + SiCl_{2(s)} \rightarrow SiCl_{3(s)}$	0.15
$Cl + SiCl_{3(s)} \rightarrow SiCl_4$	0.001
$Cl_2 + Si_{(s)} \rightarrow SiCl_{2(s)}$	0.01
$Cl_2 + SiCl_{(s)} \rightarrow SiCl_{2(s)} + Cl$	0.01
$Cl_2 + SiCl_{2(s)} \rightarrow SiCl_{3(s)} + Cl$	0.01
$Cl_2 + SiCl_{3(s)} \rightarrow SiCl_4 + Cl$	0.0001

4.5.3 Oxidation of Si

A lot of data have been reported on the plasma oxidation of silicon [110-114, 150]. It is known that O atoms and O_2 molecules will spontaneously react with a Si surface to form a SiO_x (x = 1 - 2) layer up to 1.3 *nm* in thickness. Indeed, oxygen will diffuse into the top surface layers of the silicon to form an oxide layer of a few *Angstrom*. This process is self-limiting once the oxide layer has reached the above-mentioned thickness. This layer is often referred to as the native oxide, formed when the silicon substrate has come into contact with air. O atoms are very reactive towards the silicon surface, with a sticking coefficient close to 1. O_2, on the other hand, is less eager to react with silicon, because it is more stable and therefore more inert.

Since SiO_x molecules are not volatile, etching of Si with oxygen does not occur, at least not at low surface temperatures. At temperatures above

700 *K*, Si can actually be etched with oxygen, a process often referred to as active oxidation [110-114]. In this process, SiO or SiO_2 is formed and extracted into the gas phase, but this process can only occur when the SiO_x molecules have enough energy to be transferred into the gas phase; therefore, this only happens at high substrate temperatures (> 700 *K*). In our experiments, the substrate temperature is 60 *°C*, which is too low for active oxidation to occur. For this reason, no active oxidation reactions are considered in our reaction set. **Table 14** presents the reaction set for the oxidation of silicon defined in the model, based on the available experimental data.

Table 14. Surface reaction set for the oxidation of silicon.

Surface reaction	Probability
$O + Si_{(s)} \rightarrow SiO_{(s)}$	0.99
$O + SiO_{(s)} \rightarrow SiO_{2(s)}$	0.99*
$O_2 + Si_{(s)} \rightarrow SiO_{2(s)}$	0.01
$O_2 + SiO_{(s)} \rightarrow SiO_{2(s)} + O$	0.01*

* Self-limiting, depending on SiO_2 layer thickness, as mentioned in the text.

4.5.4 Oxidation of chlorinated Si

In this section we discuss the oxidation of chlorinated Si or, in the model, $SiCl_x$(s) layers, as well as surface reactions of the ClO molecule. If a Cl_2/O_2 plasma is introduced, the silicon surface will be partially chlorinated and partially oxidized, resulting in the formation of an *oxy-chloride* layer ($SiCl_xO_y$) on the surface [88, 105, 131, 134-136, 139]. The formation mechanism of this layer has been proposed by Kogelschatz *et al* [134]. During the etching of Si, $SiCl_x$ species will redeposit on the walls and wafer followed by oxidation of the $SiCl_x$ layer. To define the oxidation of chlorinated silicon in the model, we consider step-wise reactions, where a chlorine atom is gradually replaced by an oxygen atom, to form

$SiCl_xO_y$ surface molecules. However, in our model, we only consider $SiCl_xO$ molecules for simplicity. This step-wise oxidation was also proposed by Cunge *et al* [135]. Furthermore, it has been experimentally observed that the oxygen content is higher when moving deeper into the layer, suggesting that oxygen can diffuse into the layer and oxidize the deeper $SiCl_x$ molecules [134]. Once the $SiCl_x$ layer is oxidized, it can no longer be chemically etched by chlorine, in analogy to a SiO_x layer. The chlorine is therefore *fixed* into the layer and can only be removed by physical sputtering or further oxidation [136]. The reactions that describe the oxidation of $SiCl_x$ species are summarized in **Table 15**. It should be noted that the etch rate of SiO_x (glass) by chlorine is extremely low and negligible. Therefore, these reactions do not need to be included in the reaction set.

Table 15. Surface reaction set for the oxidation of $SiCl_x$.

Surface reaction	Probability
$O + SiCl_{(s)} \rightarrow SiClO_{(s)}$	0.99
$O + SiCl_{2(s)} \rightarrow SiCl_2O_{(s)}$	0.99
$O + SiCl_{3(s)} \rightarrow SiCl_3O_{(s)}$	0.99
$O + SiClO_{(s)} \rightarrow SiO_{2(s)} + Cl$	0.99
$O + SiCl_2O_{(s)} \rightarrow SiClO_{(s)} + Cl$	0.99*
$O + SiCl_3O_{(s)} \rightarrow SiCl_2O_{(s)} + Cl$	0.99*
$O_2 + SiCl_{(s)} \rightarrow SiClO_{(s)} + O$	0.01
$O_2 + SiCl_{2(s)} \rightarrow SiCl_2O_{(s)} + O$	0.01
$O_2 + SiCl_{3(s)} \rightarrow SiCl_3O_{(s)} + O$	0.01
$O_2 + SiClO_{(s)} \rightarrow SiO_{2(s)} + Cl$	0.01*
$O_2 + SiCl_2O_{(s)} \rightarrow SiClO_{(s)} + Cl$	0.01*
$O_2 + SiCl_3O_{(s)} \rightarrow SiCl_2O_{(s)} + Cl$	0.01*

* In these reactions, the remaining O atom(s) diffuse(s) into the $SiCl_xO_y$ layer, hence, in the calculation, these atoms *disappear*.

Not much information can be found on the behavior of ClO on a silicon

surface. Since ClO is a radical it will be eager to stick and react on the surface with a probability presumably close to that of Cl or O atoms. We consider ClO to be able to both chlorinate and oxidize the silicon. As stated before, it is generally known that $SiCl_x$ can be oxidized, but SiO_x will not be chlorinated [136]. This results in the reaction set for ClO on the various surface layers, as presented in **Table 16**.

Table 16. Surface reaction set for ClO.

Surface reaction	Probability
$ClO + Si_{(s)} \rightarrow SiClO_{(s)}$	0.99
$ClO + SiO_{(s)} \rightarrow SiO_{2(s)} + Cl$	0.99
$ClO + SiCl_{(s)} \rightarrow SiCl_2O_{(s)}$	0.99
$ClO + SiCl_{2(s)} \rightarrow SiCl_3O_{(s)}$	0.99
$ClO + SiCl_{3(s)} \rightarrow SiCl_3O_{(s)} + Cl$	0.99
$ClO + SiCl_{3(s)} \rightarrow SiCl_4 + O$	0.001
$ClO + SiClO_{(s)} \rightarrow SiO_{2(s)} + Cl_2$	0.99
$ClO + SiCl_2O_{(s)} \rightarrow SiClO_{(s)} + Cl_2$	0.99*
$ClO + SiCl_3O_{(s)} \rightarrow SiCl_2O_{(s)} + Cl_2$	0.99*

* In these reactions, the remaining O atom diffuses into the $SiCl_xO$ layer, hence, in the calculation, this atom *disappears*.

4.5.5 Redeposition of etch products

$SiCl_x$ (x = 0 - 4) molecules that are etched or sputtered from the surface and launched into the plasma, can eventually redeposit on the reactor walls or again on the wafer. Naturally, the less volatile etch products will deposit faster on the walls. In general it is accepted that the more Cl atoms are bonded to the Si atom, the more volatile the molecule will be. Hence, an etched Si atom is considered to stick at the walls with a probability close to 1, whereas $SiCl_4$ is considered to be completely volatile and will not stick to the surface. In reality, it is possible that even

$SiCl_4$ will stick to the surface [150], but it is only weakly bonded and the time before it will be launched back into the plasma is short. For this reason it can be considered to *bounce off* the wall, like Ar atoms. Unfortunately, not much information can be found on the actual sticking probabilities for SiCl, $SiCl_2$ and $SiCl_3$. In [104] it is stated that Si and SiCl are not volatile, while $SiCl_{2-4}$ are (more or less) volatile. In a recent paper, Cunge *et al* [135] proposed, based on experimental results, that $SiCl_2$ should have a wall sticking probability of about 0.05. For $SiCl_3$, no information could be found in literature. In principle, this molecule should be even more volatile than $SiCl_2$. However, since it is a radical, it probably has a higher reaction affinity at the walls. Therefore, we have assumed the same sticking coefficient for $SiCl_3$ as for $SiCl_2$.
Finally, SiO and SiO_2 are considered to be non-volatile species and will therefore stick at the walls with a probability close to unity. **Table 17** summarizes the wall sticking probabilities of the various etch products. We assumed the same sticking probabilities for all surface materials.

Table 17. Non-volatile etch products and their wall sticking probabilities assumed in the model.

Etched species	Redeposition probability
Si, SiCl, SiO, SiO_2	0.99
$SiCl_2$, $SiCl_3$	0.05
$SiCl_4$	0.00 (reflected)

4.5.6 Sputter processes

a. Energy and angular dependency of the sputter yield

When an energetic ion of a few 100 *eV* bombards the surface, it will penetrate into the substrate and cause a collision cascade, which might

result in launching one or more surface atoms into the gas phase, called sputtering. A certain ion energy is required for surface atoms to be brought into the gas phase, called the threshold energy for sputtering. This value is typically 10-100 *eV* depending on the type of material and ions.

Matsunami *et al* [164] have proposed a formula based on experimental data to predict the sputter yield of various monoatomic ions on various surfaces. The sputter yields for Ar^+, Cl^+, O^+ and Si^+ on *poly*-Si, implemented in our model, are based on this formula and are plotted as a function of bombarding energy in **Figure 23**.

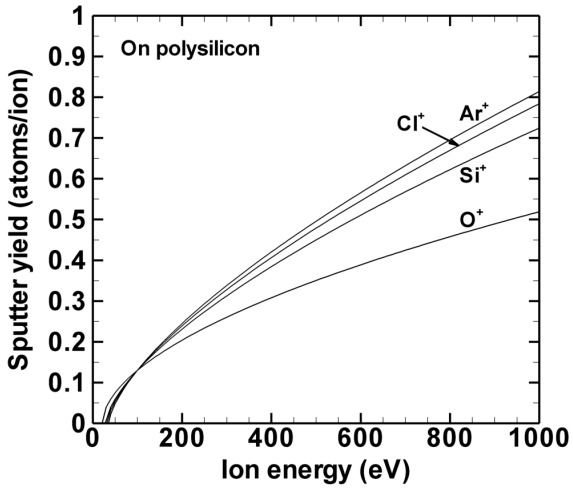

Figure 23. Sputter yields of Ar^+, Cl^+, Si^+ and O^+ on *poly*-Si, as a function of energy, for perpendicular ion bombardment, as calculated from [164].

From classical sputtering theory [165] it is known that the sputter yield increases with increasing ion energy, as more energy is transferred to the surface atoms, at least for the energy range under study in this work (0 - 1000 *eV*). However, at higher ion energies (e.g. >10 *keV*) ion implantation becomes dominant over sputtering. Indeed, at these high energies, the ion penetrates deeply into the material and the energy is transferred to

atoms deep in the material which cannot be removed.

In general, light atoms will sputter more slowly than heavier ions [165] as is also clear from **Figure 23**. However, when using very heavy ions, there is a large mass difference between ion and surface atom and energy transfer will be less efficient. For an optimal sputter yield, one should therefore choose ions with a mass close to that of the surface atoms.

It should be noted that the illustrated sputter yields are valid for ions arriving perpendicular to the surface, which is true here for practically all ions, as they are accelerated through the sheath in front of the wafer. In the FPMCS, however, where microtrench evolution is calculated, the ions can bombard the sidewalls of the trenches at any angle. The sputter yields therefore are multiplied by an angular factor that gives rise to an optimal sputter yield at around 60 degrees from the normal of the surface, as is known from classical sputtering theory [165]. The angular factor is illustrated in **Figure 24**.

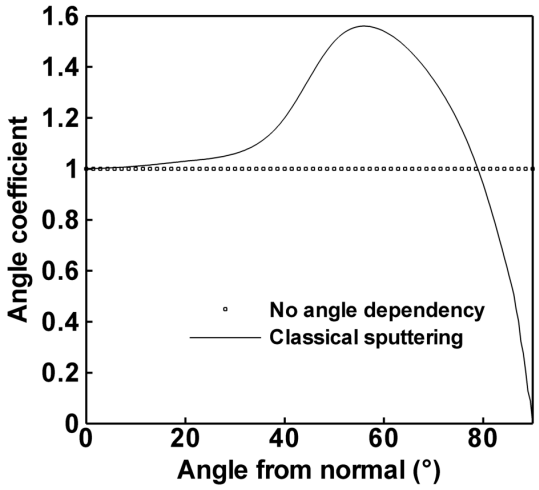

Figure 24. Illustration of the angular factor depicting the dependency of the sputter yield on the angle from the normal of the surface.

Finally, it should be noted that this is the sputter yield on pure Si. In reality, the chlorine neutral flux to the wafer will significantly increase the sputter yield due to chemical transformation of Si to $SiCl_x$ which is more easily sputtered. The flux of neutrals in this kind of systems can be about 1000 times higher than the ion flux (see Part III). Hence, also in the model the Si surface will be mostly converted into $SiCl_x$, which will be sputtered at a higher rate and at a lower threshold. This is discussed in more detail below in section *(e)* on sputtering of $SiCl_x$ layers.

b. Sputtering by molecular ions

Sputter yields of monoatomic ions on various surfaces are usually available in literature from experimental data, or they can be predicted as mentioned before [164].

For the molecular ions considered in the model (Cl_2^+, O_2^+, ClO^+, $SiCl^+$, $SiCl_2^+$, $SiCl_3^+$, $SiCl_4^+$, SiO^+ and SiO_2^+), these data are often not available, but we can consider the molecular ion as a sum of separate atoms arriving at the surface. Indeed, it is known that the ion will attract an electron from the surface (Auger electron) and become neutralized before collision with the surface. In this neutralization process, the molecule often dissociates. As a result, atomic fast neutrals are the actual species that arrive at the surface. Of course, the sum of the energies of the dissociated "parts" (or atoms) must be equal to the total energy of the original molecular ion.

For example, when a SiO_2^+ ion arrives at the surface with energy of 600 *eV*, we can assume that this ion is neutralized and dissociates, and it is actually Si + 2 O fast neutrals arriving at the wafer with a total energy of 600 *eV*. Please note that in the simulation it is still SiO_2^+ bombarding the wafer, so one positive charge is indeed arriving at the surface. Dividing the energy over the separate atoms is done based on their masses. Hence,

about 47 % of the energy will be transferred to Si and 26,5 % to each of the O atoms. Or in other words, Si will arrive with energy of 280 *eV*, and both O atoms with 160 *eV* each. This leaves us with the final equation:

$$SY[SiO_2^+](600\ eV) = SY[Si](280\ eV) + 2 \times SY[O](160\ eV)$$

where SY is the sputter yield. Since the energy dependent sputter yields of Si and O are known from experimental data, we can calculate and implement a sputter yield for SiO_2^+ and all other molecular ions based on this equation, which is a possible solution when the sputter yield for a particular ion is not experimentally available.

c. Chemical surface reactions of ions on Si

Besides sputtering, some ions can also react chemically with the surface atoms. For example, Cl^+ can penetrate the top surface layers of the substrate and cause a Si atom to be sputtered. The Cl atom (i.e. neutralized Cl^+ ion) can then be reflected or it can reside on the surface or inside the top surface layers, where it will probably react with another Si atom to form SiCl. This probability is assumed to be the same as for the neutral Cl atoms, presented above (**Table 13**).
Moreover, as can be seen in **Figure 23**, the sputter yield for ions with energies around 500 *eV*, (i.e. typical energies under study here), is lower than one; hence, not all ions will give rise to sputtering. If a sputter reaction does not occur, the ion might still react chemically with the surface. In our model, different chemical surface reactions for ions were included and were given a probability. This probability was multiplied with the sputter yield (if the reaction occurs besides sputtering) or with one minus the sputter yield (if the reaction occurs without sputtering), so that the sum of all (newly calculated) probabilities is equal to one. **Table**

18 lists these chemical reactions for ions when bombarding the *poly*-Si, as well as their corresponding probabilities. The second column indicates whether a "new surface" is formed/exposed, after sputtering of a Si atom. This is necessary in a sense that, when the Si surface atom (or in other words the Si surface "layer") is sputtered, the underlying layer must be defined as being the newly exposed surface layer.

It should be noted that reactions with Si^+ are not shown for simplicity because Si^+ can only sputter or deposit, and when the Si^+ ion deposits on the surface, there is no sputter reaction and no overall change of the surface.

The reactions listed in the table are valid for the wafer, which consists of *poly*-Si. It should be noted that for microchip manufacturing, the Si wafer is actually *mono*-Si. However, to be able to measure the etch rate experimentally, first *poly*-Si (e.g. 200 *nm*) is deposited on a SiO_2 layer. In this way, the thickness of this layer can be measured with ellipsometry before and after the etch experiment, in order to obtain the etch rate. Therefore, in our experiments, the surface conists of *poly*-Si instead of *mono*-Si.

In the simulations, after etching of a layer, the underlying layer is $Si_{(s)}$. Of course, the same reactions can also occur at the other reactor walls where the underlying material is defined to be "clean wall" (Al_2O_3), or $SiO_{2(s)}$ in the case of a coated chamber. Hence, in this case, the new surface after sputtering is SiO_2, which does not react chemically with chlorine species.

Table 18. Chemical surface reactions for positive ions on *poly*-Si included in the model. SY means sputter yield.

Surface reaction	New surface	Probability
$Ar^+ + Si_{(s)} \rightarrow Si + Ar$	$Si_{(s)}$	1.00 × SY for Ar^+
$Cl^+ + Si_{(s)} \rightarrow Si + Cl$	$Si_{(s)}$	0.01 × SY for Cl^+

$Cl^+ + Si_{(s)} \rightarrow Si$	$SiCl_{(s)}$	0.99 × SY for Cl^+
$Cl^+ + Si_{(s)} \rightarrow Si_{(s)} + Cl$	/	0.01 × (1 - SY for Cl^+)
$Cl^+ + Si_{(s)} \rightarrow SiCl_{(s)}$	/	0.99 × (1 - SY for Cl^+)
$Cl_2^+ + Si_{(s)} \rightarrow Si + Cl_2$	$Si_{(s)}$	0.99 × SY for Cl_2^+
$Cl_2^+ + Si_{(s)} \rightarrow Si$	$SiCl_{2(s)}$	0.01 × SY for Cl_2^+
$Cl_2^+ + Si_{(s)} \rightarrow Si_{(s)} + Cl_2$	/	0.99 × (1 - SY for Cl_2^+)
$Cl_2^+ + Si_{(s)} \rightarrow SiCl_{2(s)}$	/	0.01 × (1 - SY for Cl_2^+)
$O^+ + Si_{(s)} \rightarrow Si + O$	$Si_{(s)}$	0.01 × SY for O^+
$O^+ + Si_{(s)} \rightarrow Si$	$SiO_{(s)}$	0.99 × SY for O^+
$O^+ + Si_{(s)} \rightarrow Si_{(s)} + O$	/	0.01 × (1 - SY for O^+)
$O^+ + Si_{(s)} \rightarrow SiO_{(s)}$	/	0.99 × (1 - SY for O^+)
$O_2^+ + Si_{(s)} \rightarrow Si + O_2$	$Si_{(s)}$	0.99 × SY for O_2^+
$O_2^+ + Si_{(s)} \rightarrow Si$	$SiO_{2(s)}$	0.01 × SY for O_2^+
$O_2^+ + Si_{(s)} \rightarrow Si_{(s)} + O_2$	/	0.99 × (1 - SY for O_2^+)
$O_2^+ + Si_{(s)} \rightarrow SiO_{2(s)}$	/	0.01 × (1 - SY for O_2^+)
$ClO^+ + Si_{(s)} \rightarrow Si + ClO$	$Si_{(s)}$	0.01 × SY for ClO^+
$ClO^+ + Si_{(s)} \rightarrow Si$	$SiClO_{(s)}$	0.99 × SY for ClO^+
$ClO^+ + Si_{(s)} \rightarrow Si_{(s)} + ClO$	/	0.01 × (1 - SY for ClO^+)
$ClO^+ + Si_{(s)} \rightarrow SiClO_{(s)}$	/	0.99 × (1 - SY for ClO^+)
$SiCl^+ + Si_{(s)} \rightarrow Si + SiCl$	$Si_{(s)}$	0.01 × SY for $SiCl^+$
$SiCl^+ + Si_{(s)} \rightarrow Si + SiCl_{(s)}$	/ [a]	0.99 × SY for $SiCl^+$
$SiCl^+ + Si_{(s)} \rightarrow Si_{(s)} + SiCl$	/	0.01 × (1 - SY for $SiCl^+$)
$SiCl^+ + Si_{(s)} \rightarrow Si_{(s)} + SiCl_{(s)}$	/ [b]	0.99 × (1 - SY for $SiCl^+$)
$SiCl_2^+ + Si_{(s)} \rightarrow Si + SiCl_2$	$Si_{(s)}$	0.95 × SY for $SiCl_2^+$
$SiCl_2^+ + Si_{(s)} \rightarrow Si + SiCl_{2(s)}$	/ [a]	0.05 × SY for $SiCl_2^+$
$SiCl_2^+ + Si_{(s)} \rightarrow Si_{(s)} + SiCl_2$	/	0.95 × (1 - SY for $SiCl_2^+$)
$SiCl_2^+ + Si_{(s)} \rightarrow Si_{(s)} + SiCl_{2(s)}$	/ [b]	0.05 × (1 - SY for $SiCl_2^+$)
$SiCl_3^+ + Si_{(s)} \rightarrow Si + SiCl_3$	$Si_{(s)}$	0.95 × SY for $SiCl_3^+$

$SiCl_3^+ + Si_{(s)} \rightarrow Si + SiCl_{3(s)}$	/ [a]	0.05 × SY for $SiCl_3^+$
$SiCl_3^+ + Si_{(s)} \rightarrow Si_{(s)} + SiCl_3$	/	0.95 × (1 - SY for $SiCl_3^+$)
$SiCl_3^+ + Si_{(s)} \rightarrow Si_{(s)} + SiCl_{3(s)}$	/ [b]	0.05 × (1 - SY for $SiCl_3^+$)
$SiCl_4^+ + Si_{(s)} \rightarrow Si + SiCl_4$	$Si_{(s)}$	1.00 × SY for $SiCl_4^+$
$SiO^+ + Si_{(s)} \rightarrow Si + SiO$	$Si_{(s)}$	0.01 × SY for SiO^+
$SiO^+ + Si_{(s)} \rightarrow Si + SiO_{(s)}$	/ [a]	0.99 × SY for SiO^+
$SiO^+ + Si_{(s)} \rightarrow Si_{(s)} + SiO$	/	0.01 × (1 - SY for SiO^+)
$SiO^+ + Si_{(s)} \rightarrow Si_{(s)} + SiO_{(s)}$	/ [b]	0.99 × (1 - SY for SiO^+)
$SiO_2^+ + Si_{(s)} \rightarrow Si + SiO_2$	$Si_{(s)}$	0.01 × SY for SiO_2^+
$SiO_2^+ + Si_{(s)} \rightarrow Si + SiO_{2(s)}$	/ [a]	0.99 × SY for SiO_2^+
$SiO_2^+ + Si_{(s)} \rightarrow Si_{(s)} + SiO_2$	/	0.01 × (1 - SY for SiO_2^+)
$SiO_2^+ + Si_{(s)} \rightarrow Si_{(s)} + SiO_{2(s)}$	/ [b]	0.99 × (1 - SY for SiO_2^+)

[a] The ion sputters a Si atom, but resides at the surface, resulting in no net sputtering of Si atoms.

[b] These are actually deposition reactions, where the ion does not sputter but sticks to the surface.

d. Chemical surface reactions of ions on SiO_x

When a SiO_2 (glass) layer is sputtered by ions, the O atoms will be removed at a higher rate than the Si atoms, yielding a Si enrichment in the surface layer, i.e. so-called preferential sputtering [165-170]. It has been reported that oxygen is about five times more easily sputtered than silicon [166], making the top surface layer of about 9 *nm* to consist of practically pure silicon [167]. At least, this seems to be true for ions with an energy range up to 1000 *eV*. The exact mechanism for preferential sputtering is not well known. It seems that the mechanism is charge-based, in a sense that preferential sputtering of oxygen mainly occurs by ions and not by fast neutrals [165]. The removal of oxygen is therefore probably driven by the creation of charge defects in the SiO_2 layer, making oxygen to migrate out of the surface thermally. Applying fast

neutral sputtering usually densifies the SiO_2 layer instead of sputtering oxygen preferentially [168].

Based on this information, the sputter yield for oxygen in SiO_2 was defined as being five times that of Si in our model, and we have considered reactions where only oxygen is removed from SiO_2 until the layer consists of pure Si. Subsequently, from then on, the sputter yield is the same as for clean Si (cf. **Figure 23**). In practice, this results in a sputter rate for SiO_2 which is about half that for pure Si. This corresponds indeed to experimental observations, where SiO_2 is found to be sputtered more slowly than *poly*-Si. Mizutani [168] observed, for an ion energy range of 400 - 700 *eV*, that a clean Si layer is sputtered roughly twice as fast as a SiO_2 layer under the same conditions.

Finally, depending on the nature of the ion, other possible reactions were included as well, such as chemical reactions or deposition reactions, similar to the sputtering of a *poly*-Si layer. All possible reactions, for all possible bombarding ions, are listed in **Table 19**. As mentioned earlier, the sputter yield is defined as being 5 times that of *poly*-Si (**Figure 23**), and the probabilities of the chemical reactions are defined based on the same reactions of the corresponding neutral species.

For example, when Cl^+ bombards a $SiO_{(s)}$ layer, there are three possible reactions defined in the model. In the first reaction, the Cl^+ ion will sputter O from $SiO_{(s)}$ and be reflected. In the second reaction, Cl^+ will sputter O and will chlorinate the remaining $Si_{(s)}$ surface (i.e. it forms $SiCl_{(s)}$). Finally, in the third reaction, the Cl^+ ion does not sputter, and leaves the SiO layer unchanged. The total sputter yield, which is the sum of the probabilities of the first and second reaction, is 5 times the yield defined in **Figure 23**, to account for preferential sputtering of O, as stated before. Since a Cl atom will chlorinate Si with a probability of 0.99 in our model (see **Table 13** above), this fraction of 0.99 of the total sputter yield is therefore given to the reaction where Cl sticks to the

surface (i.e. second reaction). In the case of no sputtering, only one reaction can occur, i.e. the neutralization and reflection of Cl, since Cl atoms can not chemically react with a $SiO_{(s)}$ layer.

It is worth mentioning that there is a significant probability for ion deposition to occur, where the ion will actually account for deposition "during" the sputtering process due to its chemical or non-volatile nature.

Table 19. Chemical surface reactions included in the model for positive ions on $SiO_{x(s)}$. For preferential sputtering of oxygen, the sputter yields are 5 times those on *poly*-Si. *PSY* means preferential sputter yield and is equal to 5 times the sputter yield as presented in **Figure 23**. *X* is Si, SiCl, SiO or SiO_2 and *Y* is $SiCl_2$ or $SiCl_3$.

Surface reaction	Probability
$Ar^+ + SiO_{(s)} \rightarrow Si_{(s)} + Ar + O$	1.00 × PSY for Ar^+
$Ar^+ + SiO_{2(s)} \rightarrow SiO_{(s)} + Ar + O$	1.00 × PSY for Ar^+
$Cl^+ + SiO_{(s)} \rightarrow SiCl_{(s)} + O$	0.99 × PSY for Cl^+
$Cl^+ + SiO_{(s)} \rightarrow Si_{(s)} + Cl + O$	0.01 × PSY for Cl^+
$Cl^+ + SiO_{(s)} \rightarrow SiO_{(s)} + Cl$	1.00 × (1 - PSY for Cl^+)
$Cl^+ + SiO_{2(s)} \rightarrow SiCl_{(s)} + O_2$	0.33 × PSY for Cl^+
$Cl^+ + SiO_{2(s)} \rightarrow Si_{(s)} + Cl + O_2$	0.01 × PSY for Cl^+
$Cl^+ + SiO_{2(s)} \rightarrow SiO_{(s)} + Cl + O$	0.66 × PSY for Cl^+
$Cl^+ + SiO_{2(s)} \rightarrow SiO_{2(s)} + Cl$	1.00 × (1 - PSY for Cl^+)
$Cl_2^+ + SiO_{(s)} \rightarrow SiCl_{2(s)} + O$	0.01 × PSY for Cl_2^+
$Cl_2^+ + SiO_{(s)} \rightarrow Si_{(s)} + Cl_2 + O$	0.99 × PSY for Cl_2^+
$Cl_2^+ + SiO_{(s)} \rightarrow SiO_{(s)} + Cl_2$	1.00 × (1 - PSY for Cl_2^+)
$Cl_2^+ + SiO_{2(s)} \rightarrow SiCl_{2(s)} + O_2$	0.01 × PSY for Cl_2^+
$Cl_2^+ + SiO_{2(s)} \rightarrow Si_{(s)} + Cl_2 + O_2$	0.66 × PSY for Cl_2^+
$Cl_2^+ + SiO_{2(s)} \rightarrow SiO_{(s)} + O + Cl_2$	0.33 × PSY for Cl_2^+
$Cl_2^+ + SiO_{2(s)} \rightarrow SiO_{2(s)} + Cl_2$	1.00 × (1 - PSY for Cl_2^+)
$O^+ + SiO_{(s)} \rightarrow Si_{(s)} + O_2$	0.01 × PSY for O^+
$O^+ + SiO_{(s)} \rightarrow SiO_{2(s)}$	0.99 × (1 - PSY for O^+)

$O^+ + SiO_{(s)} \rightarrow SiO_{(s)} + O$	0.01 × (1 - PSY for O^+)
$O^+ + SiO_{2(s)} \rightarrow Si_{(s)} + O + O_2$	0.01 × PSY for O^+
$O^+ + SiO_{2(s)} \rightarrow SiO_{(s)} + O_2$	0.99 × PSY for O^+
$O^+ + SiO_{2(s)} \rightarrow SiO_{2(s)} + O$	1.00 × (1 - PSY for O^+)
$O_2^+ + SiO_{(s)} \rightarrow Si_{(s)} + O + O_2$	0.99 × PSY for O_2^+
$O_2^+ + SiO_{(s)} \rightarrow SiO_{2(s)} + O$	0.01 × PSY for O_2^+
$O_2^+ + SiO_{(s)} \rightarrow SiO_{(s)} + O_2$	1.00 × (1 - PSY for O_2^+)
$O_2^+ + SiO_{2(s)} \rightarrow Si_{(s)} + O_2 + O_2$	0.99 × PSY for O_2^+
$O_2^+ + SiO_{2(s)} \rightarrow SiO_{(s)} + O_2 + O$	0.01 × PSY for O_2^+
$O_2^+ + SiO_{2(s)} \rightarrow SiO_{2(s)} + O_2$	1.00 × (1 - PSY for O_2^+)
$ClO^+ + SiO_{(s)} \rightarrow Si_{(s)} + O + ClO$	0.01 × PSY for ClO^+
$ClO^+ + SiO_{(s)} \rightarrow SiClO_{(s)} + O$	0.99 × PSY for ClO^+
$ClO^+ + SiO_{(s)} \rightarrow SiO_{2(s)} + Cl$	0.99 × (1 - PSY for ClO^+)
$ClO^+ + SiO_{(s)} \rightarrow SiO_{(s)} + ClO$	0.01 × (1 - PSY for ClO^+)
$ClO^+ + SiO_{2(s)} \rightarrow Si + O_2 + ClO$	0.01 × PSY for ClO^+
$ClO^+ + SiO_{2(s)} \rightarrow SiClO_{(s)} + O_2$	0.98 × PSY for ClO^+
$ClO^+ + SiO_{2(s)} \rightarrow SiO_{(s)} + ClO + O$	0.01 × PSY for ClO^+
$ClO^+ + SiO_{2(s)} \rightarrow SiO_{2(s)} + ClO$	1.00 × (1 - PSY for ClO^+)
$X^+ + SiO_{(s)} \rightarrow Si_{(s)} + O + X$	0.01 × PSY for X^+
$X^+ + SiO_{(s)} \rightarrow Si_{(s)} + O + X_{(s)}$	0.99 × PSY for X^+
$X^+ + SiO_{(s)} \rightarrow SiO_{(s)} + X$	0.01 × (1 - PSY for X^+)
$X^+ + SiO_{(s)} \rightarrow SiO_{(s)} + X_{(s)}$	0.99 × (1 - PSY for X^+)
$X^+ + SiO_{2(s)} \rightarrow Si_{(s)} + O_2 + X$	0.01 × PSY for X^+
$X^+ + SiO_{2(s)} \rightarrow Si_{(s)} + O_2 + X_{(s)}$	0.89 × PSY for X^+
$X^+ + SiO_{2(s)} \rightarrow SiO_{(s)} + O + X$	0.001 × PSY for X^+
$X^+ + SiO_{2(s)} \rightarrow SiO_{(s)} + O + X_{(s)}$	0.099 × PSY for X^+
$X^+ + SiO_{2(s)} \rightarrow SiO_{2(s)} + X$	0.01 × (1 - PSY for X^+)
$X^+ + SiO_{2(s)} \rightarrow SiO_{2(s)} + X_{(s)}$	0.99 × (1 - PSY for X^+)

$Y^+ + SiO_{(s)} \rightarrow Si_{(s)} + O + Y$	0.95 × PSY for Y^+
$Y^+ + SiO_{(s)} \rightarrow Si_{(s)} + O + Y_{(s)}$	0.05 × PSY for Y^+
$Y^+ + SiO_{(s)} \rightarrow SiO_{(s)} + Y$	0.95 × (1 - PSY for Y^+)
$Y^+ + SiO_{(s)} \rightarrow SiO_{(s)} + Y_{(s)}$	0.05 × (1 - PSY for Y^+)
$Y^+ + SiO_{2(s)} \rightarrow Si_{(s)} + O_2 + Y$	0.85 × PSY for Y^+
$Y^+ + SiO_{2(s)} \rightarrow Si_{(s)} + O_2 + Y_{(s)}$	0.05 × PSY for Y^+
$Y^+ + SiO_{2(s)} \rightarrow SiO_{(s)} + O + Y$	0.095 × PSY for Y^+
$Y^+ + SiO_{2(s)} \rightarrow SiO_{(s)} + O + Y_{(s)}$	0.005 × PSY for Y^+
$Y^+ + SiO_{2(s)} \rightarrow SiO_{2(s)} + Y$	0.95 × (1 - PSY for Y^+)
$Y^+ + SiO_{2(s)} \rightarrow SiO_{2(s)} + Y_{(s)}$	0.05 × (1 - PSY for Y^+)
$SiCl_4^+ + SiO_{(s)} \rightarrow Si_{(s)} + SiCl_4 + O$	1.00 × PSY for $SiCl_4^+$
$SiCl_4^+ + SiO_{2(s)} \rightarrow SiO_{(s)} + SiCl_4 + O$	1.00 × PSY for $SiCl_4^+$

e. Chemical surface reactions of ions on (oxy)-chlorinated Si

Chlorine is commonly applied to etch Si because it reacts chemically to form $SiCl_x$ molecules. These molecules can desorb from the surface (i.e. etching), as explained above, but they can be much more easily sputtered by ions from the plasma, significantly increasing the etch rate. Therefore, from a macroscopic point of view, one can state that chlorine will make the silicon surface “soft” so that it can be easily removed by sputtering. However, very little information can be found on actual sputter yields of chlorinated surfaces. Hoekstra *et al* [102] have proposed a sputter yield for chlorinated silicon layers in their paper on modeling of silicon etching with an Ar/Cl_2 plasma. The sputter yields implemented in our model are based on their proposed yields. Also Materer *et al* [138] found that the sputter yield for Ar^+ with simultaneous chlorine exposure is in the range of 0.5 - 4.5 *atoms/ion* in an energy range of 35 – 1000 *eV*, which is in line with our defined sputter yields. In addition, these pre-

defined sputter yields, plotted in **Figure 25**, were validated by comparing the predicted etch rate from our model with an experimentally obtained etch rate for a pure Cl_2 plasma under similar operating conditions. We have assumed the same sputter yields for all monoatomic ions on the $SiCl_x$ layers, because of lack of data and because the relative differences between the ions are small (cf. **Figure 23** above). For ionized molecules, the sum of the sputter yields of the separate atoms was defined and the total energy is divided over the separate atoms, as explained before in section *(b)*.

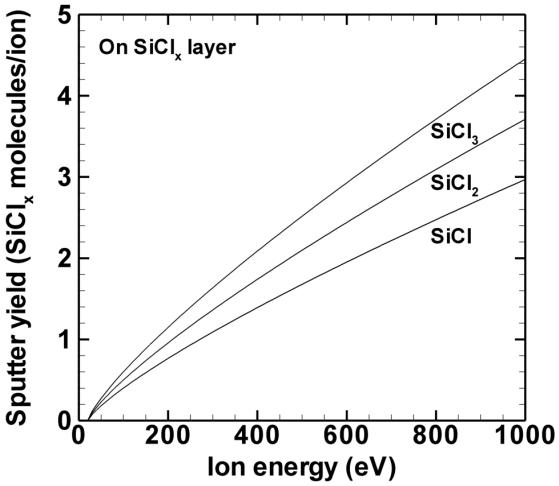

Figure 25. Sputter yields implemented in the model for monoatomic ions on the $SiCl_x$ (x = 1 - 3) surface layers, as adopted from [102]. The sputter yields are assumed to be the same for all monoatomic ions.

As with $SiO_{2(s)}$, it is perfectly possible that preferential sputtering also occurs on chlorinated surfaces where chlorine atoms are more easily sputtered than Si atoms. However, since $SiCl_x$ molecules are more volatile compared to Si atoms, and since the molecules become more volatile if more Cl atoms are bonded to the Si atom, we consider in our model that sputtering of the complete $SiCl_x$ molecules will occur instead

of preferential sputtering of chlorine. For this reason, only sputtering of $SiCl_x$ molecules is considered in our reaction set, which is presented in **Table 20**. Also different possible chemical reactions of ions with the different surfaces are listed. Again, the total sputter yields are divided into fractions for possible chemical reactions to occur (in addition to simple sputtering), where these fractions are defined based on the reaction probabilites for the corresponding neutrals of the ions (i.e. cf. **Table 13** for the chemical reactions of $Cl_{(2)}$ with Si).

Table 20. Chemical surface reactions included in the model for positive ions on $SiCl_x$ surface layers. The chemical reactions with $SiCl_{x(s)}$ (x = 1 - 3), are technically the same and are stated only once for simplicity. Of course, the overall sputter yield is different for each $SiCl_x$ layer, as illustrated in **Figure 25**. The reactions listed in this table are for the *poly*-Si wafer. On other walls (SiO_2 coating or Al_2O_3 clean wall), the new surface, after sputtering, is always $SiO_{2(s)}$ or $Al_2O_{3(s)}$ instead of $Si_{(s)}$.

Surface reaction	New surface	Probability
$Ar^+ + SiCl_{x(s)} \rightarrow SiCl_x + Ar$	$Si_{(s)}$	1.00 × SY on $SiCl_{x(s)}$
$Cl^+ + SiCl_{x(s)} \rightarrow SiCl_x + Cl$	$Si_{(s)}$	0.01 × SY on $SiCl_{x(s)}$
$Cl^+ + SiCl_{x(s)} \rightarrow SiCl_x$	$SiCl_{(s)}$	0.99 × SY on $SiCl_{x(s)}$
$Cl^+ + SiCl_{(s)} \rightarrow SiCl_{(s)} + Cl$	/	0.80 × (1 - SY on $SiCl_{x(s)}$)[a]
$Cl^+ + SiCl_{(s)} \rightarrow SiCl_{2(s)}$	/	0.20 × (1 - SY on $SiCl_{x(s)}$)[a]
$Cl^+ + SiCl_{2(s)} \rightarrow SiCl_{2(s)} + Cl$	/	0.85 × (1 - SY on $SiCl_{x(s)}$)[a]
$Cl^+ + SiCl_{2(s)} \rightarrow SiCl_{3(s)}$	/	0.15 × (1 - SY on $SiCl_{x(s)}$)[a]
$Cl^+ + SiCl_{3(s)} \rightarrow SiCl_{3(s)} + Cl$	/	0.999 × (1 - SY on $SiCl_{x(s)}$)[a]
$Cl^+ + SiCl_{3(s)} \rightarrow SiCl_4$	/	0.001 × (1 - SY on $SiCl_{x(s)}$)[a]
$Cl_2^+ + SiCl_{x(s)} \rightarrow SiCl_x + Cl_2$	$Si_{(s)}$	0.99 × SY on $SiCl_{x(s)}$
$Cl_2^+ + SiCl_{x(s)} \rightarrow SiCl_x$	$SiCl_{2(s)}$	0.01 × SY on $SiCl_{x(s)}$
$Cl_2^+ + SiCl_{(s)} \rightarrow SiCl_{(s)} + Cl_2$	/	0.99 × (1 - SY on $SiCl_{x(s)}$)[a]
$Cl_2^+ + SiCl_{(s)} \rightarrow SiCl_{2(s)} + Cl$	/	0.01 × (1 - SY on $SiCl_{x(s)}$)[a]
$Cl_2^+ + SiCl_{2(s)} \rightarrow SiCl_{2(s)} + Cl_2$	/	0.99 × (1 - SY on $SiCl_{x(s)}$)[a]
$Cl_2^+ + SiCl_{2(s)} \rightarrow SiCl_{3(s)} + Cl$	/	0.01 × (1 - SY on $SiCl_{x(s)}$)[a]
$Cl_2^+ + SiCl_{3(s)} \rightarrow SiCl_{3(s)} + Cl_2$	/	0.999 × (1 - SY on $SiCl_{x(s)}$)[a]
$Cl_2^+ + SiCl_{3(s)} \rightarrow SiCl_{4(s)} + Cl$	/	0.001 × (1 - SY on $SiCl_{x(s)}$)[a]

$O^+ + SiCl_{x(s)} \rightarrow SiCl_x + O$	$Si_{(s)}$	0.01 × SY on $SiCl_{x(s)}$
$O^+ + SiCl_{x(s)} \rightarrow SiCl_x$	$SiO_{(s)}$	0.99 × SY on $SiCl_{x(s)}$
$O^+ + SiCl_{x(s)} \rightarrow SiCl_{x(s)} + O$	/	0.01 × (1 - SY on $SiCl_{x(s)}$)[a]
$O^+ + SiCl_{x(s)} \rightarrow SiCl_xO_{(s)}$	/	0.99 × (1 - SY on $SiCl_{x(s)}$)[a]
$O_2^+ + SiCl_{x(s)} \rightarrow SiCl_x + O_2$	$Si_{(s)}$	0.99 × SY on $SiCl_{x(s)}$
$O_2^+ + SiCl_{x(s)} \rightarrow SiCl_x$	$SiO_{2(s)}$	0.01 × SY on $SiCl_{x(s)}$
$O_2^+ + SiCl_{x(s)} \rightarrow SiCl_{x(s)} + O_2$	/	0.99 × (1 - SY on $SiCl_{x(s)}$)[a]
$O_2^+ + SiCl_{x(s)} \rightarrow SiCl_xO_{(s)} + O$	/	0.01 × (1 - SY on $SiCl_{x(s)}$)[a]
$ClO^+ + SiCl_{x(s)} \rightarrow SiCl_x + ClO$	$Si_{(s)}$	0.01 × SY on $SiCl_{x(s)}$
$ClO^+ + SiCl_{x(s)} \rightarrow SiCl_x$	$SiClO_{(s)}$	0.99 × SY on $SiCl_{x(s)}$
$ClO^+ + SiCl_{(s)} \rightarrow SiCl_2O_{(s)}$	/	0.99 × (1 - SY on $SiCl_{x(s)}$)[a]
$ClO^+ + SiCl_{(s)} \rightarrow SiCl_{(s)} + ClO$	/	0.01 × (1 - SY on $SiCl_{x(s)}$)[a]
$ClO^+ + SiCl_{2(s)} \rightarrow SiCl_3O_{(s)}$	/	0.99 × (1 - SY on $SiCl_{x(s)}$)[a]
$ClO^+ + SiCl_{2(s)} \rightarrow SiCl_{2(s)} + ClO$	/	0.01 × (1 - SY on $SiCl_{x(s)}$)[a]
$ClO^+ + SiCl_{3(s)} \rightarrow SiCl_3O + Cl$	/	0.989 × (1 - SY on $SiCl_{x(s)}$)[a]
$ClO^+ + SiCl_{3(s)} \rightarrow SiCl_4 + O$	/	0.001 × (1 - SY on $SiCl_{x(s)}$)[a]
$ClO^+ + SiCl_{3(s)} \rightarrow SiCl_{3(s)} + ClO$	/	0.01 × (1 - SY on $SiCl_{x(s)}$)[a]
$X^+ + SiCl_{x(s)} \rightarrow SiCl_x + X$	$Si_{(s)}$	0.01 × SY on $SiCl_{x(s)}$[d]
$X^+ + SiCl_{x(s)} \rightarrow SiCl_x + X_{(s)}$	/ [b]	0.99 × SY on $SiCl_{x(s)}$[d]
$X^+ + SiCl_{x(s)} \rightarrow SiCl_{x(s)} + X$	/	0.01 × (1 - SY on $SiCl_{x(s)}$)[d]
$X^+ + SiCl_{x(s)} \rightarrow SiCl_{x(s)} + X_{(s)}$	/ [c]	0.99 × (1 - SY on $SiCl_{x(s)}$)[d]
$Y^+ + SiCl_{x(s)} \rightarrow SiCl_x + Y$	$Si_{(s)}$	0.95 × SY on $SiCl_{x(s)}$[e]
$Y^+ + SiCl_{x(s)} \rightarrow SiCl_x + Y_{(s)}$	/ [b]	0.05 × SY on $SiCl_{x(s)}$[e]
$Y^+ + SiCl_{x(s)} \rightarrow SiCl_{x(s)} + Y$	/	0.95 × (1 - SY on $SiCl_{x(s)}$)[e]
$Y^+ + SiCl_{x(s)} \rightarrow SiCl_{x(s)} + Y_{(s)}$	/ [c]	0.05 × (1 - SY on $SiCl_{x(s)}$)[e]
$SiCl_4^+ + SiCl_{x(s)} \rightarrow SiCl_x + SiCl_4$	$Si_{(s)}$	1.00 × SY on $SiCl_{x(s)}$

[a] If the sputter yield exceeds 1, the reactions with no sputtering of course have zero probability.

[b] The ion sputters a $SiCl_x$ molecule, but resides at the surface, resulting in no net sputtering of Si.

[c] These are actually deposition reactions, where the ion does not sputter but sticks to the surface.

[d] X = Si, SiCl, SiO or SiO_2.

[e] Y = $SiCl_2$ or $SiCl_3$.

There is not much information available on the sputter yields of $SiCl_xO_{y(s)}$ layers that are formed during the etching process. It is known that chlorine cannot chemically etch a $SiCl_xO_{y(s)}$ layer, as with $SiO_{x(s)}$ layers, or at least not at a significant rate [132]. The *oxy-chlorinated* silicon can therefore only be removed by (physical) sputtering. In the model, we have defined reactions for preferential sputtering of oxygen out of the $SiCl_xO_{y(s)}$ layer with the same probability as for the $SiO_{x(s)}$ layers. Again, depending on the nature of the ion, chemical reactions and deposition can occur as well. The sputter reactions for $SiCl_xO_{(s)}$ are listed in **Table 21**. In reality, it is definitely possible that $SiCl_xO_{y(s)}$ surface layers with y > 1 exist, but in our model we have limited the different layers to x = 0 - 3 and y = 0 - 1, in order not to overcomplicate the reaction set.

Table 21. Surface reactions included in the model for the sputtering of $SiCl_xO$ layers with x = 1 - 3. PSY is preferential sputter yield, as discussed in section *(d)*.

Surface reaction	Probability
$Ar^+ + SiCl_xO_{(s)} \rightarrow SiCl_{x(s)} + O + Ar$	1.00 × PSY for Ar^+
$Cl^+ + SiCl_xO_{(s)} \rightarrow SiCl_{x(s)} + O + Cl$	1.00 × PSY for Cl^+
$Cl^+ + SiCl_xO_{(s)} \rightarrow SiCl_xO_{(s)} + Cl$	1.00 × (1 - PSY for Cl^+)[a]
$Cl_2^+ + SiCl_xO_{(s)} \rightarrow SiCl_{x(s)} + O + Cl_2$	1.00 × PSY for Cl_2^+
$Cl_2^+ + SiCl_xO_{(s)} \rightarrow SiCl_xO_{(s)} + Cl_2$	1.00 × (1 - PSY for Cl_2^+)[a]
$O^+ + SiCl_xO_{(s)} \rightarrow SiCl_{x(s)} + O + O$	1.00 × PSY for O^+
$O^+ + SiCl_xO_{(s)} \rightarrow SiO_{2(s)} + Cl$	0.99 (x = 1) × (1 - PSY for O^+)[a]
$O^+ + SiCl_xO_{(s)} \rightarrow SiCl_{x-1}O_{(s)} + Cl$	0.99 (x = 2, x = 3) × (1 - PSY for O^+)[a, b]
$O^+ + SiCl_xO_{(s)} \rightarrow SiCl_xO_{(s)} + O$	0.01 × (1 - PSY for O^+)[a]
$O_2^+ + SiCl_xO_{(s)} \rightarrow SiCl_{x(s)} + O_2 + O$	1.00 × PSY for O_2^+
$O_2^+ + SiCl_xO_{(s)} \rightarrow SiO_{2(s)} + Cl$	0.01 (x = 1) × (1 - PSY for O_2^+)[a, b]
$O_2^+ + SiCl_xO_{(s)} \rightarrow SiCl_{x-1}O_{(s)} + Cl$	0.01 (x = 2, x = 3) × (1 - PSY for O_2^+)[a, b]
$O_2^+ + SiCl_xO_{(s)} \rightarrow SiCl_xO_{(s)} + O_2$	0.99 × (1 - PSY for O_2^+)[a]
$ClO^+ + SiCl_xO_{(s)} \rightarrow SiCl_{x(s)} + O + ClO$	0.01 × PSY for ClO^+ (x = 1, x = 2)
$ClO^+ + SiCl_xO_{(s)} \rightarrow SiCl_{x+1}O_{(s)} + O$	0.99 × PSY for ClO^+ (x = 1, x = 2)

$ClO^+ + SiCl_3O_{(s)} \rightarrow SiCl_{3(s)} + O + ClO$	0.999 × PSY for ClO^+
$ClO^+ + SiCl_3O_{(s)} \rightarrow SiCl_4 + O + O$	0.001 × PSY for ClO^+
$ClO^+ + SiCl_xO_{(s)} \rightarrow SiO_{2(s)} + Cl_2$	0.99 (x = 1) × (1 - PSY for ClO^+)[a]
$ClO^+ + SiCl_xO_{(s)} \rightarrow SiCl_{x-1}O_{(s)} + Cl_2$	0.99 (x = 2, x = 3) × (1 - PSY for ClO^+)[a, b]
$ClO^+ + SiCl_xO_{(s)} \rightarrow SiCl_xO_{(s)} + ClO$	0.01 × (1 - PSY for ClO^+)[a]
$M^+ + SiCl_xO_{(s)} \rightarrow SiCl_{x(s)} + O + M$	0.01 × PSY for M^+[c]
$M^+ + SiCl_xO_{(s)} \rightarrow SiCl_{x(s)} + O + M_{(s)}$	0.99 × PSY for M^+[c]
$M^+ + SiCl_xO_{(s)} \rightarrow SiCl_xO_{(s)} + M$	0.01 × (1 - PSY for M^+)[c]
$M^+ + SiCl_xO_{(s)} \rightarrow SiCl_xO_{(s)} + M_{(s)}$	0.99 × (1 - PSY for M^+)[c]
$N^+ + SiCl_xO_{(s)} \rightarrow SiCl_{x(s)} + O + N$	0.95 × PSY for N^+[d]
$N^+ + SiCl_xO_{(s)} \rightarrow SiCl_{x(s)} + O + N_{(s)}$	0.05 × PSY for N^+[d]
$N^+ + SiCl_xO_{(s)} \rightarrow SiCl_xO_{(s)} + N$	0.95 × (1 - PSY for N^+)[d]
$N^+ + SiCl_xO_{(s)} \rightarrow SiCl_xO_{(s)} + N_{(s)}$	0.05 × (1 - PSY for N^+)[d]
$SiCl_4^+ + SiCl_xO_{(s)} \rightarrow SiCl_{x(s)} + SiCl_4 + O$	1.00 × PSY for $SiCl_4^+$

[a] If the sputter yield exceeds 1, the reactions with no sputtering have zero probability.

[b] The extra O or O_2 missing in the equation is assumed to diffuse into the material, hence it *disappears*.

[c] M = Si, SiCl, SiO or SiO_2.

[d] N = $SiCl_2$ or $SiCl_3$

4.6 $Ar/SiH_4/O_2$ plasma chemistry

4.6.1 Species considered in the model

a. Overview

A similar way of working was used to create the reaction set of an $Ar/SiH_4/O_2$ plasma. This plasma chemistry is slightly more complex than the $Ar/Cl_2/O_2$ chemistry due to more possible reaction products between silane and oxygen. On the other hand, these plasmas are used for deposition processes (instead of etching), so no "etch products" need to be included. Of course, the surface of the substrate or the reactor walls

can still be sputtered, but this is in fact the layer that is being deposited at the same time, which consists of already included plasma species.

To describe the $Ar/SiH_4/O_2$ plasma chemistry, 36 different plasma species are taken into account in the model. The complete list of species is shown in **Table 22** while ionization energies for the positive ions are illustrated in **Table 23**. It should be noted that H_3^+ and ArH^+ are created by heavy particle collisions, not by electron impact ionization, and therefore do not have a threshold energy for ionization listed in the table. Also, SiH_4^+ is not included because SiH_4 is very likely to dissociate during electron impact ionization, rather yielding SiH_3^+ or SiH_2^+ than SiH_4^+.

Table 22. Overview of the species included in the model.

Ground state neutrals:	Ar, O_2, O, H_2, H, H_2O, OH, Si, SiH, SiH_2, SiH_3, SiH_4, SiHO, SiH_2O, SiH_3O, SiO, SiO_2
Positive ions:	Ar^+, O_2^+, O^+, H^+, H_2^+, H_3^+, ArH^+, Si^+, SiH^+, SiH_2^+, SiH_3^+, SiO^+, SiO_2^+
Excited species:	Ar*, O*
Negatively charged species:	O^-, SiH_2^-, SiH_3^-, electrons

Table 23. Overview of the ionization energies defined in the model.

Ionization	Ionization (threshold) energy (*eV*)
$Ar \rightarrow Ar^+$	15.76
$H_2 \rightarrow H_2^+$	11.47
$H \rightarrow H^+$	12.99
$O_2 \rightarrow O_2^+$	12.06
$O \rightarrow O^+$	13.62
$Si \rightarrow Si^+$	8.15
$SiH \rightarrow SiH^+$	7.91
$SiH_2 \rightarrow SiH_2^+$	8.92
$SiH_3 \rightarrow SiH_3^+$	8.14
$SiO \rightarrow SiO^+$	11.55
$SiO_2 \rightarrow SiO_2^+$	12.15

b. Excited species

A more detailed discussion on how electronic excited states are comprised into one or more collective states is already given in section 4.4.1.b. In anology to the $Ar/Cl_2/O_2$ chemistry, the excited species Ar* consist of two collective states referring to the *4s* (11.60 *eV*) and *4p* (13.10 *eV*) excited levels. Similarly, O* represents the *3s* (9.15 *eV*) and *3p* (10.73 *eV*) states. Electron impact vibrational and rotational excitations are included for O_2, H_2 and SiH_4, but not for the other molecular reaction products. O_2 includes the ground state molecule and two electronic excited levels with thresholds of 8.40 *eV* and 10.00 *eV*. For each of these three states, one rotational excitation and two vibrational excitations are included with thresholds of 0.02 *eV*, 0.19 *eV*, and 0.38 *eV*. Similarly, H_2 consists of the ground state and two electronic excited states with threshold energies of 8.80 *eV* and 11.87 *eV*. Also two rotational and two vibrational excitations are included with threshold energies of 0.04 *eV*, 0.07 *eV*, 0.52 *eV* and 1.00 *eV,* respectively. Finally, for SiH_4, two vibrational excitations are included, with thresholds of 0.11 *eV* and 0.24 *eV*.

c. Species not considered in the model

Some species are not included in the model, mostly because their densities are small or because not enough information can be found on their chemical reactions. The latter is true for positive ions of SiH_xO species. No ionization cross sections could be found for these molecules and their ions are therefore not included. Similar to the $Ar/Cl_2/O_2$ reaction set, O_2^- is not included since it is lost more rapidly by charge transfer to O^- than formed, because the threshold for the formation of O_2^-

is relatively high [147, 148]. Hence, we expect that the density of O_2^- in the plasma will be much lower than the O^- density, at least for these low pressure systems. Again, O_3 is also not included in our model, because at the very low pressure under study (10 mTorr), O_3 is not likely to be abundant in the plasma [88]. The same applies for higher silane products such as Si_2H_6 or Si_nH_{2n+2} (n > 2). Indeed, for gap filling applications, particle formation is not desired and conditions are chosen to reduce dust formation as much as possible. Dust formation is therefore negligible at the very-low pressure and low silane gas fraction investigated here and is hence not included in the model [141].

4.6.2 Plasma chemistry reactions

To describe the plasma chemistry of the $SiH_4/O_2/Ar$ gas mixture, a detailed reaction set was again constructed. The complete reaction set is subdivided according to the reactants, for the sake of clarity. Elastic collisions are included in the model but are not listed in the tables. The electron impact reaction rates are defined by energy dependent cross sections $\sigma(E)$ that are presented in the corresponding figures, while the rates of the heavy particle reactions are determined by reaction rate coefficients that are directly presented in the tables. The electron collisions are electron impact ionization, dissociative ionization, excitation and dissociation reactions, as well as electron dissociative attachment and electron-ion recombination. The heavy particle reactions include positive – negative ion recombination, charge transfer, as well as many chemical reactions to form new species, as is outlined in the tables. The reaction sets for pure Ar and pure O_2 plasma are similar to those used for the $Ar/Cl_2/O_2$ chemistry and are already presented in sections 4.4.2.a and 4.4.2.c respectively. **Tables 24** and **25** list the reactions included in the model for a pure H_2 and pure SiH_4 plasma, respectively,

while **Table 26** shows the reactions between Ar, SiH_4 and O_2 species. Similar to the $Ar/Cl_2/O_2$ reaction set, this complete set was created step by step, starting with sets for pure H_2 and SiH_4 plasma and performing numerous simulations under different operating conditions to test these sets separately before combining them.

a. Pure H_2 plasma

As mentioned earlier, for the deposition of SiO_2, an $Ar/SiH_4/O_2$ plasma is typically used. Silane will dissociate in the plasma, generating a large amount of hydrogen. Therefore, reactions for H_2 must also be considered. Similar to Cl_2 and O_2, electronic, rotational and vibrational excitations will occur, as well as dissociation and ionization. However, hydrogen is less electronegative compared to Cl_2 and O_2, and negative ions of hydrogen are usually not significantly present in the plasma [171].
On the other hand, a protonated molecular form (H_3^+) can be formed by the collision of H_2^+ with H_2, and its density typically exceeds those of H^+ and H_2^+ [171]. It should also be noted that the charge transfer reaction where the atomic ion (H^+) is formed instead of the molecular ion (H_2^+) is now favored due to the high stability of the proton. This is different compared to Cl_2 and O_2 where the molecular ion is more “stable” (see sections 4.4.2.a and 4.4.2.c above).
Table 24 lists all the different plasma reactions included for a pure H_2 plasma, where the labels of the cross sections correspond to those shown in **Figure 26**.

Table 24. Chemical reactions for pure H_2 defined in the model, as well as references where the rate coefficients or cross sections were adopted from.

Reaction	Cross section or rate constant	Reference
$e + H_2 \rightarrow H + H + e$	*σ(E)* (Label 1)	[172]
$e + H_2 \rightarrow H_2^+ + 2\ e$	*σ(E)* (Label 2)	[173]
$e + H_2^+ \rightarrow H + H^+ + e$	*σ(E)* (Label 3)	[174]
$e + H_2^+ \rightarrow H + H$	*σ(E)* (Label 4)	[174]
$e + H \rightarrow H^+ + 2\ e$	*σ(E)* (Label 5)	[175]
$e + H_3^+ \rightarrow H^+ + H_2 + e$	*σ(E)* (Label 6)	[174]
$e + H_3^+ \rightarrow H + H_2$	*σ(E)* (Label 7)	[174]
$H_2^+ + H \rightarrow H_2 + H^+$	$6.40 \times 10^{-10}\ cm^3\ s^{-1}$	[141]
$H_2^+ + H_2 \rightarrow H_3^+ + H$	$2.00 \times 10^{-9}\ [T / 298\ K]^{-0.5}\ cm^3\ s^{-1}$	[171]

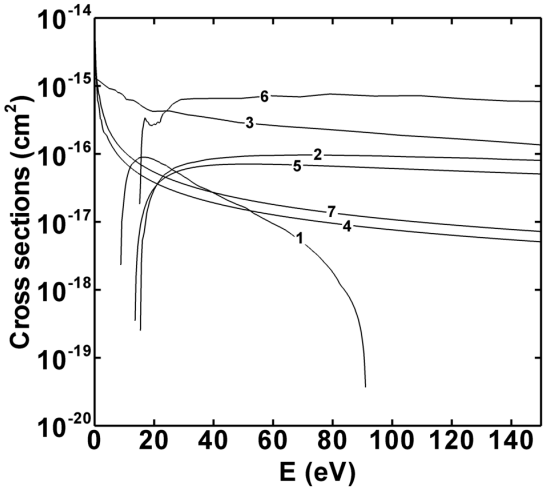

Figure 26. Cross sections as a function of electron energy for the reactions defined in the model for a pure H_2 plasma. The labels correspond to the reactions in **Table 24**.

b. Pure SiH_4 plasma

It should be noted that H and H_2 are reaction products present in the SiH_4 plasma. To properly address the chemistry of a pure SiH_4 plasma, one should therefore include the reactions listed in the following table (i.e. **Table 25**), as well as those from **Table 24** (pure H_2 plasma). The Si-H

bond is not very strong (3.3 *eV*) so SiH_4 will rapidly dissociate into various products. Indeed, under conditions as investigated in this work, SiH_4 is consumed for more than 60 % (see Chapter 9). Moreover, the threshold energies for ionization of the silane products are relatively low (i.e. 8 - 9 *eV*) compared to those of for example Cl_2 and O_2 (i.e. 11 - 13 *eV*) which results in typically higher ion densities compared to the other gases under similar conditions (see also Part III).

The electron impact reactions included in the model are various types of electron impact dissociation, dissociative ionization and dissociative attachment with SiH_4, electron impact ionization of SiH_3 and SiH_2, as well as dissociative recombination with SiH_3^+, SiH_2^+ and SiH^+.

The most important heavy particle reactions include ion-ion neutralizations and abstraction of an H atom from the various silane species by H to form H_2. The latter type of reactions typically occur because the H-H bond is stronger than the Si-H bond (4.5 *eV* compared to 3.3 *eV*) therefore favoring the reaction in this direction.

Table 25 lists all the different plasma reactions included for pure SiH_4 where the labels of the cross sections correspond to those shown in **Figure 27**.

Table 25. Chemical reactions for pure SiH_4 defined in the model, as well as references where the rate coefficients or cross sections were adopted from.

Reaction	Cross section or rate constant	Reference
$e + SiH_4 \rightarrow SiH_3 + H + e$	$\sigma(E)$ (Label 1)	[141]
$e + SiH_4 \rightarrow SiH_2 + H + H + e$	$\sigma(E)$ (Label 2)	[141]
$e + SiH_4 \rightarrow SiH + H_2 + H + e$	$\sigma(E)$ (Label 3)	[141]
$e + SiH_4 \rightarrow SiH_3^+ + H + 2\,e$	$\sigma(E)$ (Label 4)	[141]
$e + SiH_4 \rightarrow SiH_2^+ + H_2 + 2\,e$	$\sigma(E)$ (Label 5)	[141]
$e + SiH_4 \rightarrow SiH^+ + H + H_2 + 2\,e$	$\sigma(E)$ (Label 6)	[141]
$e + SiH_4 \rightarrow Si^+ + H_2 + H_2 + 2\,e$	$\sigma(E)$ (Label 7)	[141]
$e + SiH_4 \rightarrow SiH_3^- + H$	$\sigma(E)$ (Label 8)	[141]

$e + SiH_4 \rightarrow SiH_2^- + H + H$	*σ(E)* (Label 9)	[141]
$e + SiH^+ \rightarrow Si + H$	1.69 x 10^{-7} $cm^3\ s^{-1}$	[141]
$e + SiH_2^+ \rightarrow SiH + H$	1.69 x 10^{-7} $cm^3\ s^{-1}$	[141]
$e + SiH_3^+ \rightarrow SiH_2 + H$	1.69 x 10^{-7} $cm^3\ s^{-1}$	[141]
$e + SiH_3 \rightarrow SiH_3^+ + 2\ e$	*σ(E)* (Label 10)	[141]
$e + SiH_2 \rightarrow SiH_2^+ + 2\ e$	*σ(E)* (Label 11)	[141]
$SiH_4 + H \rightarrow SiH_3 + H_2$	2.68 x 10^{-12} $cm^3\ s^{-1}$	[141]
$SiH_4 + Si \rightarrow SiH_2 + SiH_2$	5.33 x 10^{-13} $cm^3\ s^{-1}$	[141]
$SiH_3 + H \rightarrow SiH_2 + H_2$	1.00 x 10^{-10} $cm^3\ s^{-1}$	[141]
$SiH_3 + SiH_3 \rightarrow SiH_2 + SiH_4$	7.00 x 10^{-12} $cm^3\ s^{-1}$	[141]
$SiH_2 + H_2 \rightarrow SiH_4$	2.00 x 10^{-13} $cm^3\ s^{-1}$	[141]
$SiH_2 + H \rightarrow SiH + H_2$	7.96 x 10^{-13} $cm^3\ s^{-1}$	[141]
$SiH_2 + H \rightarrow SiH_3$	1.11 x 10^{-12} $cm^3\ s^{-1}$	[141]
$SiH + H_2 \rightarrow SiH_3$	1.98 x 10^{-12} $cm^3\ s^{-1}$	[141]
$Si + H_2 \rightarrow SiH_2$	6.59 x 10^{-12} $cm^3\ s^{-1}$	[141]
$SiH_2^+ + SiH_4 \rightarrow SiH_3^+ + SiH_3$	1.07 x 10^{-9} $cm^3\ s^{-1}$	[141, 155]
$SiH_2^+ + H_2 \rightarrow SiH_3^+ + H$	1.01 x 10^{-10} $cm^3\ s^{-1}$	[141]
$SiH^+ + SiH_4 \rightarrow SiH_3^+ + SiH_2$	6.00 x 10^{-11} $cm^3\ s^{-1}$	[141, 155]
$SiH^+ + H_2 \rightarrow SiH_2^+ + H$	1.84 x 10^{-11} $cm^3\ s^{-1}$	[141]
$H^+ + SiH_4 \rightarrow SiH_3^+ + H_2$	5.00 x 10^{-10} $cm^3\ s^{-1}$	[141]
$H_2^+ + SiH_4 \rightarrow Si^+ + H_2 + H_2 + H_2$	3.66 x 10^{-11} $cm^3\ s^{-1}$	[141]
$H_2^+ + SiH_4 \rightarrow SiH^+ + H_2 + H_2 + H$	3.66 x 10^{-11} $cm^3\ s^{-1}$	[141]
$H_2^+ + SiH_4 \rightarrow SiH_2^+ + H_2 + H_2$	6.59 x 10^{-11} $cm^3\ s^{-1}$	[141]
$H_2^+ + SiH_4 \rightarrow SiH_3^+ + H_2 + H$	6.23 x 10^{-10} $cm^3\ s^{-1}$	[141]
$H_2^+ + SiH_4 \rightarrow SiH_3 + H_3^+$	1.83 x 10^{-11} $cm^3\ s^{-1}$	[141]
$H_3^+ + SiH_4 \rightarrow SiH_3^+ + H_2 + H_2$	5.16 x 10^{-10} $cm^3\ s^{-1}$	[141]
$SiH^+ + SiH_4 \rightarrow SiH_2^+ + SiH_3$	1.95 x 10^{-10} $cm^3\ s^{-1}$	[155]
$Si^+ + SiH_4 \rightarrow SiH_3^+ + H + Si$	6.50 x 10^{-10} $cm^3\ s^{-1}$	[155]
$Si^+ + SiH_4 \rightarrow SiH_2^+ + H_2 + Si$	2.20 x 10^{-10} $cm^3\ s^{-1}$	[155]
$Si^+ + SiH_4 \rightarrow SiH^+ + H + H_2 + Si$	2.20 x 10^{-10} $cm^3\ s^{-1}$	[155]
$SiH_3^- + SiH^+ \rightarrow SiH_3 + SiH$	5.00 x 10^{-7} $cm^3\ s^{-1}$	[141]
$SiH_3^- + SiH_2^+ \rightarrow SiH_3 + SiH_2$	5.00 x 10^{-7} $cm^3\ s^{-1}$	[141]

$SiH_3^- + SiH_3^+ \rightarrow SiH_3 + SiH_3$	5.00 x 10^{-7} cm^3 s^{-1}	[141]
$SiH_3^- + Si^+ \rightarrow SiH_3 + Si$	1.00 x 10^{-7} cm^3 s^{-1}	[141]
$SiH_3^- + H^+ \rightarrow SiH_3 + H$	1.00 x 10^{-7} cm^3 s^{-1}	[141]
$SiH_3^- + H_2^+ \rightarrow SiH_3 + H_2$	1.00 x 10^{-7} cm^3 s^{-1}	[141]
$SiH_3^- + H_3^+ \rightarrow SiH_3 + H_2 + H$	1.00 x 10^{-7} cm^3 s^{-1}	[141]
$SiH_2^- + SiH^+ \rightarrow SiH_2 + SiH$	5.00 x 10^{-7} cm^3 s^{-1}	[141]
$SiH_2^- + SiH_2^+ \rightarrow SiH_2 + SiH_2$	5.00 x 10^{-7} cm^3 s^{-1}	[141]
$SiH_2^- + SiH_3^+ \rightarrow SiH_2 + SiH_3$	5.00 x 10^{-7} cm^3 s^{-1}	[141]
$SiH_2^- + Si^+ \rightarrow SiH_2 + Si$	1.00 x 10^{-7} cm^3 s^{-1}	[141]
$SiH_2^- + H^+ \rightarrow SiH_2 + H$	1.00 x 10^{-7} cm^3 s^{-1}	[141]
$SiH_2^- + H_2^+ \rightarrow SiH_2 + H_2$	1.00 x 10^{-7} cm^3 s^{-1}	[141]
$SiH_2^- + H_3^+ \rightarrow SiH_2 + H_2 + H$	1.00 x 10^{-7} cm^3 s^{-1}	[141]
$Si + SiH_4 \rightarrow SiH + SiH_3$	3.00 x 10^{-10} cm^3 s^{-1}	[176]
$SiH + SiH_4 \rightarrow SiH_2 + SiH_3$	5.00 x 10^{-11} cm^3 s^{-1}	[176]

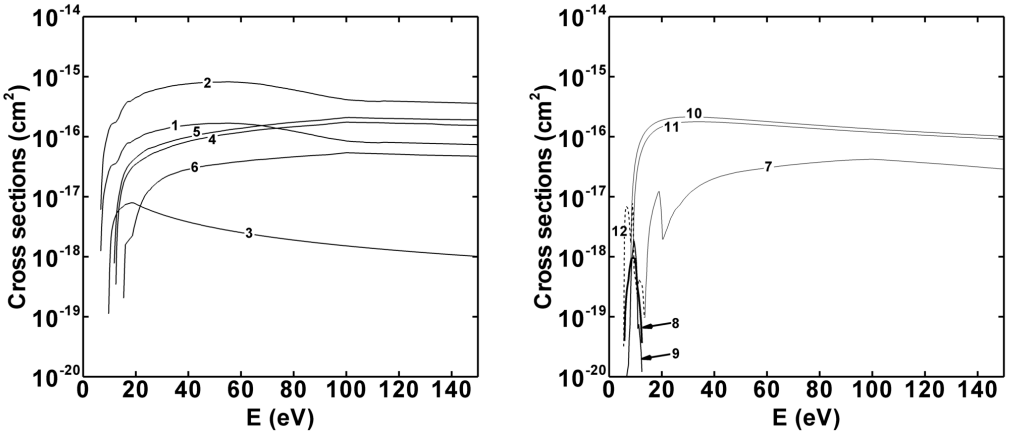

Figure 27. Cross sections as a function of electron energy for the reactions defined in the model for a SiH_4 plasma. The labels correspond to the reactions in **Table 25**. Label 12 corresponds to the electron impact reaction with H_2O, mentioned in **Table 26**.

c. Reactions between Ar, SiH_4 and O_2

The trench filling process occurs by deposition of SiO_2 with an $Ar/SiH_4/O_2$ plasma. Reactions between all possible plasma species originating from this gas mixture must therefore be considered. As mentioned before, all heavy particle reactions can be subdivided into three main groups, namely (i) ion-ion neutralization reactions, (ii) charge transfer reactions and (iii) chemical reactions, where new products are formed. Upon reaction of silane and oxygen species, a large number of SiH_xO_y products can in principle be formed, but only the most common species are included in the reaction set. Similarly, OH and H_2O are also included as being the most common reaction products between H_2 and O_2. Again, Ar does not react chemically due to its noble nature. However, it should be noted that ArH^+ is also a stable ion [171].
Charge transfer reactions are often accompanied by dissociation of the silane species. For instance, the charge transfer of Ar^+ with SiH_4 yields various silane ions (i.e. Si^+, SiH^+, SiH_2^+ and SiH_3^+). **Table 26** lists all the different plasma reactions included between Ar, SiH_4, and O_2 species.

Table 26. Chemical reactions between Ar, O_2 and SiH_4 species defined in the model, as well as the references where the rate coefficients were adopted from.

Reaction	Cross section or rate constant	Reference
$Ar^+ + O_2 \rightarrow Ar + O_2^+$	5.10×10^{-11} $cm^3\ s^{-1}$	[131]
$Ar^+ + O \rightarrow Ar + O^+$	1.00×10^{-11} $cm^3\ s^{-1}$	[131]
$SiH_3^- + Ar^+ \rightarrow SiH_3 + Ar$	5.00×10^{-7} $cm^3\ s^{-1}$	[141]
$SiH_2^- + Ar^+ \rightarrow SiH_2 + Ar$	5.00×10^{-7} $cm^3\ s^{-1}$	[141]
$SiH_3^- + ArH^+ \rightarrow SiH_3 + Ar + H$	5.00×10^{-7} $cm^3\ s^{-1}$	[141]
$SiH_2^- + ArH^+ \rightarrow SiH_2 + Ar + H$	5.00×10^{-7} $cm^3\ s^{-1}$	[141]
$Ar^+ + SiH_4 \rightarrow Ar + Si^+ + H_2 + H_2$	1.18×10^{-11} $cm^3\ s^{-1}$	[141]
$Ar^+ + SiH_4 \rightarrow Ar + SiH^+ + H + H_2$	4.20×10^{-12} $cm^3\ s^{-1}$	[141]

$Ar^+ + SiH_4 \rightarrow Ar + SiH_2^+ + H_2$	1.66 x 10^{-12} $cm^3\ s^{-1}$	[141]
$Ar^+ + SiH_4 \rightarrow Ar + SiH_3^+ + H$	2.40 x 10^{-12} $cm^3\ s^{-1}$	[141]
$Ar^+ + H_2 \rightarrow ArH^+ + H$	6.00 x 10^{-10} $cm^3\ s^{-1}$	[171]
$H_2^+ + Ar \rightarrow ArH^+ + H$	1.70 x 10^{-9} $cm^3\ s^{-1}$	[171]
$e + ArH^+ \rightarrow Ar + H$	1.00 x 10^{-7} $cm^3\ s^{-1}$	[171]
$ArH^+ + H_2 \rightarrow Ar + H_3^+$	1.50 x 10^{-9} $cm^3\ s^{-1}$	[141, 171]
$H_2^+ + Ar \rightarrow H_2 + Ar^+$	2.20 x 10^{-10} $cm^3\ s^{-1}$	[171]
$O + OH \rightarrow H + O_2$	2.40 x 10^{-11} $cm^3\ s^{-1}$	[177]
$O^* + H_2O \rightarrow OH + OH$	2.20 x 10^{-10} $cm^3\ s^{-1}$	[177]
$OH + H_2 \rightarrow H_2O + H$	7.70 x 10^{-12} $cm^3\ s^{-1}$	[177]
$OH + H \rightarrow O + H_2$	1.48 x 10^{-10} $cm^3\ s^{-1}$	[142, 143]
$O + H_2 \rightarrow OH + H$	3.44 x 10^{-10} $cm^3\ s^{-1}$	[142, 143]
$e + H_2O \rightarrow O^- + H_2$	$\sigma(E)$ (Label 12; **Figure 27**)	[142]
$SiH_4 + O \rightarrow SiH_3 + OH$	6.98 x 10^{-12} $cm^3\ s^{-1}$	[142, 143]
$SiH_4 + O^* \rightarrow SiH_3 + OH$	3.00 x 10^{-10} $cm^3\ s^{-1}$	[142, 143]
$SiH_4 + OH \rightarrow SiH_3 + H_2O$	1.40 x 10^{-11} $exp[-50.3\ K/T]$ $cm^3\ s^{-1}$	[142, 143]
$SiH_4 + O_2 \rightarrow SiH_3O + OH$	3.00 x 10^{-12} $cm^3\ s^{-1}$	[142, 143]
$SiH_3 + O \rightarrow SiH_2O + H$	2.16 x 10^{-10} $exp[-1000\ K/T]$ $cm^3\ s^{-1}$	[142, 143]
$SiH_3 + OH \rightarrow SiH_2O + H_2$	8.31 x 10^{-12} $cm^3\ s^{-1}$	[142, 143]
$SiH_3 + O_2 \rightarrow SiH_2O + OH$	6.30 x 10^{-12} $cm^3\ s^{-1}$	[142, 143]
$SiH_3 + O_2 \rightarrow SiH_3O + O$	6.30 x 10^{-12} $cm^3\ s^{-1}$	[142, 143]
$SiH_2 + O_2 \rightarrow SiH_2O + O$	3.75 x 10^{-12} $cm^3\ s^{-1}$	[142, 143]
$SiH_2 + O_2 \rightarrow SiHO + OH$	3.75 x 10^{-12} $cm^3\ s^{-1}$	[142, 143]
$SiH + O_2 \rightarrow SiO + OH$	8.50 x 10^{-11} $cm^3\ s^{-1}$	[142, 143]
$SiH + O_2 \rightarrow SiO_2 + H$	8.50 x 10^{-11} $cm^3\ s^{-1}$	[142, 143]
$SiH_3O + O \rightarrow SiH_2O + OH$	1.00 x 10^{-12} $cm^3\ s^{-1}$	[142, 143]
$SiH_3O + OH \rightarrow SiH_2O + H_2O$	1.00 x 10^{-11} $cm^3\ s^{-1}$	[142, 143]
$SiH_2O + H \rightarrow SiHO + H_2$	5.48 x 10^{-10} $exp[-5276.4\ K/T]$ $cm^3\ s^{-1}$	[142, 143]
$SiH_2O + O \rightarrow SiHO + OH$	2.99 x 10^{-11} $exp[-1547.7\ K/T]$ $cm^3\ s^{-1}$	[142, 143]
$SiH_2O + OH \rightarrow SiHO + H_2O$	1.25 x 10^{-11} $exp[-85.4\ K/T]$ $cm^3\ s^{-1}$	[142, 143]
$SiHO + H \rightarrow SiO + H_2$	3.32 x 10^{-10} $cm^3\ s^{-1}$	[142, 143]
$SiHO + O \rightarrow SiO + OH$	1.66 x 10^{-10} $cm^3\ s^{-1}$	[142, 143]

$SiHO + OH \rightarrow SiO + H_2O$	$1.66 \times 10^{-10}\ cm^3\ s^{-1}$	[142, 143]
$SiO + OH \rightarrow SiO_2 + H$	$6.65 \times 10^{-12}\ exp[-2864.3\ K/T]\ cm^3\ s^{-1}$	[142, 143]
$SiO + O_2 \rightarrow SiO_2 + O$	$2.36 \times 10^{-10}\ exp[-3266.3\ K/T]\ cm^3\ s^{-1}$	[142, 143]
$e + SiO \rightarrow SiO^+ + 2\ e$	$\sigma(E)$ (Label 20; **Figure 22**)	[163]
$e + SiO_2 \rightarrow SiO_2^+ + 2\ e$	$\sigma(E)$ (Label 21; **Figure 22**)	[163]
$SiO + O_2 \rightarrow SiO_2 + O$	$2.36 \times 10^{-10}\ exp[-3266.3\ K/T]\ cm^3\ s^{-1}$	[142, 143]
$SiO^+ + O^- \rightarrow SiO + O$	$1.00 \times 10^{-7}\ [T / 298\ K]^{0.5}\ cm^3\ s^{-1}$	[131][a]
$SiO_2^+ + O^- \rightarrow SiO_2 + O$	$1.00 \times 10^{-7}\ [T / 298\ K]^{0.5}\ cm^3\ s^{-1}$	[131][a]

[a] The reaction coefficient for this reaction is not known. Therefore, we have based the rate coefficient on the value of a similar neutralization reaction as presented in reference [131].

4.7 $Ar/SiH_4/O_2$ surface chemistry

4.7.1 Overview

When the plasma is in contact with a surface such as the substrate or the reactor walls, several processes take place. For $Ar/SiH_4/O_2$ plasmas this especially means deposition of non-volatile plasma products on the surfaces in contact with the plasma. Moreover, the surface is bombarded by plasma ions being accelerated through the sheath, giving rise to sputtering. In addition to deposition and sputtering, also chemical reactions can take place, such as oxidation of the surface. All these main processes will be discussed in more detail in the following sections. However, the surface reaction set for $Ar/SiH_4/O_2$ plasmas is built in a similar way as discussed in section 4.4 for the $Ar/Cl_2/O_2$ chemistry on Si. Therefore, only a schematic overview of the surface reactions is presented for simplicity.

4.7.2 Deposition of non-volatile products

The main process under study for the $Ar/SiH_4/O_2$ plasma is the filling of trenches with SiO_2. This process is mainly due to the deposition of low volatile plasma species. These are not only SiO_y (y = 1, 2) but also SiH_x (x = 0 - 3) and SiH_xO (x = 1 - 3), which will later become oxidized to form SiO_2 (see below). The deposition probabilities, or sticking coefficients, of these species are given in **Table 27**.

Table 27. Schematic overview of the deposition reactions included in the model.

Reaction	Probability
$Si + surface \rightarrow Si_{(s)} + surface$	1.00
$SiH + surface \rightarrow SiH_{(s)} + surface$	1.00
$SiH_2 + surface \rightarrow SiH_{2(s)} + surface$	0.40
$SiH_3 + surface \rightarrow SiH_{3(s)} + surface$	0.30 [a]
$SiH_4 + surface \rightarrow SiH_4 + surface$	1.00 (reflected)
$SiH_xO + surface \rightarrow SiH_xO_{(s)} + surface$	1.00 (x = 1 - 3)
$SiO_y + surface \rightarrow SiO_{y(s)} + surface$	1.00 (y = 1, 2)

[a] If SiH_3 is not deposited/incorporated in the layer, it will abstract H from the surface and be returned as SiH_4 [178, 179].

The less volatile a species, the higher is its sticking or deposition probability. Generally it is accepted that when more H atoms are bonded to Si, the molecule becomes more volatile, similar to $SiCl_x$ molecules. Indeed, a Si atom, or SiH, is considered to be not volatile and it will stick to the wall with a probability of 1.00 [176] while SiH_4 is a gas and it will be completely reflected from the surface. SiH_2 and SiH_3 are considered to be low-volatile. Ramalingam *et al* [178] and Walch et al [179] have concluded from molecular dynamics simulations that SiH_3 can only deposit on the surface if it attaches to a dangling bond from the surface. Otherwise it will most likely abstract H from the surface, since SiH_3 has

one dangling bond, and it will then be reflected as SiH_4 [180]. Both Kessels *et al* [176] and Agarwal *et al* [181] have stated that the surface reaction probability of SiH_3 is close to 0.3 and this value was adopted in our simulations (see **Table 27**). SiH_2 has two dangling bonds, so it is less likely for SiH_2 to abstract two H atoms and be reflected as SiH_4. Therefore SiH_2 is considered to deposit on the surface, or if not, be reflected as SiH_2. Sriraman *et al* [180] have obtained a wall loss probability of 0.4 for SiH_2 based on molecular dynamics simulations, and this value is therefore adopted in our model as the deposition probability, and no H surface abstraction reactions are included for SiH_2, in contrast to SiH_3.

4.7.3 Chemical surface reactions of O, O_2, OH and H

As mentioned earlier, it is well known that O atoms and O_2 molecules will spontaneously react with Si to form a SiO_x (x = 1 - 2) layer up to 1.3 *nm* in thickness. O atoms and OH molecules are considered to be reactive towards the SiH_x or SiH_xO surface (x = 0 - 3), with a reaction probability close to unity [150]; see **Table 28**. O_2, on the other hand, is less eager to react since it is more inert, and therefore a reaction probability of 0.01 is assumed (see **Table 28**). Actual etching of Si with oxygen, a process often referred to as active oxidation, happens only at high substrate temperatures (> 700 *K*) [110 - 114, 150] which is higher than the temperature considered in this work (60 *°C*). For this reason, no etching reactions with oxygen are considered.

Table 28. Schematic overview of chemical surface reactions included in the model for O, O_2, OH and H.

Reaction	Probability
$SiH_{x(s)} + O \rightarrow SiH_xO_{(s)}$ (x = 0 - 3)	1.00
$SiO_{(s)} + O \rightarrow SiO_{2(s)}$	1.00
$SiH_xO_{(s)} + O \rightarrow SiH_{x-1}O_{(s)} + H$ (x = 1 - 3)	1.00 [a]
$SiH_{x(s)} + O_2 \rightarrow SiH_xO_{(s)} + O$ (x = 0 - 3)	0.01
$SiO_{(s)} + O_2 \rightarrow SiO_{2(s)} + O$	0.01
$SiH_xO_{(s)} + O_2 \rightarrow SiH_{x-1}O_{(s)} + H$ (x = 1 - 3)	0.01 [a]
$SiH_{x(s)} + OH \rightarrow SiH_{x+1}O_{(s)}$ (x = 0 - 3)	1.00
$SiO_{(s)} + OH \rightarrow SiO_{2(s)} + H$	1.00
$SiH_xO_{(s)} + OH \rightarrow SiH_{x-1}O_{(s)} + H$ (x = 1 - 3)	1.00 [a]
$SiH_{x(s)} + H \rightarrow SiH_{x-1(s)} + H_2$ (x = 1 - 2)	1.00
$SiH_{3(s)} + H \rightarrow SiH_{2(s)} + H_2$	0.955
$SiH_{3(s)} + H \rightarrow SiH_4$	0.045 [b]
$SiH_xO_{(s)} + H \rightarrow SiH_{x-1}O_{(s)} + H_2$ (x = 1 - 3)	1.00

[a] In these reactions, O or O_2 or OH diffuses into the surface layer and is therefore lost from the reaction.

[b] The active etching of Si in the form of SiH_4 by H atoms is discussed in more detail by Amantides *et al* [182].

Also different processes for H on the surface can occur [183, 184], such as H adsorption, H abstraction (to form H_2), etching of $SiH_{3(s)}$ (to form SiH_4) [182], diffusion into the surface layer and insertion of H into Si-Si bonds. It is also known that H can induce crystallization of amorphous silicon by perturbation of the Si-Si bonds [185]. This has an advantage in terms of charge mobility for transistor fabrication. Of all the above processes, the abstraction of a H-atom from the surface to form H_2 through an Eley-Rideal mechanism is the most likely to occur, since it is characterized by a zero activation energy barrier [184]. Therefore, this process is included in our model, with unit reaction probability for both $SiH_{x(s)}$ and $SiH_xO_{(s)}$ surface layers (x = 1 - 3; see **Table 28**). However, for a $SiH_{3(s)}$ surface, the formation of volatile SiH_4 upon impact of H atoms is

also included, with a reaction probability of 0.045. This value is adopted from Amantides *et al* [182]. Incorporation of H into Si-Si bonds has a threshold energy of about 0.1 *eV* [181] which is much higher than the plasma gas temperature in our work or the surface temperature (60 *°C*), so this process will not likely occur for neutral H, but it can happen for H^+ and H_3^+ ions since they are accelerated through the sheath. H_2 and H_2^+ are less likely to chemically react since they are more inert. For this reason no chemical reactions for these species are included in the surface reaction scheme.

4.7.4 Sputter processes

Besides deposition reactions, the surface is also sputtered by ions. As mentioned before, when an ion with energy of a few 100 *eV* arrives at the substrate, it will penetrate into the surface and cause a collision cascade, which might result in launching one or more surface atoms into the gas phase, called sputtering. Matsunami *et al* [164] have proposed a formula based on experimental data to predict the sputter yield of various monoatomic ions on various surfaces. Similar to the $Ar/Cl_2/O_2$ surface reaction set, the sputter yields (SY) for Ar^+, Si^+, O^+ and H^+ on *poly*-Si, implemented in our model, are based on this formula and are plotted as a function of bombarding energy in **Figure 28**. For molecular ions such as SiO_2^+, these data are often not available, but we can consider the molecular ion as a sum of separate atoms arriving at the surface. This procedure is already explained in more detail in section 4.5.6.b.

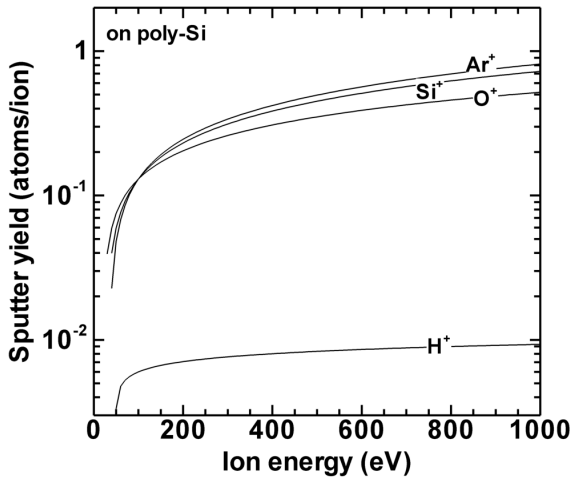

Figure 28. Energy dependent sputter yields for the monoatomic ions included in the model, adopted from [164].

It should be noted that the sputter yields presented in **Figure 28** are valid for ions arriving perpendicular to the surface, which is true for most ions when they are accelerated through the sheath. To account for an angular dependent sputter yield, which is important at the trench sidewalls during the trench filling process, the sputter yields are multiplied by an angular factor that gives rise to an optimal sputter yield at around 60 degrees from the normal of the surface, as is known from classical sputtering theory [165]. The energy and angular dependency is already discussed in more detail in section 4.5.6.a.

Besides sputtering, some ions can also react chemically with the surface atoms. For example, O^+ can penetrate the top surface layers of the substrate and cause a Si atom to be sputtered. The O atom (i.e. neutralized O^+ ion) can then be reflected or it can reside on the surface or inside the top surface layers, where it will probably react with another Si atom to form $SiO_{(s)}$. This probability is assumed to be the same as for the neutral O atoms, as presented in **Table 28**. In this way, ion deposition is also included in our model.

In practice, the surface will have a SiH_xO_y composition close to SiO_2. Indeed, since SiH_x species are more volatile than pure Si, we consider them to be sputtered more easily. We could not find reliable data for the sputter yields of SiH_x layers; therefore, we assumed values based on yields proposed by Hoekstra *et al* [102] for sputtering $SiCl_x$ layers under similar operating conditions.

As was also mentioned in section 4.5.6.d, when a SiO_2 layer is sputtered, the O atoms will be removed at a higher rate than Si, yielding a Si-rich surface layer. This process is known as preferential sputtering [165-169, 186]. Similar to the $Ar/Cl_2/O_2$ surface chemistry set, the sputter yield for oxygen in SiO_2 was therefore defined as being five times that of Si in our model, and we have considered reactions where only oxygen is removed from SiO_2 until the layer consists of pure Si. Subsequently, from then on, the sputter yield is the same as for clean Si (cf. **Figure 28**).

The schematic overview of sputter reactions is presented in **Table 29**. Finally it should be noted that sputtering by H^+, H_2^+ and H_3^+ is negligible compared to the other ions due to their low mass and therefore poor energy transfer. However, incorporation of H into Si-Si bonds is likely to happen by these ions (see last two reactions in **Table 29**).

Table 29. Schematic overview of sputter reactions included in the model. SY is sputter yield and PSY is preferential sputter yield which is considered 5 times the SY.

Reaction	Probability
$SiH_{x(s)} + X^+ \rightarrow SiH_x + X$ (x = 0 - 3)	SY [a,b]
$SiH_xO_{y(s)} + X^+ \rightarrow SiH_xO_{y-1} + X + O$ (x = 0 - 3) (y = 1, 2)	PSY [a, b, c]
$SiH_{x(s)} + H^+ \rightarrow SiH_{x+1(s)}$ (x = 0 - 2)	1.00 [d]
$SiH_{x(s)} + H_3^+ \rightarrow SiH_{x+1(s)} + H_2$ (x = 0 - 2)	1.00 [d]

[a] See **Figure 28** for the values of the sputter yields.

[b] X = Ar, Si, O_2, O, SiH, SiH_2, SiH_3, SiH_4, SiO or SiO_2.

[c] Oxygen is preferentially sputtered, compared to SiH_x, therefore O is sputtered "first".

[d] For x = 3, volatile SiH_4 is formed.

Part III

Results and discussion

Chapter 5

Ar/Cl_2 ICP: Effects of pressure, bias and power

5.1 Introduction

During a wafer processing step, after choosing the proper chemistry (i.e. gas mixture), maybe the most basic and obvious process parameters to vary are gas pressure, substrate bias and source power. The applied pressure and power have a direct effect on the plasma characteristics while the substrate bias mostly influences the wafer surface process. It is common to tune these process parameters until the desired result occurs. As mentioned earlier, as device dimensions decrease, trenches are etched in Si with higher aspect ratio. Therefore, it is necessary that these processes are as efficient as possible in terms of anisotropy, uniformity, selectivity and etch rate. To optimize these etch processes, it is necessary to understand the effects of operating conditions such as gas pressure, source power and substrate bias on the plasma characteristics since the etch process is strongly dependent on the plasma composition and the

This chapter is based on the following publication: S Tinck, W Boullart and A Bogaerts, Simulation of an Ar/Cl_2 inductively coupled plasma: study of the effect of bias, power and pressure and comparison with experiments, J. *Phys. D: Appl. Phys.* 41 (2008) 065207

characteristics of the ion and radical fluxes to the substrate. To investigate the influence of these conditions on the plasma within the reactor volume, numerical simulations will be performed that provide us with detailed information of the plasma behavior. These simulation results will be compared to experimentally measured etch rates to study the effect of the plasma characteristics on the etch process itself.
Modeling the effects of these general process parameters on the plasma behavior was done in an early stage of the work presented in this thesis; therefore the simulations are performed for an Ar/Cl_2 mixture (still without O_2 or etch products) and without (detailed) surface reactions. Nevertheless, some simple surface reactions are included such as recombination of Cl radicals to Cl_2, neutralization of ions and relaxation of excited species at the walls.
In the following sections first general plasma characteristics will be discussed for the Ar/Cl_2 plasma under operating conditions typically applied for Si etching (in STI). Next, the effects of pressure, substrate bias and source power on the bulk plasma characteristics will be discussed in more detail based on numerical results and experimentally obtained etch rates.

5.2 General plasma characteristics

5.2.1 Plasma species density profiles

Calculations were performed for a 10 % Ar and 90 % Cl_2 plasma in a TCP reactor as shown in **Figure 29** under the following operating conditions: 5 *mTorr* total gas pressure, 100 *sccm* total gas flow rate, 250 *W* source power, -200 *V* dc bias at the substrate electrode and an operating frequency of 13.56 *MHz* applied to the coil and to the substrate electrode.

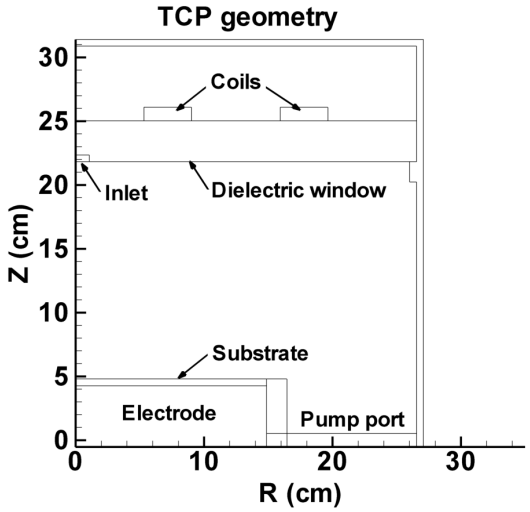

Figure 29. Two-dimensional transformer coupled plasma (TCP) reactor geometry used in the model. The left axis is the symmetry axis of the cylindrically symmetrical reactor.

Figure 30 shows the calculated density profiles of different plasma species in the reactor volume, averaged over one rf cycle. The gas species (Cl_2 and Ar) and especially Cl radicals are most present in the reactor. The Cl_2 and Ar densities have a maximum at the inlet and their profiles spread out more or less uniformly throughout the reactor volume. Their densities reflect well the 90 % Cl_2 and 10 % Ar gas ratio. The calculated gas flow lines are also indicated. The density profile of the Cl radicals is also fairly uniform in the reactor. Comparing the Cl radical density with the Cl_2 density in the main region of the plasma, we find that Cl_2 dissociates for almost 50 % into radicals, at the conditions under study. This is mostly due to electron impact dissociation of Cl_2.

The Cl_2^+ ions are the most abundant positive ions present in the plasma and so the flux of positive ions to the substrate mainly consists of Cl_2^+ ions. The maximum density of the Cl_2^+ ions is at the nozzle in the center of the reactor chamber because it is mostly formed from Cl_2 by electron impact ionization.

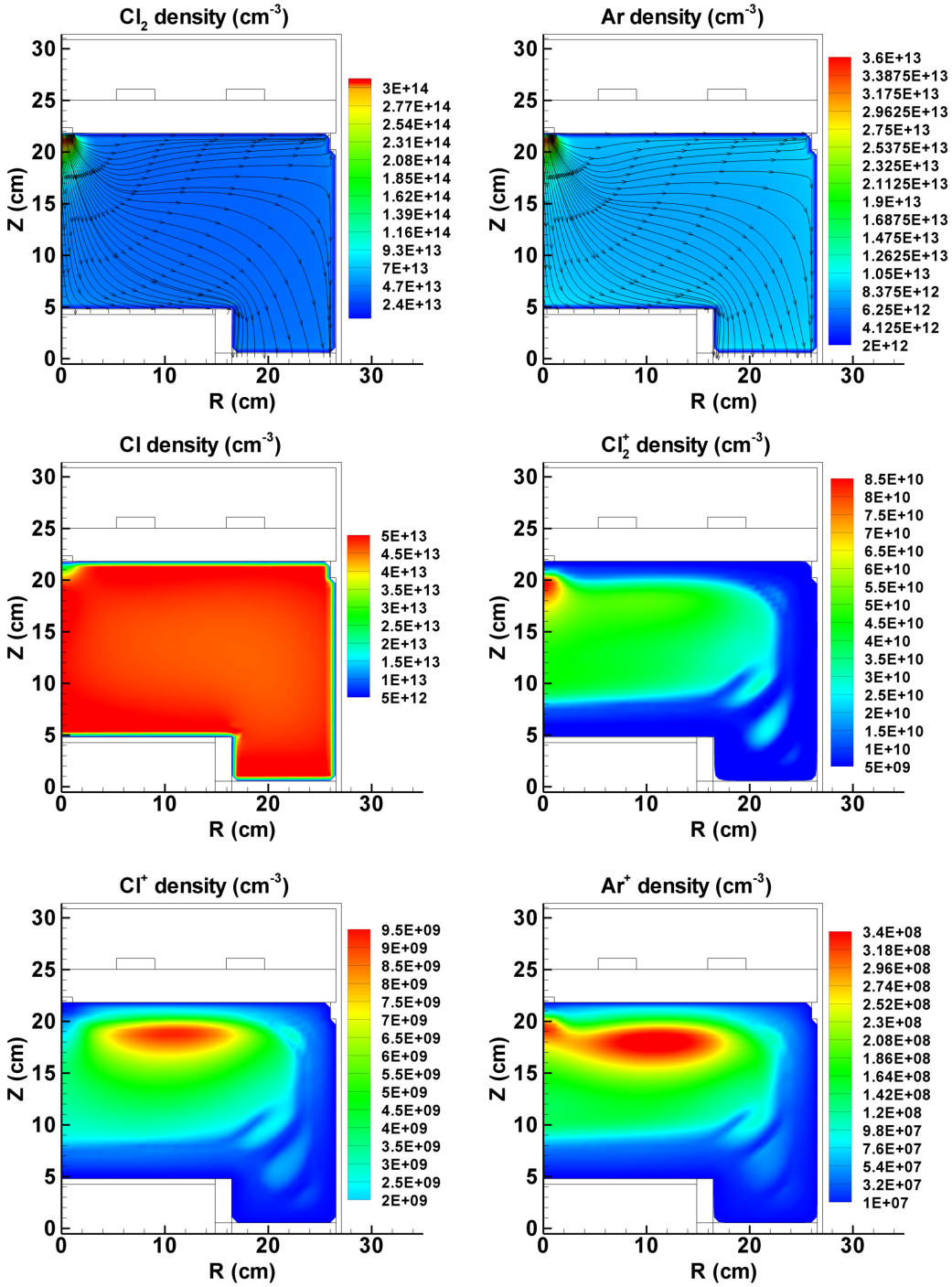
Cl2 density (cm-3)
3E+14
2.77E+14
2.54E+14
2.31E+14
2.08E+14
1.85E+14
1.62E+14
1.39E+14
1.16E+14
9.3E+13
7E+13
4.7E+13
2.4E+13
Ar density (cm-3)
3.6E+13
3.3875E+13
3.175E+13
2.9625E+13
2.75E+13
2.5375E+13
2.325E+13
2.1125E+13
1.9E+13
1.6875E+13
1.475E+13
1.2625E+13
1.05E+13
8.375E+12
6.25E+12
4.125E+12
2E+12
Cl density (cm-3)
5E+13
4.5E+13
4E+13
3.5E+13
3E+13
2.5E+13
2E+13
1.5E+13
1E+13
5E+12
Cl2+ density (cm-3)
8.5E+10
8E+10
7.5E+10
7E+10
6.5E+10
6E+10
5.5E+10
5E+10
4.5E+10
4E+10
3.5E+10
3E+10
2.5E+10
2E+10
1.5E+10
1E+10
5E+09
Cl+ density (cm-3)
9.5E+09
9E+09
8.5E+09
8E+09
7.5E+09
7E+09
6.5E+09
6E+09
5.5E+09
5E+09
4.5E+09
4E+09
3.5E+09
3E+09
2.5E+09
2E+09
Ar+ density (cm-3)
3.4E+08
3.18E+08
2.96E+08
2.74E+08
2.52E+08
2.3E+08
2.08E+08
1.86E+08
1.64E+08
1.42E+08
1.2E+08
9.8E+07
7.6E+07
5.4E+07
3.2E+07
1E+07
Z (cm)
R (cm)
0
5
10
15
20
25
30

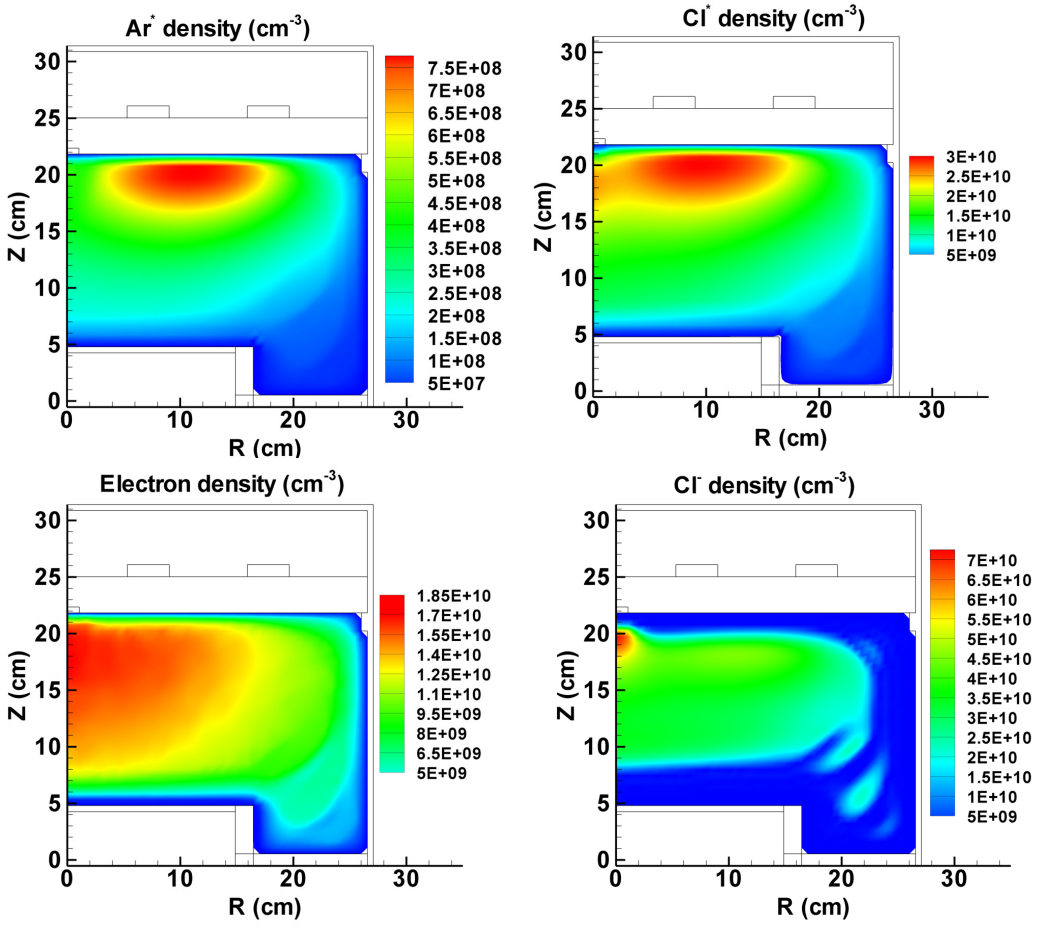

Figure 30. Calculated 2D plasma species density profiles for a 90 % Cl_2 and 10 % Ar gas mixture. The operating conditions are: 5 *mTorr* total gas pressure, 100 *sccm* gas flow rate, 250 *W* source power, -200 *V* dc bias at the substrate and 13.56 *MHz* operating frequency at the coil and at the substrate electrode.

The maximum Cl_2^+ density is still roughly 100 times smaller than the Cl radical or Cl_2 gas species densities because Cl_2^+ easily dissociates into radicals by electron impact dissociative recombination ($e + Cl_2^+ \rightarrow Cl + Cl$). Cl^+ and Ar^+ are mainly formed by electron impact ionizations from Cl and Ar, and also from the excited species Cl* and Ar* since these reactions have a lower threshold than the direct ionization from Cl or Ar.

Therefore, the maximum densities of Cl^+, Ar^+, Cl* and Ar* are in the same location within the reactor volume, where the electron temperature is the highest due to the highest power deposition (see below).

The density of the negative ion Cl^- is higher than the electron density and is highest at the inlet because it is only formed from Cl_2 by electron impact dissociative attachment ($e + Cl_2 \rightarrow Cl^- + Cl$).

These results are well compared and validated with results from literature. Dong-Pyo *et al* [68] have measured an electron density with a Langmuir probe of 1.7×10^{11} cm^{-3} for an Ar/Cl_2 plasma with 90 % Cl_2 at 700 *W* applied power, 2 *Pa* pressure and -200 *V* dc bias. This density is higher because the applied power is much higher than in our case. They also found with optical emission spectroscopy (OES) that the densities of Cl and Cl_2 species are in the same order of magnitude, with the radical density slightly higher than the density of Cl_2 due to the relatively easy dissociation of Cl_2 into radicals, which is also found in our simulation results.

Sung-Mo *et al* [69] also determined nearly identical relative densities of the Cl and Cl_2 species with OES at operating conditions of 10 *mTorr*, 700 *W* applied source power and -300 *V* dc bias.

Efremov *et al* [70] have applied a 0-dimensional model to calculate plasma species densities under the following input parameters: 15 *mTorr*, 700 *W* applied power, -200 *V* dc bias. They found for a 90 % Cl_2 and 10 % Ar mixture that the chlorine ion densities were in the order of 10^{11} cm^{-3} and that the Ar^+ density was in the order of 10^9 cm^{-3}. This is in good agreement with our results taking into account that the applied power is only 250 *W* in our simulations. They also found with OES that, under the same conditions, the Cl density is slightly higher that he Cl_2 density.

In another paper, Efremov *et al* [71] calculated a Cl density in the order of 10^{14} cm^{-3} for a 90 % Cl_2 and 10 % Ar mixture at 2 *Pa* and 700 *W* applied power, by means of their 0-dimensional model. This is also in

good agreement with our results taking into account that the pressure is roughly three times higher in their experiment and Cl_2 easily dissociates into radicals. Their calculated results also show that the total positive ion and electron densities are in the order of 10^{11} *cm*$^{-3}$ which is again in good agreement with our results keeping in mind the much higher power deposition of 700 *W*.

Collison *et al* [77] calculated a Cl^- density of 2×10^{10} *cm*$^{-3}$, for a 50/50 Ar/Cl_2 ICP, with inlet flow rate of 100 *sccm*, 500 *W* source power at 10 *mTorr* and 13.56 *MHz*, which is slightly lower than our results, which is logical since the Cl_2 fraction in the gas mixture is higher in our case.

Grapperhaus *et al* [61] investigated a 50/50 Ar/Cl_2 discharge, with inlet flow rate of 50 *sccm*, 400 *W* source power, 100 *V* rf bias amplitude at 10 *mTorr*, and they measured a peak electron density of 4.6×10^{11} *cm*$^{-3}$. This value is slightly higher than our results because their ICP reactor has a thinner dielectric plate, resulting in a higher power deposition.

Calculations performed by Hoekstra *et al* [76] resulted in a maximum Ar^+ density of 6.2×10^{11} *cm*$^{-3}$ for a pure Ar gas at 5 *mTorr* gas pressure, 800 *W* source power and 100 *V* rf bias amplitude.

The numerical simulations of Ventzek *et al* [62] predicted a maximum plasma density of 2.3×10^{11} *cm*$^{-3}$ for an Ar plasma at 13.56 *MHz* operating frequency and 10 *mTorr* gas pressure with 500 *W* source power.

Subramonium *et al* [74] investigated 80/20 Ar/Cl_2 pulsed ECR plasmas at 30 *mTorr*, 300 *W* source power, 10 *kHz* pulse frequency and 20 *sccm*. The electron density as well as the Cl^- density was calculated to be in the order of 10^{10} *cm*$^{-3}$, where the Cl^- density was slightly lower than the electron density. This reversed trend is explained by the different Ar/Cl_2 ratio.

Hoekstra *et al* [75] discussed for a 70/30 Ar/Cl_2 plasma at 10 *mTorr*, 500 *W* source power and 100 *V* rf bias amplitude that the positive ion density was in the order of 3×10^{11} *cm*$^{-3}$. This is in good agreement with our

results keeping in mind that the applied source power and the gas pressure in our basic case are 250 *W* and 5 *mTorr* respectively. These authors predicted a maximum radical density of 3.7×10^{13} cm^{-3} under these conditions.

Ventzek *et al* [53] studied a 70/30 Ar/Cl_2 plasma, at 700 *W* source power, 5 *mTorr* pressure and 80 *sccm* and found that the electron density is in the order of 10^{11} cm^{-3}, but they also discussed that at a higher percentage of Cl_2, the electron density becomes lower. They also observed that the time averaged Cl_2 density was 1.9×10^{13} cm^{-3} and the Cl density 1.8×10^{13} cm^{-3}, which is in good agreement with our results keeping in mind that they only use 30 % Cl_2 in their gas mixture. The negative ion density was found to be 7.7×10^{10} cm^{-3} under these conditions.

Finally, Vasenkov *et al* [187] measured for an Ar/C_4F_8 ICP at 3 *mTorr*, 400 *W* and 3.39 *MHz* that the maximum electron density was 6×10^{10} cm^{-3} which is in good agreement with our calculated results keeping in mind the different operating conditions.

5.2.2 Potential distribution

The potential distribution in the reactor volume, averaged over time in the rf cycle, is illustrated in **Figure 31**. It is fairly uniform throughout the reactor volume and in the order of 50 *V*, except in the sheath at the substrate, where the potential drops significantly towards the substrate, over a distance of ≈ 0.6 *mm*. Here, the ions are accelerated to bombard the substrate. The time-averaged (or dc) bias at the substrate is ≈ -200 *V*. The variation of the plasma potential and the potential at the substrate electrode as a function of time during one rf cycle is plotted in **Figure 32**. The rf amplitude of the substrate electrode is around 250 *V* and the potential at the substrate varies from ≈ -450 *V* to ≈ 80 *V* creating a negative time averaged dc bias of ≈ -200 *V*. The plasma potential remains

positive during the rf cycle, varying between 1 *V* and 110 *V*, resulting in a time-averaged plasma potential of ≈ 50 *V*.

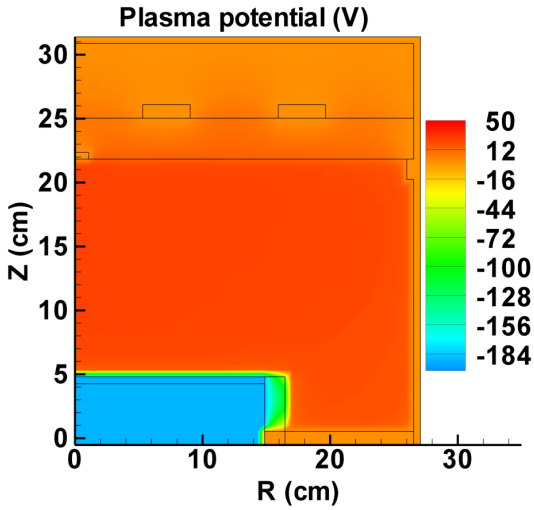

Figure 31. Calculated potential distribution in the reactor volume, time-averaged over one rf cycle at 13.56 *MHz* (≈ 74 *ns*) and operating conditions as described in **Figure 30**.

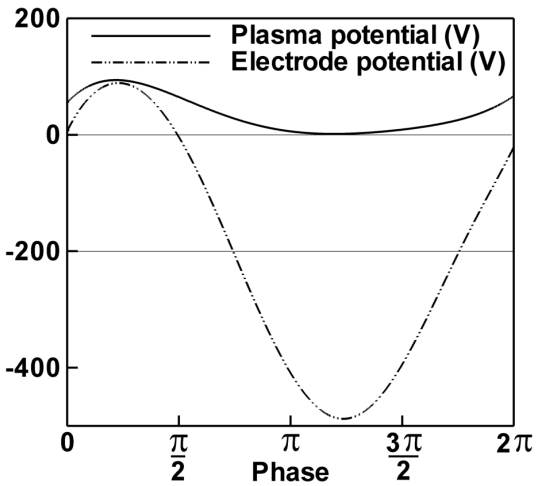

Figure 32. Calculated potential in the plasma and at the substrate electrode, as a function of time, during one rf cycle (≈ 74 *ns*) under the operating conditions as described in **Figure 30**.

Our results concerning the plasma potential are in reasonable agreement with results from literature. Subramonium *et al* [74] observed that the maximum plasma potential was 42 *V* for a 80/20 Ar/Cl_2 pulsed plasma at 20 *mTorr*, 300 *W* source power and 20 *sccm* at a pulse frequency of 20 *kHz*. The average plasma potential in the reactor volume calculated by Hoekstra *et al* [76] was nearly 30 *V* for a pure Ar plasma at 5 *mTorr* gas pressure, 800 *W* source power and 100 *V* rf bias amplitude.
Similar calculations were performed by Ventzek *et al* [62] who found a maximum plasma potential of 13.8 *V* for an Ar plasma at 13.56 *MHz* operating frequency and 10 *mTorr* gas pressure with 500 *W* source power. Ventzek *et al* [52] also observed for a 70/30 Ar/Cl_2 plasma, at 700 *W* source power, 5 *mTorr* pressure, 75 *V* rf bias amplitude and 80 *sccm* that the maximum plasma potential was around 30 *V* and the maximum electron temperature around 5 *eV*. In another paper, Ventzek *et al* [188] investigated a 85/12/3 $Ar/CF_4/O_2$ plasma at 15 *mTorr*, 75 *V* rf bias and 900 *W* source power, and found that the plasma potential was in the order of 10 - 30 V and the electron energy ≈ 3 *eV*.

5.2.3 Gas and electron temperature

The calculated gas and electron temperature profiles are plotted in **Figure 33**. The gas temperature reaches a maximum of 700 *K*, i.e. clearly above room temperature, due to the energy transfer of high-energetic plasma species to the background gas.
The electron temperature is highest where the power deposition is at maximum, i.e. directly under the quartz plate, between the coil windings.
Our calculated electron temperature can be well compared with results from literature. Indeed, Ventzek *et al* [62] found an average electron temperature of 4 *eV* for an Ar plasma at 13.56 *MHz* operating frequency and 10 *mTorr* gas pressure with 500 *W* source power and Subramonium

et al [74] observed that the average electron temperature was roughly 4 *eV* for a 80/20 Ar/Cl_2 pulsed plasma at 20 *mTorr*, 300 *W* source power, 10 *kHz* pulse frequency and 20 *sccm*. Similar calculations were performed by Hoekstra *et al* [75] who found, for a 70/30 Ar/Cl_2 plasma at 10 *mTorr*, 500 *W* source power and 100 *V* rf bias amplitude, a temperature of about 600 - 700 *K* for the neutral species when hitting the substrate. Dong-Pyo *et al* [68] have measured an electron temperature with a Langmuir probe of about 4 *eV* for an Ar/Cl_2 plasma with 90 % Cl_2 at 700 *W* applied power, 2 *Pa* chamber pressure and -200 *V* dc bias. The electron temperature is slightly higher because their applied power is 700 *W* instead of 250 *W* used in our simulations.

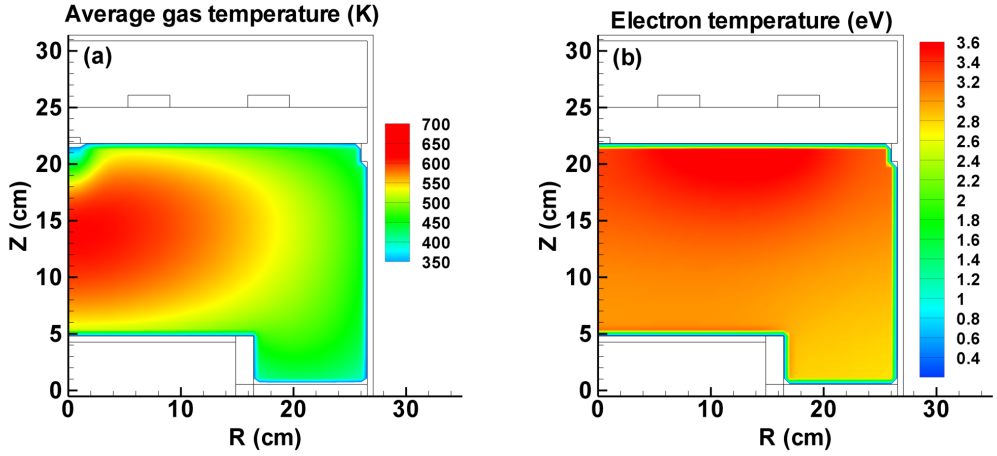

Figure 33. Calculated gas **(a)** and electron **(b)** temperature profiles for the operating conditions as described in **Figure 30**.

Similarly, Efremov *et al* [70, 71] also applied a Langmuir probe to measure an electron temperature of about 3 - 4 *eV* for a 90 % Cl_2 and 10 % Ar mixture under the following input parameters: 15 *mTorr*, 700 *W* applied power, -200 *V* dc bias, which is again in good agreement with our simulation results.

A peak electron temperature of roughly 10 *eV* was calculated by

Subramonium *et al* [189] for a pure Cl_2 pulsed ECR plasma at 10 mTorr, 300 *W* source power, 10 *kHz* pulse frequency and 100 *sccm* gas flow rate. Finally, Fuller *et al* [190] used emission spectroscopy to measure the electron temperature in Ar/Cl_2 plasmas at a pressure of 18 *mTorr*, and a source power of 600 *W*. They found that the electron temperature increased from about 4 *eV* for pure Cl_2 plasmas to about 6 *eV* for pure Ar plasmas.
Hence it can be concluded that our calculation results are in reasonable agreement with literature data, so our calculations can be applied to make predictions on the effects of numerous operating conditions such as gas pressure, substrate bias and power.

5.3 Experimentally obtained etch rates

A series of Si wafers was etched and the etch rate was measured under similar operating conditions as used in the simulations to investigate the effects of pressure, bias and power on the actual etching process.
A set of 300 *mm* blanket *poly*-Si wafers was etched in a TCP reactor (LAM Research 2300 Versys Kiyo) for 15 *s* after a stabilization step of 5 *s*. The wafer consisted of 200 *nm poly*-Si on top of a 100 *nm* SiO_2 layer to be able to measure the thickness of the *poly*-Si with ellipsometry (KLA-Tencor SCD100) at 21 different locations on the wafer before and after the etch process, in order to calculate the etch rate.
First, a blanket *poly*-Si wafer was etched for 15 *s* under the same operating conditions as defined in the simulations. Again, these are: 5 *mTorr* total gas pressure, 10 % Ar and 90 % Cl_2 gas mixture, -200 *V* dc substrate bias, 250 *W* source power, 100 *sccm* gas flow rate and 13.56 *MHz* frequency at the coil and the substrate electrode. The etch rate obtained under these operating conditions is depicted in **Figure 34**. It was found to be in the order of 160 - 180 *nm* min^{-1} at the operating

conditions under study.

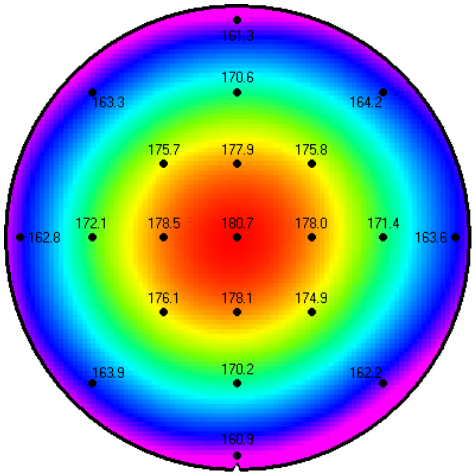

Figure 34. Measured etch rate (*nm min*$^{-1}$) profile of a 300 *mm* blanket *poly*-Si wafer. The local etch rate was obtained from the experimentally measured thickness at various points on the wafer. The operating conditions are the same as in **Figure 30**.

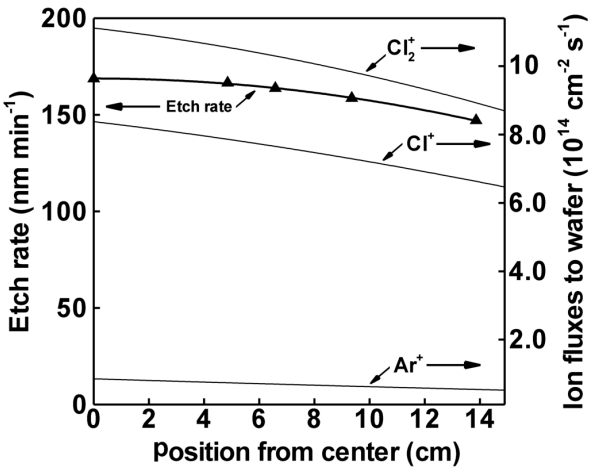

Figure 35. The thick solid line represents the measured etch rate as a function of position on the wafer, referring to the left vertical axis. The thin lines represent the calculated ion fluxes as a function of position on the wafer, referring to the right vertical axis. The operating conditions are the same as in **Figure 30**.

It is clear that the etch rate reaches a maximum at the center of the wafer. This is due to higher ion fluxes at the center, which is illustrated in **Figure 35**, showing the computed ion fluxes together with the measured etch rate, on various locations of the wafer. The uniformity of the etch process is clearly dependent on the uniformity of the ion fluxes. The Cl_2^+ flux is highest due to the fact that its density is highest in the bulk plasma (see section 5.2.1 above). The radical flux to the substrate is not shown in the figure, but was found to be very uniform (see **Figure 36** below), with a value in the order of 10^{18} cm^{-2} s^{-1}.

5.4 Effect of gas pressure

Essentially, increasing the chamber pressure means introducing more species in the reactor. A consequence is that the mean free path is smaller and hence the collision frequency higher, resulting in more reactions between the various plasma species. A change in pressure can therefore significantly affect the bulk plasma characteristics.

Typical pressures applied for wafer processing (e.g. etching) are 1 - 100 *mTorr*. Calculations were performed for the same operating conditions as described in **Figure 30**, but now the pressure was varied from 5 *mTorr* to 80 *mTorr*.

It was found that at higher pressure, the radical density in the bulk plasma is increased due to the easy dissociation of Cl_2 into radicals by electron impact. This effect is also observed in the magnitude of the radical flux to the substrate at different pressures, as shown in **Figure 36(a)**. The Cl radical flux as a function of position on the wafer for different pressure values is illustrated in **Figure 36(b)**. It is clear that this flux is indeed very uniform. On the other hand, our calculations predict that the magnitude of the total ion flux to the substrate did not change as explicitly with pressure, as illustrated in **Figure 37**.

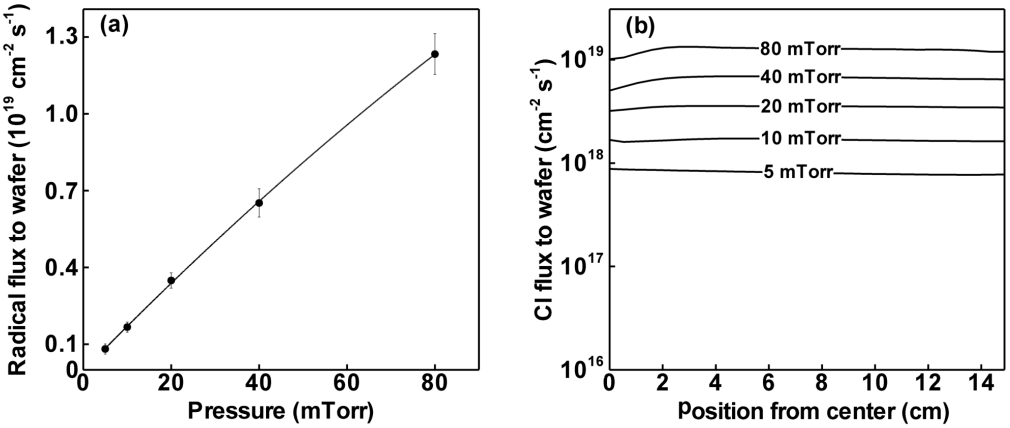

Figure 36. Calculated Cl radical flux to the substrate: **(a)** as a function of pressure. The error bars are a measure for the uniformity of the flux from center to edge of the substrate. **(b)** as a function of position on the wafer, for different pressure values. The other operating conditions are the same as in **Figure 30**.

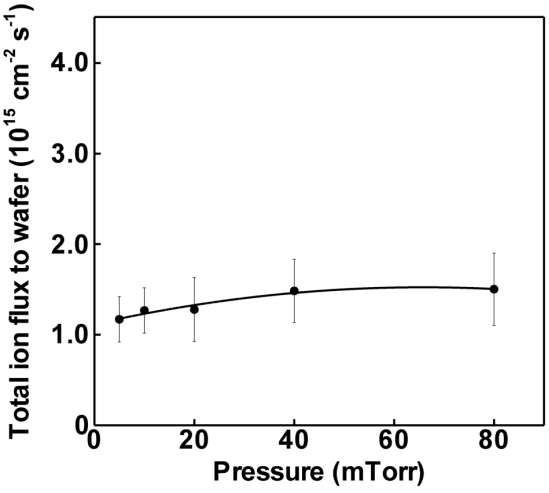

Figure 37. Calculated ion flux to the substrate as a function of pressure. The error bars are a measure for the uniformity of the flux from centre to edge of the substrate. The other operating conditions are the same as in **Figure 30.**

This is because, at higher pressure, the formation as well as the neutralization of the ions is increased due to more collisions, resulting in

a relatively small change of the total ion flux to the wafer. Indeed, at the very low-pressure range under study, if the pressure is increased, more species are present in the reactor and more will be ionized; hence the total ion density increases with pressure. This is illustrated in **Figure 38** showing the total ion density profiles at 5 and 80 *mTorr* (in a similar color scheme). At the same time, a higher pressure will result in more neutralization reactions. The maximum ion density is therefore less "smeared out" at higher pressure resulting in a rather small increase in ion flux to the substrate when increasing the pressure from 5 to 80 *mTorr*.

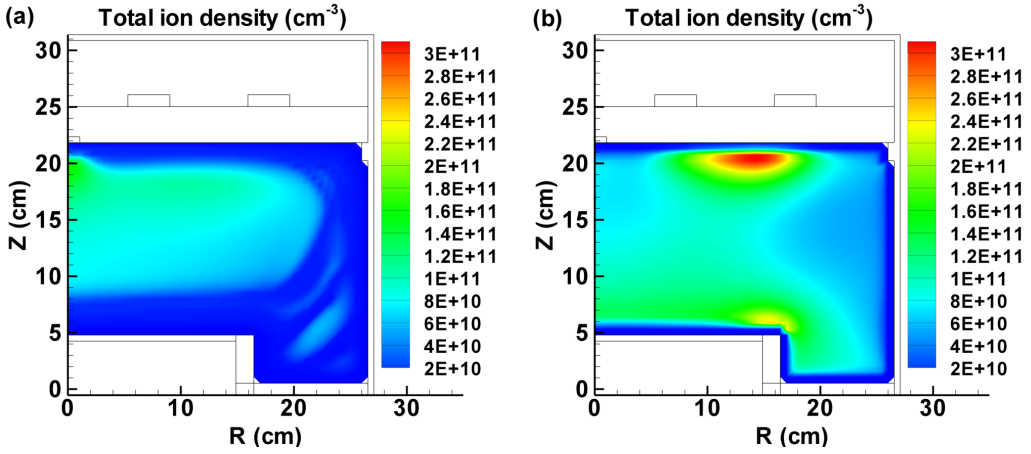

Figure 38. Calculated total ion density at 5 *mTorr* **(a)** and 80 *mTorr* **(b)**. The other operating conditions are the same as in **Figure 30**.

Moreover, the composition of the ion flux changes slightly with pressure. At higher pressure, the charge exchange reactions of Ar^+ and Cl^+ with Cl_2 to form Cl_2^+ are favored, resulting in a higher fractional flux of Cl_2^+ as plotted in **Figure 39**. For a gas mixture of 90 % Cl_2 and 10 % Ar, the total ion flux consists mainly of Cl_2^+ ions, from about 80 % at lower pressure (5 *mTorr*) to 90 % at 80 *mTorr*. This effect was also observed by Hoekstra *et al* [75], although more pronounced since these authors

studied a 70 % Ar and 30 % Cl_2 gas mixture.

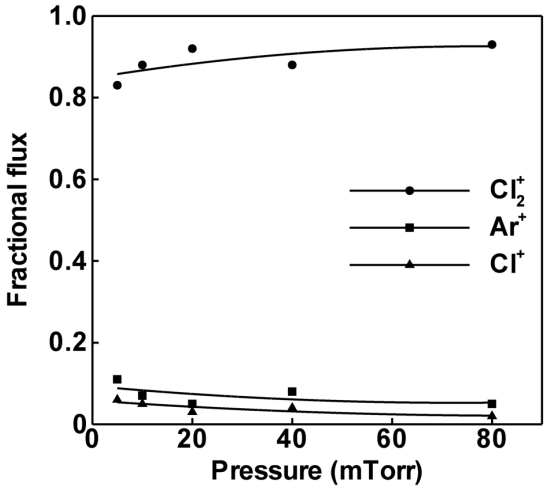

Figure 39. Calculated fractional fluxes of the Cl_2^+, Cl^+ and Ar^+ ions to the substrate. The other operating conditions are the same as in **Figure 30**.

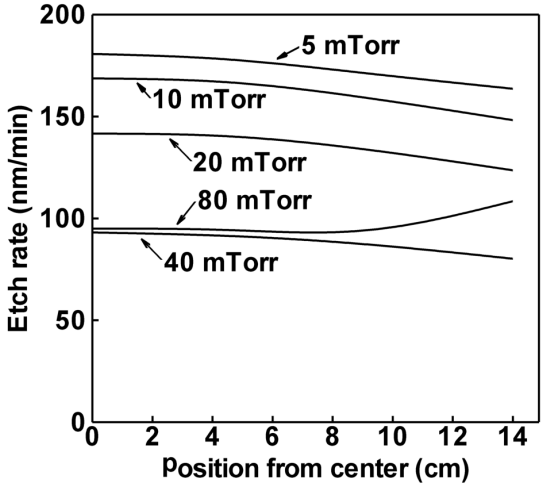

Figure 40. Measured etch rate as a function of position on the wafer at different pressure values. The other operating conditions are the same as in **Figure 30**.

Experimentally, it was found that the etch rate decreases at higher pressure, as plotted in **Figure 40**. This is because, at higher pressure, the mean energy of the ions bombarding the substrate is lower due to more collisions when accelerated towards the substrate. Subsequently, a lower ion energy results in less sputtering and a lower etch rate. Moreover, the angle distribution in which the ions hit the substrate is also broadened at higher pressure which results in a less anisotropic ion flux to the substrate. This effect is also discussed by Collison *et al* [190] for a N_2 plasma, where it was found that the electron temperature decreases with increasing pressure. The same effect was also observed by Sung-Mo *et al* [69] who experimentally investigated the dependence of the pressure on the etch rate and of MgO thin films with Ar/Cl_2 plasmas. They also reported that the etch rate decreases with increasing pressure. The calculated energy and angular distributions of the Ar^+ ions at 5 *mTorr*, 20 *mTorr* and 80 *mTorr* are plotted in **Figure 41**.

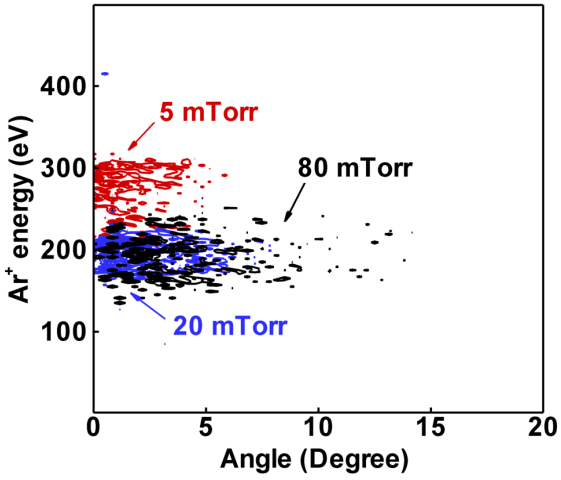

Figure 41. Calculated Ar^+ energy and angular distributions obtained at different pressure values. The other operating conditions are the same as in **Figure 30**.

The energy and angular distributions of the other ions were found to be very similar. However, the energy distribution of the Cl_2^+ ions is slightly narrower since the Cl_2^+ ion has a higher mass and therefore a longer transit time through the sheath. This effect will be discussed in more detail in section 5.5 on the effect of the substrate bias.
It is clear that at lower pressure, the mean value of the energy is significantly higher what explains the higher etch rate. The mean value of the angle in which the ions hit the wafer is also lower at lower pressure, resulting in a desired more anisotropic flux to the substrate.
The range of angles of incidence of the bombarding ions seems to be in reasonable agreement with the theoretical predictions of Hoekstra *et al* [75]. These authors observed for a 70/30 Ar/Cl_2 plasma at 10 *mTorr*, 500 *W* source power and 100 *V* rf bias amplitude that the average angle of incidence of Cl_2^+ ions was ≈ 8° and that the ion energy distribution slightly broadened with increasing pressure.
Comparing our calculated results with the measured etch rates, we can conclude that the etch rate of Si by an Ar/Cl_2 plasma is mainly dependent on the energy of the ions bombarding the substrate and seems not to be significantly affected by the radical flux. Although the radical flux is much higher than the ion flux, the actual chemical etching of Si (to form $SiCl_4$) is very slow. However, sputtering of $SiCl_x$ layers is much faster and the etch rate therefore is mainly dependent on the energy of the ions (i.e. sputter yield).

5.5 Effect of substrate bias

The bias voltage is created by the electrode underneath the wafer and controls the acceleration of the ions towards the substrate. By tuning the ion energy (i.e. also the sputter yield) the etch process can be controlled. Calculations were performed for the same operating conditions as

described in section 5.2.1, with the dc bias now varied from -100 *V* to -300 *V*. It was found that a variation of the substrate bias at these operating conditions has no significant effect on the bulk plasma characteristics. As a consequence, the radical flux to the substrate was found to be nearly constant for different values of the dc bias, as shown in **Figure 42(a)**. The increase of the total ion flux to the wafer with dc bias, however, is more pronounced with dc bias as illustrated in **Figure 42(b)**.

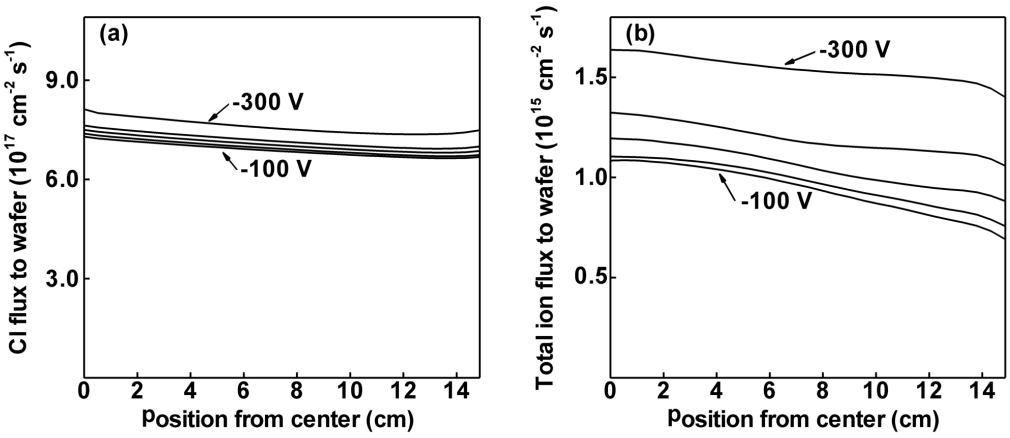

Figure 42. Calculated radical **(a)** and ion **(b)** fluxes as a function of position on the substrate at different values of the dc bias. The other operating conditions are the same as in **Figure 30**.

Furthermore, increasing the substrate bias has a distinct influence on the energy of the ions hitting the substrate as illustrated in **Figure 43**. Indeed, the energy (in *eV*) of the ions hitting the substrate is roughly in the same order as the dc bias (in *V*).

The bimodal character of the energy distributions is due to the fact that the transit time (i.e. the time of the ions travelling through the sheath before hitting the substrate) is shorter than one rf cycle. At 13.56 *MHz*, an rf cycle takes ≈ 74 *ns*. The transit time of the ions is typically ≤ 30 *ns*

which is shorter than the rf cycle due to a fairly thin sheath (≈ 0.06 *cm*). The latter is due to a relatively high plasma density. Hoekstra *et al* [75] found for a 70/30 Ar/Cl_2 plasma at 10 *mTorr*, 500 *W* source power and 100 *V* rf bias amplitude a sheath thickness of about 0.05 *cm*, which is in good agreement with our results. This means that the ions do not only feel the time averaged dc bias but also a time specific bias depending on the phase within the rf cycle when the ions enter the sheath. Therefore, the energy distributions have two maxima, which correspond to the highest and lowest values of the substrate rf bias amplitude. The sheath thickness is increased when the substrate bias becomes more negative. However, at the same time, the ions are more accelerated, which results in an overall decrease of the transit time in the sheath and hence an increasing width of the energy distribution [75]. Therefore, at larger substrate bias, the rf frequency should be increased if a smaller energy distribution width is desired.

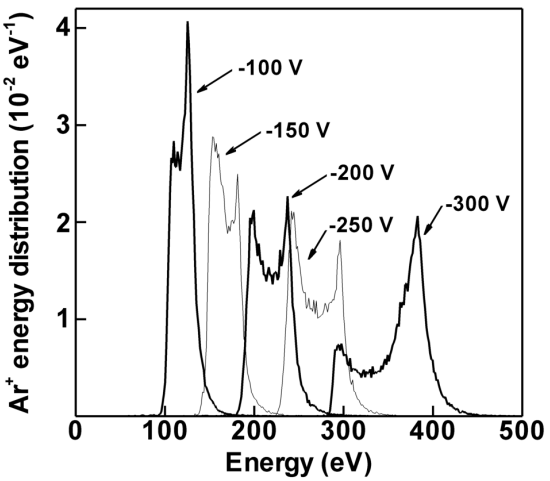

Figure 43. Calculated Ar^+ ion energy distributions at the wafer at different values of the substrate bias. The energy distributions of the Cl^+ and Cl_2^+ ions are comparable with the distributions of Ar^+ and are therefore not shown. However, the distribution of Cl_2^+ is slightly narrower since Cl_2^+ has a larger mass. The other operating conditions are the same as in **Figure 30**.

These results are in good correlation with observations made by Ventzek *et al* [62], who calculated an energy distribution of Ar^+ ions hitting the substrate ranging from 50 *eV* to 55 *eV* at a dc bias of also 50 - 55 *V* for an Ar plasma at 13.56 *MHz* operating frequency and 15 *mTorr* gas pressure with 500 *W* source power. Similarly, in reference [52] these authors found for a 85/12/3 $Ar/CF_4/O_2$ plasma at 15 *mTorr*, 75 *V* rf bias and 900 *W* source power, that the dc bias was -53 *V* and that the energy of the ions was calculated in the vicinity of 50-55 *eV*.
Finally, Hoekstra *et al* [75] found that the energy distributions of the Ar^+, Cl^+ and Cl_2^+ ions have minima and maxima of roughly 20 *eV* and 80 *eV* for a dc bias of -32 *V*, for a 70/30 Ar/Cl_2 plasma at 10 *mTorr*, 500 *W* source power and 100 *V* rf bias amplitude which is also in agreement with our calculated results.

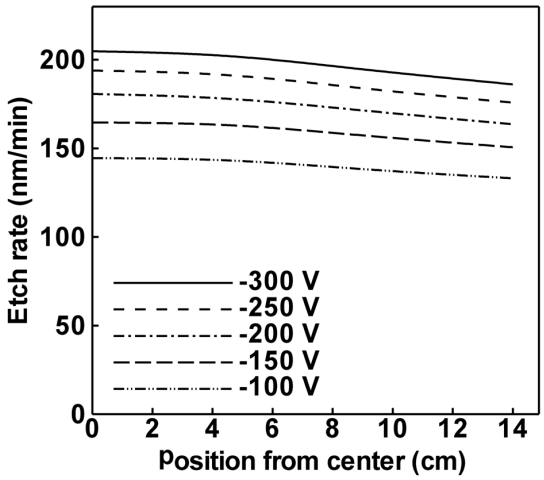

Figure 44. Measured etch rates at different values of the substrate bias. The uniformity is comparable to the uniformity of the ion fluxes to the substrate. The other operating conditions are the same as in **Figure 30**.

Experimentally it is found that the etch rate increases when the substrate bias becomes more negative, as is illustrated in **Figure 44**. The variation of the etch rate with dc bias, as well as the uniformity, are in good agreement with the calculated ion fluxes plotted in **Figure 42(b)**. This indicates that the etch rate is indeed strongly determined by the ions bombarding the wafer, rather than by the radicals accounting for chemical etching.

A similar effect was experimentally observed by Sung-Mo *et al* [69] who investigated the etch rate and selectivity of MgO thin films with Ar/Cl_2 plasmas at different substrate bias and also found that the etch rate increased with substrate bias, as expected.

5.6 Effect of source power

Where the substrate bias controls the ion energy, the source power will control the magnitude of the ion flux. Indeed, applying a higher power from the coil will result in the formation of stronger electromagnetic fields, in a larger acceleration of the electrons in the plasma, and subsequently in more dissociation and ionization processes.

Calculations were performed for the same operating conditions as in section 5.2.1, where the source power now is varied between 250 *W* and 1000 *W*. All calculated species densities (except for Cl* and Ar*) in the bulk plasma are plotted as a function of applied source power in **Figure 45**.

It is clear that the neutral species (Cl_2, Cl and Ar) decrease in density, whereas all ion species densities increase, when a higher source power is applied. This increasing trend of the ion densities is due to the fact that the average electron temperature is increased from roughly 3.5 *eV* to 4.2 *eV*, increasing the formation of ions by electron impact reactions. The Cl radical density decreases slightly due to the fact that at higher electron

temperature the direct ionization and excitation of Cl by electron impact reactions becomes slightly more important compared to the formation of Cl radicals from Cl_2 by electron impact dissociation. The drop in background gas densities is attributed to the increased loss by ionization and excitation and especially to the increased background gas temperature from roughly 600 *K* to 1800 *K*. It should be noted that the simulations are performed for a very low pressure of 5 *mTorr*. As expected, a higher pressure will lower the average gas temperature. For example, the gas temperature at 1200 *W* and 40 *mTorr* is in the order of 800 *K*.

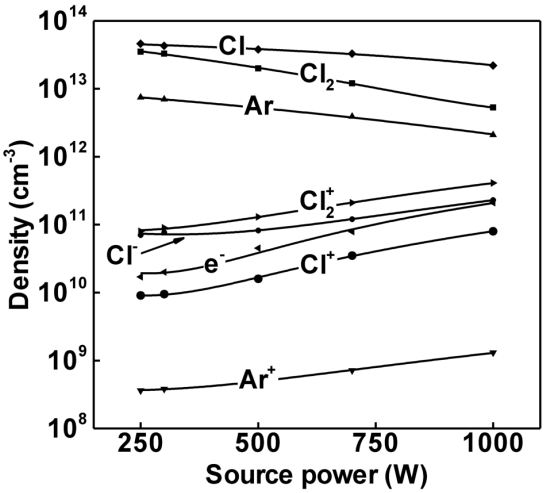

Figure 45. Calculated plasma species densities in the bulk plasma as a function of source power. The other operating conditions are the same as in **Figure 30**.

The fact that the electron and background gas temperature both increase with source power, is expected because there is more electric heating of the electrons and ions, and consequently, more energy transfer from energetic plasma species to the background gas.

Our results are in good agreement with results from Ventzek *et al* [52] who found for a 70/30 Ar/Cl_2 plasma, at 5 *mTorr* pressure and 80 *sccm*

that the peak electron density increases from 1.4×10^{10} cm^{-3} to 8.2×10^{11} cm^{-3} when source power is increased from 100 *W* to 2000 *W*.

Moreover, Efremov *et al* [71] have applied a 0-dimensional self-consistent model to investigate the effect of the source power on the electron density for a 20 % Cl_2 and 80 % Ar mixture at 2 *Pa*. They observed a similar effect where the electron density increases with applied source power, which is in agreement with our simulation results.

The increase in ion density in the bulk plasma results in an increase of the calculated ion fluxes to the substrate, while the radical flux appears not to change significantly with source power. This can be seen in **Figure 46(a)**.

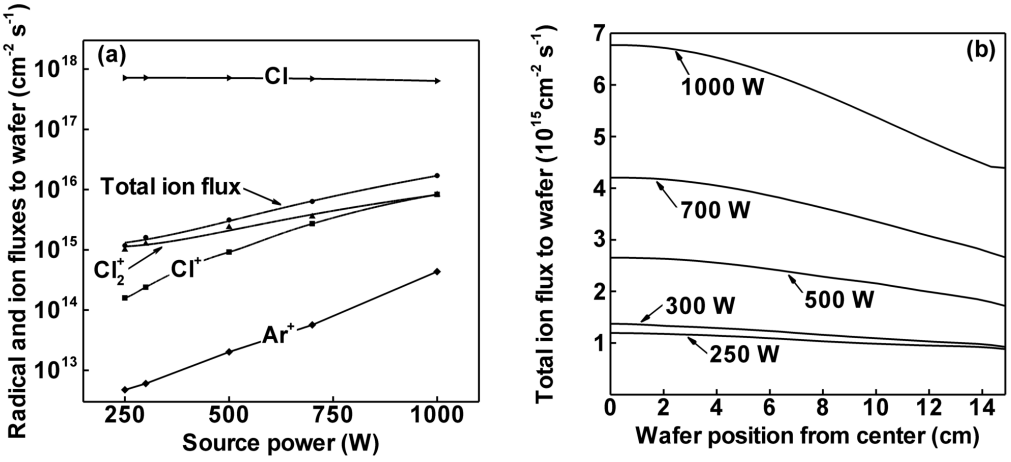

Figure 46. **(a)** Calculated ion and radical fluxes to the substrate as a function of source power. **(b)** Total ion fluxes as a function of position on the substrate at different values of the source power. The other operating conditions are the same as in **Figure 30**.

The Cl radical flux is, however, still much higher than the ion fluxes even at relatively high source power, as expected. Important to notice is that the total ion flux changes from roughly 80 % Cl_2^+ at 250 *W* to 50 % Cl_2^+ (with 50 % Cl^+ and Ar^+ < 1 %) at 1000 *W*. This is due to the fact that at

higher source power, and hence higher electron energy, the ionization of Cl radicals into Cl^+ by electron impact also becomes important compared to the ionization of Cl_2 into Cl_2^+ by electron impact. Subsequently, the Cl^+ ions are more easily formed at higher electron energy and source power.
In **Figure 46(b)**, the total ion fluxes are plotted as a function of position on the wafer, for different values of the source power. Again, it is clear that the ion fluxes increase with source power and that they are fairly uniform, although the uniformity decreases at higher power.
These results can be well compared with reported calculation results at higher source power. Indeed, Grapperhaus *et al* [61] found for a 50/50 Ar/Cl_2 discharge, with inlet flow rate of 50 *sccm*, 400 *W* source power, 100 *V* rf bias amplitude at 10 *mTorr*, an average total ion flux of 4×10^{16} cm^{-2} s^{-1}. This value is still somewhat higher than our results because their ICP reactor has a thinner dielectric plate, resulting in a higher power deposition.
Subramonium *et al* [74] investigated 30/70 Ar/Cl_2 pulsed plasmas at 30 *mTorr*, 300 *W* source power, 10 *kHz* pulse frequency, 20 *sccm* with no substrate bias and found that the average total ion flux to the substrate was roughly 6×10^{15} cm^{-2} s^{-1}. Hoekstra *et al* [62] obtained for a 70/30 Ar/Cl_2 plasma at 10 *mTorr*, 500 *W* source power and 100 *V* rf bias amplitude that the resulting dc bias was -32 *V* and the ion fluxes in the order of 10^{16} cm^{-2} s^{-1}. The radical flux was in the order of 10^{17} cm^{-2} s^{-1}. This is lower due to the fact that they used only 30 % Cl_2. Similarly, Ventzek *et al* [52] predicted for a 70/30 Ar/Cl_2 plasma, at 700 *W* source power, 5 *mTorr* pressure and 80 *sccm* that the ion fluxes as well as the radical flux were in the order of 10^{16} cm^{-2} s^{-1}. This is in reasonable agreement with our results since they applied 700 *W* source power, increasing the ion fluxes, and they used a 30 % Cl_2 gas, resulting in a lower radical flux than for a 90 % Cl_2 gas. Finally, it was also shown by Grapperhaus *et al* [61] that the magnitude of the ion flux is more strongly

dependent on the applied source power and to a less extent on the substrate bias. The calculated energy distributions of Ar^+ ions hitting the substrate at different values of source power are plotted in **Figure 47**. The Cl_2^+ and Cl^+ energy distributions are comparable with the distributions of Ar^+ and are therefore not shown. At higher source power, the plasma density is increased, resulting in the formation of a thinner sheath. As a consequence, the transit time is shorter, resulting in a broader energy distribution for the ions. This effect was also discussed by Hoekstra *et al* [75, 76]. In addition, also the plasma potential increases with power, resulting in a higher average energy of the ions arriving at the wafer as is also clear from **Figure 47**.

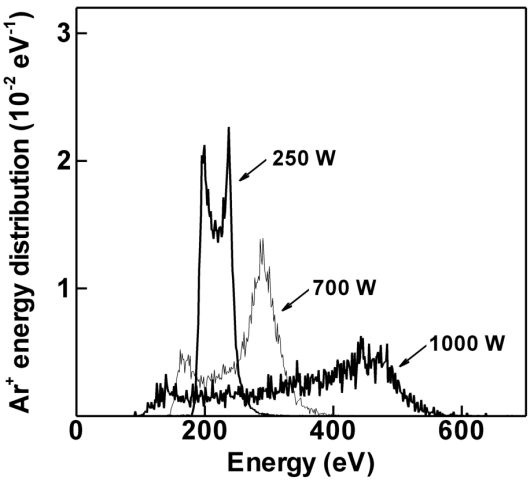

Figure 47. Calculated Ar^+ energy distributions at different values of source power. The other operating conditions are the same as in **Figure 30**.

Experimentally, it was found that the etch rate increases with source power, as is shown in **Figure 48**. As mentioned before, this is due to the fact that the ion flux to the substrate is higher at increased source power. Indeed, comparing the measured etch rates in **Figure 48** with the total ion fluxes in **Figure 46(b)** clearly illustrates that the trend in etch rates,

upon variation of the source power, is very similar to the trend in calculated ion fluxes as a function of source power. Also the uniformity of the etch processes can be well compared with the calculated ion fluxes. This suggests again that the etch process is mainly determined by the ion fluxes rather than by the Cl radical flux, at the operating conditions under study.

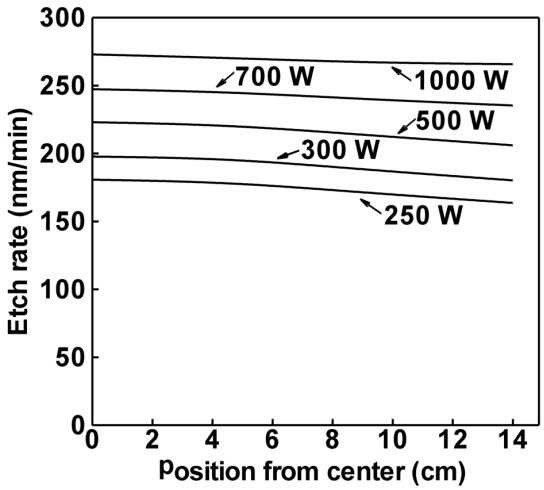

Figure 48. Measured etch rates at different values of source power. The other operating conditions are the same as described in **Figure 30**.

Collison *et al*[190] experimentally measured an etch rate of 250 *nm* min^{-1} for a pure Cl_2 inductively coupled plasma at 10 *mTorr* pressure and 800 *W* source power, which is in good agreement with our etch rate measurements.

Finally, the same trend, where the etch rate increases with source power, was also experimentally found for other substrates. Sung-Mo *et al* [69] observed an increasing etch rate of SiO_2 and MgO with source power for an Ar/Cl_2 plasma.

5.7 Conclusions

The effect of total gas pressure, substrate bias and source power on the bulk plasma characteristics, on ion and radical fluxes to the substrate, and on the experimentally obtained etch rates was studied for a 10 % Ar and 90 % Cl_2 ICP under the following operating conditions: 5 *mTorr* total gas pressure, 100 *sccm* gas flow rate, 250 *W* source power, -200 *V* dc bias at the substrate electrode and an operating frequency of 13.56 *MHz* applied to the coil and to the substrate electrode.
In general it can be concluded that, under the investigated operating conditions, the etch rate is more strongly affected by the energy and flux of the ions bombarding the substrate and in less extent by the magnitude of the radical flux, even though the radical flux is roughly 100 times higher than the total ion flux. This is due to the fact that the chemical etching by Cl is, in fact, relatively slow compared to the sputtering of the chlorinated Si surface.

5.7.1 Effect of pressure

In the low-pressure range under study (5 - 80 *mTorr*), if the chamber pressure is increased, more species are present in the reactor which results in a significant increase in neutrals, such as Cl which is considered important for chemical etching, as well as ions due to more ionization reactions. However, since the collision frequency is also higher at higher pressure, the total ion density tends to decrease faster towards the substrate due to more neutralization reactions. Therefore, an increased pressure will account for a significantly higher flux of Cl radicals but only a slightly increased ion flux towards the wafer.

Moreover, the composition of the ion flux changes with pressure. At the investigated pressure range from 5 *mTorr* to 80 *mTorr*, the fraction of Cl_2^+ is increased from 80 % to about 90 % due to a favoured charge exchange reaction from Cl^+ and Ar^+ to Cl_2^+.
Moreover, since the ions collide more at higher pressure, their average energy when bombarding the surface is lower. This eventually results in a smaller sputter yield and a lower etch rate at higher pressure, even if the ion and radical flux is higher.
In addition, the width of the angle distribution of the ions when hitting the substrate becomes larger at higher pressure, resulting in a less anisotropic flux which is not desired for etching high aspect ratio trenches with high profile control. Therefore, it can be concluded that lower pressures offer the advantage of a faster and more anisotropic etch process.
Finally, it should be noted that the lower gas residence time at lower pressure also offers the advantage of faster etch product removal out of the chamber, which will decrease undesired redeposition processes.

5.7.2 Effect of substrate bias

The main purpose of tuning the substrate bias is to control the energy of the ions bombarding the substrate. At increased bias, this results in an increase in the sputter yield and hence, the etch rate, which is observed numerically as well as experimentally. Moreover, the energy distribution of the ions arriving at the substrate becomes broader when the substrate bias is increased due to a smaller transit time of the ions through the sheath. Indeed, the sheath thickness is increased when the substrate bias becomes more negative. However, at the same time, the ions are more accelerated, which results in an overall decrease of the transit time in the sheath and hence a larger width of the energy distribution.

It can be concluded that increasing the substrate bias can improve the etch rate due to more sputtering; however, the energy distribution also widens which results in less control of the ion energy and a higher probability for damage. On the other hand, the energy distribution can also be narrowed by applying a higher operating frequency.

5.7.3 Effect of source power

At higher source power the gas and electron temperature increase as well as the total ion density resulting in an increase of ion flux to the substrate. So, by varying the source power, the ion density in the plasma and hence the ion flux towards the wafer can be controlled.
The composition of the ion flux changes drastically with source power under the studied operating conditions: from ≈ 80% Cl_2^+ at 250 *W* to 50% Cl_2^+ at 1000 *W* due to a more favored formation of Cl^+ compared to Cl_2^+.
Moreover, the energy distribution of the ions arriving at the substrate becomes broader at higher source power due to a thinner sheath. Indeed, because the plasma density is higher at higher power, the sheath thickness decreases and subsequently the transit time decreases as well.

Chapter 6

$Ar/Cl_2/O_2$ ICP: Effect of plasma behavior on the etch process

6.1 Introduction

In the previous chapter, the effects of process parameters such as gas pressure, substrate bias and source power on the bulk Ar/Cl_2 plasma characteristics were investigated. Indeed, by tuning these operating conditions, the bulk plasma properties can be controlled. Subsequently, by tuning the plasma behavior, the wafer surface process can be controlled for a desired processing step (which is ultimately the goal), whether it is etching or deposition.

As the previous chapter describes the results obtained in an earlier phase of this PhD work, only Ar/Cl_2 mixtures were investigated. However, in reality usually a small fraction of O_2 is added to the gas mixture. Indeed, as mentioned in Chapter 4, $Ar/Cl_2/O_2$ plasmas are commonly applied for the selective etching of Si in STI. Chlorine is known to react with a Si surface to form $SiCl_4$, which is a volatile etch product. Since

This chapter is based on the following publication: S Tinck, W Boullart and A Bogaerts, Investigation of etching and deposition processes of $Cl_2/O_2/Ar$ inductively coupled plasmas on silicon by means of plasma–surface simulations and experiments, *J. Phys. D: Appl. Phys.* 42 (2009) 095204

this chemical process is isotropic, a small fraction of O_2 is typically added to the gas mixture to protect the sidewalls from lateral chemical etching in order to increase the anisotropy. Indeed, oxygen will react with silicon to form a SiO_x layer which can not be chemically etched by chlorine. In this way, the sidewalls of the trenches are protected from further chemical etching while the bottom is still etched properly due to the strongly directional sputtering of the SiO_x layer by the plasma ions.
Therefore, in this chapter, simulation results are presented for $Ar/Cl_2/O_2$ plasmas where special attention is paid to which plasma properties have a profound effect on the etch rate rather than investigating the bulk plasma itself. In the first section the main plasma properties that control the etch process are discussed. These are the magnitudes of the fluxes of the different plasma species towards the wafer, the energy of the species bombarding the surface and the angle at which they arrive. The latter is especially important for anisotropic etching of trenches.
In addition, the effects of oxygen gas fraction on the resulting etch rate are investigated numerically as well as experimentally in the succeeding section. Finally, the ratio of ion to oxygen atom flux can have a large influence on the resulting etch process. Therefore, the effect of pressure on the etch rate is investigated numerically and experimentally as well in this chapter.

6.2 Experimental details

A series of 300 *mm* blanket *poly*-Si wafers was etched in a Transformer Coupled Plasma (TCP) reactor (LAM Research 2300 Versys Kiyo) for 20 *s* after a stabilization step of 5 *s* to break through the native oxide on the wafer. Before the set of wafers was etched, the quartz top window was heated for 30 *min* to a stable temperature (≈ 100 *°C*) to make sure the

oxygen flux from the dielectric window is stable during the processing of the different wafers. The wafers consisted of 200 *nm poly*-Si on a 100 *nm* SiO_2 layer. The thickness of the wafers was measured with spectroscopic ellipsometry (KLA-Tencor SCD100) at different points on a straight line across the wafer before and after the etch process to calculate the etch rate.
The blanket *poly*-Si wafers were etched under the following operating conditions: 100/0-14/12 *sccm* $Cl_2/O_2/Ar$ gas flow rate, 20 - 80 *mTorr* total gas pressure, 500 - 1200 *W* top electrode power, -100 to -500 *V* dc bias at the substrate electrode and an operating frequency of 13.56 *MHz* applied to the coil and to the substrate electrode.

6.3 General simulation results

Calculations were performed for a $Cl_2/O_2/Ar$ plasma under the same operating conditions as mentioned above in the experimental part.
The etch process is directly dependent on the fluxes of the different plasma species arriving at the wafer as well as on the energies and angles of these species when bombarding the surface.

6.3.1 Fluxes towards the wafer surface

Figure 49 shows the calculated fluxes of the plasma species as a function of position on the wafer. The neutral gas species Cl, Cl_2, Ar, O_2 and O have the largest fluxes to the substrate because of their highest densities in the plasma. The ion fluxes are roughly 1000 times lower than the other (neutral) fluxes, which is typical for an ICP reactor. The fluxes of the excited species are not shown because their densities (and fluxes) are much smaller (roughly 1000 times) than their ground state

equivalents and are, therefore, neglected in the surface simulations.
At first sight it is clear that the fluxes are quite uniform, which is desired for a uniform etch rate on the complete surface of the wafer. However, it should be noted that the plot has a logarithmic scale so that the radial variations are not so clearly visible. Indeed, although quite uniform, the total ion flux reaches a maximum at the edge of the wafer, while the O flux is at maximum in the centre of the wafer. Depending on the amount of oxygen present in the gas mixture, this can lead to a significant change in etch rate and bad uniformity as will be shown in the following section 6.4 on the effect of oxygen gas flow and which will also be discussed in more detail in the following chapter.

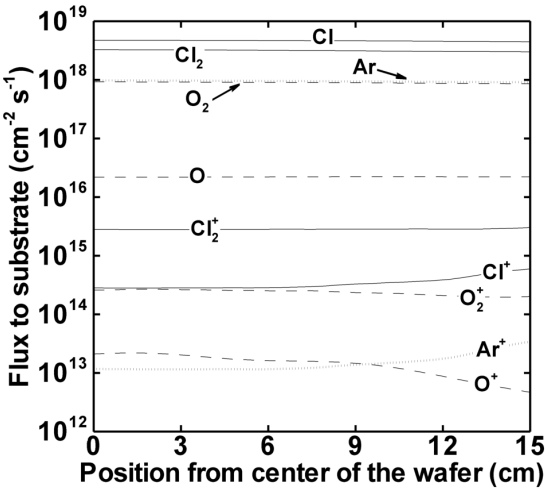

Figure 49. Calculated fluxes of the different plasma species arriving at the substrate surface as a function of position on the wafer. The operating conditions are: 100/12/14 *sccm* $Cl_2/Ar/O_2$ gas flow, 40 *mTorr* total gas pressure, 1000 *W* top electrode power, -500 *V* dc bias at the substrate electrode and an operating frequency of 13.56 *MHz* applied to the top and to the substrate electrode.

6.3.2 Angular distributions of ions and neutrals

Most ions arrive at the wafer perpendicular to the wafer surface because they are accelerated to the substrate by the electric field generated by the substrate electrode. The calculated angular distributions of the ions and the neutrals bombarding the substrate can be seen in **Figure 50**. The angle distribution of the ions is much narrower because the neutrals can arrive at the substrate surface from any given direction while the ions are accelerated to the wafer by the electric field.

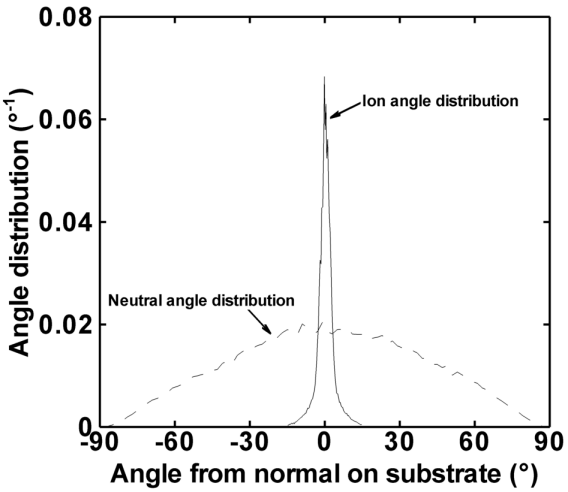

Figure 50. Calculated angular distributions of the ions and the neutral species, averaged over all different ions or neutrals, respectively, when arriving at the substrate under the same operating conditions as in **Figure 49**.

6.3.3 Energy distributions of ions and neutrals

Figure 51 shows the calculated energy distributions of the ions and the neutrals arriving at the substrate. The ion energy distribution has two

maxima (bimodal character) due to the radio frequent potential of the substrate electrode for creating the dc bias of -500 *V* [85], as was already discussed in the previous chapter. The neutral species are not accelerated by the electric field and, therefore, they are characterized by a Maxwellian distribution at low average energy.

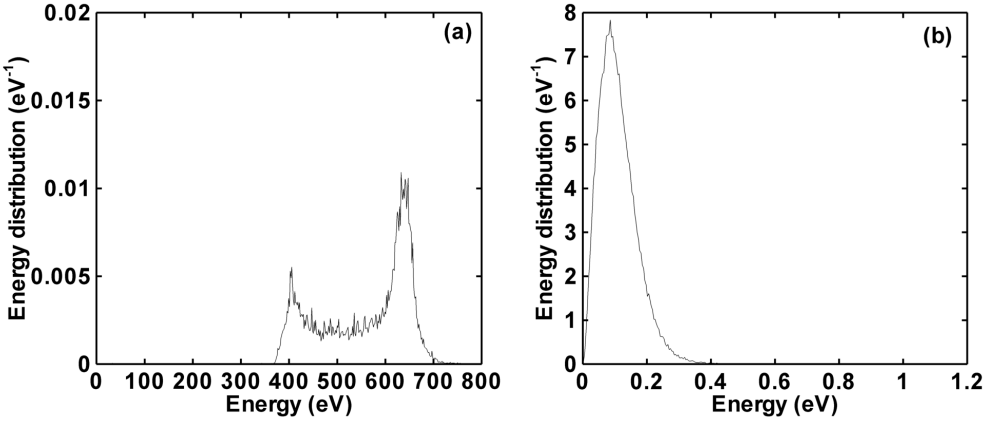

Figure 51. Calculated energy distributions of the ions **(a)** and the neutral species **(b)** when arriving at the substrate for the same operating conditions as in **Figure 49**.

6.4 Effect of O_2 gas flow on the etch process

The fluxes of the different plasma species to the substrate as a function of O_2 gas flow are plotted in **Figure 52**. When the oxygen flow is increased, the densities and hence fluxes of the various oxygen species are higher as expected. This, in turn, will result in more oxidation of the *poly*-Si.

As mentioned before, a small fraction of O_2 is added to the Ar/Cl_2 mixture to protect the Si sidewalls from lateral etching by forming an oxide layer which prevents chemical etching by chlorine neutrals. However, if the oxygen gas fraction is too high, oxidation is dominant over etching and the etch rate drops significantly.

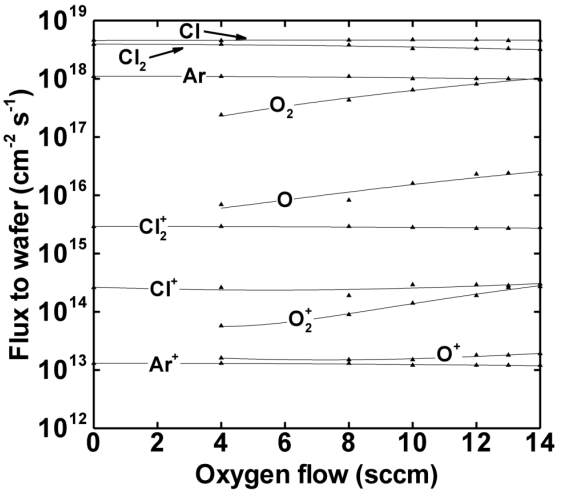

Figure 52. Calculated fluxes of the most relevant plasma species to the substrate at the central location on the wafer as a function of the O_2 fraction. The other operating conditions are the same as in **Figure 49**.

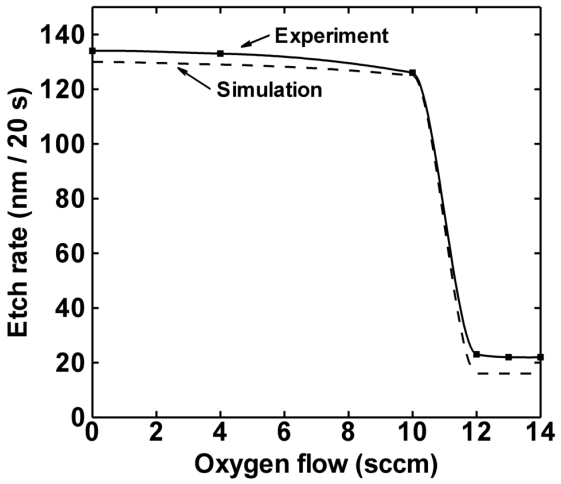

Figure 53. Experimentally measured (solid line) and calculated (dashed line) etch rate as a function of the O_2 gas flow, at the central location of the wafer. The operating conditions are the same as in **Figure 49**.

Indeed, as can be seen in **Figure 53**, the calculated etch rate, at the central location on the wafer, decreases abruptly between 10 *sccm* and 12 *sccm* O_2 flow under these operating conditions. Moreover, at 12 *sccm* O_2 flow or higher, the formation of oxygen "islands" on *poly*-Si becomes dominant.

It is interesting to see that, while the oxygen flux from the plasma is changing only slightly as a function of oxygen fraction, the etch rate abruptly drops to a very low value, which is found in the simulations as well as experimentally. This sudden decrease in etch rate, also referred to as the "etch stop phenomenon" will be investigated in more detail in the following chapter.

Moreover, the formation of this etch-blocking oxide layer occurs first in the centre of the wafer rather than at the border. **Figure 54** shows the measured etch rate at different points on a line across the wafer at different oxygen fractions under the same operating conditions as in **Figure 49**.

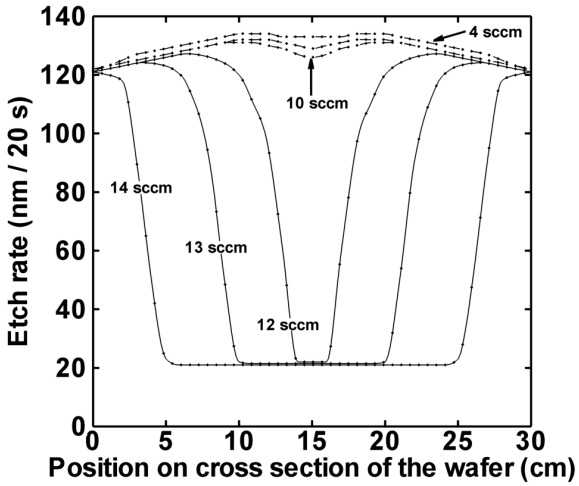

Figure 54. Experimentally measured etch rates at different positions on a cross section of the substrate for different values of the oxygen gas flow at 40 *mTorr*. The other operating conditions are the same as in **Figure 49**.

At low oxygen fraction (4 - 10 *sccm*; dashed lines) the average etch rate is ≈ 130 *nm* per 20 *s* and fairly uniform across the wafer. However, at an oxygen flow of 12 *sccm*, the etch rate suddenly drops significantly in the centre of the wafer. At even higher oxygen fractions, the central area where the etch rate is very low, becomes wider. Although fluxes are fairly uniform across the wafer, the oxygen flux still has a maximum at the centre of the wafer, while the ion flux has a maximum at the edge of the wafer. Indeed, the maximum ion density follows the shape of the coil and hence has a toroidal shape. The maximum ion density is therefore located straight above the edge of the wafer instead of the centre. These slight differences in uniformity of the O and ion flux will result in a passivation layer preferentially formed in the centre of the wafer rather than on the edge. Again, this will be discussed in more detail in the following chapter.

6.5 Effect of pressure on the etch process

The fluxes of the various plasma species to the *poly*-Si wafer as a function of pressure are shown in **Figure 55**. Of course, densities of gas species are higher in the reactor chamber when pressure is increased and, therefore, also the neutral gas species fluxes to the substrate as expected. However, the flux of the oxygen atoms decreases slightly due to the fact that recombination reactions are favored at higher pressure. Indeed, O atoms are mostly formed by electron impact dissociation of O_2, which occurs mostly in the upper part of the reactor underneath the coil where the electron density is highest. When moving downward in the reactor, O is lost more rapidly at higher pressure due to more recombination reactions to form O_2 or ClO. The total flux of oxygen containing species still increases with pressure as expected.

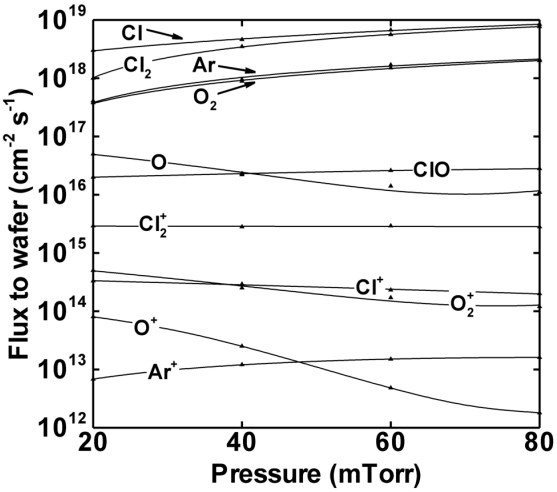

Figure 55. Calculated fluxes of the different plasma species to the substrate at the central location on the wafer as a function of pressure. The other operating conditions are the same as in **Figure 49**.

It should be noted that this effect is not true for atomic chlorine due to the fact that the Cl-Cl bond can be broken much more easily. Therefore, dissociation of Cl_2 is much more pronounced compared to oxygen, making the Cl radical density increase with pressure as expected. As discussed before in the previous chapter, the total ion density (and hence flux) varies only slightly with pressure.

The experimentally measured and calculated etch rates at the central location of the wafer are plotted as a function of pressure in **Figure 56**. The total oxygen-containing flux increases significantly at higher pressure as was illustrated in **Figure 55**, resulting in a more significant formation of an etch-blocking oxide layer. At the same time, the ion flux is practically constant as a function of pressure. These two effects result in the fact that the etch rate decreases significantly when pressure is increased.

Similar to the case when the O_2 gas fraction was varied, the formation of this etch-blocking oxide layer occurs first in the centre of the wafer as is

clear from **Figure 57**, showing the measured etch rate at different points on a line across the wafer at different pressures.

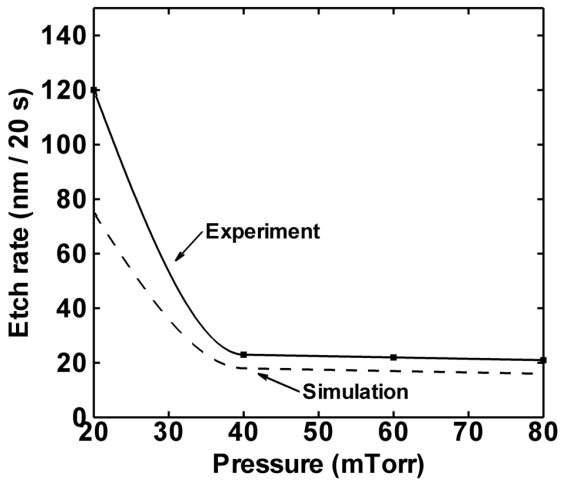

Figure 56. Experimentally measured (solid line) and calculated (dashed line) etch rate as a function of the gas pressure, at the central position on the wafer. The operating conditions are the same as in **Figure 49**.

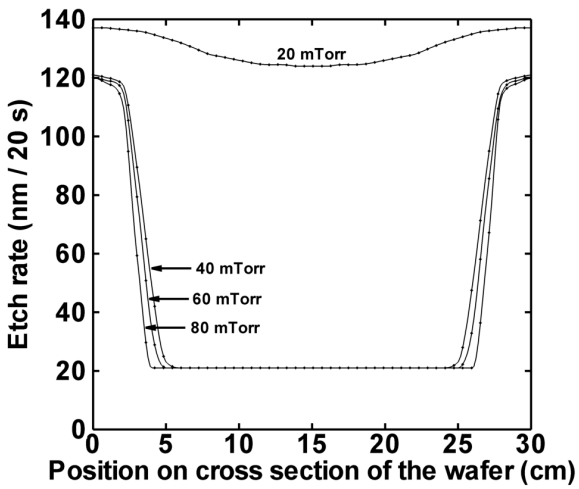

Figure 57. Experimentally measured etch rates at different positions on a cross section of the substrate for different chamber pressures at 14 *sccm* O_2. The other operating conditions are the same as in **Figure 49**.

Again, this is due to slight differences in uniformity of the O and ion fluxes to the wafer which result in the formation of a passivation layer rather in the centre of the wafer than on the edge.

6.6 Conclusions

The etching of Si with $Cl_2/O_2/Ar$ inductively coupled plasmas is investigated numerically and experimentally under the following operating conditions: 100/0-14/12 *sccm* $Cl_2/O_2/Ar$ gas flow, 20 - 80 *mTorr* total gas pressure, 1000 *W* power deposition, -500 *V* dc bias at the substrate electrode and an operating frequency of 13.56 *MHz* applied to the top electrode and to the substrate electrode.
It is found that, under the mentioned operating conditions, the etch rate drops abruptly at ≈ 11 *sccm* O_2 (at 40 *mTorr*). This is due to the fact that the oxygen species concentration is sufficiently high to form etch-blocking passivation layers. The same effect was found for increasing the total gas pressure. Indeed, at higher pressure, the O_2 flux increases, while the ion fluxes are more or less constant, resulting in a reduced etch rate. It was found that, under the mentioned operating conditions, the etch rate drops significantly at a pressure of 20 *mTorr* (at 14 *sccm* O_2). Therefore, it can be concluded that, in order to perform a highly uniform etch process of a *poly*-Si wafer with $Cl_2/O_2/Ar$ plasmas, it is recommended that the pressure and oxygen gas flow is kept low enough to avoid the formation of undesired etch-blocking passivation layers.
This so-called “etch stop phenomenon” will be discussed and explained in more detail in the next chapter.

Chapter 7

The etch stop phenomenon

7.1 Introduction

As mentioned earlier, $Ar/Cl_2/O_2$ plasmas are commonly applied for the selective etching of silicon in STI. Indeed, a small fraction of O_2 is added to the gas mixture to protect the sidewalls from lateral chemical etching. However, if the O_2 fraction exceeds a certain value, the etch rate will be drastically reduced due to more oxidation and less chlorination of the Si as discussed in the previous chapter.

Since SiO_2 can not be etched chemically by chlorine, the etch rate drops significantly, stopping the etching process completely. This phenomenon is therefore often referred to as "etch stop" [192] and is investigated in more detail in this chapter.

The etch stop problem originated as a reproducibility problem. It was found that, during the STI etching of several wafers after each other, the etch rate dropped significantly after a few wafers even if the operating conditions were kept the same. It was concluded by Shamiryan *et al* [192] that the gradual heating of the top dielectric window was the origin of the

---

This chapter is based on the following publication: S Tinck, D Shamiryan and A Bogaerts, Simultaneous etching and deposition processes during the etching of silicon with a $Cl_2/O_2/Ar$ inductively coupled plasma, *Plasma Process. Polym.* 8 (2011) 490-99

problem. When the top dielectric window gradually heats up during the etch experiments, evaporation of (previously deposited) low-volatile etch products from this window (due to sputtering) is enhanced. At the same time, the wafer is efficiently cooled down to 60 *°C* from the bottom, resulting in an effective 70 - 80 *°C* at the upper surface of the substrate during the etch experiments. Subsequently, the non-volatile (or low-volatile) etch products will more likely redeposit on the wafer instead of on the dielectric window if the temperature of the latter is higher.
In the following section, the mechanism of the formation (and growth) of this etch stop layer will be studied in detail by varying the oxygen fraction in the gas mixture, by means of experiments and modeling. Indeed, by varying the O_2 content in the plasma in a controlled way while keeping the temperature of the dielectric window controlled, we can investigate different regimes such as successful etching of silicon, formation of a rough surface and growth of an etch stop oxide layer.

7.2 Experimental details

To investigate the etch stop phenomenon, experiments were performed in a Lam Research 2300 Versys Kiyo 300 *mm* wafer reactor with a planar coil on top of the chamber. However, the quartz dielectric window was replaced by a ceramic material of which the temperature can be controlled. This is different from the experimental results discussed in the previous chapter where the dielectric window temperature could not be controlled yet and was heated deliberately to a stable temperature of 100 *°C*.
To increase the uniformity and reproducibility of the etching processes, the chamber walls were coated with a $SiCl_xO_y$ layer before each etching experiment. Indeed, wall loss of Cl (mostly to form Cl_2) is much lower on this coating compared to the clean reactor as will be illustrated in the

next chapter, increasing the uniformity of the Cl density in the plasma and hence the uniformity of the etch process. Moreover, by introducing a new coating before each new etch experiment, process control and reproducibility are increased in general, which will also be discussed in more detail in the following chapter.

The wafers consisted of 200 *nm poly*-Si on a 100 *nm* SiO_2 layer. The thickness of the layers was measured with an ellipsometer (KLA-Tencor F5) at different points on a straight line across the wafer before and after the etch process to calculate the etch rate or the deposition rate.

The blanket *poly*-Si wafers were etched under the following operating conditions: 40 *mTorr* total gas pressure, 600 *W* coil power, -500 *V* dc bias on the substrate, 13.56 *MHz* applied separately to both the coil and the substrate, 300 *K* gas temperature, 60 *°C* window, walls and wafer temperature, 100 *sccm* Cl_2, 12 *sccm* Ar and a varying flow of O_2 between 0 and 100 *sccm*. Also the etch time was varied to a maximum of 60 *s*.

It should be noted that these operating conditions are slightly different from those applied in Chapter 6. Indeed, all operating conditions are the same except for the power and the top window temperature. In the previous chapter, 1000 *W* power was applied while only 600 *W* in this chapter. Also, the top dielectric window temperature was heated to a stable 100 *°C* in Chapter 6, while in this chapter the window temperature is controlled at 60 *°C*.

7.3 Etch and deposition processes as a function of O_2 flow

The etch stop phenomenon is illustrated in **Figure 58**, where the measured and calculated etch rates at the center of the wafer are plotted as a function of O_2 flow. It should be noted that this plot is fairly similar

to **Figure 53** from Chapter 6. However, compared to **Figure 53**, the etch rate now is slightly lower (at low oxygen content) due to the lower power applied in this chapter.

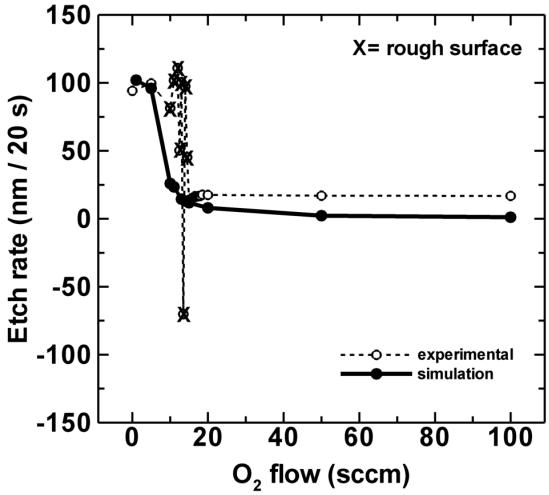

Figure 58. Measured and calculated etch rates at the center of the wafer as a function of oxygen flow.

At low O_2 flow (from 0 to about 10 *sccm*), *poly*-Si is being etched successfully by chlorine at a rate of about 300 *nm* min^{-1}. At very low oxygen content (i.e. less than 10 *sccm*) the isotropic chemical etching of *poly*-Si by chlorine neutrals creates undercutting effects, as seen in **Figure 59(a)**, which is a result obtained from the Monte Carlo profile model (FPMCS; section 3.4.8). When the oxygen fraction is increased to 12 *sccm*, a protective oxide layer is formed on the sidewalls to increase the anisotropy, as illustrated in **Figure 59(b)**. This profile looks like a nearly ideal etch profile. The chemical etching of the formed $SiCl_xO_y$ sidewall layer occurs at a very low rate and is negligible. This oxide layer can therefore only be removed by sputtering, hence the formation of a narrow and deep trench. When the oxygen flow is increased even more to values of 15 *sccm*, the thickness of the remaining *poly*-Si layer could not

be measured properly by the ellipsometer, hence the bouncing data points in the experimental result of **Figure 58**. This occurs when the remaining layer after the etch process is rough, not allowing a well-resolved ellipsometry measurement. The formation of a rough layer is most probably due to a balanced competition between etching and redeposition of non-volatile etch products. Indeed, the formation of a rough layer was also predicted by the model as shown in **Figure 59(c)**.

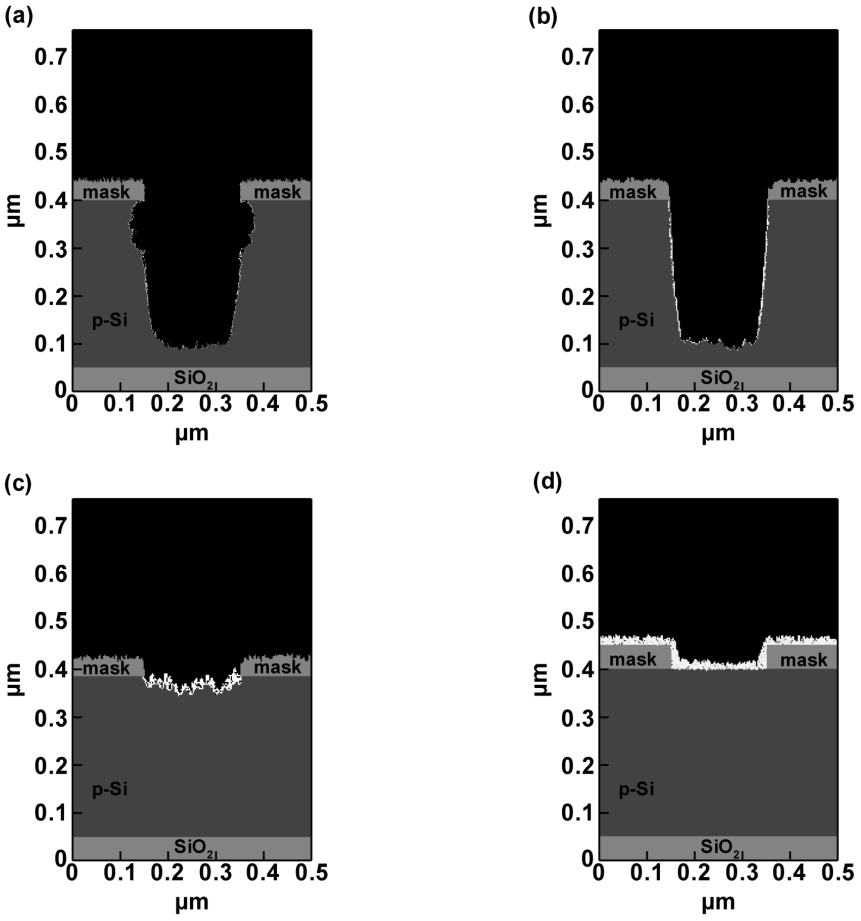

Figure 59. Calculated etch profiles for 1 *min* of etching at increasing oxygen fraction, i.e. 5 *sccm* **(a)**, 12 *sccm* **(b)**, 14 *sccm* **(c)** and 20 *sccm* **(d)**. The white thin layer in figures **(b-d)** represents the SiO_2 layer.

Finally, when the oxygen fraction is above 20 *sccm*, oxidation of the *poly*-Si is dominant, reducing the etch rate to a value close to zero, as is obvious from **Figure 58**. Indeed, no *poly*-Si is etched and, in addition, non-volatile products deposit, so an oxide layer is actually growing, as illustrated in **Figure 59(d)**.

In addition to the simulated etch profiles that illustrate the different etch regimes, **Figure 60** shows two SEM pictures where the transition of normal etching to roughness, and eventually to full etch stop, is visible.

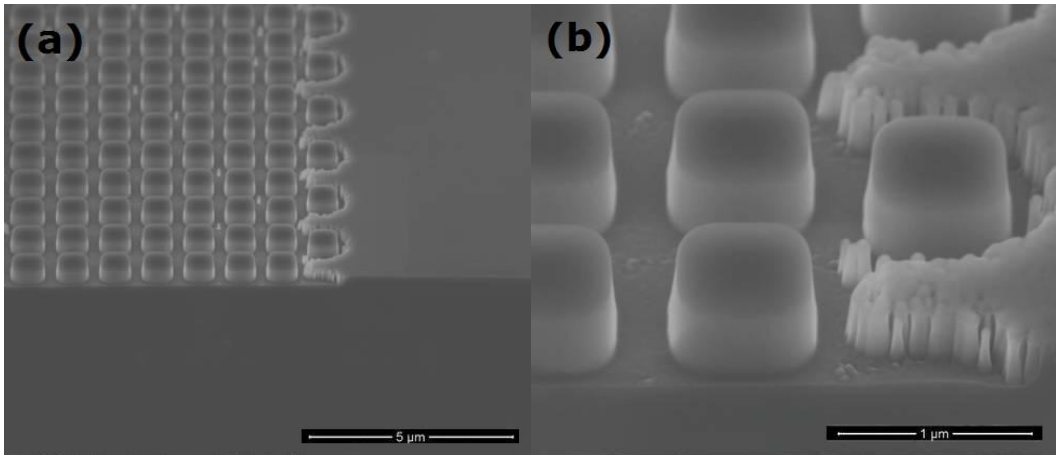

Figure 60. **(a)** SEM picture of a patterned wafer, illustrating the transition from normal etching (left), to a rough layer (middle) and eventually to full etch stop (right). The black bar represents 5 *µm*. **(b)** Close-up of the rough transition layer. The black bar represents 1 *µm*.

Although most experiments were performed on blanket silicon wafers, we used a patterned wafer to clearly see the transition when taking SEM pictures. In **Figure 60(a)**, the left side shows a normal etching regime, clearly visible due to the patterning. In the middle, a small roughness layer is visible, and eventually a full etch stop is observed at the right side of the figure. **Figure 60(b)** is a close up of the rough transition layer. This layer is smaller in size compared to the roughness on the blanket Si wafers because the actual area of etching is decreased due to the

patterning. The region where a rough layer is formed has indeed a very low total etch rate, and a rough surface comparable to the simulation result.

The reason why there is redeposition of non-volatile etched species (**Figure 59(d)**) is because the formation of this etch-blocking SiO_2 layer occurs first in the center of the wafer, while simultaneously, *poly*-Si is still etched at the edge of the wafer (as is illustrated in **Figure 62** below). This is probably attributed to three effects: First, in this particular reactor geometry, the gas nozzle is located in the center of the top window right above the center of the wafer (see **Figure 61** below). In order to maintain the (ultra) high vacuum in the chamber, the nozzle size is usually very small, like a needle. Therefore, to obtain the desired overall gas flow of more than 100 *sccm*, the gas must be injected through the nozzle at very high speeds. For this reason, the jet-like gas flow will directly arrive at the center of the wafer, creating a higher flow of neutral oxygen in this central area. Second, the maximum ion density is not found in the center of the chamber but the density profile is characterized by a torus shape following the geometry of the coil. This results in a slightly higher ion flux and hence a higher sputter rate at the edge of the wafer, reducing the probability for formation of an oxide layer. This is illustrated in **Figure 61(a)** where the calculated density profile and flux lines for the ions are shown. For the sake of simplicity, the sum of all ions present in the plasma is presented. Third, atomic oxygen has a much higher affinity to oxidize Si than O_2 [151], and since O will stick to the walls and recombine to O_2, the density of atomic oxygen is slightly higher in the center of the chamber, allowing for a higher flux of O to the center of the wafer and hence a higher oxidation rate in the center of the wafer. This is illustrated in **Figure 61(b)** where the density profile of atomic oxygen is presented, as well as the flux lines. Indeed, all three effects increase the probability for the formation of an etch stop layer in

the center of the wafer rather than at the edge.

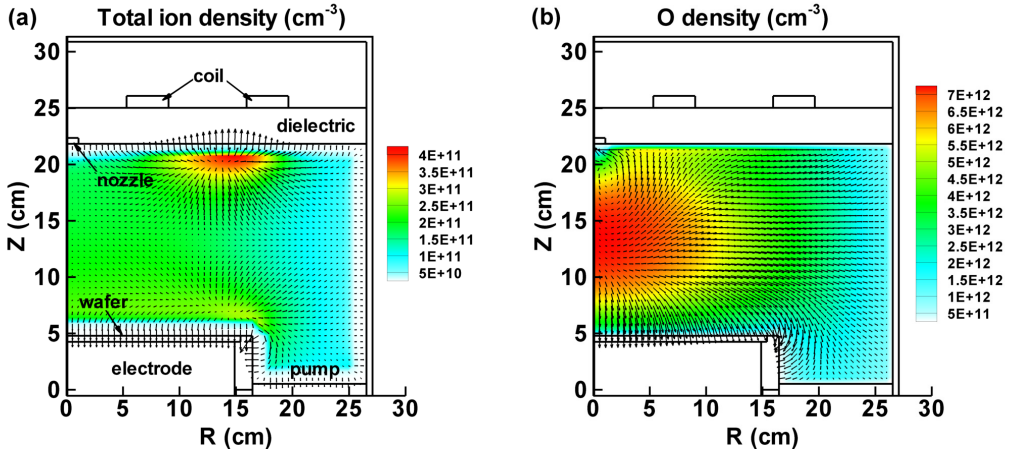

Figure 61. Calculated density profiles and corresponding flux lines for the (sum of all) ions **(a)** and for atomic oxygen **(b)** at conditions mentioned in section 7.2.

The formation of an etch-stopping layer in the center of the wafer is clearly visible from the experimental results presented in **Figure 62(a)**. In this plot, the etch rates on a straight line across the wafer are shown, for different oxygen flows. From this figure it can be concluded that, at 10 *sccm* of O_2, there is no formation of an oxygen island and Si is being etched successfully at a rate of ca. 300 *nm min*$^{-1}$. However, at 12 *sccm* O_2, there is a minor local decrease in the etch rate in the center of the wafer, due to the deposition of a small SiO_2-containing layer. This can be deduced from **Figure 62(b)** where the thickness of the deposited oxide layer is plotted for exactly the same conditions. Furthermore, at 15 *sccm* O_2, a significant SiO_2 island is formed of about 13 *nm* in thickness (after 20 *s*), blocking the etching of the *poly*-Si almost completely.

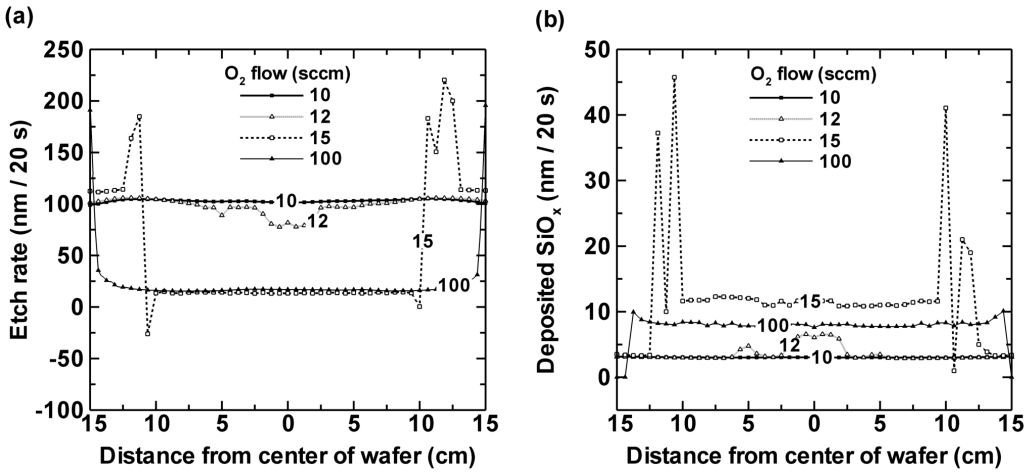

Figure 62. Experimentally measured *poly*-Si etch rates **(a)** and oxide layer growth rates **(b)** on a straight line across the wafer, at different oxygen flows.

The formation of this etch-stopping oxide layer occurs when the deposition rate of non-volatile etch products is higher than the sputter rate, resulting in the actual growth of a $SiCl_xO_y$ containing layer, which has a composition close to SiO_2, as will be discussed later in section 7.6.
Indeed, the growth of this layer is clearly dependent on the redeposition rate of etch products, as can be seen in **Figure 62(b)** when comparing the film thickness at 15 *sccm* to the thickness at 100 *sccm*. At 15 *sccm*, the thickness is about 13 *nm* after 20 *s*, compared to only 10 *nm* at 100 *sccm* O_2. This is due to the fact that at 15 *sccm* O_2, there is still *poly*-Si being etched at the edge of the wafer (see **Figure 62(a)**) and therefore, there is a source of non-volatile etch products that can redeposit on the oxide island. On the other hand, at 100 *sccm* O_2, the complete wafer is oxidized, and almost no *poly*-Si can be etched anymore (see **Figure 62(a)**), hence no etched species are launched in the plasma and the oxide layer therefore does not increase in thickness as rapidly.
Indeed, from the simulation results it can be concluded that the total etch product density decreases roughly two orders of magnitude going from 15 *sccm* O_2 flow to 100 *sccm*, as will be discussed later in section

7.5. It should be noted that only the non-volatile etch products will account for redeposition, whereas the most abundant etch products, i.e. $SiCl_2$, $SiCl_3$ and $SiCl_4$, are more volatile and have wall loss probabilities close to zero. So, in the case of 15 *sccm* O_2, both etching and deposition occur simultaneously on the wafer. At the edge, Si is being removed while in the center a $SiCl_xO_y$ layer is being grown (with a composition close to SiO_2) due to the redeposition of the etched species.

The measured size of the etch stop area, or more specifically defined as the fraction of the total wafer area, is plotted as a function of O_2 flow in **Figure 63**, together with the calculated wafer averaged SiO_2 surface fraction. In general, reasonable agreement is reached between the measured and calculated results. It should be noted that at low oxygen flow (1 - 10 *sccm*) there was no experimental evidence of an etch stop island in the center of the wafer (see dashed line). However, most likely there is already a fraction of the wafer surface oxidized (as can be seen from the calculated plot), but simply not with a significant thickness to be measured experimentally.

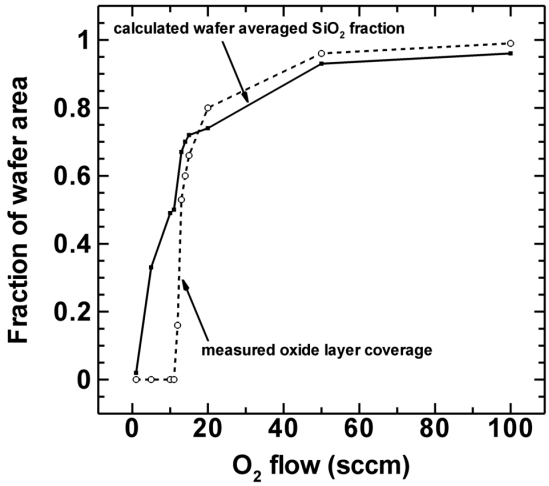

Figure 63. Measured etch stop island size, plotted as a fraction of the total wafer area (dashed line), and calculated SiO_2 wafer averaged surface coverage (solid line), as a function of oxygen flow.

7.4 Etch and deposition processes as a function of time

Another way to verify whether the growth of this oxide layer is indeed due to the redeposition of etched species, is to study the etch rate at different etch times for 15 *sccm* O_2. Indeed, in our experiments, wafers of 200 *nm poly*-Si on SiO_2 were utilized; hence we should expect that the growth of this oxide island stops after the etching of the 200 *nm poly*-Si. Indeed, this can be concluded from **Figures 64(a-d)**. In **Figure 64(a)** the removed *poly*-Si is plotted as a function of time at 15 *sccm* O_2. At the edge of the wafer, the amount of etched *poly*-Si increases linearly with time during the first 30 *s*, as expected. After about 30 *s*, the 200 *nm poly*-Si is completely removed; hence the etched amount of *poly*-Si remains constant after this time. In the center of the wafer, almost no *poly*-Si is etched due to the formation of the etch stop layer, as mentioned before.
Figure 64(b) presents the thickness of the etch stop oxide layer as a function of etch time in the center of the wafer. It is clear that this layer increases in thickness during the time that *poly*-Si is removed at the edge of the wafer. After 30 *s*, this layer is no longer growing, but it decreases in thickness due to sputtering. These results suggest that the growth of the oxide layer is indeed dependent on the redeposition rate of non-volatile etch products that are etched from the edge of the wafer.
Figures 64(c, d) show similar results, but for a complete cross section of the wafer, at 15 *sccm* O_2, for different etch times. It is obvious from **Figure 64(c)** that the etching of Si at the edge of the wafer increases linearly as a function of time until 30 *s*, and then remains constant, whereas virtually no etching is observed in the center. Likewise, in **Figure 64(d)** it is illustrated that the thickness of the deposited SiO_x

layer at the center increases as a function of time until 30 *s*, after which it starts to decrease again due to sputtering.

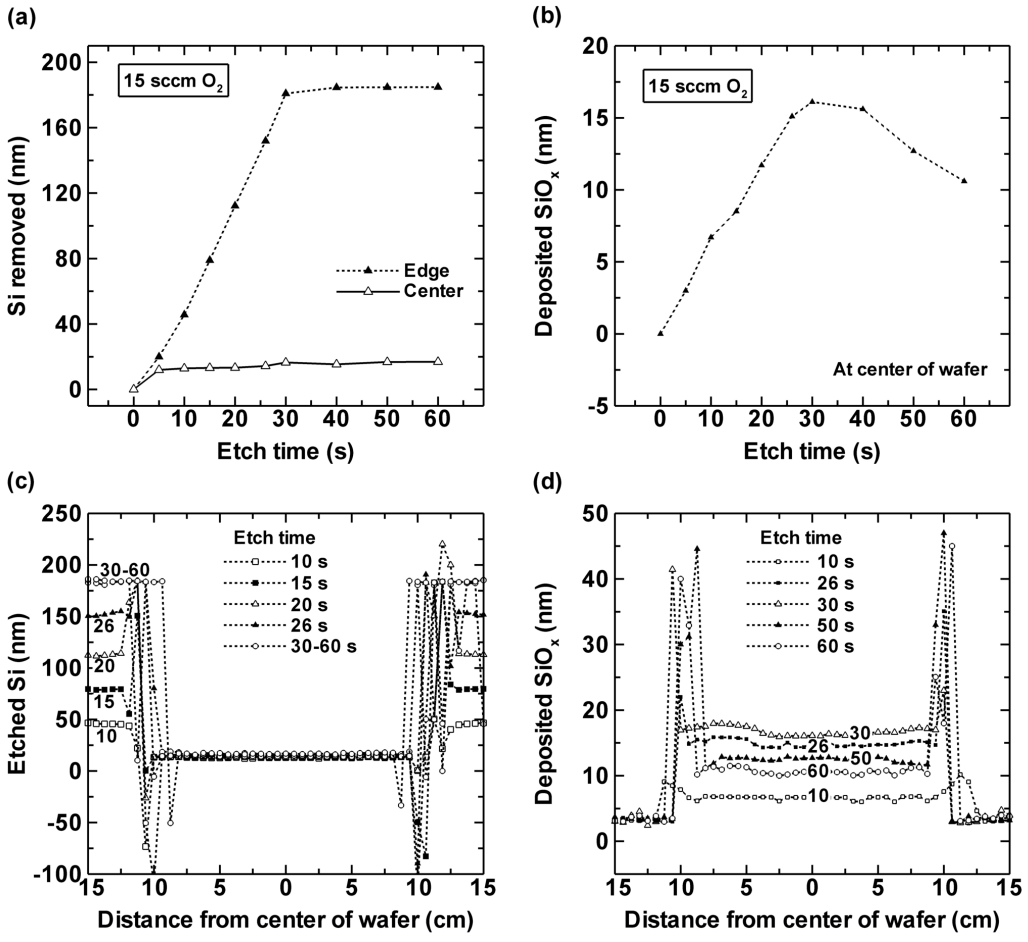

Figure 64. **(a)** Si removed at edge and center of wafer as a function of etch time. **(b)** Etch stop layer thickness at center of wafer as a function of etch time. **(c)** Si removed and **(d)** etch stop layer thickness on a straight line across the wafer, for different etch times, at 15 *sccm* O_2.

7.5 Relation between etch rate and plasma composition

The abrupt change in the etch rate at varying O_2 flow, as was observed in **Figure 58**, is not found back in the oxygen content of the plasma itself, as illustrated in **Figures 65(a, b)** showing the volume averaged densities of most species as a function of O_2 flow. Indeed, the densities of oxygen containing species steadily increase, as expected. The steady increase of O_2 gas fraction and the abrupt change in etch rate suggest the competitive nature between chlorination and oxidation of the silicon surface. However, the most significant change is the total etch product density in the plasma which changes abruptly together with the etch rate. The highest etch product density (~$10^{14\text{-}15}$ cm^{-3}) is expected at low oxygen content where the etch rate is highest (~300 *nm*). $SiCl_2$, $SiCl_3$ and $SiCl_4$ are the main etch products with comparable densities to each other, although $SiCl_2$ always has a slightly higher density. As the oxygen content steadily increases, the etch product density in the plasma decreases abruptly to a value in the order of 10^{11} cm^{-3}.

Moreover, as the densities of the plasma species and their fluxes towards the wafer are strongly correlated, the fluxes of the (non-volatile) etch products towards the wafer show the same trends as a function of oxygen flow, as is clear from **Figure 66(a, b)**. Indeed, at 15 *sccm*, where the formation of an etch stop layer occurs due to dominant oxidation over chlorination, the total flux of (non-volatile) etch products to the wafer is in the order of 10^{18} cm^{-2} s^{-1}, whereas at 100 *sccm* it is about two orders of magnitude lower ($10^{15\text{-}16}$ cm^{-2} s^{-1}).

As mentioned before in **Figure 62(b)**, the growth of the etch stop layer is highest at 15 *sccm* which also indicates that the formation of this layer is

mainly based on redeposition of etch products. Although $SiCl_2$ and $SiCl_3$ are considered to be quasi-volatile, with a low deposition probability of 0.05, they are the most important species for deposition since their flux is roughly three orders of magnitude higher than the low-volatile species (compared to Si, SiCl, SiO and SiO_2). Technically these species are easily sputtered again from the surface, but if they are oxidised before being sputtered, they are trapped in the oxy-chloride layer which is sputtered more slowly, resulting in actual layer growth.

At low oxygen content, the ions that account most for sputtering of the wafer surface are $SiCl^+$, $SiCl_2^+$ and $SiCl_3^+$, with fluxes in the order of 10^{15} cm^{-2} s^{-1}, with $SiCl^+$ always being slightly higher. The reason why $SiCl^+$ is the highest is due to electron impact dissociative ionization of $SiCl_2$ (to $SiCl^+$ + Cl), which is the most important etch species at low oxygen fraction. As mentioned before, at higher oxygen content, the etch product density decreases significantly and hence this applies also to the corresponding ions. Therefore, at high oxygen content and etch stop, the most important ions for sputtering become Cl_2^+, ClO^+ and O_2^+.

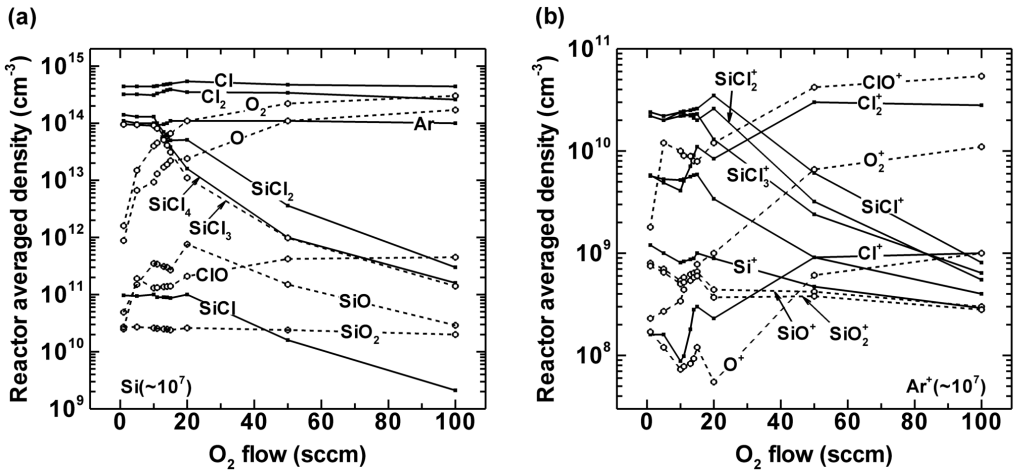

Figure 65. Reactor averaged densities of the various neutral species **(a)** and charged species **(b)** as a function of oxygen flow. The other operating conditions are the same as in section 7.2.

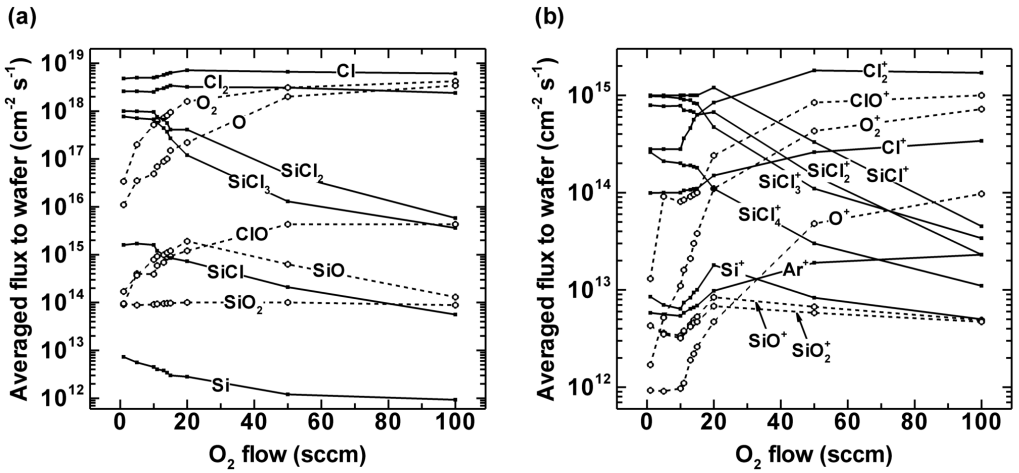

Figure 66. Radially averaged fluxes towards the wafer of the relevant neutral species **(a)** and charged species **(b)** as a function of oxygen flow. The other operating conditions are the same as in section 7.2.

7.6 Surface composition of wafer and reactor walls

Finally, the calculated surface compositions of the wafer and the reactor wall as a function of O_2 flow are illustrated in **Figures 67(a, b)**. At low oxygen fraction (i.e. below 10 *sccm*), the wafer surface is mainly chlorinated ($SiCl_3$) which is expected at 40 *mTorr* gas pressure. At this pressure, the fluxes of Cl and Cl_2 are at least 100 times higher than the ion fluxes, so the wafer surface will always be strongly chlorinated during the etching process. Therefore, the fraction of bare Si is only in the order of 10^{-3}. On the other hand, when more oxygen is added to the gas mixture, the fraction of SiO_2 on the surface tends to rapidly increase, as expected, and at 20 *sccm*, the wafer surface is already predominantly composed of SiO_x, as is clear from **Figure 67(a)**.

As mentioned before, $SiCl_x$ layers can be oxidized to $SiCl_xO$ layers and

eventually to SiO_2, replacing chlorine from the layer by oxygen [135]. On the other hand, a $SiCl_xO_y$ or SiO_x layer will not be chlorinated since the Si-O bond is stronger than the Si-Cl bond (6.4 *eV* vs. 3.9 *eV*). For this reason, the formation of a SiO_x layer is favored compared to a $SiCl_x$ layer. When the amount of oxygen in the plasma is increased, it is, therefore, expected that the surface of the wafer and the reactor walls rapidly tends to be covered with SiO_2. Moreover, since the SiO_2 layer can not be removed chemically, it can only be removed by physical sputtering. For this reason it is expected that the fraction of SiO_2 is even higher on the reactor walls due to limited sputtering, as is indeed obvious when comparing **Figure 67(b)** with **Figure 67(a)**.

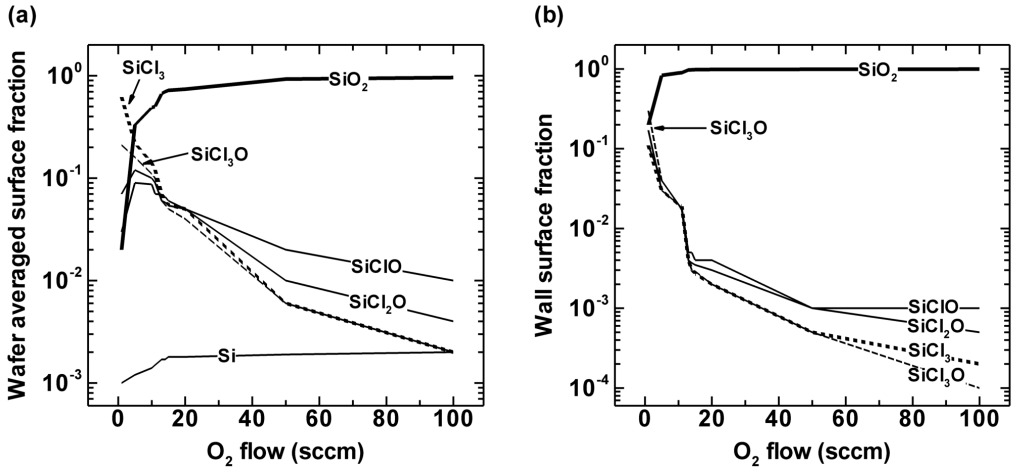

Figure 67. Calculated wafer **(a)** and reactor wall **(b)** surface composition as a function of O_2 flow. The other operating conditions are the same as in section 7.2.

The chemical composition of the deposited $SiCl_xO_y$ layer, at 15 *sccm* O_2, was investigated experimentally by TOFSIMS, and the result is illustrated in **Figure 68**. The intensity of the sputtered chlorine from this layer is much lower in signal compared to the oxygen containing species (O and SiO_2), proving that the deposited layer is indeed mainly composed of SiO_2. This again indicates the dominant oxidation over chlorination

under these conditions, where $SiCl_x$ surface species are gradually converted into SiO_x. It should be noted that the intensities do not represent the composition in an exact way due to a different sensitivity and sputter yield for the different species. After about 400 *s*, the $SiCl_xO_y$ passivation layer was completely removed. From here, only Si is sputtered and the signals converge to zero.

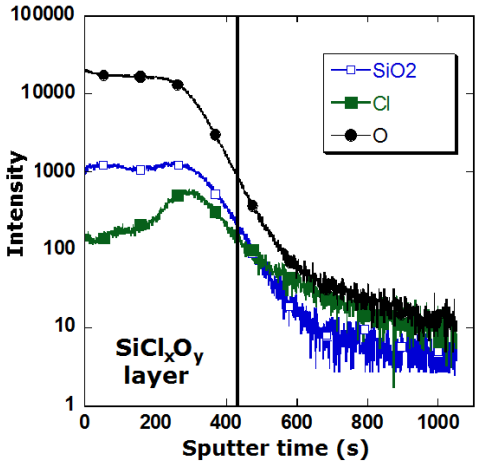

Figure 68. TOFSIMS intensities of SiO_2, O and Cl resulting from the $SiCl_xO_y$ layer deposited at 15 *sccm* O_2.

7.7 Effect of dielectric window temperature

As mentioned in section 7.1, the etch stop problem originated as a reproducibility problem. Indeed, it was found that the etch rate dropped significantly after a few wafers during wafer-after-wafer STI etching, even if the operating conditions were kept the same. It was found by Shamiryan *et al* [192] that heating of the top dielectric window was the origin of the problem because low-volatile etch products evaporate more easily from a heated top window and hence redeposit more on the cooled wafer.

A similar conclusion can be drawn from the results obtained in this work. Indeed, as mentioned before, the experimentally measured etch rates discussed in the previous chapter were obtained under slightly different operating conditions as applied in this chapter where the etch stop phenomenon is studied in more detail. More specifically, all operating conditions are actually the same, except for power (i.e. 1000 *W* compared to 600 *W* now) and dielectric window temperature. The experimental results presented in the previous chapter were obtained in a reactor with a quartz dielectric window of which the temperature could not be controlled. For this purpose, the window was first heated up to a stable 100 *°C* before doing wafer-after-wafer etch experiments.

In comparison to this, the experimental results presented in this chapter are obtained in the same reactor, but with a different dielectric window, of which the temperature can be controlled. As mentioned before, the dielectric temperature now was fixed at 60 *°C*.

It is therefore interesting to compare the results of Chapters 6 and 7 to see where the etch stop occurs first. The measured etch rate across the wafer for 12 *sccm* O_2 gas flow obtained in the previous chapter and obtained here are illustrated in **Figure 69** for comparison.

In **Figure 69** it can be clearly seen that the temperature of the dielectric window has a profound effect on the formation of an etch stop layer. At 12 *sccm* O_2 flow, there is only formation of a small roughness layer in the case where the dielectric is controlled at 60 *°C*, whereas a full etch stop is observed in the case where the dielectric is 100 *°C*. Indeed, even if power is higher (1000 *W* compared to 600 *W*), which results in a higher etch rate (at least at the edge of the wafer), there is still more formation of an etch stop layer in the centre, which is a direct result of the hotter dielectric window (100 *°C* compared to 60 *°C*).

If the temperature of the dielectric window is not controlled (i.e. the 100 *°C* case), the window is heated mostly in the centre due to

(inefficient) cooling from the side of the window. This is also a reason why the etch stop occurs preferably in the centre of the wafer. A heated dielectric will enhance the evaporation of redeposited etch products which eventually leads to a higher redeposition rate on the cooled wafer.

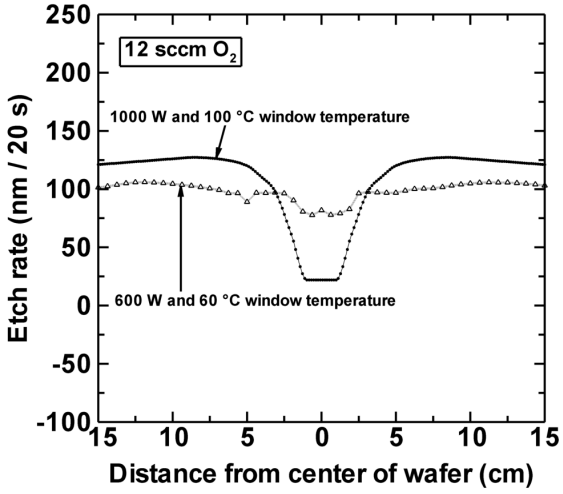

Figure 69. Measured etch rates across a line on the wafer at 12 *sccm* O_2 flow, at 1000 *W* source power and 100 °*C* dielectric window temperature (solid line), and at 600 *W* source power and 60 °*C* dielectric window temperature (dashed line).

7.8 Conclusions

The growth mechanism of an etch-stopping oxide layer during the etching of silicon with an $Ar/Cl_2/O_2$ plasma, as applied in shallow trench isolation (STI), was investigated in detail by means of experiments and modeling. The oxygen gas fraction was varied and different etching or deposition regimes were observed. At very low oxygen content (below 10 *sccm*), silicon was found to be etched successfully, however, with undercutting effects due to the predominant isotropic chemical etching by chlorine neutrals. When the fraction of oxygen was increased slightly

(up to about 12 *sccm* under the stated operating conditions), silicon is still etched successfully and the trench sidewalls are protected by an oxide layer, resulting in a desired anisotropic etch process.

However, if the fraction of oxygen is increased even more (to about 14 *sccm*), the resulting wafer surface was found to be very rough, suggesting a competition between oxidation and chlorination of the silicon. At even higher oxygen flow (15 *sccm*), an etch-stopping oxide layer was formed in the centre of the wafer, which increased in thickness during the etch experiment. Simultaneously, at the border of the wafer, silicon was still etched successfully. At very high oxygen content (e.g. 100 *sccm*), the etch stop layer covered the complete wafer, but the layer did not increase in thickness as much as in the case of 15 *sccm*. This indicates that the growth of the etch stop layer results from the redeposition of non-volatile etch products.

The same could be concluded when investigating the etch rate and the formation of an SiO_x layer as a function of the etch time. Indeed, when all 200 *nm poly*-Si was etched from the border of the wafer, the growth of the central oxide layer decreased again due to sputtering and the lack of redepositing etch products.

The abrupt change in etch rate on the wafer as a function of O_2 flow was observed both in the experimental and simulation results, but it was not found back in the oxygen content of the plasma, suggesting that the strong change in etch rate is indeed a consequence of the competitive nature between chlorination and oxidation of silicon. The most important effect here was the significant drop in etch product density at increasing O_2 content. For this reason, the growth rate of the oxide layer decreased with increasing oxygen fraction, which proves again that the layer formation is indeed based on etch product redeposition. At low oxygen fraction, the most important ions were the ionised etch products $SiCl^+$, $SiCl_2^+$ and $SiCl_3^+$, whereas at higher oxygen content Cl_2^+, ClO^+ and O_2^+

were the dominant ions.

The surface composition was investigated by means of modeling and it was found that when the oxygen flow is increased, the composition on wafer and walls quickly became mainly SiO_2 due to the fact that, in this chemical system, a silicon chloride layer can be oxidised, while a silicon oxide layer can not be chlorinated (see section 4.5.4).

Finally, the effect of the dielectric window temperature could be investigated by comparing results where, in one case, the dielectric temperature was fixed at 60 *°C* and, in another case, it was heated to a stable 100 *°C*. It was found that the etch stop layer is formed more rapidly at higher dielectric window temperature due to facilitated evaporation of etch products from the dielectric window. This, in turn, enhances redeposition on the cooled-down wafer decreasing the etch rate significantly.

Chapter 8

Effect of chamber wall coating

8.1 Introduction

To increase wafer-after-wafer processing reproducibility, it is common to clean the chamber after each etching step and introduce a new coating before each new processing step. It is well known that the nature of the reactor walls can have a significant influence on the etching process, especially at these low pressures where the ratio of wall interactions to gas phase interactions is relatively large [132].

During the etching process, etch products are launched into the plasma and can alter the general plasma properties as well as the chamber coatings by redeposition [101]. Coating the reactor chamber, e.g. with SiO_2 or an *oxy-chloride* coating, before each etch experiment is a widely used preparation step for obtaining higher etch uniformity and higher wafer-to-wafer reproducibility. Indeed, a common way to introduce a coating is to apply a $SiCl_4/O_2$ based plasma which will deposit a $SiCl_xO_{y(s)}$ layer close to $SiO_{2(s)}$.

In the following sections it will be discussed how a SiO_2 or *oxy-chloride*

This chapter is based on the following publication: S Tinck, W Boullart and A Bogaerts, Modeling $Cl_2/O_2/Ar$ inductively coupled plasmas used for silicon etching: effects of SiO_2 chamber wall coating, *Plasma Sources Sci. Technol.* 20 (2011) 045012

coating on the reactor walls can affect the overall plasma behavior and etch rate. For this, simulations are performed to gain a better insight in the properties of a Cl_2/Ar plasma, with and without O_2, during plasma etching of Si.
Special attention is paid to the behavior of etch products coming from the wafer or the walls, and how the chamber walls can affect the plasma and the resulting etch process.

8.2 Plasma behavior in clean and coated chamber

To obtain a better insight in the effects of the reactor walls on the plasma behavior and the etch process, two different case studies are modeled for an Ar/Cl_2 plasma. In the first case, the reactor walls are considered to be initially completely clean. In the second case, a SiO_2 coating is applied on the walls. Hence, in the latter case, oxygen will be loaded into the plasma due to sputtering of the SiO_2 coating, even though oxygen is not part of the injected (Ar/Cl_2) gas mixture. It is important to study both conditions, as both cases are applied in experiments. It should be noted that the clean chamber is considered not to release oxygen in the simulations. In reality, there will always be a small amount of oxygen sputtered from the dielectric window which is inevitable during plasma processing.
Figure 70 illustrates the reactor geometry that was considered for this work, based on the *Lam Research 2300 Versys Kiyo* reactor for etching of 300 *mm* wafers, which was also considered in the previous chapters. Operating conditions are the following: 40 *mTorr* gas pressure, 600 *W* coil power, -500 *V* dc bias at the substrate, 100 *sccm* Cl_2, 12 *sccm* Ar, 13.56 *MHz* operating frequency applied at both coil and substrate, and 60 °C wall temperature. The dielectric window, of which the temperature can

be controlled, consists of a ceramic material which does not release oxygen as easily as quartz. For plotting results on surface composition and etch/deposition rates at the wafer, reactor walls and top window (see below), a path along the borders of the geometry is followed, starting at the left bottom (i.e. at the center of the wafer), moving up along the sidewall and going from right to left along the top dielectric window.

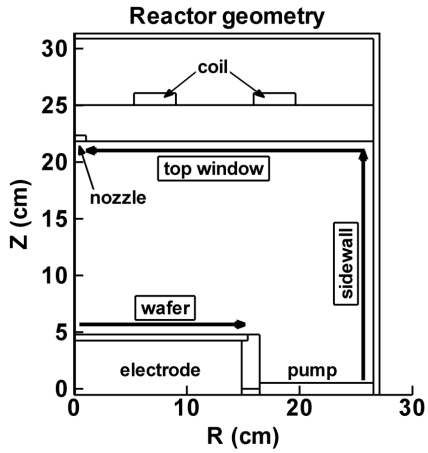

Figure 70. Two-dimensional reactor geometry defined in the model. The reactor sidewalls are assumed to be either clean (Al_2O_3) or SiO_2 coated. The left axis is the symmetry axis of the cylindrically symmetrical reactor.

Figure 71(a - j) presents a set of two-dimensional plasma density profiles throughout the reactor. The corresponding flux lines are also illustrated, to visualize the flow of these plasma species. Flow lines that point in all directions from the same location denote a local source for the specified species from where it diffuses to lower density regions. Moreover, flow lines that come together in one particular area denote a local sink for that species. The Cl atom density profiles in both the clean and coated reactor are illustrated in **Figures 71(*a, b*)**, whereas the Cl_2 molecule density profiles in both reactors are shown in **Figures 71(c, d)**. The Cl atoms and Cl_2 molecules are the most abundant species in the reactor,

with volume averaged densities in the order of 10^{14} cm^{-3}, followed closely by the most common etch products $SiCl_2$, $SiCl_3$ and $SiCl_4$, which have densities in the same order. The total ion density is close to 10^{11} cm^{-3}. In the model, the gas flow is adjusted to keep a constant pressure in the chamber. The gas temperature is calculated in the model, based on power deposition in the plasma, and was found to be close to 400 *K*. In this way, gas depletion by heating of the gas is taken into account following the ideal gas law.

As is clear from **Figure 71(a, b)**, the volume averaged Cl density is more than twice as high in the coated chamber compared to the clean chamber. Indeed, as appears from the density gradients near the reactor walls in **Figure 71(a)**, in the clean chamber a much larger fraction of atomic Cl is lost to the walls (and later on returned as Cl_2 or $SiCl_4$), i.e., the calculated overall wall sticking (or loss) probability of Cl on the reactor walls is 0.7, compared to only 0.001 in the coated chamber. Indeed, the deposited oxy-chloride layer at the reactor walls in the coated chamber (see below) cannot be chemically etched by Cl atoms, so that a large fraction of the Cl atoms will be reflected from the wall. Hence the density of Cl atoms will be more than twice as high in the coated chamber (4.5×10^{14} cm^{-3}) compared to the clean chamber (1.8×10^{14} cm^{-3}). At lower pressure, this difference is expected to be even larger, as experimentally found at 20 *mTorr* by Cunge *et al* [132]. Moreover, the Cl radical loss probability at the wafer was calculated to be 0.03 in both coated and clean chamber. No difference is found here due to a very low oxygen fraction at the surface which is in turn due to heavy ion bombardment.

Figures 71(*c*) and **71(*d*)** present the Cl_2 density profiles. In the clean chamber, the volume averaged density is 5.5×10^{14} cm^{-3} while in the coated chamber it is 3.2×10^{14} cm^{-3} which illustrates indeed that the walls in the clean chamber are a large source for molecular chlorine.

The O and O_2 density profiles in the coated chamber are illustrated in **Figures 71(*e*)** and **71(*f*)**, respectively. Their maximum densities are both in the order of 10^{11} cm^{-3}, which is more than three orders of magnitude lower than the Cl and Cl_2 densities. Indeed, the O atoms and O_2 molecules do not originate from the gas mixture, but are only launched from the walls. It is indeed clear that both O atoms and O_2 molecules diffuse from the walls to the centre of the chamber. Eventually oxygen will redeposit on the wafer but is sputtered again rapidly due to heavy ion bombardment on the wafer. Their maximum densities are therefore near the centre of the reactor, above the wafer.

The most common etch products are $SiCl_2$, $SiCl_4$ and $SiCl_3$ with comparable densities close to 1.1×10^{14} cm^{-3}. The density profiles of $SiCl_3$, and of the corresponding ion, $SiCl_3^+$, in the coated chamber are plotted in **Figures 71(g)** and **71(h)**, respectively. The densities of the other etch products have comparable profiles. SiCl has a volume averaged density in the order of 10^{11} cm^{-3}, while pure Si has a negligible density in the plasma. Moreover, SiO and SiO_2 have comparable densities close to 7×10^9 cm^{-3}. From **Figure 71(g)** it is clear that the etch products are launched in the plasma from the wafer, as expected, from where they can redeposit on the walls, or they can be pumped out.

Different density profiles are found for SiO_2 and SiO_2^+ (see **Figures 71(*i*, *j*)**). The maximum density of SiO_2 is not directly located at the walls or the wafer as in the case of $SiCl_3$. Indeed, SiO_2 molecules are not sputtered directly from the walls in our model but sputtered oxygen will react with etch products to form SiO and SiO_2, explaining why the maximum is expected in the centre of the plasma, following the profile of atomic oxygen (**Figure 71(*e*)**). SiO_2^+ has a low density (10^8 cm^{-3}) compared to the ions of the most important etch products ($SiCl_2^+$, $SiCl_3^+$ and $SiCl_4^+$). Their densities are all in the order of 10^{10} cm^{-3}, with $SiCl^+$ and $SiCl_2^+$ having the highest densities (2.4×10^{10} cm^{-3}).

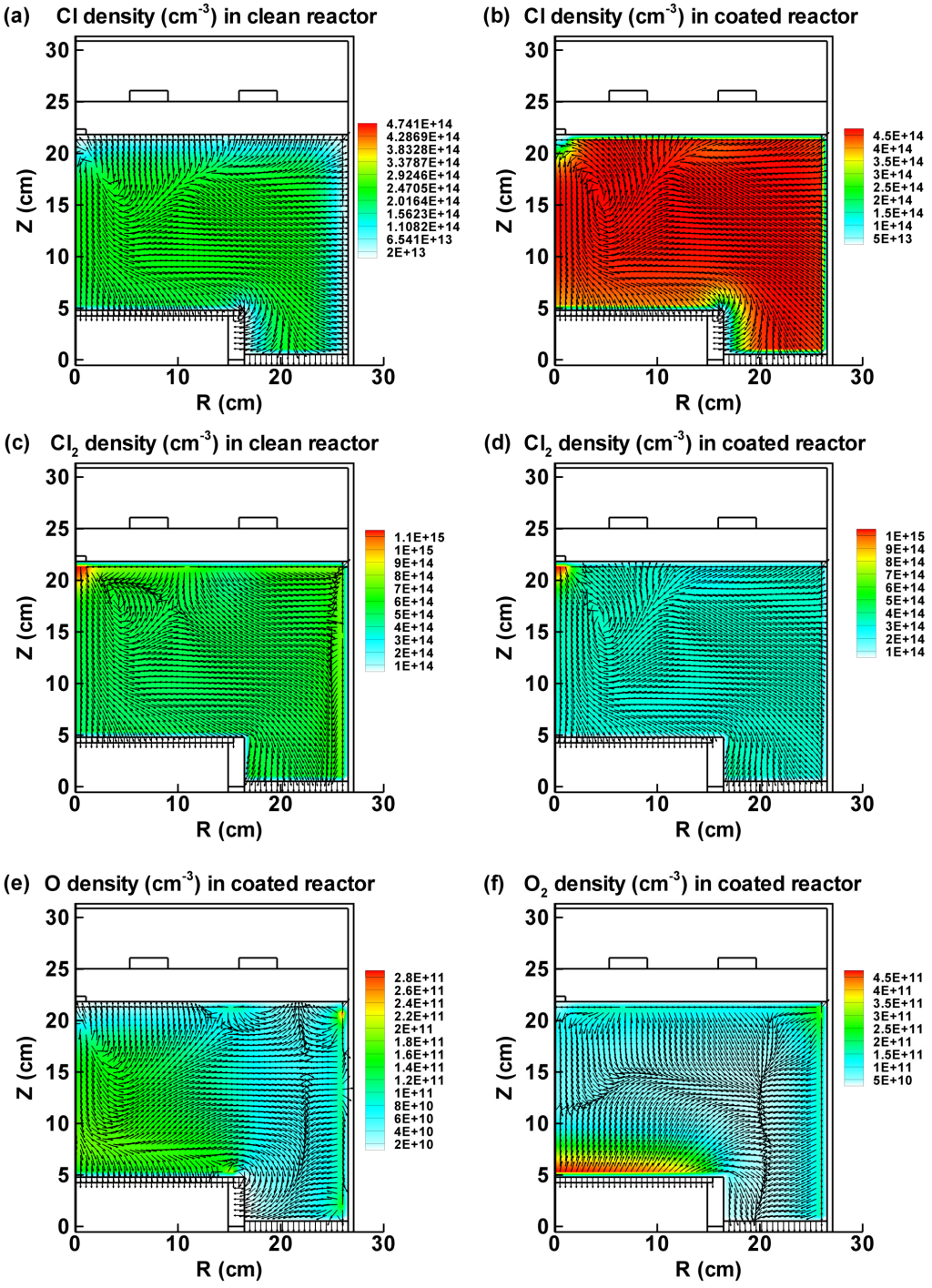
(a) Cl density (cm-3) in clean reactor
4.741E+14
4.2869E+14
3.8328E+14
3.3787E+14
2.9246E+14
2.4705E+14
2.0164E+14
1.5623E+14
1.1082E+14
6.541E+13
2E+13
(b) Cl density (cm-3) in coated reactor
4.5E+14
4E+14
3.5E+14
3E+14
2.5E+14
2E+14
1.5E+14
1E+14
5E+13
(c) Cl2 density (cm-3) in clean reactor
1.1E+15
1E+15
9E+14
8E+14
7E+14
6E+14
5E+14
4E+14
3E+14
2E+14
1E+14
(d) Cl2 density (cm-3) in coated reactor
1E+15
9E+14
8E+14
7E+14
6E+14
5E+14
4E+14
3E+14
2E+14
1E+14
(e) O density (cm-3) in coated reactor
2.8E+11
2.6E+11
2.4E+11
2.2E+11
2E+11
1.8E+11
1.6E+11
1.4E+11
1.2E+11
1E+11
8E+10
6E+10
4E+10
2E+10
(f) O2 density (cm-3) in coated reactor
4.5E+11
4E+11
3.5E+11
3E+11
2.5E+11
2E+11
1.5E+11
1E+11
5E+10
Z (cm)
R (cm)
0
5
10
15
20
25
30

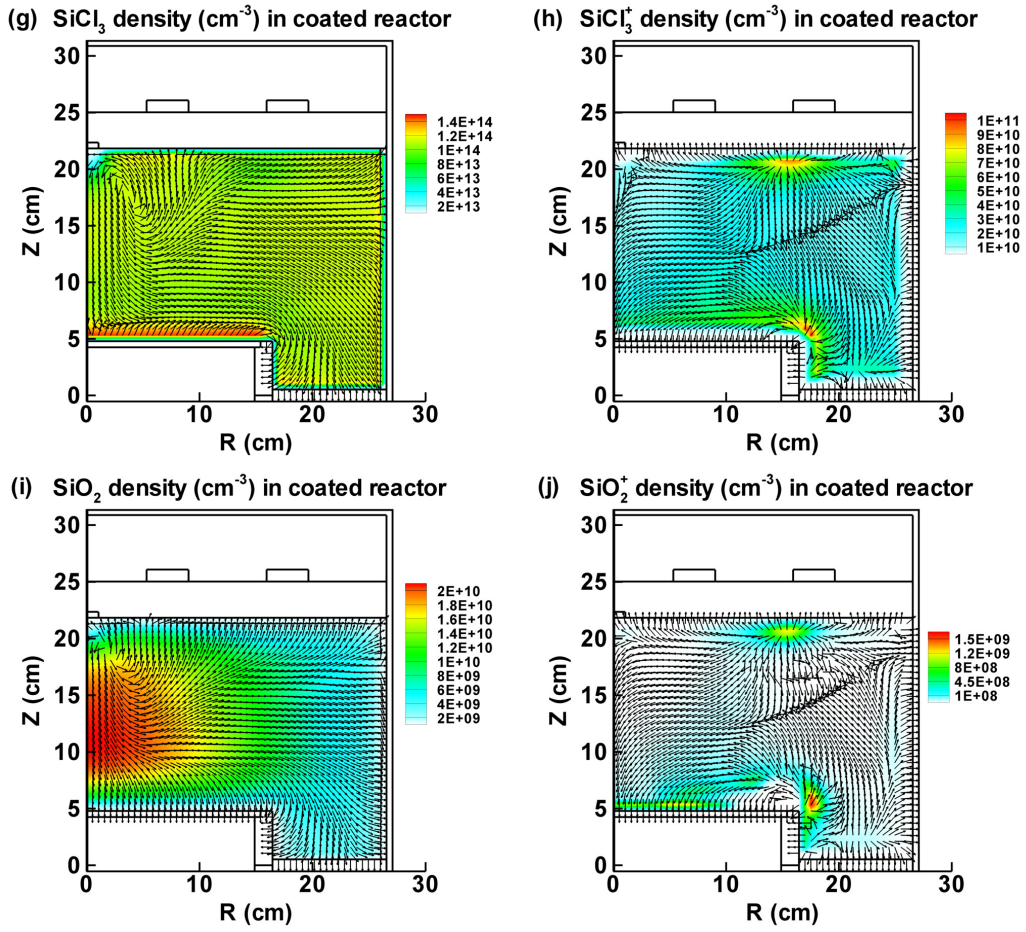

Figure 71. Calculated density profiles of Cl atoms in the clean **(a)** and coated **(b)** chamber, of Cl_2 molecules in the clean **(c)** and coated **(d)** chamber, and of O atoms **(*e*)**, O_2 molecules **(*f*)**, $SiCl_3$ molecules **(*g*)**, $SiCl_3^+$ ions **(*h*)**, SiO_2 molecules **(*i*)** and SiO_2^+ ions **(*j*)** in the coated chamber. It should be noted that the color schemes in the different plots are not relative to each other and that the illustrated flux arrows do not represent the magnitude of the fluxes, but only the direction of the movement.

It should be noted that the density of Cl_2^+ is calculated to be only 5.5×10^9 cm^{-3}, so $SiCl^+$ and $SiCl_2^+$ can be considered the most important ions for sputtering of the wafer surface. This is in agreement with a conclusion made by Cunge *et al.* [135] based on their experimental work. Indeed, the flux to the wafer was calculated to be about 1×10^{15} cm^{-2} s^{-1}, while the flux of Cl_2^+ was only 2×10^{14} cm^{-2} s^{-1}.

8.3 Surface compositions of wafer and walls

Figure 72 illustrates the surface fractions of redeposited etch products on the wafer, sidewall and top window in the clean chamber **(*a*)** and the coated chamber **(*b*)**, plotted along the path illustrated in **Figure 70**.

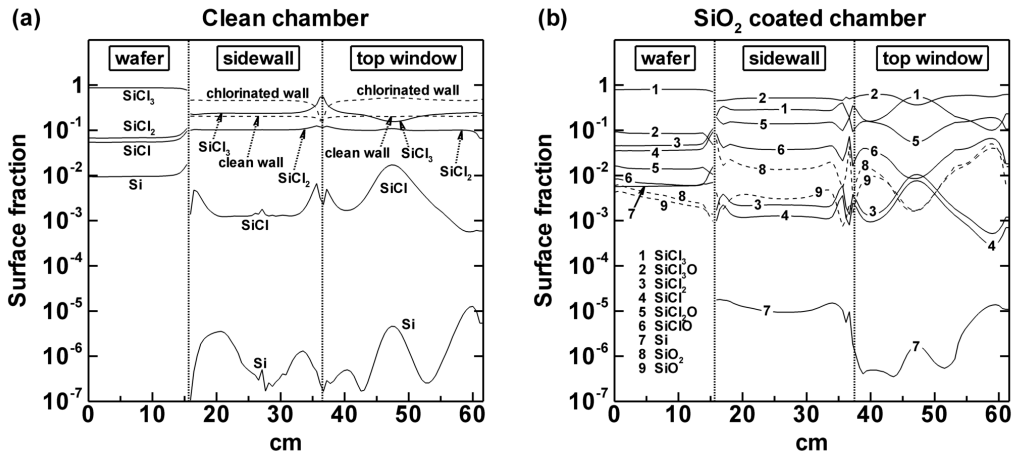

Figure 72. Surface layer compositions on the wafer, sidewall and top window in an initially clean **(*a*)** and SiO_2 coated **(*b*)** chamber, plotted along the path indicated in **Figure 70**.

During the etching process, the wafer is for more than 90 % chlorinated ($SiCl_3$), independent of the fact whether the chamber walls are coated or not. The remaining fraction of 10 % is occupied by $SiCl_2$ and SiCl, with less than 0.01 % of free *poly*-Si (in the clean chamber). In some papers it is reported that the most abundant species on the wafer is SiCl [103, 46, 193]. However, these results were all obtained at 4 *mTorr* or less, where the ratio of neutral to ion flux is much lower. Even though $SiCl_3$ is the most easily sputtered, at 40 *mTorr*, a highly chlorinated surface is to be

expected because the flux of Cl is about 10^{18} cm^{-2} s^{-1}, while the total ion flux was found to be at most in the order of 10^{15} cm^{-2} s^{-1}. Hence, the surface will always be rapidly chlorinated before it has a chance to be sputtered.

It is important to note that the fraction of oxygen on the wafer was found to be very low, even in the coated chamber. Indeed, in the coated chamber oxy-chloride species ($SiCl_xO$, x = 1 - 3) occupied only about 9 % of the complete wafer surface and SiO_x (x = 1 - 2) even less (< 0.01 %). This illustrates that the direct effect of oxygen, originating from the walls, on the etch rate was found to be small.

In the clean chamber, the reactor walls become covered by etch products for about 35 % (mostly $SiCl_3$). 45 % of the wall was found to be chlorinated (i.e. Al_2O_3 saturated by Cl), whereas the remaining 20 % remains clean. Comparable results were observed by Lee *et al* [101] although their results were obtained at lower pressure. The same is true for the top window, although the deposited etch product fraction was found to be lower right underneath the coil where power deposition, and hence sputtering, is the highest. The product fraction here is about 25 % as is clear from **Figure 72(*a*)**.

The deposited etch products only form a thin layer of a few *nm* on the walls. This is due to the fact that when the walls are covered with $SiCl_2$ and $SiCl_3$, they will be further chlorinated to $SiCl_4$, which will be released again into the gas phase. This is different for the coated chamber where an actual deposited layer is grown on the sidewalls as a function of time. Later in section 8.4, we will discuss the thickness of the deposited layer in the clean and coated chamber in more detail.

Indeed, in the SiO_2 coated chamber, the reactor walls are mostly covered with an *oxy-chloride* layer (51 % $SiCl_3O$, 14 % $SiCl_2O$ and 4 % SiClO) during the etching process. The remaining surface is occupied by $SiCl_3$ (28 %), SiO_2 (1 %) and SiO (0.3 %). The remaining 1.7 % is occupied by

$SiCl_x$ (x = 1, 2) and pure Si. The overall chemical composition of the deposited layer on the walls was calculated as $SiCl_{2.75}O_{0.7}$. It should be noted that this predicted surface composition is a direct result of the defined reactions in our model, where not all reaction probabilities are exactly known, so the value should be interpreted with caution. However, the most important reactions are quite well known from experimental data and the result is therefore expected to be quite close to the *real* value. Kogelschatz *et al* [134] reported a composition of the deposited layer close to $SiCl_3O$, but with more oxygen deeper into this layer. Hence, reasonable agreement is found between our prediction and these experimental results.

It should also be noted that the surface model does not take the depth of surface layers into account, so a possible gradient in oxygen fraction through this layer could not be resolved by the model.

As can be deduced from **Figure 72(*b*)**, the surface composition of the top window directly underneath the coil is slightly different from the composition of the sidewalls, in the case of the coated chamber. Indeed, in this region, where the plasma density is highest, sputtering is very important, reducing the growth of a deposition layer. Since the layer which is grown on the wall and dielectric consists mainly of $SiCl_3O$, oxygen will be preferentially sputtered more at the dielectric right underneath the coil, leaving a layer which consists of less oxygen (mainly $SiCl_3$ 52 %).

In the clean chamber, enhanced sputtering at the top window will also occur, and as stated before, the fraction of deposited species will therefore be slightly lower. Since the flux of Cl is roughly 1000 times higher than the total ion flux, the surface will always be mostly chlorinated, even at the top window.

8.4 Etch or deposition rate at wafer and walls

The overall etch or deposition rate at the wafer, sidewall and top window is plotted in **Figure 73**, for both the clean and coated chamber. The calculated etch rate at the wafer is around 300 $nm\ min^{-1}$ in the coated chamber, which is a bit higher than in the clean chamber, due to a higher density (and flux) of Cl atoms, as was illustrated in **Figure 71(a, b)** and was also reported in [132, 133, 135], so that chemical etching is enhanced. The increase at the edge of the wafer is due to the higher ion flux, since the edge of the wafer is more directly underneath the maximum ion density (as also mentioned earlier in Chapter 6 and 7).

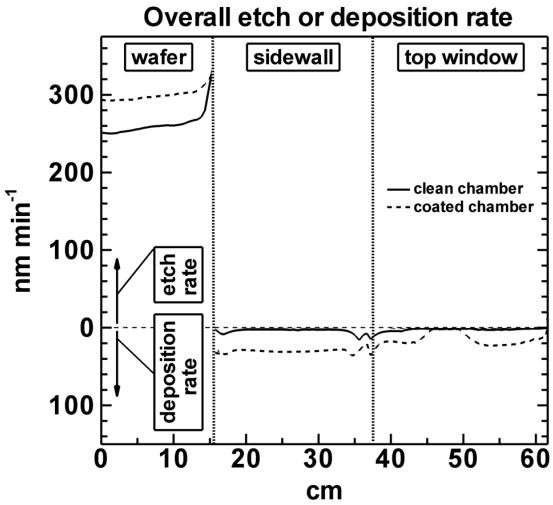

Figure 73. Calculated etch or deposition rate at the wafer, sidewall and top window, plotted along the path indicated in **Figure 70**, for the coated chamber (dashed line) and clean chamber (solid line).

In the clean chamber, the deposition of etch products seems to happen at a very slow rate, about 2.5 *nm* per minute. Indeed, the walls can only be chlorinated (i.e. covered with Cl atoms or Cl_2 molecules), or be covered by etch products, mostly $SiCl_3$ and $SiCl_2$, which can be sputtered again from the wall or be further chlorinated to volatile $SiCl_4$. At the dielectric window right underneath the coil, deposition of etch products was found to be negligible due to enhanced sputtering of the window in this area.
On the other hand, in the coated chamber, a layer of about 30 *nm* is deposited after one minute of etching. This is in reasonable agreement with experimental data from Kogelschatz *et al* [134], who reported a deposited layer of about 10-14 *nm* after 40 *s* of etching, at 20 *mTorr* gas pressure and 50 *sccm* total gas flow in a pure Cl_2 plasma.
Indeed, in the coated chamber, non-volatile etch products that redeposit on the wall, can be oxidized by oxygen present in the plasma. This $SiCl_xO$ layer can not be etched chemically and is also sputtered more slowly, hence trapping the etch products in a growing deposition layer during the etching process. As stated before, in the case of the clean chamber, the deposition of non-volatile species on the top window seems to be completely absent, due to the enhanced sputtering of the top window directly underneath the coil. In fact, our calculations predict actually a small net amount of sputtering on the top window, but the rate was found to be very low and practically negligible. This is in line with the experimental evidence that the top dielectric window is sputtered very slowly during wafer processing [105].

8.5 Main differences in clean and coated chamber

Table 30 illustrates the most relevant differences in the Ar/Cl_2 plasma properties between the clean and coated chamber. As mentioned above, Cl atoms are lost at the walls in the clean chamber at a much higher probability (0.7), making the volume averaged density of Cl atoms less than half the density in the coated chamber (with calculated wall loss probability of about 0.001). In the clean chamber, the ratio of $[Cl]/[Cl_2]$ is small (0.32) compared to the value in the coated chamber (1.40) where more Cl atoms than Cl_2 molecules are present in the plasma. The overall etch rate is higher in the coated chamber than in the clean chamber, because of the higher Cl density (and flux). The total density of etched species is, therefore, also slightly higher in the coated chamber than in the clean chamber, but in both cases it is in the order of 10^{14} cm^{-3}.
Although a significant amount of $SiCl_x$ species is trapped in the growing $SiCl_xO$ layer at the walls of the coated chamber, the density of etch products is still slightly higher in the coated chamber due to the increased etch rate. The latter effect seems to be more important than the trapping of etch products at the walls, although the density of etch products can be sensitive to operating conditions such as gas flow and pressure [132]. The fraction of etch products in the plasma itself is significant in both cases (37 % in the clean chamber and 38 % in the coated chamber). It is observed that the effect of redeposition of etch products on the wafer, slowing down the etch rate, is negligible, as is also reported in [170, 193]. There are slightly more etch products in the coated chamber, due to the higher etch rate. Therefore, the effect of a higher Cl radical density in this chamber seems to be more important

than redeposition of etch products on the wafer.
Finally, in the coated chamber, some oxygen species are present in the plasma, whereas they are absent in the clean chamber. It seems that in an Ar/Cl_2 plasma with SiO_2 coating, the amount of oxygen loaded in the plasma is not very high but in the same order as the ion densities (10^{11} cm^{-3}). Most oxygen in the plasma is present in the form of O_2 (50 %), and O (42 %) and to a lower extent as ClO (2 %) and SiO_x products (8 %).

Table 30. Summary of the most important differences of the Ar/Cl_2 plasma in the clean and coated chamber.

Property	Clean chamber	Coated chamber
Cl density (vol. averaged)	1.8×10^{14} cm^{-3}	4.5×10^{14} cm^{-3}
$[Cl]/[Cl_2]$ ratio	0.32	1.40
Cl wall loss probability	0.7	0.001
Averaged wafer etch rate	~260 $nm\ min^{-1}$	~300 $nm\ min^{-1}$
Total etch product density	3.1×10^{14} cm^{-3}	3.7×10^{14} cm^{-3}
Etch product fraction in plasma	0.37	0.38
Most common etch products	35 % $SiCl_4$	30 % $SiCl_4$
	23 % $SiCl_3$	29 % $SiCl_3$
	41 % $SiCl_2$	40 % $SiCl_2$
Total oxygen containing species density	/	1.8×10^{11} cm^{-3}
		48 % O_2
		42 % O
		2 % ClO
		8 % SiO_x

8.6 Conclusions

It is known from experiments that introducing a SiO_2 or *oxy-chloride* coating to the reactor walls can have beneficial effects on the etch process, such as increased etch rate and uniformity. Therefore we have investigated in more detail how the nature of the walls affects the plasma

and hence the etching mechanism. For this, simulations are performed of an Ar/Cl_2 inductively coupled plasma where oxygen is introduced from a SiO_2 wall coating. Surface processes such as physical sputtering, enhanced chemical sputtering and chemical etching, as well as deposition reactions (see sections 4.5.2 - 4.5.6), are combined with the general plasma simulations to obtain information on the effects of the reactor walls on the plasma properties. Two cases were studied, i.e. an Ar/Cl_2 plasma in a clean reactor (where no oxygen is present), and in a SiO_2 coated chamber where oxygen is loaded from the walls.

The fraction of etch products in the plasma was found to be significant in both cases (37 % in the clean chamber and 38 % in the coated chamber). The etch rate was slightly higher in the coated chamber (300 $nm\ min^{-1}$ compared to 260 $nm\ min^{-1}$ in the clean chamber). The effect of redeposition of etch products on the wafer, slowing down the etch rate, was found to be negligible at the conditions under study. Moreover, it was found that the oxygen content in the plasma, originating from the SiO_2 coating, was low and does not have a direct effect on the etch rate. However, recombination of Cl on the walls was found to be the most significant process for affecting the etch mechanism. The etch rate was found to be higher in the coated chamber due to a higher density of atomic chlorine in the reactor. This, in turn, is due to a drastic decrease in wall loss probability (0.7 in the clean chamber compared to 0.001 in the coated chamber).

Furthermore, the surface compositions and the etch and deposition rates on the wafer, the sidewalls and the top window were investigated. It was found that, in the clean chamber, the walls are mostly chlorinated (45 %) or covered with redeposited etch products (35 %), mostly $SiCl_3$. The deposited layer in the clean chamber was found to be very thin (growing 2.5 $nm\ min^{-1}$) due to wall sputtering and further chlorination to volatile $SiCl_4$, which is an important wall loss mechanism for Cl radicals in the

clean chamber. In the coated chamber, an oxy-chloride layer is deposited at a rate of about 30 *nm min*$^{-1}$ during the etching process, with a calculated chemical surface composition of $SiCl_{2,75}O_{0,7}$. However, at the top window beneath the coil, the deposited oxy-chloride layer is sputtered more easily, inhibiting the growth of a deposition layer in this area. Cl radicals are lost less rapidly at the walls in this case since there can be no further chlorination of the oxide layer.

Chapter 9

$Ar/SiH_4/O_2$ ICP: Investigating the deposition process

9.1 Introduction

In the previous chapters, Ar/Cl_2 and $Ar/Cl_2/O_2$ plasmas used for etching of Si have been investigated. The next step in shallow trench isolation (STI), after the Si trench etch, is the filling of these trenches with isolating material (SiO_2). For this purpose, an $Ar/SiH_4/O_2$ ICP is typically applied. To gain a better insight in this deposition process, results are presented on the plasma properties during the plasma enhanced chemical vapor deposition process (PECVD) for different gas ratios in the $Ar/SiH_4/O_2$ gas mixture, as well as on the shape of the filled trenches and the chemical surface compositions of the deposited layers.

PECVD is an appropriate process for microtrench (gap) filling during STI in semiconductor device processing as applied in the microelectronics industry [194]. As microdevice nodes continue to shrink, the requirements for a decent gap filling process become increasingly

This chapter is based on the following publication: S Tinck and A Bogaerts, Modeling $SiH_4/O_2/Ar$ inductively coupled plasmas used for filling of microtrenches in shallow trench isolation (STI), *Plasma Process. Polym.* (2011) *Submitted for publication*

challenging. To continue to meet these requirements, the PECVD process needs to be optimised and better understood. Usually high operating power and low pressure, as well as substrate bias and gas mixture, must be carefully chosen for a stable gap filling process. For mechanical and electrical stability, both structure damage and voids in the deposited layer must be avoided and therefore a well balanced operating process must be found. Both the balance between deposition rate and sputtering rate, as well as sputter deposition and ion angle, have proven to have a major effect on the resulting deposition process [195]. Sputter deposition, where the ions from the plasma are deposited into the surface layer (during sputtering of the surface), is found to be important for filling the trenches successfully.

As mentioned above, to deposit SiO_2 in the microtrenches, typically an Ar/SiH_4/O_2 plasma is applied or variations such as SiH_4/O_2 and SiH_4/N_2O mixtures diluted with Ar, H_2 or He [196]. SiH_4 is the precursor gas, while an oxidising agent (e.g. O_2) is added to the mixture to grow a SiO_2 film. Park and Rhee [197] have experimentally investigated the growth mechanism of low temperature SiO_2 films deposited by PECVD. The gas mixture under study in their work was SiH_4/N_2O. They concluded that SiH_2O and SiH_3O are probably the main film precursor molecules and that oxygen can remove residual -OH in the deposited layer, resulting in near stoichiometric SiO_2 films. However, gas ratios in combination with plasma power need to be chosen carefully to obtain an optimal gap fill process [197].

In the following sections, simulation results are presented to investigate the effects of different gas ratios in an Ar/SiH_4/O_2 gas mixture on the plasma properties and on the resulting deposition process.

9.2 General plasma characteristics

Simulations are performed for a reactor geometry of an ICP used for gap filling applications as applied in STI [194]. The two-dimensional geometry is presented in **Figure 74**. This reactor is slightly different from the one applied for etching of Si as discussed in previous chapters. Indeed, the reactor has two coils, i.e. a planar coil on top of the chamber and a cylindrical coil surrounding the chamber. At the bottom of the chamber the silicon substrate is located, which is a 300 *mm* wafer placed on top of the substrate electrode that attracts the ions from the plasma.

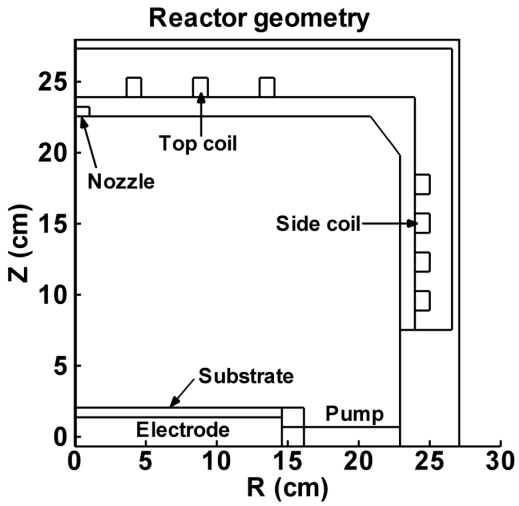

Figure 74. Two-dimensional reactor geometry defined in the model. The left axis is the symmetry axis of the cylindrically symmetrical reactor.

Calculations are performed for the following operating conditions typically used for gap filling in STI: 13.56 *MHz* operating frequency applied both at the substrate and the coil, 10 *mTorr* total gas pressure, 4400 *W* total coil power where 1300 *W* comes from the top coil, 3500 *W*

substrate bias power, 60 °C wall and substrate temperature, 500 *sccm* total gas flow rate and varying ratios of Ar/SiH_4/O_2 gas mixture (see below).

For these conditions, the effects on the plasma characteristics of power deposition and other process parameters such as nozzle position have already been theoretically investigated by Kushner [56] for almost similar gas mixtures (with He instead of Ar). In our work, the influence of different gas mixtures on both the plasma and deposition process is investigated. It was found that a gas mixture of 16 % Ar, 30 % SiH_4 and 54 % O_2 gives rise to proper gap filling conditions, as will be demonstrated below. Hence, before focusing on the effect of the different gas ratios on the gap filling process, we will first present in **Figure 75(a - f)** several plasma properties under these conditions, to illustrate the general plasma characteristics in this ICP reactor.

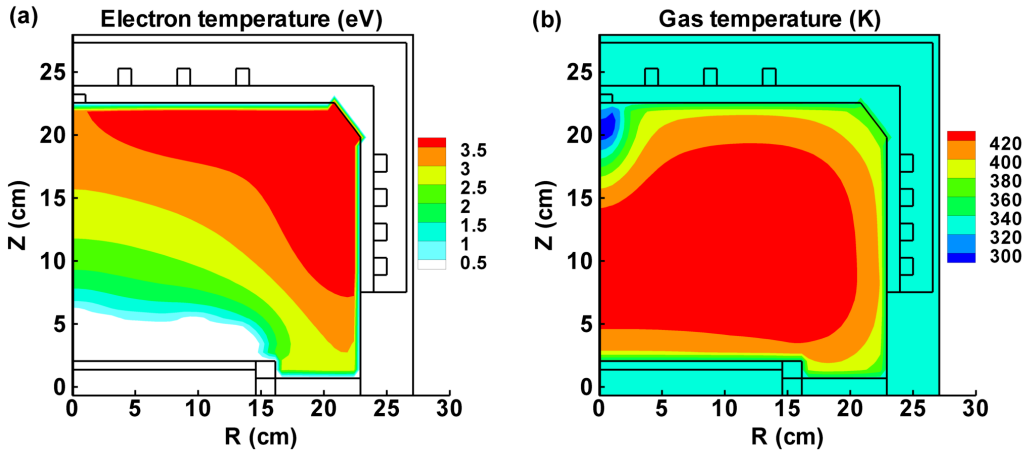

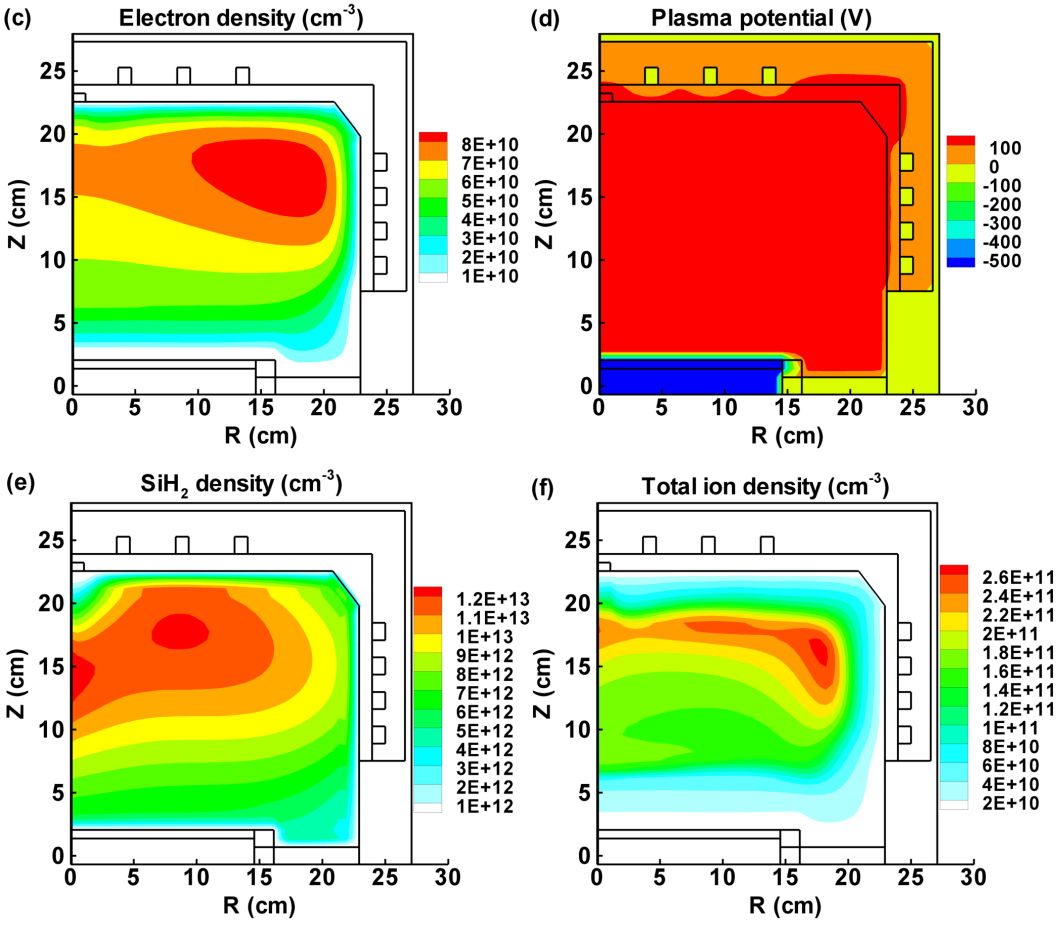

Figure 75. 2D contour plots of **(a)** electron temperature, **(b)** gas temperature, **(c)** electron density, **(d)** plasma potential, **(e)** SiH_2 density and **(f)** total ion density. The operating conditions are: 13.56 *MHz* applied at coil and substrate electrode, 10 *mTorr* total gas pressure, 4400 *W* total coil power, 3500 *W* substrate bias power, 60 °C wall and substrate temperature, 500 *sccm* gas flow rate, and a gas mixture of 16 % Ar, 30 % SiH_4 and 54 % O_2.

The electron temperature is illustrated in **Figure 75(a)** with a maximum near the top and side coils, resembling the shape of the power deposited from these coils. The maximum electron temperature is about 4 *eV*. **Figure 75(b)** shows the gas temperature. The gas is injected in the chamber at room temperature (293 *K*) and is heated slightly above 400 *K*

in the reactor chamber.

The electron density (**Figure 75(c)**) has a torodial shaped maximum which is a direct consequence of the power deposition of both top and side coils. The maximum density is slightly shifted to the center of the chamber, compared to the power deposition and maximum electron temperature (cf. **Figure 75(a)**) due to the fact that electrons are lost rapidly to the walls at this low pressure. The rapid loss of electrons to the walls is also the reason why the plasma potential has a rather high positive value of about 100 *V*. Indeed, due to the high power from coils and substrate bias, the electrons are strongly accelerated and they can escape from the bulk plasma relatively easily due to the rather long mean free path (close to 1 *cm* at 10 *mTorr*).

Finally, **Figure 75(e)** and **75(f)** show the density profiles of SiH_2 and of the sum of all ions, respectively. SiH_2, together with SiH_3O, is the most important precursor for the gap filling process, as will be illustrated below. Its density is highest in the center of the reactor since SiH_2 is lost at the walls by deposition. The same is true for the profile of the ions that are neutralized at the reactor walls. The density profiles of most plasma species have similar shapes and are quite uniform above the wafer which is desired for a uniform deposition process. In the following sections, the effects of Ar and O_2 gas fraction will be discussed.

9.3 Effect of Ar gas fraction

As mentioned before, it was found that the above mentioned operating conditions, more specifically a gas mixture of 16 % Ar, 30 % SiH_4 and 54 % O_2, yielded a successful trench filling. To illustrate this, and to understand better why this specific gas mixture is optimal, the fraction of Ar is varied while keeping a constant SiH_4/O_2 ratio of nearly 1:2. Indeed, SiH_4 is considered the precursor for filling the trenches, while

oxygen will convert the SiH_x species into SiO_2, which is the desired isolating material for gap filling. The Ar fraction was varied from 5 % to 90 % and the reactor averaged plasma species densities are presented in **Figure 76(a - d)**.

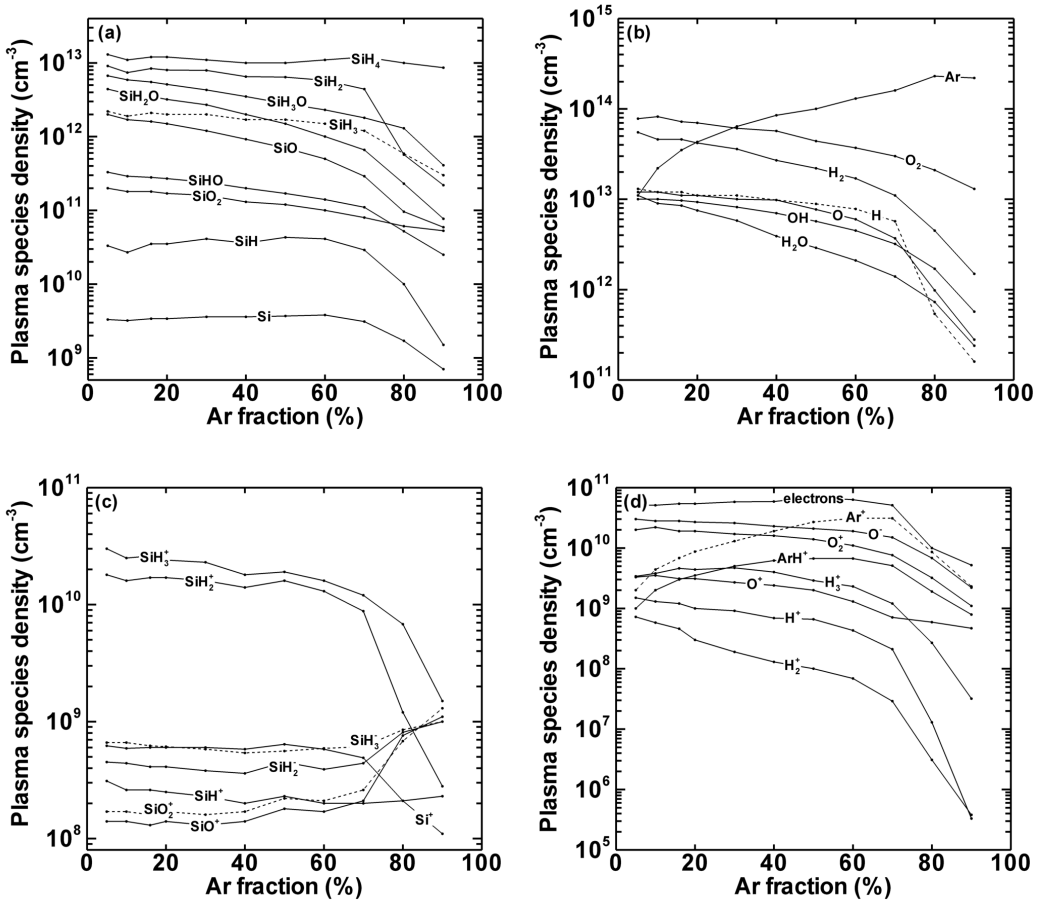

Figure 76. Reactor averaged species densities as a function of Ar gas fraction, divided over four plots for clarity: **(a)** neutral Si-containing species, **(b)** other neutral species, **(c)** Si-containing ions, **(d)** remaining ions and electrons. The other operating conditions are the same as in **Figure 75**, and the ratio between SiH_4 and O_2 was kept constant at nearly 1:2. Some lines are dashed for clarity.

The densities of all plasma species included in the model are shown

except for Ar* and O*, since they were found to be negligible compared to the densities of their ground state counterparts. For clarity, the results are subdivided in four plots showing **(a)** the neutral Si-containing species, **(b)** the remaining neutral species, **(c)** Si-containing ions and **(d)** remaining ions and electrons.

From **Figure 76** it can be concluded that Ar, O_2 and H_2 are the most abundant species in the plasma. Apart from Ar, all other neutral species densities decrease at higher Ar gas fraction, as expected. Although SiH_4 is the most abundant Si-containing species, it is consumed for more than 60 %. It should be realized that SiH_4 does not account for deposition since it is volatile, so the most important species for deposition are therefore SiH_2, SiH_3O, SiH_3 and SiH_2O. SiO, SiHO and SiO_2 have lower densities and fluxes to the substrate and are less important for the deposition process. This is certainly true for SiH and Si, which have very low densities, in spite of the fact that they have a sticking probability of 1. O and OH, which are present at high densities, will oxidize the surface, but they will not account for deposition as they do not contain Si. Finally, the H atoms have a flux close to that of O, and are important for abstracting H from the surface, facilitating chemical conversion of SiH_x to SiO_2.

Figure 76(c, d) illustrates the densities of the various ions as a function of Ar fraction. The total ion density is not presented, but it exhibits a similar trend as the electron density, depicted in **Figure 76(d)**. The total ion density is largely dependent on the total power deposition and varies therefore only slightly as expected. However, it tends to decrease at very high Ar fraction (80 - 90 %). The reason for this is explained as follows. SiH_4 is ionized more easily than Ar because it has a lower ionization threshold (i.e. 12.20 *eV* to form SiH_3^+ and 13.50 *eV* to form SiH_2^+, compared to 15.76 *eV* to form Ar^+). Therefore, a higher Ar fraction, or a lower fraction of silane, will result in less total ionization and a lower

total ion density. On the other hand, when the Ar fraction increases, the mixture tends to change from a molecular plasma to an atomic plasma. Since atoms cannot be rotationally or vibrationally excited, the electrons have more energy for ionization processes in an atomic gas mixture. Both effects seem to result in a practically constant total ion density when the Ar fraction is varied. Only at > 80 % Ar the first effect seems to dominate and eventually results in a decrease of the total ion density. The densities of Ar^+ and ArH^+ first increase with Ar gas fraction and then decrease at even higher Ar fraction (**Figure 76(d)**) for a similar reason.
The most important ions that will account for sputtering of the substrate are SiH_3^+, SiH_2^+ and O_2^+ at low Ar fraction, but at an Ar fraction above 40 %, Ar^+ and ArH^+ become more important as expected (**Figure 76(c, d)**).
Some other less important Si-containing ions (i.e. SiH_2^-, SiH_3^-, SiO^+ and SiO_2^+) increase in density when the silane fraction is reduced, which might be unexpected at first sight (**Figure 76(c)**). The most important losses for these ions are neutralization with ions of opposite charge. SiH_2^- and SiH_3^- are lost mostly through neutralization with H^+ and H_2^+, whose densities decrease faster than those of the Si-containing species at higher Ar gas fraction, as can be seen in **Figure 76(d)**. Similarly, SiO^+ and SiO_2^+ are lost due to neutralization with O^-, the most abundant negative ion, which also decreases in density at higher Ar percentage.
The resulting gap filling process is dependent on two major effects, namely the deposition rate of low-volatile Si-containing species and the sputtering by ions. By varying the Ar gas fraction, we can clearly see a different contribution from both effects. **Figure 77** shows the total flux of species that account for deposition, together with the total flux of ions accounting for sputtering, both on the left axis. On the right axis, the resulting deposition rate is plotted, which is a result from the analytical surface model (SKM; section 3.4.6). As mentioned before, the most important species that account for deposition are SiH_2, SiH_3O, SiH_3 and

SiH_2O. Their relative contributions to the total deposition flux resemble those for the reactor averaged densities as presented in **Figure 76(a)**. The same is true for the contributions of the total ion flux where SiH_3^+, SiH_2^+ and O_2^+ at low Ar fraction, and Ar^+ at an Ar fraction above 40 %, are the most important ions for sputtering (**Figure 76(c, d)**).

As is clear from **Figure 77**, the depositing flux decreases with increasing Ar fraction as expected, while the ion flux is practically constant, except at higher Ar fraction. As a result, the ratio between deposition and sputtering decreases at higher Ar fraction. For example, at 10 % Ar, the deposition flux is about 35 times higher than the ion flux, while at 90 % Ar, this ratio is close to 10. It should be noted that not all species will deposit since the probability for sticking/deposition is not always 1 for all species (see section 4.7.2). In addition, the ions have high energy (close to 600 *eV*) so that more than one surface atom/molecule can be sputtered per ion. It is clear from **Figure 77** that this balance between deposition and sputtering has a profound effect on the resulting deposition rate, which decreases more or less linearly with Ar fraction.

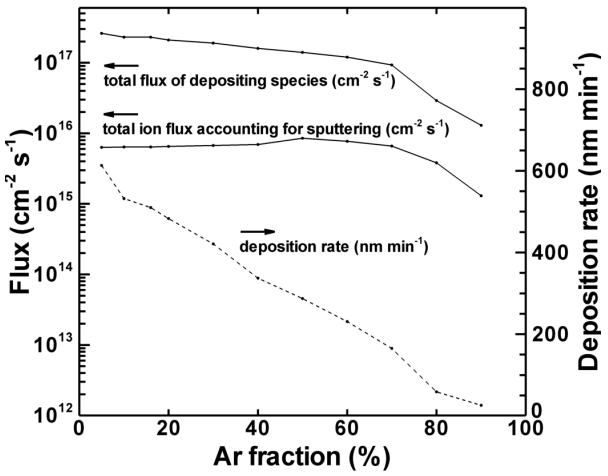

Figure 77. Total flux of all species that account for deposition (left axis), and of all ions that account for sputtering (left axis), as well as the calculated deposition rate (right axis) as a function of Ar gas fraction.

At a low Ar fraction of 5 %, the deposition rate is around 500 - 600 *nm min*$^{-1}$, while at an Ar fraction of 90 % the deposition rate has dropped to a value close to zero.

It should be noted that the deposition rate is calculated in the analytical surface model which does not take microtrench structures into account. It treats the surfaces of the substrate and the reactor walls as a one-dimensional line in the 2D geometry, so that only the upper layer surface properties are calculated. The deposition rate is simply predicted by counting the number of deposition reactions while substracting the number of sputter reactions. More detailed results on the deposition process in the trenches can be seen in **Figure 78(a - c)** which illustrates calculation results obtained with the microscale Monte Carlo feature profile model (FPMCS; section 3.4.8).

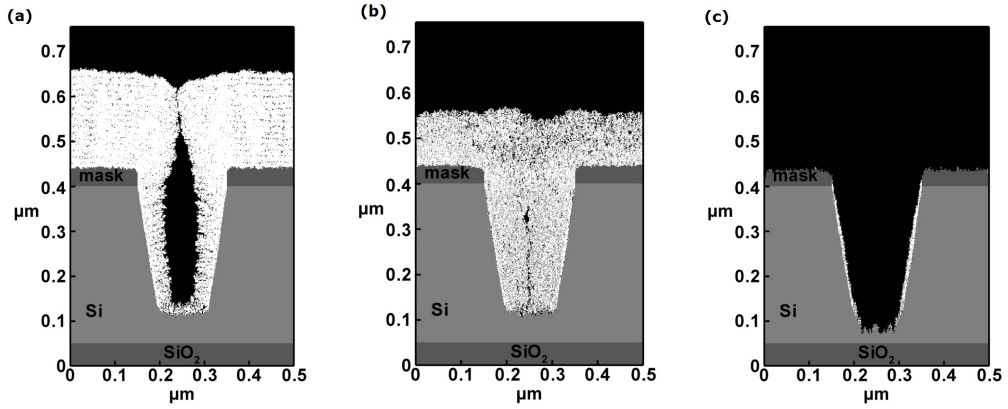

Figure 78. Calculated deposition profiles at **(a)** 5 % Ar, where a void is formed, **(b)** 16 % Ar where a proper gap filling process takes place, and **(c)** 80 % Ar, where trench damage occurs.

At low Ar percentage (5 %, **Figure 78(a)**), the deposition flux is very high, resulting in dominant deposition over sputtering, as was also shown in **Figure 77**. This results in serious void formation. Hence, the deposited layer is not appropriate for device fabrication due to a lack of electronic and mechanical stability. Indeed, during wafer processing, the wafer is

heated and cooled down on various occasions, increasing the risk of structural damage if voids are present in the layer.

At 16 % Ar (**Figure 78(b)**), the deposition rate is slightly lower, but void formation is inhibited as desired. Finally at higher Ar fraction (> 60 %; **Figure 78(c)**), there is a strong competition between sputtering of the layer and deposition, resulting in deposition on the sidewalls, but also in damaging the device at the bottom and the mask, which must be avoided of course.

The chemical composition of the deposited layer was calculated in the analytical surface model and was found to be $SiH_{0,5}O_{1,14}$. This chemical composition was predicted to be roughly the same for all investigated Ar gas fractions (ranging from 5 % to 90 %). It should be noted, however, that in the analytical surface model only the properties of the top surface monolayer are calculated. As mentioned before, the SiO_2 layer becomes Si-rich at the surface due to preferential sputtering of oxygen. This is why a rather low ratio of 1.14 is predicted for O:Si in the chemical composition of the top surface layer. In the underlying layers, the composition is closer to SiO_2, as can be concluded from **Figure 78** where the deposited layer (white) has a near-SiO_2 composition.

From these results it can be concluded that the shape of the deposited layer inside the trenches can be controlled by varying the ratio between deposition and sputtering. This, in turn, can be achieved by varying the fractions of Ar and precursor gas (SiH_4) in the gas mixture. We found that an Ar gas fraction close to 16 % yields optimal conditions for proper gap filling. This value is indeed found back in typical gap filling recipes in the STI process [198].

Finally, it should be realized that in the plasma, not a very large fraction of the silane species is oxidized, as was clear from **Figure 76**, while the deposited layer is close to SiO_2. This indicates that mostly silane species with high hydrogen content, such as SiH_2 and SiH_3, deposit and that

they are subsequently oxidized on the surface (to SiO_2) rather than in the plasma. This is schematically illustrated in **Figure 79**.

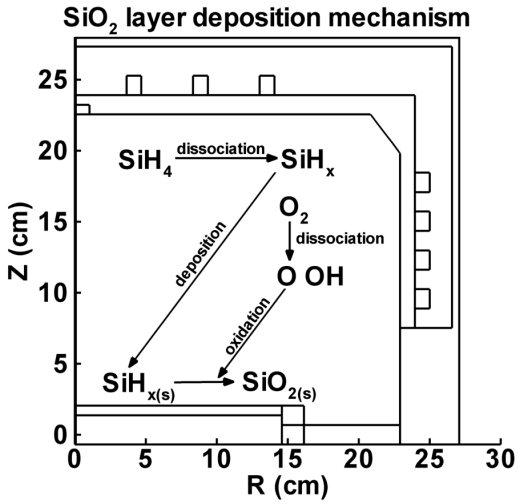

Figure 79. Schematic illustration of the mechanism for deposition of a SiO_2 layer from an $Ar/SiH_4/O_2$ plasma.

9.4 Effect of SiH_4/O_2 ratio

The plasma characteristics and deposition process were also numerically investigated while varying the SiH_4/O_2 ratio. As mentioned before, we found that the trenches are filled succesfully with SiO_2 when applying a gas mixture of 16 % Ar, 30 % SiH_4 and 54 % O_2. To understand why this specific SiH_4/O_2 ratio gives rise to successful gap filling, we have varied the oxygen fraction between 20 % and 80 %, while keeping the Ar fraction constant at 16 %. The plasma species densities are presented in **Figure 80(a - d)** as a function of O_2 gas fraction. The densities are again subdivided into four plots for the sake of clarity. **Figure 80(a)** shows densities of the neutral Si-containing species, **80(b)** of the remaining neutrals, **7(c)** of the Si-containing ions and **80(d)** of the remaining ions and free electrons. The Ar* and O* densities are not plotted due to their

low values compared to the densities of their ground state equivalents.

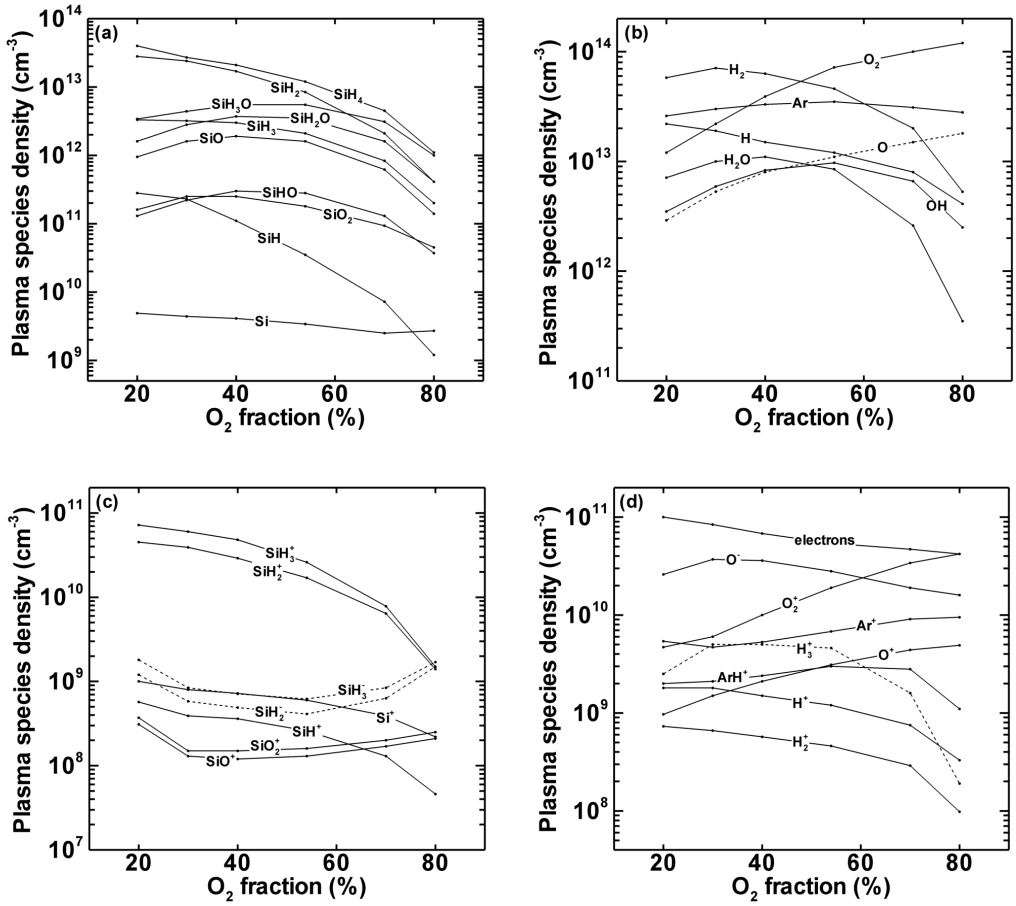

Figure 80. Reactor averaged species densities as a function of O_2 gas fraction, while the Ar fraction was kept constant at 16 %, divided over four plots for clarity: **(a)** neutral Si-containing species, **(b)** other neutral species, **(c)** Si-containing ions, **(d)** remaining ions and electrons. The other operating conditions are the same as in **Figure 75**.

The neutral species densities change as a function of O_2 fraction as expected (**Figure 80(a, b)**). Indeed, when the fraction of O_2 is increased, the densities of all Si-containing species decrease, while the reaction products between oxygen and silane (i.e. SiHO, SiH_2O, SiH_3O, SiO and SiO_2) tend to show maxima at intermediate fractions of O_2 and SiH_4. Moreover, the Si-containing ions all decrease in density upon increasing

oxygen fraction, except SiH_2^-, SiH_3^-, SiO^+ and SiO_2^+ which exhibit local minima at a certain O_2 fraction for the same reasons as described in section 9.3 when the Ar fraction was varied. At higher O_2 fraction and lower silane fraction, less ions are generated and the total ion density (and electron density) decreases slightly, as also discussed in section 9.3. Both the amounts of precursor gas (SiH_4) and oxidising agent (O_2) change as a function of O_2 gas fraction, so we can expect a variation in deposition rate, as well as in chemical composition of the deposited layer. **Figure 81** shows the total flux of depositing species (SiH_3, SiH_2, SiH, Si, SiHO, SiH_2O, SiH_3O, SiO and SiO_2), the total ion flux and the fluxes of the oxidizing species (O_2, O and OH) on the left axis, as well as the resulting deposition rate on the right axis, as a function of O_2 percentage.

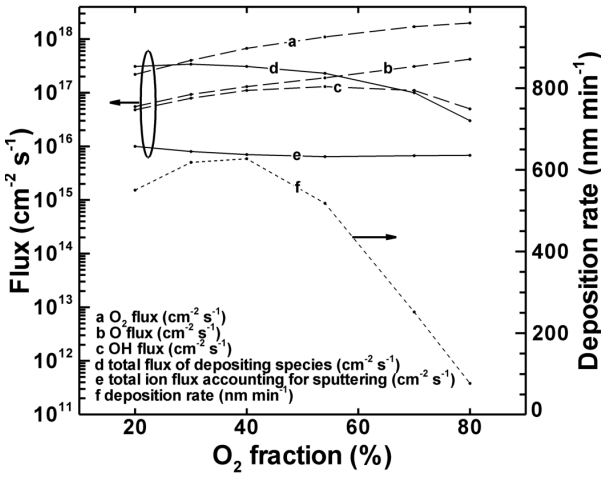

Figure 81. (Left axis) wafer averaged fluxes of **(a)** O_2, **(b)** O, **(c)** OH, **(d)** all species that account for deposition and **(e)** all ions that account for sputtering, as a function of O_2 gas fraction. (Right axis) calculated deposition rate as a function of O_2 gas fraction **(f)**.

Similar to the case where the Ar fraction was varied (**Figure 77**), the flux of depositing species is almost 40 times higher than the ion flux at the lowest O_2 fraction (and highest silane content) investigated, whereas it is

only one order of magnitude higher at 80 % O_2 (and 4 % of SiH_4). This results in a decrease of the deposition rate at increasing O_2 fraction as expected.

Similar conclusions can be drawn for the shape of the deposited layer in the trench as shown in **Figure 82(a - c)**. If the deposition rate is close to 600 *nm min*$^{-1}$, at a fraction of 40 % O_2 or lower, deposition is dominant and a void is created (see **Figure 82(a)**). As mentioned earlier, a successful filling process occurs at 54 % O_2 (see **Figure 82(b)**, which corresponds in fact to the same conditions as given in **Figure 78(b)**). At very low deposition rate, i.e. above 60 % of O_2, the mask and bottom of the trench are damaged, as is clear from **Figure 82(c)**.

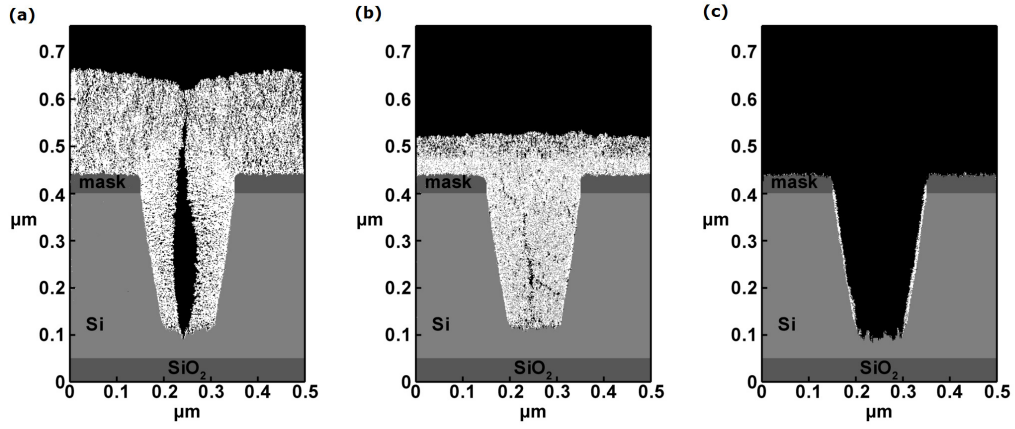

Figure 82. (a) Calculated deposition profiles at (a) 30 % O_2, where a void is formed, (b) 54 % O_2 where a proper gap filling process occurs, (c) 70 % O_2, where trench damage occurs.

It is interesting to note from **Figure 81** that the deposition rate increases from 20 % to 40 % O_2 even when the precursor gas fraction is decreased. The explanation for this is that, at low oxygen fraction, the species that accounts most for deposition is SiH_2, which does not deposit with a probability of unity. If more oxygen is present, SiH_xO (x = 1 - 3) species

become more important for deposition, and they are characterized by a deposition probability equal to 1, and this explains the increase in the total deposition rate.

Naturally, the fluxes of the oxidizing agents increase with O_2 fraction, so we can expect an increase in oxygen content in the chemical composition of the deposited layer. The chemical composition of the top surface layer, or more specifically, the surface fraction of deposited species in this layer, is plotted in **Figure 83** as a function of O_2 gas fraction.

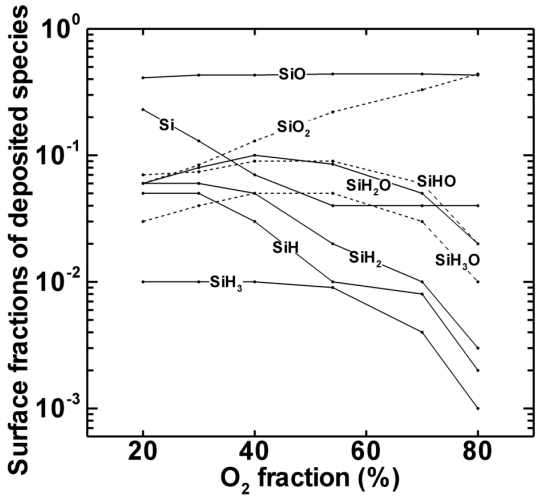

Figure 83. Calculated surface fractions of deposited species, or in other words, chemical composition of the top surface layer of the deposited layer in the trench as a function of O_2 content in the gas mixture.

It should be noted that this is, again, the chemical composition of the top surface layer which should have a lower oxygen content than the bulk of the deposited layer due to preferential sputtering of oxygen from the surface. For this reason, the fraction of clean Si on the surface is relatively high (23 %) at low oxygen content. At the lowest investigated O_2 gas fraction of 20 % (and consequently a SiH_4 fraction of 64 %), the deposited layer has a chemical composition of $SiH_{0,49}O_{0,75}$ which is

indeed Si-rich. However at high O_2 gas fraction (90 %), the composition is $SiH_{0,12}O_{1,40}$. As mentioned before, the bulk deposited layer contains even more oxygen, being close to SiO_2 with a negligible amount of hydrogen.

9.5 Conclusions

$Ar/SiH_4/O_2$ ICPs, used for the filling of Si trenches with SiO_2 by means of PECVD as applied in STI, have been investigated numerically. The gas fractions of all three components were varied and the influence on the plasma characteristics and on the gap filling process was discussed. It was found that the most important species that account for deposition are SiH_2, SiH_3O, SiH_3 and SiH_2O while the most important ions that account for sputtering of the layer are SiH_3^+, SiH_2^+, O_2^+ and Ar^+.

The Ar gas fraction was varied while the SiH_4/O_2 ratio was kept fixed at around 1:2. It was found that the deposition process is strongly influenced by the ratio of deposition versus sputtering. By varying the Ar fraction, this ratio can be tuned until a desired deposition rate is achieved. If the Ar fraction is too low (< 16 %), the deposition rate is dominant over sputtering, creating an undesired void when the trench is filled. At an Ar fraction above 60 %, the deposition rate is too slow, resulting in damaging of the bottom of the trench and of the mask by sputtering. From the results it can be concluded that a gas mixture of 16 % Ar, 30 % SiH_4 and 54 % O_2 results in a proper trench filling process.

The SiH_4/O_2 ratio was varied while the Ar fraction was kept constant at 16 %, and it was found that both the deposition rate and the chemical composition of the deposited layer were influenced. At the lowest investigated O_2 fraction of 20 %, which yields a SiH_4/O_2 ratio of 3.2:1, the chemical composition of the top surface of the deposited layer was calculated as $SiH_{0,49}O_{0,75}$ which is considered Si-rich due to preferential sputtering of oxygen. The bulk of the deposited layer has a higher oxygen

fraction, yielding a composition close to SiO_2, even at a low oxygen gas fraction of 20 %, as could be concluded from the trench profile results where the bulk deposited layer was calculated.

Finally, it was found that oxidised Si-containing plasma species (SiH_3O, SiH_2O, SiHO, SiO and SiO_2) did not constitute the largest part of the plasma composition, indicating that rather low-volatile silane species (mainly SiH_3, SiH_2 as well as SiH_3O and SiH_2O) are deposited and subsequently become oxidized, instead of being directly oxidized in the plasma before they deposit on the walls.

Summary

Over the last few decades, integrated circuits have caused a revolution in the microelectronics industry and can be found in virtually all electronic equipment. To increase functionality and power of the electronic devices, integrated circuits have consistently been manufactured with smaller feature sizes over the years, allowing more components (i.e. transistors) to be packed on each chip. However, successfully shrinking the active components in the 21st century is not obvious. Since the dimensions of parts of the components are currently reaching the atomic-scale-range, the downscaling of reliable electronic devices becomes increasingly more difficult and eventually limited.

Plasma etching and deposition are currently the only commonly used technologies that meet the high resolution requirements for fabricating nanoscale electronic devices. Indeed, the creation of active components happens through various processing steps, and a significant number of these steps involve plasmas. In particular, inductively coupled plasmas (ICPs) are commonly applied for various processing steps such as etching and deposition of surface layers because, in this type of reactors, both the flux and energy of the ions arriving at the substrate can be controlled separately to allow for a proper desired surface process.

The first step in chip manufacturing, even before transistors are fabricated, is shallow trench isolation (STI). Indeed, the active components (transistors) that are built upon the substrate (i.e. Si wafer)

must be isolated from each other to prevent current leakage between adjacent components. Therefore, to isolate active areas on the wafer surface, shallow trenches are etched in the Si and subsequently filled with isolating material such as SiO_2. The STI etching step is typically performed with an $Ar/Cl_2/O_2$ plasma since chlorine shows good etch selectivity between Si and the mask, while O_2 protects the sidewalls of the trenches from lateral etching.
For the STI deposition step, usually an $Ar/SiH_4/O_2$ plasma is applied, where SiH_4 is the precursor for deposition of a SiH_x layer, while O_2 will convert the layer to form SiO_2 during deposition.

Not only the transistors need to shrink, but also the isolating trench width that separates them from each other. In order to be able to improve and optimize the STI process, a good insight in the underlying mechanisms is therefore needed. It is, however, experimentally not obvious to obtain a great deal of information on the plasma properties during the etching or deposition, making it difficult to improve these processes. For this reason, numerical investigations can be an interesting alternative or addition.

The goal of this work was, therefore, to obtain a better understanding of the etching and deposition processes as applied in STI by performing numerical simulations, as well as experiments for validation. The two processing steps of STI under study in this work were the trench etching of Si with an $Ar/Cl_2/O_2$ ICP and the deposition of SiO_2 with an $Ar/SiH_4/O_2$ ICP, as mentioned above. The model applied for these investigations is the so-called hybrid plasma equipment model (HPEM), developed by Kushner and co-workers. This model was briefly explained in **Chapter 3**.

In **Chapter 4**, it was illustrated how the complex plasma and surface chemistries are translated into a reaction set which can be implemented in the computational model to predict the plasma properties under various operating conditions. Reaction sets were presented for the bulk plasma chemistry of, on the one hand, $Ar/Cl_2/O_2$ plasmas used for etching of Si, and on the other hand, $Ar/SiH_4/O_2$ plasmas used for deposition of SiO_2, as well as detailed reaction sets describing the possible surface processes, such as chemical etching, surface oxidation, sputtering and deposition reactions.

In **Chapter 5**, the effects of typical operating conditions, such as pressure, power and substrate bias, on the general Ar/Cl_2 plasma properties and resulting etch process were investigated both numerically and experimentally. This investigation was carried out in an early stage of the work for an Ar/Cl_2 plasma where the O_2 reaction set was not yet included in the simulations. In general it was found that changing the pressure allows for tuning the ratio between the neutral flux and the ion flux. In this way, the balance between chemical etching and (physical) sputtering can be altered. Moreover, a higher pressure results in a lower average ion energy towards the wafer, as well as a broadened angle distribution. For a highly anisotropic etching process, a low operating pressure is therefore more appropriate. By varying the substrate bias, the energy of the ions sputtering the surface can be altered and subsequently the etch rate can be controlled. However, increasing the bias also widens the energy distribution of the ions when arriving at the substrate, increasing the risk of (mask) damage at too high bias voltage. Finally, the source power will influence the amount of charged species in the plasma and hence the fluxes of ions towards the wafer. By tuning the source power, also the balance between chemical etching and sputtering can be controlled for a desired wafer process.

Subsequently, in **Chapter 6**, by adding O_2 to the Ar/Cl_2 gas mixture, the etch process was investigated under various operating conditions, including gas mixtures with different ratios of Cl_2/O_2, and it was studied which plasma properties have the most significant influence on the resulting etch rate. These were found to be (i) the fluxes of the various plasma species towards the wafer, (ii) the energy of the species (especially ions) when arriving at the wafer and (iii) the angle at which they collide with the surface. The latter is important for anisotropic trench etching. Moreover, it was found that at higher O_2 content, the etch rate drops abruptly and significantly to a value close to zero due to dominant oxidation of Si over etching.

The simultaneous etching and deposition processes on the substrate as a function of Cl_2/O_2 gas ratio, as briefly discussed in Chapter 6, was investigated in more detail experimentally and numerically in **Chapter 7**, including, at this stage, also $SiCl_{0-4}$ and SiO_{1-2} etch products in the calculations. When increasing the O_2 gas fraction, different etching regimes can occur at the wafer. It was found that at very low oxygen content, Si is etched with some undesired undercutting effects, while at slightly higher O_2 content, the sidewalls are protected by an oxide layer preventing lateral etching for a desired trench etching process. Adding even more O_2 to the mixture will eventually result in the formation of a rough surface layer where there is a balance between etching and redeposition of etch products. Finally, at even higher oxygen flow, the oxidation is dominant and practically no Si is etched at all. Moreover, instead of etching, an actual oxide layer is grown in the center of the wafer during etching at the border of the wafer. It was found that the growth of the oxide layer is due to the redeposition of low-volatile etch products present in the plasma.

It is common to clean the chamber and introduce a new wall coating in between etch experiments because this increases the wafer-after-wafer etching reproducibility and it can have beneficial effects for the etching process in terms of etch rate and uniformity. This formed the subject of the studies discussed in **Chapter 8**. For this purpose, two computational case studies have been performed; one where the walls are considered "clean" without loading oxygen into the plasma, and the other where a SiO_2 coating is present in the chamber. In the latter case, O can be sputtered from the surface and loaded into the plasma. It was found that the oxygen content in the plasma was very low and did not affect the etch rate directly. However, the oxy-chloride layer formed at the walls cannot be etched by Cl, reducing the wall loss probability of Cl and hence increasing the Cl radical density in the bulk plasma. This, in turn, has beneficial effects in terms of etch rate and etch uniformity.

Finally, in **Chapter 9**, the SiO_2 deposition process was numerically investigated as well, by varying the gas fractions of Ar, SiH_4 and O_2 in the gas mixture. Under these different conditions the properties of the plasma were investigated as well as the resulting trench filling process. By varying the Ar gas fraction, the balance between the deposition rate and the sputter rate can be controlled for an optimal trench filling process. Indeed, it was found that, at too low Ar fraction, deposition was dominant which resulted in void formation. Furthermore, at too high Ar fraction, sputtering is dominant which results in trench damage. A proper balance was found at 16 % Ar, 54 % O_2 and 30 % SiH_4. By changing the ratio of SiH_4/O_2, the chemical composition of the deposited layer can be altered. However, at the lowest O_2 fraction under study in this work (20 %), the bulk deposited layer still had a composition close to SiO_2, as desired.

In conclusion, the studies performed during this PhD work contribute to a better understanding of the bulk plasma and the surface processes during plasma treatment (i.e. etching of Si and deposition of SiO_2). By combining modeling results with experimental data, more information can be obtained on the underlying physics and chemistry, and this can eventually lead to achieving the goals, i.e. successfully fabricate integrated circuits with smaller dimensions.

One of the future challenges in the microelectronics industry is that device dimensions continue to shrink, and leakage current becomes more and more pronounced. For this purpose, new architectures and new materials with better electrical properties are currently investigated. It might therefore be of interest to use the model applied in this work to investigate also other types of chemistries and reactor geometries, which will be used in the future to fabricate even smaller devices, provided that sufficient data is available to properly implement the chemical reactions for both the bulk plasma as well as the surface processes.

Samenvatting

In de afgelopen decennia hebben geïntegreerde circuits een ware revolutie teweeg gebracht in de micro-elektronica industrie en zijn ze te vinden in zo goed als alle elektronische apparaten. Om de functionaliteit en het vermogen van het elektronisch apparaat te kunnen verhogen, zijn geïntegreerde circuits in de afgelopen jaren steeds gefabriceerd met kleinere afmetingen zodat meer actieve componenten (zoals transistoren) kunnen geplaatst worden op een computerchip. Het succesvol verkleinen van de actieve componenten is echter niet evident in de 21ste eeuw. Omdat de onderdelen van de transistoren stilaan afmetingen aannemen van atomaire schaal, wordt het verkleinen van betrouwbare elektronische apparaten steeds moeilijker en uiteindelijk beperkt.

Plasma etsen en depositie zijn momenteel de enige vaak gebruikte technologieën die voldoen aan de hoge-resolutie behoeften voor het fabriceren van elektronische apparaten op nanochaal. Het fabriceren van een computerchip omvat vele stappen, waar een significant deel van deze stappen gebeurt door middel van plasma's. In het bijzonder worden vooral inductief gekoppelde plasma's gebruikt bij verscheidene fabricatiestappen zoals etsen en depositie omdat, in dit type van reactors, zowel de flux als de energie van de ionen die arriveren aan het substraat afzonderlijk kunnen gecontroleerd worden voor het bereiken van het gewenste oppervlakteproces.

De eerste stap in het creëren van een computerchip, zelfs voor dat de

transistoren worden gebouwd, is het proces genaamd “shallow trench isolation” (STI). De transistoren die worden opgebouwd vanop het substraat (een Si wafer) moeten namelijk geïsoleerd worden van elkaar om lekstroom te vermijden. Dus, om de actieve gebieden te isoleren van elkaar worden eerst geulen geëtst in het Si substraat die vervolgens opgevuld worden met isolatormateriaal (SiO_2). Het STI etsproces gebeurt typisch met een $Ar/Cl_2/O_2$ plasma omdat chloor goede selectiviteit vertoont tussen het etsen van Si en het masker, terwijl O_2 de zijwanden van de geul beschermt tegen ongewenst lateraal etsen.
Voor het STI depositieproces wordt typisch een $Ar/SiH_4/O_2$ plasma aangewend omdat SiH_4 de precursor is voor depositie van SiH_x terwijl O_2 de gedeponeerde laag zal oxideren tot een gewenste SiO_2 laag.

Niet alleen de transistoren moeten verkleind worden, maar ook de breedte van de geulen die de transitoren isoleren van elkaar. Om het STI proces te kunnen optimaliseren, is daarom een goed inzicht nodig in de onderliggende mechanismen. Het is echter experimenteel niet evident om veel informatie te verkrijgen over de plasma-eigenschappen tijdens etsen of depositie, wat het niet gemakkelijk maakt om het STI proces te optimaliseren. Om deze reden zijn numerieke simulaties een interessant alternatief of op zijn minst complementair aan experimenten.

Het doel van dit onderzoek was daarom om een beter inzicht te verkrijgen in de ets- en depositieprocessen zoals toegepast in STI, door zowel numerieke simulaties uit te voeren als experimenten om de simulaties te kunnen valideren. De twee processen die onderzocht werden in dit doctoraatswerk zijn het etsen van Si met een $Ar/Cl_2/O_2$ plasma en het deponeren van SiO_2 in de etskanaaltjes met een $Ar/SiH_4/O_2$ plasma zoals eerder vermeld. Het computationeel model gebruikt voor dit onderzoek is het zogenaamde “hybrid plasma equipment model” (HPEM), dat

ontwikkeld werd door Kushner en medewerkers. Dit model werd kort beschreven in **Chapter 3** van dit doctoraatswerk.

In **Chapter 4** werd geïllustreerd hoe de complexe plasma- en oppervlaktechemie werden vertaald naar een reactieset die in het computationeel model kan worden geïmplementeerd om de plasma-eigenschappen te voorspellen onder verschillende procesvoorwaarden. Reactiesets werden besproken voor de bulk plasma chemie van enerzijds een $Ar/Cl_2/O_2$ plasma gebruikt voor etsen en anderzijds een $Ar/SiH_4/O_2$ plasma gebruikt voor depositie. Bovendien werden ook reactiesets besproken die de oppervlakteprocessen beschrijven, zoals chemisch etsen, oxidatie, sputtering en depositie.

In **Chapter 5** werden de effecten van typische procesparameters zoals druk, vermogen en spanning aan het substraat, op het Ar/Cl_2 plasmagedrag en het etsproces onderzocht door middel van simulaties en experimenten. Dit onderzoek werd uitgevoerd in een vroeg stadium van dit doctoraatswerk toen O_2 reacties nog niet toegevoegd waren aan de Ar/Cl_2 reactieset. Er kon worden besloten dat, door het variëren van de druk, de verhouding tussen de fluxen van neutralen en ionen kon worden gecontroleerd. Op deze manier kan een gewenste balans verkregen worden tussen chemisch etsen en (fysisch) sputteren. Bovendien resulteert een hogere druk in een lagere gemiddelde energie en een bredere hoekverdeling van de ionen die het substraat bombarderen. Voor een anisotroop etsproces is daarom een lagere druk meer geschikt. Door het variëren van de substraatspanning kan de energie van de ionen die het oppervlak bombarderen worden gecontroleerd, wat een direct effect heeft op de etssnelheid. Een hogere spanning verbreedt echter ook de energiedistributie zodat bij hogere ionenenergie er meer kans bestaat op beschadiging (van het masker).

Tenslotte heeft het aangelegd vermogen een invloed op de hoeveelheid ionen die gecreëerd worden in het plasma en daarom ook op de ionenflux naar het substraat. Door het variëren van het vermogen kan daardoor de verhouding tussen chemisch etsen en sputteren ook gecontroleerd worden voor het gewenste oppervlakteproces.

Vervolgens werd in **Chapter 6** het etsproces verder onderzocht onder verschillende reactorcondities, waaronder verschillende Cl_2/O_2 verhoudingen, nadat O_2 aan het Ar/Cl_2 gasmengsel werd toegevoegd. Er werd onderzocht welke plasma-eigenschappen er een invloed hebben op het etsproces. Deze zijn (i) de fluxen van de verschillende plasmadeeltjes naar het substraat, (ii) de energie waarmee de deeltjes arriveren aan het substraat (wat vooral belangrijk is voor de ionen die sputteren), en (iii) de hoek waaronder de deeltjes botsen aan het oppervlak, wat belangrijk is voor het anisotropisch etsen van een Si geul. Bovendien kon er worden besloten dat bij een hogere O_2 fractie de etssnelheid abrupt en significant afnam omdat oxidatie hier dominant was ten opzichte van chemisch etsen door chloor.

De gelijktijdige ets- en depositieprocessen aan het substraat, als functie van de Cl_2/O_2 gasverhouding zoals kort vermeld in Chapter 6, werden meer gedetailleerd onderzocht door middel van experimenten en simulaties in **Chapter 7**. In dit stadium van het doctoraatswerk werden ook etsproducten zoals $SiCl_{0-4}$ en $SiO_{1,2}$ mee in rekening gebracht in de simulaties. Bij het geleidelijk verhogen van de zuurstoffractie in het plasma kunnen verschillende “ets-regimes” plaatsvinden. Inderdaad, bij zeer lage zuurstoffractie wordt Si succesvol geëtst, maar met wat ongewenste “undercutting”. Bij een iets hogere zuurstoffractie worden de zijwanden van de geul beschermd zodat een gewenst etsproces kan plaatsvinden. Als vervolgens de zuurstoffractie nog meer toeneemt, kan

er een ruwe oppervlaktelaag gevormd worden door een precies evenwicht tussen etsen en depositie van etsproducten. Tenslotte, als er nog meer zuurstof aanwezig is in het gas, wordt Si helemaal niet meer geëtst maar wordt er een laag gegroeid op het substraat. Dit is mogelijk omdat etsproducten die geëtst werden aan de rand van de wafer, kunnen redeponeren in het centrum van de wafer met groei van een oxidelaag tot gevolg.

Het is gebruikelijk om de reactorkamer te reinigen en een nieuwe coating aan te brengen tussen ieder etsexperiment. Dit wordt gedaan om de reproduceerbaarheid van wafer-na-wafer etsprocessen te verhogen. Bovendien kan een coating gunstig zijn voor het etsproces in termen van etssnelheid en uniformiteit. Dit werd verder onderzocht in **Chapter 8**. Hiervoor werden twee verschillende situaties gedefinieerd in de simulaties. Enerzijds werd een reactor gedefinieerd met “zuivere” wanden (die per definitie geen zuurstof loslaten in het plasma), en anderzijds werd een reactor gedefinieerd waarin een SiO_2 coating was aangebracht. In de tweede situatie kan zuurstof gesputterd worden van de coating en in het plasma terechtkomen. Er werd echter gevonden dat de zuurstoffractie in het plasma in de gecoate kamer zeer laag was en geen direct effect had op het etsproces. De oxy-chloride laag die gevormd wordt tijdens het etsproces zorgt er echter wel voor dat veel minder Cl wordt verloren aan de wand in de gecoate kamer vergeleken met de “zuivere” kamer. Dit had tot gevolg dat de densiteit en uniformiteit van Cl atomen verhoogde in de gecoate kamer, wat resulteerde in een hogere en meer uniforme etssnelheid.

Tenslotte werd in **Chapter 9** het SiO_2 depositieproces onderzocht door middel van simulaties. De invloed van de verschillende gascomponenten op het plasma en het depositieproces werd onderzocht door verscheidene

gasverhoudingen te definiëren tussen Ar, SiH_4 en O_2. Door de Ar fractie te variëren, kon de verhouding tussen depositie en sputteren gecontroleerd worden voor een optimaal depositieproces. Inderdaad, bij een te lage Ar fractie is depositie dominant wat resulteert in de vorming van holtes in de gedeponeerde laag. Is de Ar fractie te hoog, dan is sputtering dominant zodat er beschadiging van de geul plaatsvindt in plaats van depositie. Er werd gevonden dat de geulen succesvol werden opgevuld bij een gasmengsel van 16 % Ar, 30 % SiH_4 en 54 % O_2. Door het variëren van de SiH_4/O_2 verhouding kon de chemische samenstelling van de gedeponeerde laag gecontroleerd worden. Nochtans had bij de laagste O_2 fractie onderzocht in dit werk (20 %) de gedeponeerde laag nog altijd een chemische samenstelling in de buurt van SiO_2, zoals gewenst.

Tot slot kan worden geconcludeerd dat de studies uitgevoerd in dit doctoraatswerk bijdragen tot het verkrijgen van een beter inzicht in zowel de bulk plasma-eigenschappen als de ets- en depositieprocessen. Door simulaties te combineren met experimentele data kan er meer informatie verkregen worden over het onderzochte proces, wat uiteindelijk kan leiden tot het bereiken van het doel: het succesvol fabriceren van geïntegreerde circuits met kleinere afmetingen.

Uitdagingen voor de toekomst zijn het nog verder verkleinen van de elektronische componenten omdat lekstroom hier steeds belangrijker wordt. Nieuwe geometrieën en materialen met betere elektrische eigenschappen worden daarom tegenwoordig volop ontwikkeld. Het model toegepast in dit doctoraatswerk kan ook gebruikt worden om andere soorten chemie en reactorgeometrieën te onderzoeken, mits er voldoende data ter beschikking is om de reactiesets voor zowel het bulk plasma als de oppervlakteprocessen naar behoren te implementeren in het model.

Publications

1. **S Tinck**, W Boullart and A Bogaerts, Simulation of an Ar/Cl_2 inductively coupled plasma: study of the effect of bias, power and pressure and comparison with experiments, J. *Phys. D: Appl. Phys.* 41 (2008) 065207

2. **S Tinck**, W Boullart and A Bogaerts, Investigation of etching and deposition processes of $Cl_2/O_2/Ar$ inductively coupled plasmas on silicon by means of plasma–surface simulations and experiments, *J. Phys. D: Appl. Phys.* 42 (2009) 095204

3. **S Tinck** and A Bogaerts, Computer simulations of an oxygen inductively coupled plasma used for plasma-assisted atomic layer deposition, *Plasma Sources Sci. Technol.* 20 (2011) 015008

4. **S Tinck**, W Boullart and A Bogaerts, Modeling $Cl_2/O_2/Ar$ inductively coupled plasmas used for silicon etching: effects of SiO_2 chamber wall coating, *Plasma Sources Sci. Technol.* 20 (2011) 045012

5. **S Tinck**, D Shamiryan and A Bogaerts, Simultaneous etching and deposition processes during the etching of silicon with a $Cl_2/O_2/Ar$ inductively coupled plasma, *Plasma Process. Polym.* 8 (2011) 490-99 *Selected as* **Cover picture**

6. **S Tinck** and A Bogaerts, Modeling $SiH_4/O_2/Ar$ inductively coupled plasmas used for filling of microtrenches in shallow trench isolation (STI), *Plasma Process. Polym.* (2011) *Submitted for publication*

7. A Bogaert, C De Bie, M Eckert, V Georgieva, T Martens, E Neyts, and **S Tinck**, Modeling of the plasma chemistry and plasma–surface interactions in reactive plasmas, *Pure Appl. Chem.* 82 (2010) 1283–99

8. F Gou, E Neyts, M Eckert, **S Tinck** and A Bogaerts, Molecular dynamics simulations of Cl^+ etching on a Si(100) surface, *J. Appl. Phys.* 107 (2010) 113305

9. D Shamiryan, E Danilkin, **S Tinck**, M Klick, A Milenin, M Baklanov and W Boullart, Influence of the top chamber window temperature on the STI etch process, *ECS Transactions* 27 (2010) 731-36

Conference contributions

1. **S Tinck**, W boullart and A Bogaerts, Modeling of an Ar/Cl_2 ICP: effect of bias, power and pressure. **Poster presentation** at the 1st International workshop of Plasma Etch and Strip in Microelectronics (PESM 2007), 10-11 September 2007, Leuven, Belgium

2. **S Tinck**, W boullart and A Bogaerts, Simulation of $Ar/Cl_2/O_2$ inductively coupled plasmas used for anisotropic etching of silicon. **Poster presentation** at the 19th European Conference on the Atomic and Molecular Physics of Ionized Gases (ESCAMPIG 2008), 15-19 July 2008, Granada, Spain

3. **S Tinck**, W boullart and A Bogaerts, Numerical Simulations of inductively coupled plasmas used for etching applications. **Oral Presentation** at the 2nd International workshop of Plasma Etch and Strip in Microelectronics (PESM 2009), 26-27 February 2009, Leuven, Belgium

4. **S Tinck**, W boullart and A Bogaerts, Numerical simulations of inductively coupled plasmas used for STI etching. **Oral presentation** at the 62nd Annual Gaseous Electronics Conference (GEC 2009), 20-23 October 2009, Saratoga Springs, New York, USA

5. **S Tinck**, W boullart and A Bogaerts, Modeling the influence of gas composition in an $Ar/Cl_2/O_2$ inductively coupled plasma used for STI etching. **Poster presentation** at the 3rd International workshop of

Plasma Etch and Strip in Microelectronics (PESM 2010), 4-5 March 2010, Grenoble, France

6. **S Tinck**, W boullart and A Bogaerts, Modeling of $Ar/Cl_2/O_2$ and $Ar/SiH_4/O_2$ inductively coupled plasmas used for anisotropic etching of silicon and deposition of SiO_x. **Poster presentation** at the 20th European Conference on the Atomic and Molecular Physics of Ionized Gases (ESCAMPIG 2010), 13-17 July 2010, Novi Sad, Serbia

7. **S Tinck**, W boullart and A Bogaerts, Modeling $Ar/Cl_2/O_2$ and $Ar/SiH_4/O_2$ inductively coupled plasmas used for anisotropic etching of silicon and deposition of SiO_x. **Poster presentation** at the 63rd Gaseous Electronics Conference and 7th International Conference on Reactive Plasmas (GEC + ICRP 2010), 4-8 October 2010, Paris, France

8. **S Tinck**, W boullart and A Bogaerts, Simulating plasma + surface processes for the etching of Si with an $Ar/Cl_2/O_2$ inductively coupled plasma. **Oral presentation** at the 4th International workshop of Plasma Etch and Strip in Microelectronics (PESM 2011), 5-6 May 2011, Mechelen, Belgium

9. **S Tinck** and A Bogaerts, Computer modeling of inductively coupled plasmas: plasma chemistry and feature profile simulations for a better understanding of plasma etching and deposition. **Invited oral presentation** at the 3rd International Conference on Microelectronics and Plasma Technology (ICMAP 2011), 4-7 July 2011, Dalian, China

Bibliography

[1] Abaey J M Chandrakasan A Nikolic B 2003 *Digital Integrated Circuits, 2nd Edition.* ISBN 0130909963

[2] *International Technology Roadmap for Semiconductors* www.itrs.net

[3] Maini A K 2007 *Digital Electronics Principals, Devices and Applications.* ISBN 0470032145

[4] Williams J 1991 *Analog circuit design: Art, Science and Personalities.* ISBN 0750696400

[5] Thomas M Haveman R 1990 *CRC Press*, Boca Raton

[6] Moore G 1965 *Electronics* **38** (8)

[7] Garrou P Bower C Ramm P 2008 *Handbook of 3D Integration, Technology and Applications of 3D Integrated Circuits 2nd Edition.* ISBN 3527320349

[8] Borkar S 2011 *Proc. Design Autom. Conf.* 214–19

[9] Kaeslin H 2008 *Digital Integrated Circuit Design, from VLSI Architectures to CMOS Fabrication.* ISBN 0521882672

[10] Bogaerts A Neyts E Gijbels R Van der Mullen J 2002 *Spectrochim. Acta B* **57** 609-58

[11] Liebermann M Lichtenberg A 2005 *Principles of Plasma Discharges and Materials Processing* ISBN 0471720011

[12] *Lam Research Corporation* www.lamrc.com

[13] Helix M Vaidyanathan K Streetman B Dietrich H Chatterjee P 1978 *Thin Solid Films* **55**(1) 143-48

[14] Wolf S 2002 *Silicon processing for the VLSI Era, Vol. IV Deep-submicron Process Technology* ISBN 0961672171

[15] Gudmundsson J Kimura T Lieberman M 1999 *Plasma Sources Sci. Technol.* **8** 22-30

[16] Gudmundsson J Lieberman M 1998 *Plasma Sources Sci. Technol.* **7** 1-12

[17] Laidler K 1987 *Chemical Kinetics, 3d edition.* ISBN 0060438623

[18] Mohamed K King G Read F 1976 *J. Phys. B At. and Mol. Phys.* **9** 3159-64

[19] Malek K Coppens M 2003 *J. Chem. Phys.* **119** 2801-11

[20] Ashida S Liebermann M 1997 *Jpn. J. Appl. Phys.* **36** 854-61

[21] Perrin J Leroy O Bordage M *1996 Contrib. Plasma Phys.* **36** 3
[22] Jones J 1924 *Proc. R. Soc. Lond. A* **106** 463–77
[23] Gordillo-Vazquez F Albella J 2002 *Plasma Source Sci. Technol.* **11** 498–12
[24] Gordillo-Vazquez F Albella J 2003 *J. Appl. Phys.* **9** 6085–90
[25] Gordillo-Vazquez F Albella J 2004 *Plasma Source Sci. Technol.* **13** 50–57
[26] Smirnov B 2007 *Plasma Processes and Plasma Kinetics.* ISBN 3527406814
[27] Denysenko I Xu S Long J Rutkevych P Azarenkov N Ostrikov K 2004 *J. Appl. Phys.* **95** 2713–24.
[28] Yuji T Sung Y 2007 *IEEE Trans. Plasma Sci.* 35 1027–32
[29] Dorai R Kushner M *Semiconductor Research Corporation*, publication P006741
[30] Kolobov V Arslanbekov R 2003 *Microel. Engin.* **69** 606-15
[31] Kolobov V 2000 IEEE *International Conference on Plasma Science* 165
[32] Salabas A 2003 *Fluid Model for Charged Particle Transport in Capacitively Coupled Radio-frequency Discharges, PhD Thesis*
[33] Ostrikov K Yoon H Rider A Ligatchev V 2007 *Physica Scripta* **76** 187-95
[34] Ostrikov K Yoon H Rider A Vladimirov S 2007 *Plasma Proc. Polym.* **4** 27–40
[35] Oda A Suda Y Okita A 2008 *Thin Solid Films* 516 6570–74.
[36] Okita A Suda Y Ozeki A *et al.* 2006 *J. Appl. Phys.* **99** 014302
[37] Kroese D Taimre T Botev Z 2011 *Handbook of Monte Carlo Methods.* ISBN 0470177934
[38] Ivanov V Proshina O Rakhimova T Rakhimov A Herrebout D Bogaerts A 2002 *J. Appl. Phys.* **91** 6296–02
[39] Bultinck E Mahieu S Depla D Bogaerts A 2009 *Plasma Process. Polym.* **6** S784-88
[40] Bultinck E Bogaerts A *New J. Phys.* **11** 103010
[41] Bultinck E Mahieu S Depla D Bogaerts A 2009 *New J. Phys.* **11** 023039
[42] Baguer N Bogaerts A Donko Z Gijbels R Sadeghi N 2005 *J. Appl. Phys.* **97** 123305
[43] Bogaerts A 2009 *Spectrochimica Acta B* **64** 1266-79
[44] Bogaerts A 2009 *Spectrochimica Acta B* **64** 124-40
[45] Baguer N Bogaerts A Gijbels R 2003 *J. Appl. Phys.* **94** 2212-22
[46] Gou F Neyts E Eckert M Tinck S 2010 *J. Appl. Phys.* **107** 113305
[47] Georgieva V Todorov I Bogaerts A 2010 *Chem. Phys. Lett.* **485** 315-19
[48] Neyts E Bogaerts A 2006 *Phys. Chem. Chem. Phys.* **8** 2066-71
[49] Neyts E Bogaerts A Van de Sanden M 2006 *J. Phys. D: Appl. Phys.* **39** 1948-53
[50] Neyts E Bogaerts A Gijbels R Benedikt J Van de Sanden M 2005 *Nucl. Instr. Meth. Phys. Res. B* **228** 315-18
[51] Kushner M 2009 *J. Phys. D: Appl. Phys.* **42** 194013
[52] Ventzek P Grapperhaus M Kushner M 1994 *J. Vac. Sci. Technol. B* **12** 3118-37

[53] Yang Y 2010 *Modeling Discharge and Surface Processes in Capacitively Coupled Reactors, PhD thesis*

[54] Zhang D 2000 *Surface Reaction Mechanisms in Plasma Etching Processes, PhD thesis*

[55] Kinder R 2001 *Modeling of Wave Heated Discharges in Plasma Processing Reactors, PhD thesis*

[56] Subramonium P 2003 *Simulation of Transients and Transport in Plasma Processing Reactors, PhD thesis*

[57] Hoekstra R 1998 *A Model of Energy and Angular Distributions of Fluxes to the Substrate and Resulting Surface Topology for Plasma Etching Systems, PhD thesis*

[58] Vyas V 2005 *Transport in Low Pressure Plasma Reactors for Material Processing, PhD thesis*

[59] Sankaran A 2003 *Surface Reaction Mechanisms for plasma processing of Semiconductors, PhD thesis*

[60] Grapperhaus M 1998 *Multi-scale Transport Phenomena in Low-Pressure Plasmas, PhD thesis*

[61] Grapperhaus M and Kushner M 1997 *Appl. Phys.* **81** 569-77

[62] Ventzek P Hoekstra R Kushner M 1994 *J. Vac. Sci. Technol. B* **12** 461-77

[63] O'Mara W Herring R Hunt L 1990 *Handbook of Semiconductor Silicon Technology* ISBN 0815512370

[64] Aleksic J Zielke P Szymczyk J 2002 *Ann. of New York Ac. of Sci.* **972** 158-63

[65] Mahony C Escoffier C Maguire P Corr C Gomez S Costa E Bricha I Graham W 2001 American Physical Society 54th Annual Gaseous Electronics Conference, abstract JWP.026

[66] Lee Y Na S Song S Kim Y Lee N Ahn J 2003 *J Proc. Int. Symp. Dry Process.* **3** 167-72

[67] Shin M Na S Lee N Ahn J 2006 *Thin Solid Films* **506–507** 230–34

[68] Dong-Pyo K Kyoung-Tae K Chang-Il K Efremov A 2004 *Thin Solid Films* **447–448** 343–48

[69] Sung-Mo G Dong-Pyo K Kyoung-Tae K Chang-Il K 2005 *Thin Solid Films* **475** 313–17

[70] Efremov A Dong-Pyo K and Chang-Il K 2005 *Thin Solid Films* **471** 328–35

[71] Efremov A Gwan-Ha K Jong-Gyu K Bogomolov A Chang-Il K 2007 *Microelectron. Eng.* **84** 136–43

[72] Efremov A Dong-Pyo K Chang-Il K 2004 *Plasma Sci. IEEE Trans.* **32** 1344–51

[73] Fuller N Donnely V Herman I 2002 *J. Vac. Sci. Technol. A* **20** 170–73

[74] Subramonium P Kushner M 2002 *J. Vac. Sci. Technol. A* **20** 325–34

[75] Hoekstra R Kushner M 1996 *J. Appl. Phys.* **79** 2275–86
[76] Hoekstra R Kushner M 1995 *J. Appl. Phys.* **77** 3668–73
[77] Collison W Kushner M 1996 *Appl. Phys Lett.* **68** 903–05
[78] Tachibana K 1986 *Phys. Rev. A* **34** 1007–15
[79] Rapp J Englander-Golden P 1965 *J. Chem. Phys.* **43** 1464-79
[80] McFarland R Kinney J 1965 *Phys. Rev.* **137** A1058
[81] Rogoff G Kramer J Piejak R 1986 *IEEE Trans. Plasma Sci.* **14** 103–11
[82] Ellis H Pai R McDaniel E Mason E Viehland L 1976 *At. Data Nucl. Data Tables* **17** 177
[83] Ikezoe Y Matsuoka S Takabe M Viggiano A 1987 *Gas Phase Ion–Molecule Reaction Rate Constants through 1986* ISBN 1290030312
[84] *NIST Chemical Kinetics Database 17*, www.nist.gov
[85] Tinck S Boullart W Bogaerts A 2008 *J. Phys. D: Appl. Phys.* **41** 065207
[86] Hsu C Nierode M Coburn J Graves D 2006 *J. Phys. D: Appl. Phys.* **39** 3272–84
[87] Efremov A Kim D Kim C 2004 *Vacuum* **75** 237–46
[88] Thorsteinsson E Gudmundsson J 2010 *Plasma Sources Sci. Technol.* **19** 055008
[89] Bradley J Whytock D and Zalenski T 1973 *J. Chem. Soc. Faraday Trans. 1* **69** 1251–56
[90] Kim S Lieberman M Lichtenberg A 2006 *J. Vac. Sci. Technol. A* **24** 2025–40
[91] Baer S Hippler H Rahn R Siefke M Seitzinger N Troe J 1991 *J. Chem. Phys.* **95** 6463–70
[92] Gleason J Nesbitt F Stief L 1994 *J. Chem. Phys.* **98** 126–31
[93] Evans D Rosocha L Anderson G Coogan J 1993 *J. Appl. Phys.* **74** 5378–86
[94] O'Connor C Tafadar N Price S 1998 *J. Chem. Soc. Faraday Trans.* **94** 1797–03
[95] Flesch R Schürmann M Plenge J Hunnekuhl M Meiss H Bischof H Rühl E 1999 *Phys. Chem. Chem. Phys.* **1** 5423–28
[96] Sailer W Tegeder P Probs M Drexel H Grill V Scheier P Mason N Illenberg E Tilmann D 2001 *Chem. Phys. Lett.* **344** 471–78
[97] Bloss W Nickolaisen S Salawitch R Friedl R Sander S 2001 *J. Phys. Chem. A* **105** 11226–39
[98] Hanel G Fedor J Gstir B Probst M Scheier P Märk T D, Tegeder P Mason N 2002 *J. Phys. B: At. Mol. Opt. Phys.* **35** 589–99
[99] Zhu R Lin M 2003 *J. Chem. Phys.* **107** 3836–40
[100] Zhu R Lin M 2003 *J. Chem. Phys.* **118** 8645–55
[101] Lee C Graves D Lieberman M 1996 *Plasma Chem. Plasma Process.* **16** 99–120
[102] Hoekstra R Grapperhaus M Kushner M 1997 *J. Vac. Sci. Technol. A* **15** 1913–21
[103] Dane D Mantei T 1994 *Appl. Phys. Lett.* **65** 478–80

[104] Kielbauch M Graves D 2003 *J. Vac. Sci. Technol. A* **21** 116–26
[105] Agarwal A Kushner M 2008 *J. Vac. Sci. Technol. A* **26** 498–12
[106] Knizikevicius R 2006 *Appl. Surf. Sci.* **253** 1581–83
[107] Weaver G Leone S 1995 *Surf. Sci.* **328** 197–14
[108] Guo Q Sterratt D Williams E 1996 *Surf. Sci.* **356** 75–91
[109] Engstrom J Bonser D Engel T 1992 *Surf. Sci.* **268** 238–64
[110] Massoud H 1995 *Microelectron. Eng.* **28** 109–16
[111] Gusev E Lu H Gustafsson T Garfunkel E 1995 *Appl. Surf. Sci.* **104-105** 329–34
[112] Hildebrandt S Kraus A Kulla R Neddermeyer H 1999 *Appl. Surf. Sci.* **141** 294–304
[113] Daineka D Pradère F Châtelet M 2002 *Surf. Sci.* **519** 64–72
[114] Albao M Liu D Choi C Gordon M Evans J 2004 *Surf. Sci.* **555** 51–67
[115] Madix R Susu A 1970 *Surf. Sci.* **20** 377–400
[116] Davis J Mullins C 1997 *Surf. Sci. Lett.* **380** L513–20
[117] Manenschijn A Van Der Drift E Janssen G Radelaar S 1991 *Microelectron. Eng.* **13** 451–54
[118] Hacker D Marshall S Steinberg M 1960 *J. Chem. Phys.* **35** 1788–92
[119] Madix R Susu A 1972 *J. Catal.* **28** 316–21
[120] Kim Y Boudart M 1991 *Langmuir* **7** 2999–05
[121] Gordiets B Fereira C Nahorny J Pagnon D Touzeau M Vialle M 1995 *J. Phys. D: Appl. Phys.* **29** 1021–31
[122] Pantelides S Ramamoorthy M 1999 *J. NonCryst. Solids* **254** 38–56
[123] Matsuo S Yamamoto M Sadoh T Tsurushima T Gao D Furukawa K Nakashima H 2000 *J. Appl. Phys.* **88** 1664–69
[124] Balat-Pichelin M Badie J Berjoan R Boubert P 2003 *Chem. Phys.* **291** 181–94
[125] Franzreb K Lörincik J Williams P 2004 *Surf. Sci.* **573** 291–09
[126] Richard N Estève A Djafari-Rouhani M 2005 *Comput. Mater. Sci.* **33** 26–30
[127] Hemeryck A Richard N Estève A Djafari-Rouhani M 2007 *Surf. Sci.* **601** 2082–88
[128] Osano Y Ono K 2008 *J. Vac. Sci. Technol. B* **26**, 1425-39
[129] McNevin S 1990 J. *Vac. Sci. Technol. B* **8** 1185
[130] McNevin S 1991 *J. Vac. Sci. Technol. A* **9** 816
[131] Tinck S Boullart W Bogaerts A 2009 *J. Phys. D: Appl. Phys.* **42** 095204
[132] Cunge G Sadeghi N Ramos R 2007 *J. Appl. Phys.* **102** 093305
[133] Kim T Aydil E 2003 *J. Electrochem. Soc.* **150** G418–27
[134] Kogelschatz M Cunge G Sadeghi N 2004 *J. Vac. Sci. Technol. A* **22** 624–35
[135] Cunge G Vempaire D Ramos R Touzeau M Joubert O Bodard P Sadeghi N 2010 *Plasma Sources Sci. Technol.* **19** 034017

[136] Cunge G Sadeghi N Ramos R 2007 *J. Appl. Phys.* **102** 093304
[137] Materer N Goodman R Leone S 2000 *J. Phys. Chem. B* **104** 3261–66
[138] Materer N Goodman R Leone S 2000 *J. Vac. Sci. Technol. B* **18** 191–96
[139] Guha J Donnely V 2009 *J. Vac. Sci. Technol. A* **27** 515–20
[140] Kovalgin A Boogaard A Brunets I Holleman J Schmitz J 2007 *Surf. & Coat. Tech.* **201** 8849-53
[141] Kushner M 1988 *J. Appl. Phys.* **63** 2532-51
[142] Kushner M 1993 *J. Appl. Phys.* **74** 6538-53
[143] De Bleecker K Herrebout D Bogaerts A Gijbels R Descamps P 2003 *J. Phys. D: Appl. Phys.* **36** 1826-33
[144] Chang C McVittie J Li J Saraswat K 1993 *IEDM* **93** 853-56
[145] Hsiau Z Kan E McVittie J Dutton R 1997 *IEEE Trans. on Elec. Dev.* **44** 1375-85
[146] Moylan C Green S Brauman J 1990 *Int. J. Mass Spectrom. Ion Process.* **96** 299–07
[147] Kouznetsov I Lichtenberg A Lieberman M 1996 *Plasma Sources Sci. Technol.* **5** 662–76
[148] Kossyi I Kostinsky A Matveyev A Silakov V 1992 *Plasma Sources Sci. Technol.* **1** 207–20
[149] Kleinert P Schmidt D Kirchhof J Funke A 1980 *Krist. Tech.* **15** 85–90
[150] Vitale S Smith B 2003 *J. Vac. Sci. Technol. B* **21** 2205–11
[151] Tinck S Bogaerts A 2011 *Plasma Sources Sci. Technol.* **20** 015008
[152] Kimura T Lichtenberg A Lieberman M 2001 *Plasma Sources Sci. Technol.* **10** 430–39
[153] Panda S Economou D Meyyappan M 2000 *J. Appl. Phys.* **87** 8323–33
[154] Eliasson B Hirth M Kogelschatz U 1987 *J. Phys. D: Appl. Phys.* **20** 1421–37
[155] Sommerer T Kushner M 1992 *J. Appl. Phys.* **71** 1654–73
[156] Moravej M Yang X Hicks R Penelon J Babayan S 2006 *J. Appl. Phys.* **99** 093305
[157] Becker K Mahoney J Gutkin M Tarnovsky V Basner R 2006 *Japan. J. Appl. Phys.* **45** 8188–91
[158] Basner R Gutkin M Mahoney J Tarnovsky V Deutch H Becker K 2005 *J. Chem. Phys.* **123** 054313
[159] Gutkin M Mahoney J Tarnovsky V Deutch H Becker K 2009 *Int. J. Mass Spectrom.* **280** 101–06
[160] Mahoney J Tarnovsky V Becker K 2008 *Eur. Phys. J. D* **46** 289–93
[161] Husain D Norris P 1978 *J. Chem. Soc. Faraday Trans. 2* **74** 106–14
[162] Le Picard S Canosa A Reignier D Stoecklin T 2002 *Phys. Chem. Chem. Phys.* **4** 3659–64

[163] Joshipura K Vaishnav B Gangopadhyay S 2007 *Int. J. Mass Spectrom.* **261** 146–51
[164] Matsunami N Yamamura Y Itikawa Y Itoh N Kazumata Y Miyagawa S Morita K Shimizu R Tawara H 1984 *At. Data Nucl. Data Tables* **31** 1–80
[165] Smentkowski V 2000 *Prog. Surf. Sci.* **64** 1–58
[166] Collart E Visser R 1989 *Surf. Sci. Lett.* **218** L497–04
[167] Lang B 1989 *Appl. Surf. Sci.* **37** 63–77
[168] Mizutani T 1995 *J. Non-Cryst. Solids* **181** 123–34
[169] Seah M Nunney T 2010 *J. Phys. D: Appl. Phys.* **43** 253001
[170] Bogart K Donnely V 2000 *J. Appl. Phys.* **87** 8351–60
[171] Bogaerts A Gijbels R 2002 *Spectrochimica Acta B* **57** 1071-99
[172] Corrigan S 1965 *J. Chem. Phys.* **43** 4381-86
[173] Hayashi M 1979 *J Phys-Paris* **40** 45-46
[174] Chan C 1983 *Reaction cross-sections and rate coefficients related to the production of positive ions, Lawrence Berkeley Lab. Report No.* LBID-632
[175] Banks P 1966 *Planet. Sp. Sci.* **14** 1085-03
[176] Kessels W Nadir K Van De Sanden M 2006 *J . Appl. Phys.* **99** 076110
[177] Atkinson R Baulch D Cox R Crowley J Hampson R Hynes R Jenkin M Rossi M Troe J 2004 *Atmos. Chem. Phys.* **4** 1461-38
[178] Ramalingam S Maroudas D Aydil E Walch S 1998 *Surf. Sci.* **418** L8-13
[179] Walch S Ramalingam S Sriraman S Aydil E Maroudas D 2001 *Chem. Phys. Lett.* **344** 249-55
[180] Sriraman S Aydil E Maroudas D 2004 *J. Appl. Phys.* **95** 1792-04
[181] Agarwal S Valipa M Hoex B Van De Sanden M Maroudas D Aydil E 2005 *Surf. Sci.* **598** 35-44
[182] Amantides E Stamou S Mataras D 2001 *J. Appl. Phys.* **90** 5786-98
[183] Sriraman S Valipa M Aydil E Maroudas D 2006 *J. Appl. Phys.* **100** 053514
[184] Agarwal S Sriraman S Takano A Van De Sanden M Aydil E Maroudas D 2002 *Surf. Sci. Lett.* **515** L469-74
[185] Sriraman S Agarwal S Aydil E Maroudas D 2002 *Nature* **418** 62-65
[186] Kim D Lee G Lee S Kim D 2006 *J. Cryst. Growth* **286** 71-77
[187] Vasenkov V Kushner M 2003 *J. Appl. Phys.* **94** 5522–29
[188] Ventzek P Sommerer T Hoekstra R Kushner M 1993 *Appl. Phys. Lett.* **63** 605–07
[189] Subramonium P Kushner M 2001 *Appl. Phys. Lett.* **79** 2145–47
[190] Collison W Ni T Barnes M 1998 *J. Vac. Sci. Technol. A* **16** 100–07
[191] Rauf S Kushner M 1997 *J. Appl. Phys.* **81** 5966–74

[192] Shamyrian D Danilkin E Tinck S Klick M Milenin A Baklanov M Boullart W 2010 *ECS Trans.* **27** 731-36

[193] Tuda M Ono K Nishikawa K 1996 *J. Vac. Sci. Technol. B* **14** 3291-98

[194] Chen Y Yuan H Zhang Z Li N Chan D Chen J Li X Zhao G 2010 *ECS Trans.* **27** 679-83

[195] Nishimura H Takagi S Fujino M Nishi N 2002 *Jpn. J. Appl. Phys.* **41** 2886-93

[196] Boogaard A Kovalgin A Brunets I Aarnink A Holleman J Wolters R Schmitz J 2007 *Surf. & Coat. Tech.* **201** 8976-80

[197] Park Y Rhee S 2004 *Surf. & Coat. Tech.* **179** 229-36

[198] Schaekers M IMEC *private communication*